UNIVERSITAT DE BARCELONA

DEPARTAMENT DE QUÍMICA FÍSICA

PROBING THE PASSIVITY OF IRON BY ELECTROCHEMICAL SCANNING TUNNELING MICROSCOPY AND SPECTROSCOPY

Ismael Díez-Pérez

TESIS DOCTORAL

UNIVERSITAT DE BARCELONA

DEPARTAMENT DE QUÍMICA FÍSICA

Programa de Doctorat de: **Química**. Química Física.
Bienni 1999-2001

PROBING THE PASSIVITY OF IRON BY ELECTROCHEMICAL SCANNING TUNNELING MICROSCOPY AND SPECTROSCOPY

Memòria que presenta Ismael Díez-Pérez per optar al títol de Doctor per la Universitat de Barcelona.

Directors:

FAUSTO SANZ CARRASCO
Catedràtic del Departament de Química Física de la Universitat de Barcelona,
PAU GOROSTIZA LANGA
Investigador Ramón i Cajal de la Universitat de Barcelona

Barcelona, octubre de 2006

A mi família

Contents

Preface 1

STATE OF THE ART AND MOTIVATION 1
The history of passivity 1
Motivation 3
OBJECTIVES 5
STRUCTURE 6

Chapter 1: The oxide│solution interface 9

1.1 THE SEMICONDUCTOR│SOLUTION INTERFACE 9

1.1.1 Introduction 9
1.1.2 Charge distribution at the semiconductor│liquid interface 10
1.1.2.1 Previous background 10
1.1.2.2 The origin of the electrical double layers 12
1.1.2.3 The electrochemical (electrolyte) double layer 14
The Helmholtz Double Layer 15
The Diffuse Double Layer 16
Specific ions adsorption 17
1.1.2.4 The space charge region in the semiconductor 19
Basic concepts 19
Charge distribution and Capacitance behavior in the semiconductor SCL 23
Surface States 29
1.1.2.5 Building up the diagram of the semiconductor│electrolyte interface 33
1.1.3 Electron transfer at the semiconductor│liquid interface 34
1.1.3.1 General 34
1.1.3.2 Electron transfer across the semiconductor SCL 39
Kinetics under depletion conditions 40
Kinetics under accumulation: degenerated semiconductor 45
Kinetics at deep depletion 46
1.1.3.3 Diffusion-controlled electron transfer 47

1.2 IMPACT OF THE SEMICONDUCTOR MODEL ON PASSIVE FILMS 50

1.2.1 General 50
1.2.2 Thermodynamic aspects 51

1.2.3 The band model on oxide films 52
1.2.3.1 Main trends 52
1.2.3.2 Nature of the highly defective oxide structure 54
1.2.3.3 Mobility gap 57
1.2.3.4 Surface and Interface states 58
1.2.4 Current transport through oxide films 58
1.2.4.1 General 58
1.2.4.2 Models for the passive film growth: ionic transport 60
Mott-Cabrera model 60
Sato and Cohen's model 61
Fehlner and Mott's model 63
Point Defect Model (PDM) 64
1.2.4.3 Electronic transport in passive films 67
Tunneling regime through thin passive films 68
Electronic conduction through thick semiconducting passive films 69
Electronic conduction through thick insulating passive films 71
1.2.4.4 The role of the passive film in metal corrosion 71
Classical view 72
Semiconductor view 74

1.3 *In situ* STUDIES OF METAL PASSIVE FILMS 79

1.3.1 Introduction 79
1.3.2 Recent advances on the electrochemical characterization 80
1.3.3 *In situ* structural and chemical properties 83
1.3.4 *In situ* studies of passive film growth dynamics and electronic properties by SPM techniques 86
1.3.5 *In situ* measurements of passive film breakdown in chloride media 88

Chapter 2: Experimental developments 91

2.1 GENERAL 91

2.2 FUNDAMENTALS OF STM 92

2.2.1 Origin and operation mode 92
2.2.2 Tunneling formalism 92
2.2.2.1 General models 92
2.2.2.2 The ECTSM model 94

2.3 ELECTROCHEMISTRY IN SCANNING PROBE MICROSCOPY: BASIC CONCEPTS AND APPLICATIONS 95

2.4 PREPARATION OF RELIABLE PROBES FOR ELECTROCHEMICAL TUNNELING SPECTROSCOPY 107

2.5 ELECTROCHEMICAL TUNNELING SPECTROSCOPY TO FINGERPRINT ELECTRODE ELECTRONIC STRUCTURE 115

Chapter 3: Fe passivity: electrochemistry and ECSTM 131

3.1 GENERAL 131

3.2 FIRST STAGES OF THE ELECTROCHEMICAL GROWTH OF THE PASSIVE FILM ON IRON 133

3.3 THE CATHODIC REDUCTION OF THE IRON PASSIVE FILM GROWN ON UNTRA-FLAT IRON THIN FIMS 143

Chapter 4: Fe passivity: *in situ* electronic structure 169

4.1 GENERAL 169

4.2 DIRECT EVIDENCE OF THE ELECTRONIC CONDUCTION OF THE PASSIVE FILM ON IRON BY ECSTM 171

4.3 ELECTRONIC BARRIERS IN THE IRON OXIDE FILM GOVERN ITS PASSIVITY AND REDOX BEHAVIOR: EFFCT OF ELECTRODE POTENTIAL AND SOLUTION pH 181

Chapter 5: Fe passivity breakdown in chloride media 195

5.1 GENERAL 195

5.2 THE IRON PASSIVE FILM BREAKDOWN IN CHLORIDE MEDIA MAY BE MEDIATED BY TRANSIENT CHLORIDE-INDUCED SURFACE STATES LOCATED WITHIN THE BAND GAP 197

Chapter 6: Conclusions 209

Appendix A: ECTS studies of thiol-modified Au(111) 213

A.1 INTRODUCTION 213

A.2 EXPERIMENTAL DETAILS 214
Sample preparation 214
Voltammetry 214
ECSTM & ECTS measurements 214

A.3 RESULTS AND DISCUSSION 216
A.3.1 Electrochemical and ECSTM characterization 216
A.3.2 Barrier height (ϕ_B) measurements 218
A.3.3 ECTS measurements 220

A.4 CONCLUSIONS 221

Appendix B: Symbols and acronyms 223

Appendix C: Selected publications 229

Appendix D: Resum en català 233

Agraïments 257

References 261

Preface

STATE OF THE ART AND MOTIVATION

The history of passivity

I am still particularly surprised that after almost two centuries since the first *formal* description of *passivation* as: “a thermodynamically expected metal dissolution reaction under certain conditions is kinetically hindered by orders of magnitude” by Schönbein in 1836 [1], it is still today a matter of strong debate that generates an important amount of scientific documents (communications, papers, reviews or even specialized books). Why has it brought such a wild interest to engineers and scientists? Since *passivity breakdown* is one of the main causes of material *corrosion*, the answer appears to be quite straight forward: in 2002, corrosion drained about 3.1 % of the gross domestic product (GDP) from the US economy, and in 2004, its direct economy lost was about $364 billion which equals the losses associated with hurricane *Katrina*. Same dramatic effects can be also found in most of the industrialized countries around Europe, which score around a 3-4 % lost of their total economy. I found a particular guessed right comment in the march 2006 edition of *Materialstoday* made by Bob Rapp from the Ohio State University in his article *“Corrosion, a study of degradation”*. He pointed out referring corrosion phenomena: “since we bear this hidden loss every year, corrosion is the largest continuing technical calamity of our time”. This is indeed the real *leitmotiv* that has driven so many researchers to find out the possible pathways of corrosion of metal and alloys with outstanding industrial applications, *e. g*. Fe, Cu, Ni, steels, magnetic alloys among others. The last consequence of this situation was the emerging of a new field called *Corrosion Science and Engineering* which actually joins a large amount of adepts and has relevant symposiums in the main electrochemical and solid-state technology meetings. Increasing the amount of knowledge on corrosion mechanisms will assist on designing new and more robust methods of corrosion protection. As a quick picture, some quotidian engineering systems whose reliable performance and safety depend upon corrosion protection, are: ships and oil platforms in ocean and seas, electronic circuit boards, buried pipelines, prosthesis body parts, transportation vehicles (cars, trucks and airplanes), food packaging, tanks for storage of chemicals or water purification plants.

In order to see the scientific environment where passivity and corrosion field are framed, let us give now a quick chronologic tour around the fundamental studies on metal passivity and corrosion. Originally, they have been approached from the Electrochemistry discipline; the standard electrochemical three-electrode configuration has offered the possibility to accurately control the kinetics of the redox processes that occur on the metal electrode surface during its passivation and/or corrosion in a certain aqueous electrolyte. For decades, aqueous corrosion was an exclusive matter of the so-called conventional electrochemical techniques (corrosion potential, galvanostatic and potentiostatic measurements, chrono-amperommetry, cyclic voltammetry, etc.). They brought the first fundamental descriptions of the most reasonable (electro)chemical reactions pathways to explain electrode passivation and corrosion behavior of a huge variety of metal electrodes in contact to different aqueous environments. Following up this line, Impedance Electrochemical Spectroscopy (EIS) techniques allowed to elaborate the first quantitative electrical models of the passive

film│electrolyte interface in the way of gaining knowledge on its electronic properties. But it was not until the middle of the 20th century when Mott and Schottky [2,3] separately fixed the basis of the semiconductor model approach for oxide passive film on metals by demonstrating for the first time the rectifying properties of metal│semiconductor contacts. It represented the beginning of the *gold rush* for metal passivity which reached its highest splendor with the advent of Gerischer's model in the sixties [4]. Within the later 20 years, many researchers used systematically this semiconductor theory for quantitatively interpreting the kinetics of electron and ion transfer reactions (ETR and ITR) at passive metal│electrolyte interfaces. Special mention has the works of Sato in the eighties [5] who extended Gerischer's model to explain the onset of some well-known electrochemical processes responsible of the electrode corrosion: transpassivity and pitting breakdown.

Another important challenge on metal passive layers has been the elucidation of its chemical and crystalline structure. The atomic organization of the passive film is important since it often determines the electrical properties that finally control its protecting or passivating character. Likewise, structural defects also play an important role in passive film growth and corrosion. A considerable amount of *ex situ* spectroscopic data has been already collected from the middle of the past century until the present time [6,7]. However, concern about possible structural changes on the passive film during the electrode excursion from the wet electrochemical environment to the spectroscopic chamber for *ex situ* experiments, has placed emphasis on the use of *in situ* spectroscopic methods to study film structure and chemistry of the oxide layer│electrolyte interface [8-13]. Major technical advances on this mean have taken place during the last 2 decades and they will be reviewed in detail in section 1.3. To mention the most relevant, the work of Davenport *et al.* [12,13] on iron passive films has become, up to now, one of the most cited structural models for the Fe passive layer. Among the most employed synchrotron radiation techniques, high resolution *in situ X-ray absorption near edge* (XANES) and *in situ* synchrotron *X-ray diffraction* (XRD) have been the most fruitful spectroscopic techniques to resolve the structure and chemistry of these oxide thin layers under electrochemical control. Ongoing projects in this direction are actually under course in our lab, trying to overcome the experimental challenges derived from the implementation of the electrochemical set up in the synchrotron line.

Finally, it is also worthy to highlight the contributions of the ancient *scanning probe microscopy* (SPM) techniques to the Corrosion Science field. Since the first demonstration in 1986 by Bard and coworkers [14], of the SPM capability to work in a liquid environment under electrochemical control, some examples of their use on passive films started to timidly arise in the bibliography [15,16]. At this point, I would like to point out the pioneer work presented by O'Bockris at early nineties [17], showing the first real *Electrochemical Scanning Tunneling Microscopy* (ECSTM) topographical images at the nanoscale of an iron electrode surface while it is reversibly oxidized in a borate buffer solution. Although their experimental limitations, I have to recognize my great devotion for this document which represented the starting point of our research, and, from my point of view, it opened up a broad fan of possibilities. Nowadays, it is a matter of fact that SPM techniques have brought important contributions to the Electrochemistry field in a wide manner. If one performs a quick search within the last 5 years in any scientific database with the fields "electrochemistry" and "STM or AFM", you will get more than 100 hints, some of them linked to prestigious journals like *science* or *nature*. It is a clear proof of the continuous development that SPM techniques are

experienced, which extends also to other scientific disciplines in the same order of magnitude. In the scenario of passivity, we can find recent examples of Ryan and Marcus [18-20] on iron and copper passive films respectively, most of them stemming yet from the actual decade, that demonstrate the real capability of the ECSTM technique to get direct *in situ* atomic resolution of the oxide passive layers (see section 1.3 for further details). The major problems to interpret *in situ* STM data on semiconducting oxides, like most passive films on metals, arise from the poor consensus concerning the tunneling conditions for the proper probe of the oxide surface. For this purpose, a quantitative knowledge of the electronic distribution levels of the oxide│liquid interface is required. This is probably the main lack of information and requires of a special attention in order to elaborate an in-depth study. All these issues are treated in this Ph.D. which will constitute the main block of this work.

After this brief excursion along the history of *passivity*, we can state that we face a strongly multidisciplinary matter whose major advances have taken place thanks to the close interaction with other fields like: solid state physics, surface science, chemical equilibrium, advanced spectroscopic and microscopic techniques, everything managed in an electrochemical environment. From a general point of view, I would say that *passivity* and, more generally, *aqueous corrosion* has progressed in a stepwise fashion taking profit of the new technical and/or scientific advances on other fields. And there seems to be no end in sight.

Motivation

This Ph.D. was born in a privileged scenario. When we embarked in this Ph.D. project at the Physical Chemistry department, we had all elements required to submerge into the interdisciplinary field of *passive films*. Our research group works as a part of the *Laboratory of Electrochemistry and Materials* (LCTEM), with more than 20 years experience on applied electrochemical processes like Ni and Zn electroplating on iron-based substrates [21,22]. At that time, there was a great interest on gaining a more fundamental picture of the passivation-corrosion mechanisms that developed on the surface of the employed substrates. This Ph.D. adventure had its beginning on some preliminary attempts where we observed that the presence of an electrochemically growth passive film on an iron electrode surface could determine the properties of the electroplated coating deposited on top. To illustrate this phenomenon, figure 1 shows the first stages of Zn electrodeposition onto two different iron polycrystalline substrates, a routine process on many industrial applications. At first sight, it is evident that the coating morphology on the previously passivated surface (Fig. 1A) completely differs from the oxide-free one (Fig. 1B), and their final properties like hardness, corrosion resistance or surface roughness, will be strongly affected by the initial surface state. Soon did we realize that the presence of a passive film is definitely far from being a mere physical barrier and that its electric properties strongly determine the redox behavior of the electrode underneath. At this point, we were prompted to invest our efforts on elaborating a **quantitative** picture of the electronic band diagram of the Fe│passive film│electrolyte contact which, in turn, will provide us of the necessary background to explain the first stages of any redox process that is developed on the oxide│electrolyte interface including the oxidation-reduction of the passive film itself and the passive film breakdown.

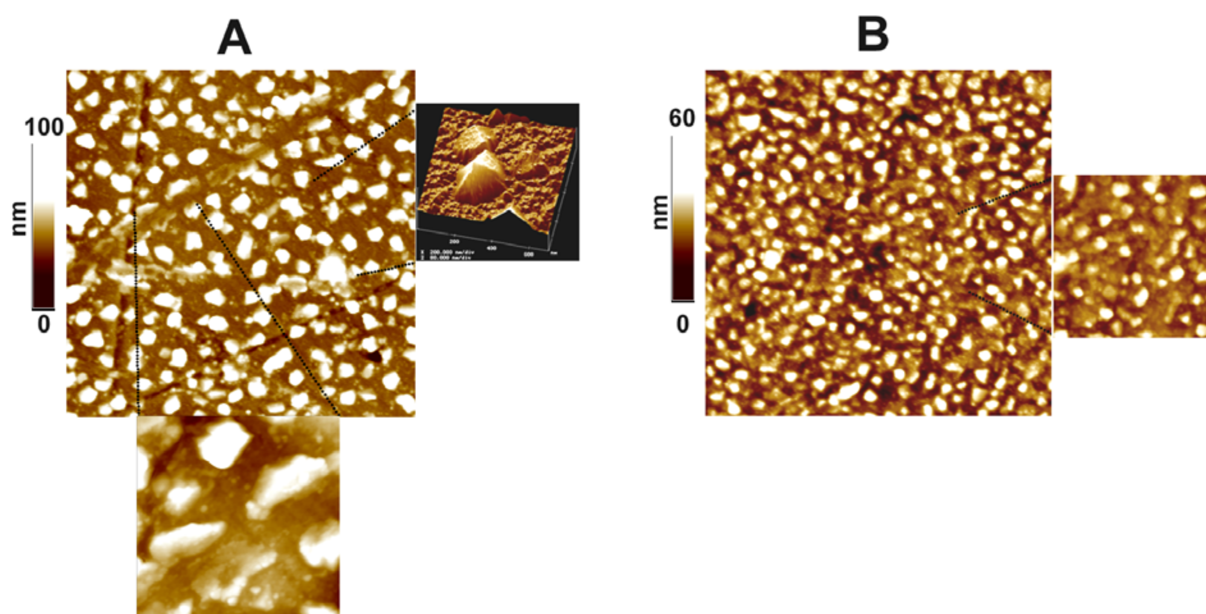

Figure 1: *Atomic Fore Microscopy* images showing first stages of Zn electrodeposition on a: (A) passivated Fe and (B) free-oxide Fe substrates. Main images are 5x5 μm^2 and some zooms are 3x3 and 2x2 μm^2 respectively.

The starting perspectives of such a project were, indeed, quite promising. On the one hand, the recent Ph.D. thesis entitled: "*Metal deposition on silicon from fluoride solutions*" carried out by Pau Gorostiza, seated the basis of *Semiconductor Electrochemistry* in our lab. On the other hand, our research group was, at that time, embarked in a parallel project which involved the use of SPM techniques as the principal characterization methods. Merging both fields, the structure of this Ph.D. was then outlined. After an initial electrochemical characterization of the system in the LCTEM lab, we succeed in coupling our three-electrode configuration into an STM microscope. Special efforts were put on the cell design which finally resulted in a robust ECSTM system that allowed the first *in situ* topographic and electric measurements of the Fe oxide│borate buffer interface under a strict electrochemical control (see section 2.3). Additional *ex situ* microscopy and spectroscopy techniques were also used in combination to elaborate the first oxide growth mechanism and the quantitative electronic band diagram picture of the interface. Convinced that the different transitions of the electronic properties on the iron oxide surface governed its passivity and redox behavior, we wanted to go further in its electrical characterization and were embarked in the design of a new methodology to perform real *electrochemical tunneling spectroscopy* (ECTS). Although its experimental realization had been previously demonstrated on other ideal semiconducting electrodes [23,24], several technical difficulties had braked its wide fan of possibilities. Within the last two years of this Ph.D, we have invested efforts to solve the main technical problems and presented by the first time a novel procedure to record reproducible *in situ* electronic spectra of an electrode│electrolyte interface as a function of the oxidation state of the substrate (see sections 2.4 and 2.5). Their benefits go far beyond this study as we will see in the *Appendix A* of this Ph.D. Indeed, the studied reversible iron oxidation process constituted an unbeatable warming-up system to validate the new methodology. We found especially advantageous the combination of ECTS with the capacitance data of the same interface on determining its corresponding band diagram in a quantitative energy scale.

Finally, the last year of the Ph.D. work have been devoted to the analysis and interpretation of the *in situ* tunneling spectroscopy data which have been employed firstly, to elaborate a complete mechanism of the formation and dissolution of the iron passive layer as well as to revisit the concept of *passivity* from an electronic point of view. All these background was finally used on the quantitative electronic characterization of the passivity breakdown process of an iron electrode in the presence of chloride. The picture deduced in this last study is probably the highest impact feature of the present work since it directly addresses to the real capabilities that the technique shows on a dynamic process of remarkable technical impact. Actually, our research group has put continuity on this project and the developed methodology here is being employed at some research lines. In short, *in situ* measurements of the electronic properties of Au thiol-modified electrodes or the study of the charge transfer mechanisms through redox biological molecules are currently under course.

The realization of this Ph.D. Thesis required of a solid training stage on both semiconductor electrochemistry and SPM fields. An important part of the knowledge on SPM techniques was acquired during my fruitful stage at Miquel Salmeron's lab in the Lawrence Berkeley National Lab (Berkeley, CA) in 2000, where I familiarized with advance SPM working modes. Later on, a second stay in 2003 at Philippe Allongue's lab served to reinforce some of the basic concepts of semiconductor electrochemistry mainly concerning capacitance responses and other practical aspects.

OBJECTIVES

The main goal of this Ph.D. Thesis is to reach an *in situ* quantitative picture of the redox behavior of a passivated iron electrode in its working electrolyte. We know that this is a highly ambitious objective and so it is necessary to overcome some previous characterization stages to reach the final goal. Of course, an accurate preliminary electrochemical characterization of the system is firstly required. Then, it is essential to look at the *in situ* kinetic characterization of the oxide growth in the whole iron electrochemical range in order to analyze its topography, thickness and growth behavior. Next stage is to *in situ* characterize the electronic properties of the iron electrode surface, also within the entire electrochemical range, since they mostly govern its redox reactivity. Both major objectives need of a novel *in situ* electrochemical methodology to be developed. The final results of these experiments will bring a complete quantitative view of the redox behavior of the iron electrode in its entire electrochemical potential range, and the deduced model in the passive region will serve to explain outstanding redox processes that take place on these surfaces like for example passivity breakdown in the presence of chloride. While accounting for the classical concepts of semiconductor electrochemistry, the final models must take into account also the recent advances in the structural and chemical characterization. Although *in situ* electrochemical techniques have been the most employed in this work, additional *ex situ* microscopic and spectroscopic characterization has been eventually used.

STRUCTURE

This Ph.D. Thesis is presented in the *journal format*. It means that the main results will be given as the presentation of the corresponding publications in *Peer Review* journals of the field. The general structure has been built in three separated blocks: the first block, composed by two chapters, settles the necessary scientific and technical background for the discussion and interpretations of results:

- **Chapter 1** is intended to be a general introduction that begins with a quick overview to the basic concepts of the semiconductor electrochemistry with special emphasis on the thermodynamic description of the semiconductor | solution interface. Next, the kinetics of the electron transfer on a semiconductor electrode is also outlined and compared to the metal case. In the next section of this chapter, the previous background is used to briefly descript the general semiconductor models for the oxide passive film case and also to revisit the concept of passivity. This chapter ends with a detailed summary of the most recent advances regarding fundamental studies of the passivation-corrosion process on metal electrodes by using *in situ* techniques. Special care is taken on *in situ* structural and electrical characterization methods on metal passive films. Although our contributions in this review have been omitted from this section, they will be soon found in the original publication (*Current Opinion in Solid State & Materials*, 2006, submitted). Along this introduction, the iron passive film is especially reviewed as the main system of interest.

- **Chapter 2** deals with the detailed description of our ECSTM experimental setup and the methodology employed to perform reliable electrochemical tunneling spectroscopy of the electrode | solution interface. The principles of the technique as well as our main technical contributions are described. Since these data constitute an important contribution of this thesis, they are presented in three different publications: (a) Electrochemistry in *Scanning Probe Microscopy: Basic Concepts and Applications*. Phantom Report (2003), (b) *Anal. Chem.* **76** (2004) 5218 and (c) *Anal. Chem.* (2006) *in press*. On the whole, these results settle the main experimental basis for our forthcoming studies.

The second block corresponds to the main experimental block of this Ph.D. It is presented within the next three chapters and deal with the electrochemical studies of passivation and corrosion processes of a polycrystalline iron electrode:

- **Chapter 3** includes sample preparation procedures and previous *ex situ* topographic and spectroscopic characterization of the polycrystalline iron electrodes. A summary of the electrochemical characterization at different pHs is also presented as well as a complete *in situ* study of the kinetics of the iron oxide growth by ECSTM. The results are presented in an extensive journal (*J. Electrochem. Soc.* **148** (2001) B307) which has, as the main aim, merging all the scattered data on electrochemical iron oxide growth and going deeper into some of the most critical points of its mechanisms. This section finishes with a parallel study of the passivation on well-defined iron thin film substrates that complements previous electrochemical characterization and allows to complete the chemical mechanisms of the iron passive film formation and reduction. This work has been submitted to *J. Phys. Chem. B* (2006).

- **Chapter 4** begins with the first results on the electronic properties of the iron passive film probed by ECSTM imaging and first quantification of the semiconducting properties

of the iron passive film. These results are presented on a separate publication (*J. Electrochem. Soc.* **150** (2003) B348). The second part is devoted to the *in situ* examination of the electronic properties during the entire oxidation process of the iron electrode, from its metallic state until its final surface passivation. This study involves the *in situ* records of electronic spectra (presented in the form of *Conductograms*) and the measurement of surface energy barriers, both by the ECTS technique. Their posterior quantification is intended to be used as a model to predict the electrode reactivity in a certain electrolytic medium. The details of this part are picked up in a recent publication (*Electrochem. Commun*. **8** (2006) 1595).

- **Chapter 5** tackles into the fundamental view of the passivity breakdown on the iron surface in the presence of chloride anions. The methodology described in the previous chapter is here used to describe the influence of chloride anions on the electronic properties of the iron passive film and how these changes can ultimately take to the onset of the electrode corrosion. Some additional *ex situ* characterization is also perform in order to give a complete picture of the first stages of this outstanding process. Again, results are presented in the form of publication (*Electrochem. Commun.*, **8** (2006) 627).

The last block includes chapter 6 and *Appendixes*:

- **Chapter 6** corresponds to the general conclusion of the Ph.D. Thesis.

Appendix A is an example of the capability of this ECTS methodology that is presented as a preliminary study of the *in situ* electronic properties of functionalized gold electrodes with a simple decanethiol molecule. This way, we want to test the applicability of this technique to study the electrochemical reactivity of a completely different interface (Au | thiol | electrolyte) which has an enormous impact on microelectronics engineering. *Appendixes B* and *C* correspond respectively to a detailed list with the symbols and acronyms employed throughout the text and a list of selected publications related to this PhD. work.

Chapter 1

The oxide | solution interface

1.1 THE SEMICONDUCTOR | SOLUTION INTERFACE

1.1.1 Introduction

In the *Electrochemistry* discipline, the electrode has been traditionally considered as a mere source or sink of electrons provided by a low resistivity electronic conductor. Today, it is clear that the chemical reactivity of electrode surfaces play an important role in many outstanding fields like electro-catalysis, corrosion, crystal growth or electro-sensing, and that this reactivity is directly related to the particular distribution of energy levels at the solid | electrolyte interface. The use of semiconductor electrodes has experienced a tremendous increase in the previous mentioned fields. The ET (ET) at semiconductor | electrolyte interfaces proceeds only through discrete energy levels, i.e., via the conduction or the valence band or via surface states, and therefore, not only the amount of electrons (as occurs on metal electrodes) but also the electron energy, become now the relevant parameters. This fact implies that reactions occurring on a semiconductor electrode depend not only on the applied potential, but also on the availability of free charge carriers at the electrode surface. The modern work of *Semiconductor Electrochemistry* dates back to mid-1950's when the first protocols to prepare well-oriented germanium and silicon single crystals became available [25]. Since then, the study of semiconductor electrodes has strongly influenced the concepts of electrochemistry, and its scientific impetus has been, to a large extend, motivated by their immediate industrial applications on photo-electrochemical energy conversion devices (solar cells) [26], photo-detoxification plants of organic waste [27], etching processes and device fabrication in microelectronics [28] or photo-plating and photography [29]. As deduced from the above lines, semiconductor electrochemistry is a rich interdisciplinary matter (even in its name) that constitutes the meeting-point among (electro)chemistry and solid-state physics.

Within the next sections of this chapter, we will introduce the main concepts that will be needed for a quantitative interpretation of the experimental results presented in the forthcoming chapters 2, 3, 4 and 5. Rather than presenting an exhaustive review, we pretend to outline the main features of the energy diagram at the semiconductor | electrolyte interface, with special emphasis on the semiconductor side, which is the less familiar part from a pure electrochemical point of view. For an extended review, check [30-32].

1.1.2 Charge distribution at the semiconductor | liquid interface

1.1.2.1 Previous background

Within the next lines we are going to descript the general picture of the electron energy distribution resulting when a semiconductor electrode is brought in contact to an electrolytic medium. Obviously, certain separate background, on the one hand, on classical semiconductor band diagram models, and on the other hand, on the electron energy distribution of redox species in the electrolyte, is required. As mentioned, this background can be easily reached from some comprehensive reviews [30,31,33] and will not be treated in depth here. Notwithstanding, we found useful to make a short incise to briefly describe some concepts, less familiar for a pure electrochemist, that will be further employed in the model's discussion.

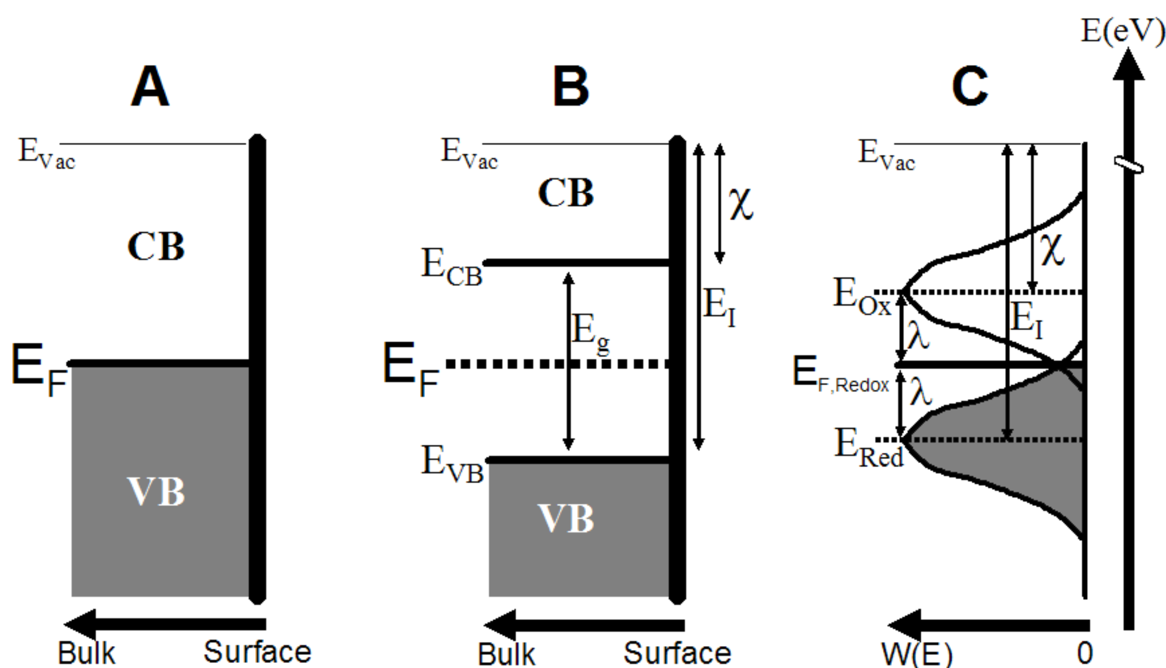

Figure 1.1: Bulk fluctuating energy levels for a: (A) metal and (B) semiconductor. E_{CB} and E_{VB} are conduction and valence band energy levels respectively. E_F denotes the Fermi level and E_g is the forbidden band gap between the bottom of the conduction band (CB) and the top of the valence band (VB). The electron affinity and ionization energy are χ and E_I respectively. All energies are given versus the vacuum level E_{vac}=0. In (C), the distribution of the energy levels of a redox couple in the electrolyte is represented as electronic energy states in analogy to the standard representation of the solid electrode. λ denotes the reorganization energy of the solvation shell (see text). Since the band diagram in (C) is an energetic representation of the electrolyte, the abscise axis represents a probability of the energy levels occupancy. Gray filled areas mean occupied states.

From a pure electrochemical point of view, the band models of metal and semiconductor substrates sketched in figures 1.1A and B are eventually employed. However, in applied electrochemistry the electrolyte is usually described in terms of redox potentials ($U_{Ox/Red}$) quoted versus a standard hydrogen electrode (SHE), while its representation in electronic energy levels (in an absolute energy scale) is rarely used (Fig. 1.1C). As we will see, this representation is advantageous regarding the study of charge transfer between a redox species in the solution and a semiconductor electrode. For this purpose, it is firstly necessary to define a **Fermi energy for the redox system** $E_{F,redox}$. In terms of solid-state physics, the electronic states in the electrolyte are discrete states localized at the electro-active species of the redox

couple, being the oxidized form the empty state and the reduced form the occupied state (see Fig. 1.1C). With this qualitative reasoning, the Fermi energy (given in eV) of the redox system can be expressed as:

$$E_{F,redox} = -e \cdot U_{Ox/\mathrm{Re}d}(SHE) - 4.5 \tag{1.1}$$

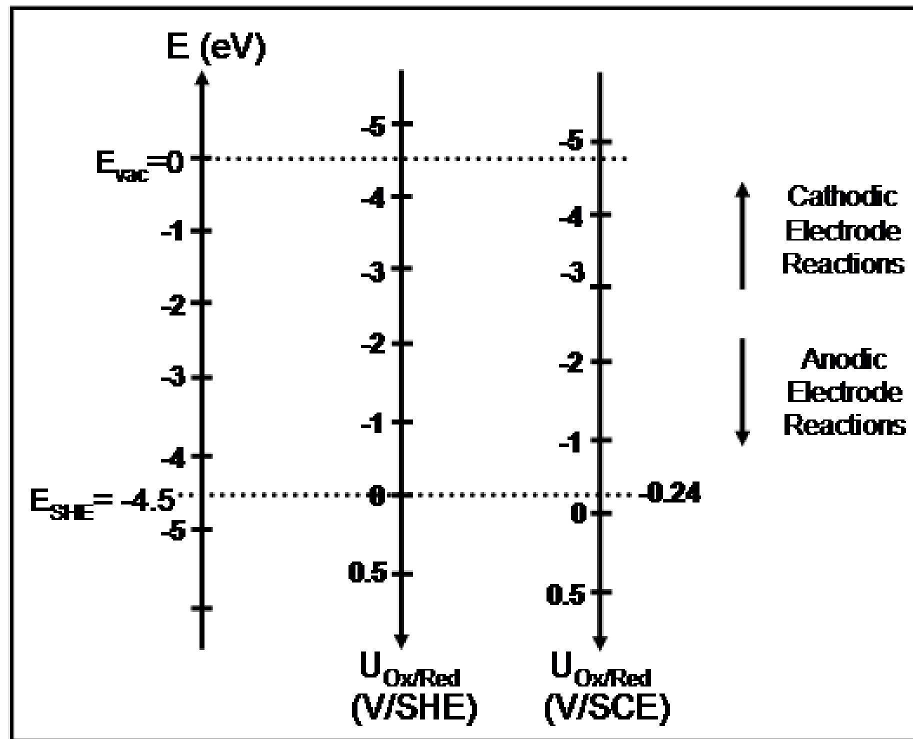

Figure 1.2: Correspondence between the absolute electronic energy scale in the solid (vacuum level reference) and the electrochemical energy scale in the electrolyte (standard hydrogen electrode (SHE) and saturated calomel electrode (SCE) scales).

Note that the redox potential scale ($U_{Ox/Red}$) and the electron energy scale have opposite sign and that the zero energy level of electrons in the SHE scale has been determined to be about -4.5 eV in the absolute energy scale [34] (see Fig. 1.2). Equation 1.1 allows then to directly correlate the energy scales in both solid substrate and electrolyte, which will be greatly advantageous to build up the band diagram of the electrode│electrolyte interface. Figure 1.2 is a visual guide of the correspondence between the electrochemical and the absolute electron energy scales. To end with this incise, it is noteworthy to point out the role of the solvent in this electrolyte energy diagram. The $E_{F,redox}$ level represents the average of the actual electronic states in the oxidized (E_{Ox}) and reduced (E_{Red}) forms:

$$E_{F,redox} = \frac{E_{Ox} + E_{\mathrm{Re}d}}{2} \tag{1.2}$$

While the density of energy states in a solid can be obtained by solving the Schrödinger's equation over a three-dimensional periodic lattice of atoms (giving rise to the energy band structure represented in Fig. 1.1), in the case of redox species the difference between the energy levels corresponding to empty (E_{Ox}) and occupied (E_{Red}) energy states is determined

by the *rearrangement* or *relaxation energy shift* of the ion solvation shell; when an electron is transferred from the solid to the unoccupied level of a redox ion in the electrolyte, the polar solvent molecules surrounding the ion will rearrange in order to accommodate the new charge excess. This process bears a reorganization energy λ described by the *Frank-Condon* electron energy shift which stems from semiconductor physics usage [35]. Taking same rearrangement energy values for both oxidized and reduced species as a first approximation, λ yields:

$$\lambda = \frac{E_{Ox} - E_{Red}}{2} \qquad (1.3)$$

From Dogonadze and Marcus approaches [36,37], λ is approximately equal to 1 eV. Since thermal fluctuations in the solvent result in fluctuations in the polarization of the ion, E_{Ox} and E_{Red} levels are better represented by probability distributions (see Fig. 1.1C).

At this point, it is important to stress that despite the analogy among the different energy distributions of figure 1.1, the direct comparison of the band energy model in the electrolytic ion with that in the semiconductor is limited. Note that the X-axis in the former case represents the probability distribution of the energy levels while in the semiconductor case refers to the distance coordinate within the crystal lattice. The different nature of both systems implies a different behavior during the electronic transitions; when an electronic transition takes place in a solid semiconductor, it represents the total energy change of the system, and the spatial distribution of the resulting energy levels at the surface will be essential to understand its electronic behavior (see section 1.1.2.4). However, the energy levels distribution in the electrolyte case is localized at the ion core, where each state represents a different energetic configuration of the system (eventually accompanied of a chemical change). In any case, this bands model representation provides a general picture of the thermodynamically available energy levels for electrons and thus, they will be useful to predict the most probable pathways for ET between both sites of the electrode│electrolyte interface.

1.1.2.2 The origin of the electrical double layers

Having in mind the previously scenario, when a solid phase (metal or semiconductor) is immersed in an electrolytic medium, the electrons will be transferred from the higher E_F phase towards the lower until the equilibrium condition:

$$E_{F,solid} = E_{F,redox} \qquad (1.4)$$

is accomplished. This implies to reach the same charge (Q) of opposite sign on both sides of the interface (electroneutrality):

$$Q_{Solid} = -Q_{el} \qquad (1.5)$$

As a result, both net charges at the solid surface and the arrangement of ions in the electrolyte at the interface plane, experience a modification in their distribution with respect to the bulk. *Electrical double layers* are then created at both sides of the solid│electrolyte plane. This concept has been largely treated in Electrochemistry for the simplest case of a

metal│electrolyte interface [33] where the electrochemical double layer at the electrolyte side is the dominant term. In general, the relevance of such electrical double layers arises from their dominant influence on the ET across the interface, *i.e.* the (electro)chemical processes occurring at the electrode surface. Basically, in the case of a metal electrode the charge carriers density at the solid surface is very high (the order of 10^{22} cm^{-3}) so that the charge distribution is concentrated just bellow the surface. However, since the charge carriers density in semiconductors is usually much smaller (typically 10^{17} cm^{-3}) than in a metal solid, the spatial distribution of the charge can extend over a considerable distance bellow the interface, creating the so called *space charge layer* (SCL) or *space charge region* (SCR) in the semiconductor side. This fact makes the semiconductor│electrolyte interface particularly more complex regarding the study of the ET. Figure 1.3 presents a complete picture of the charge distribution over the electrical double layers created at a semiconductor│electrolyte contact.

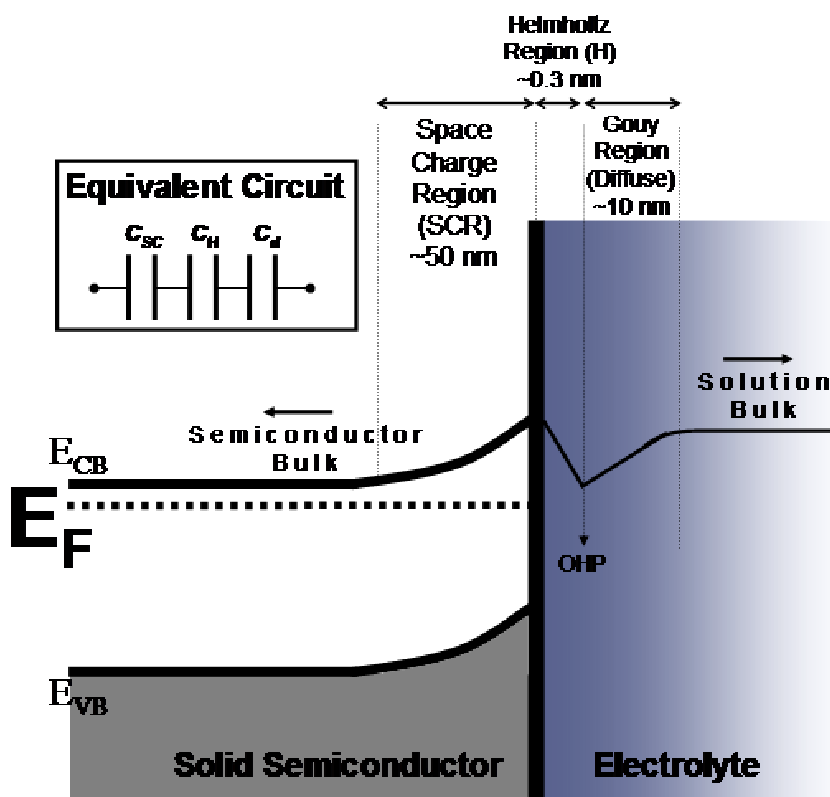

Figure 1.3: Schematic representation of the double layers created in a semiconductor│electrolyte contact. The Gouy-Chapman (diffuse layer) thickness would correspond to a highly diluted electrolyte.

In the absence of current flow, each of these individual double layers has an associated stored charge that can be expressed as a differential capacitance *C* (given in $\mu F/cm^2$) represented by a simple "parallel plate" model:

$$C = \frac{dQ}{dV} = \frac{A\kappa\varepsilon_o}{s} \tag{1.6}$$

where *A* and *s* are the area and the separation of the charge being stored, respectively, and κ represents the dielectric constant. In a simple approach, the whole interface can be

represented as a composition of various capacitors in series, each one representing one of the electrical double layers sketched in Figure 1.3 (see equivalent circuit in the figure inset):

$$\frac{1}{C_{Total}} = \frac{1}{C_{SC}} + \frac{1}{C_{el}} \tag{1.7}$$

As a result, the potential drop across the interface (so called Galvani potential ϕ) is partitioned between the semiconductor (SC) and the electrolyte (el):

$$\Delta\phi_{Total} = \Delta\phi_{SC} + \Delta\phi_{el} \tag{1.8}$$

and related to the electrode potential ($U_{electrode}$) through $U_{electrode} = \Delta\phi_{Total} + const$, being the constant determined by the choice of the reference electrode.

The potential profile across an electrical double layer can be obtained by analyzing the variation of the electric potential drop as a function of the distance x perpendicular to the interface, or in other words, by solving Poisson's equation assuming no potential dependence along y and z coordinates:

$$\frac{d^2U(x)}{d^2x} = \frac{\rho(x)}{\kappa\varepsilon_0} \tag{1.9}$$

where ρ is the charge density.

Within the forthcoming sections 1.1.2.3 and 1.1.2.4, we will analyze separately the capacitances and potential distributions at both electrolyte (C_{el}, ϕ_{el}) and semiconductor (C_{SC}, ϕ_{SC}) sides of the interface.

1.1.2.3 The electrochemical (electrolyte) double layer

The first model that gave rise to the term *electrical double layer* was put forward in the 1850's by Helmholtz. Since them, the electrical double layer has been a hallmark on the classical electrochemical theory which focused essentially on the electrical structure of the electrolyte side as the dominant term on ET studies on metal electrodes. Although this becomes the most complex part of the double layer structure in a solid│electrolyte contact, it has been largely described in the basic electrochemical bibliography [33] and here just a short flash will be given.

Within the electrolyte double layer, the electrostatic potential at the interfacial plane of the electrolyte (ϕ_{el}) is different from that in solution bulk. This potential difference results from the diffusion of ions and polar solvent molecules toward the interface to compensate an opposite sign charge at the solid surface. The simplified capacitance term of the electrochemical double layer distinguishes two different charged regions as outlined in figure 1.3:

$$\frac{1}{C_{el}} = \frac{1}{C_H} + \frac{1}{C_d} \tag{1.10}$$

The total capacitance of the electrolyte double layer is then a composition in series of the so called *Helmholtz* and *diffuse* (Gouy) electrical layers.

The Helmholtz Double Layer

This electrical double layer, also called *compact* layer, is the strongest contribution to the total potential drop across the electrochemical (or electrolyte) double layer and so extremely important in the ET at both semiconductor and metal electrodes. In the absence of *specific absorption* (see concept at the end of this section), it can be described by two parallel charged planes: one corresponds to the charge located at the surface of the solid, and the other corresponds to the arrangement of solvated ions in solution that are being attracted by the solid surface charge (see Fig. 1.4A). This latter plane is commonly called *outer Helmholtz plane* (OHP) and its separation is in the order of the solvent molecule length $x_{OHP} \approx 0.5$ nm (see Fig. 1.3 and 1.4B). This simple model developed by Helmholtz assumes then a planar parallel capacitor representation for the Helmholtz layer. With this assumption, solving Poisson's equation (1.9) for the simple case of two charged Helmholtz planes yields a linear dependence for the voltage drop ($\Delta\phi_H$) versus the perpendicular distance x to the surface:

$$\Delta\phi_H = \phi_S - \phi_{OHP} \tag{1.11}$$

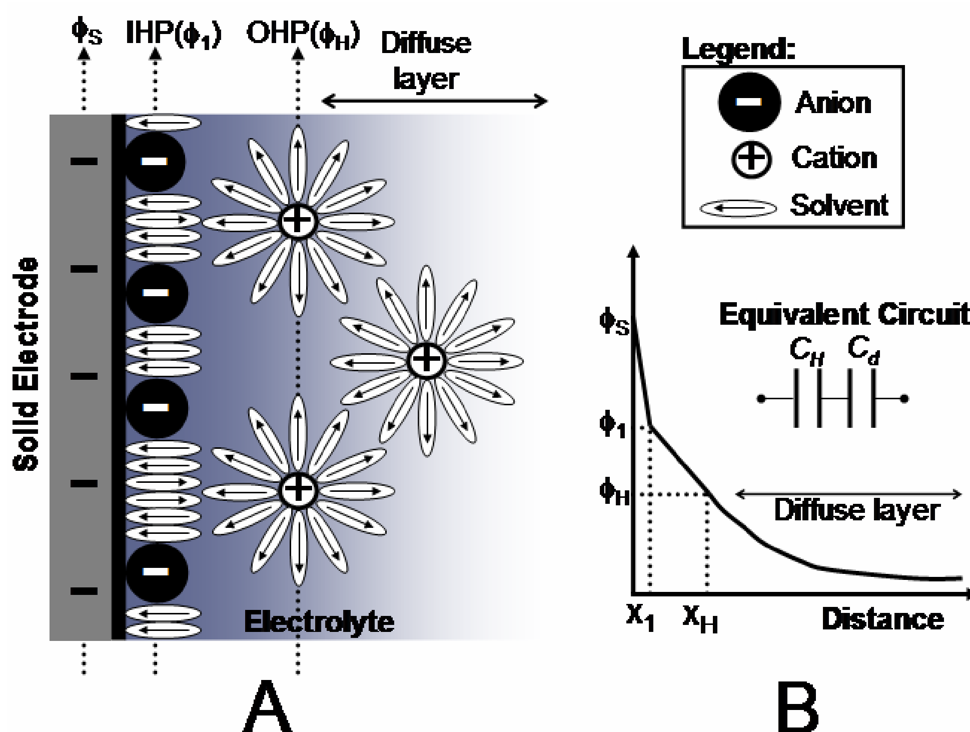

Figure 1.4: (A) Complete model of the electrolyte double layer formed near a negatively charged electrode surface (ϕ_S). Specific anion absorption is also represented as the inner Helmholtz plane (IHP). (B) Legend of (A) plot and potential distribution of the electrolyte double layer. x_1 and x_H are the inner and Helmholtz separations respectively. Inset plot represents the partitioning of the total electrolyte double layer capacitance (C_{el}).

where ϕ_S and ϕ_{OHP} are electrical potentials at the solid surface and at the OHP, respectively (see Fig. 1.4). Equation (1.9) can be then integrated for a fixed $\Delta\phi_H$ value and the capacitance of the Helmholtz layer takes a constant value equal to:

$$C_H = \frac{\kappa\varepsilon_o}{x_{OHP}} \tag{1.12}$$

which is independent of the external applied potential $U_{electrode}$. Experimental values of C_H in aqueous solutions are in the order of 10 μF/cm^2, which implies an effective dielectric constant of $\kappa \approx 5$. Considering the simple case of no specific adsorption on the electrode surface, only water molecules will be present within the compact layer, and so that such a low κ value (compare to κ=80 in the water bulk) will be explained by their low dipole rotation in such a highly polarized medium. Similar values of κ have been obtained for water absorbed on highly charged mica substrates by means of advanced SPM techniques that use AC electrical modulation [39].

It must be stressed here that while in the case of metal│electrolyte interface the potential of the Helmholtz layer adjust almost exclusively by electron exchange between both phases, in the semiconductor│electrolyte case same adjustment can proceed through both electron exchange and/or ion adsorption-desorption process. The dominating process will determine the final potential drop $\Delta\phi_H$ and it will essentially depend on the density of charge carriers in the semiconductor substrate, i.e. the highest the charge carrier density, the most probable the ET process will be.

The Diffuse Double Layer

The *Diffuse* or *Gouy* electrolyte layer refers to a region of the solution in the electrode vicinity where a space charge region is generated by an excess of ions of one sign (see Fig. 1.4). The ions attracted to form the OHP do not suffice to compensate all the charge at the electrode surface, and the residual electric field normal to the surface results in the formation of the so-called *Gouy* electric double layer. This model assumes the presence of an excess of solvated ions near the OHP which are now not constricted within a parallel plane and thus they present a higher level of movement. The voltage distribution across the Gouy region ($\Delta\phi_d$) can be then evaluated by introducing a Boltzmann distribution for the density of mobile charges into the potential profile *U(x)* of equation (1.9), yielding the relation:

$$\frac{\partial\phi_d}{\partial x} = \sqrt{\frac{8k_B T c_{el}}{\kappa\varepsilon_0}} \cdot \sinh\left(\frac{e\Delta\phi(x)}{2k_B T}\right) \tag{1.13}$$

By integration of Eq. (1.13) and assuming $\sinh(ze\phi(x)/2k_BT) = (ze\phi(x))/(2k_BT)$, it yields:

$$\ln\phi(x) = \sqrt{\frac{2z^2e^2c_{el}}{\kappa\varepsilon_0 k_B T}} \cdot x + const \tag{1.14}$$

which is represented in Figure 1.4B [33,40]. The capacitance of the diffuse layer C_d can be calculated by substituting Eq. (1.13) into Gauss's law from electrostatic formalism $q = \kappa\varepsilon_0(d\phi/dx)$, and differentiating it with respect to the potential it is obtained:

$$C_d = \sqrt{\frac{2e^2 \kappa \varepsilon_0 c_{el}}{k_B T}} \cdot \cosh\left(\frac{e\Delta\phi_{el}}{2k_B T}\right) \quad (1.15)$$

where c_{el} is the ionic concentration given in ions/cm^3. Expression (1.15) shows that the capacitance increases with the solution concentration c_{el} and with the electric potential $\Delta\phi_{el}$ in agreement with experimental results. This dependence also points out why the capacitive contribution of the diffuse region is in many cases neglected; if working in an aqueous electrolyte at a concentration in the order of 0.1 M (high ionic strength, *I*) and taking a value of κ=80 (water dielectric constant), the diffuse capacitance reaches a value in the order of F/cm^2, largely over the C_H so that the C_d term in expression (1.10) can be neglected. To give a practical picture, if we take the parallel plane capacitor model, the potential across the diffuse layer in such experimental conditions is dropped within ~0.1 nm which means that its space charge region will concentrate at the OHP and will be undistinguishable to the Helmholtz layer. In practice, the electrolyte double layer is frequently termed *Helmholtz* layer and, in the absence of specific ion adsorption, its capacitance C_{el} takes the constant value given in equation (1.12).

Specific ions adsorption

In previous sections, we analyzed the general charge distribution of the electrolyte near a solid electrode surface in the absence of *chemical* or *specific* ion-surface interactions. From an energetic point of view, the *specific absorption* term refers to a complex energy cycle of various steps that involves the solvation energy lost of the specific adsorbing ion and the energy gain corresponding to the ion-surface bond formation. Since this interaction clearly depends on the chemical nature of the ion rather than on its charge distribution, it has been commonly called *specific* or *chemical adsorption*. The specific absorbed ions are then located among the solvent molecules within the compact layer and define the so-called *inner Helmholtz plane* (IHP) in analogy with the OHP (see Fig. 1.4A). When specific absorption takes place, the charge associated to those absorbed species becomes the major contribution to the voltage drop across the Helmholtz layer ($\Delta\phi_H \approx \Delta\phi_I$ in Fig.1.4). Given the close proximity of the IHP to the surface electrode, the potential drop can be assumed to be linear (see Fig. 1.4B). However, calculations of the $\Delta\phi_I$ are of great complexity due to the number of ions susceptible to adsorb that present different charges and chemical affinities. Equally, the correlation of the compact capacitance equated in expression (1.12) is no longer possible and each system must be separately analyzed.

As for its chemical nature, this process can indeed involve a variety of chemical reactions on the electrode surface. In aqueous media, the relative adsorption of H^+/OH^- ions constitutes the central topic. It is of special interest when studying oxides or oxide covered electrodes (as it is the target of this Ph.D.) which are commonly –OH terminated (the surface is *hydroxilated*). In this case, the potential drop across the electrochemical double layer ($\Delta\phi_{el}$) will be determined by the adsorption equilibriums:

$$H_S^+ + OH_{sol}^- \longrightarrow H_2O \quad (1.16a)$$

$$OH_S^- + H_{sol}^+ \longrightarrow H_2O \quad (1.16b)$$

where suffixes *S* and *sol* denote surface and solution respectively. From equations (1.16), it is expected that the resulting net charge at the interface, *i.e.* the interfacial potential distribution, depends on the electrolyte *pH*. The point of zero charge (pzc) of the oxide is then defined as the *pH* value at which the concentrations of H_S^+ and OH_S^- are equalized. The first examples of aqueous H^+/OH^- adsorption was performed on Germanium and Silicon substrates which constitute the milestone substrates in semiconductor electrochemistry [41,42]. Taking the example of Ge, it was found experimentally that $\Delta\phi_{el}$ varies with *pH* at a ratio of -60 mV/*pH* and was ascribed to the dissociation equilibrium:

$$\equiv Ge - OH + OH^- \Leftrightarrow \equiv Ge - O^- + H_2O \tag{1.17}$$

whose equilibrium condition yields to a *Nernstian* relation of the electrical potential drop across the layer equal to:

$$\Delta\phi_H = \frac{RT}{F} pH + const \tag{1.18}$$

Expression (1.18) gives rise to a 58 mV/*pH* ratio, in good agreement with the experimental results. We will see in chapter 4 that it is possible to find also this kind of behavior for oxide passive films on metallic systems and we will analyze its transcendence on the kinetics of ET through these layers.

Adsorption of large anions from aqueous solutions is also a frequent specific adsorption process that modifies the voltage distribution across the Helmholtz layer. This process usually involves only relatively large anions like I^-, Br^-, Cl^- whose specific adsorption is facilitated by their lower solvation energies. In contrast, cations in solution present higher charge density thus involving higher hydration energies and therefore, a poor specific adsorption. Despite the lack of knowledge, the presence of absorbed, non-reactive anions can have enormous consequences on the electrode redox behavior, particularly on semiconductor | electrolyte interfaces where the adsorption-desorption equilibrium is an essential process in the electrolyte double layer formation. In short, such large anions in aqueous electrolytes have a different effective charge compare to the couple H^+/OH^- ions that they are replacing, and therefore, they strongly modify the charge distribution and the electron exchange behavior at the interface [43]. Moreover, the adsorption of anions can themselves provide surface states (see sub-section *surface states* in 1.1.2.4) in the electronic energy levels distribution of the solid | electrolyte interface, fact that can completely modify the electrochemical behavior of the electrode [44].

To end with this topic, it is noteworthy to remark that a chemical precipitation process can be also included as a kind of adsorption at the solid | electrolyte interface. Of course this process results in the formation of a second phase, giving rise to a completely new interface that will have to be treated a part.

These two last processes have become outstanding topics on passivity up to the point of controlling passivation and/or corrosion of the metal electrode. In chapters 3 to 5, we will have the opportunity to observe the influence of those processes on the passivation-corrosion behavior of an iron electrode.

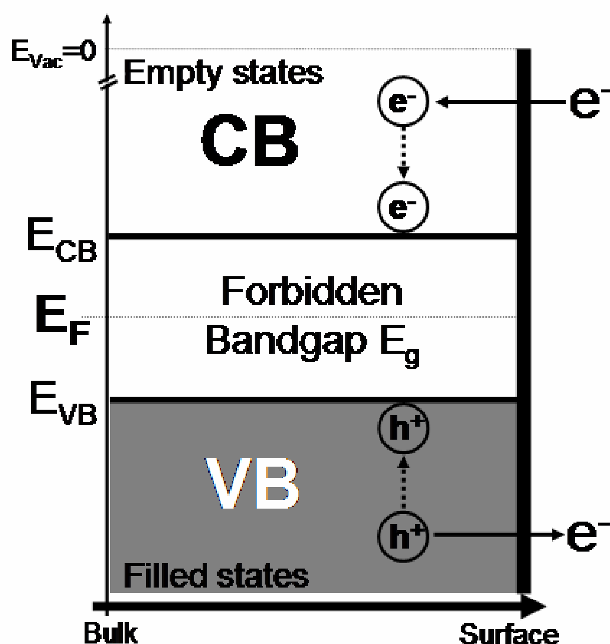

Figure 1.5: Electronic energy states or band diagram in a semiconductor. Possible electrochemical routes are indicated.

1.1.2.4 The space charge region in the semiconductor

The last point of this section deals with the analysis of the electrical double layer structure of the interface at the semiconductor side. As already pointed in section 1.1.2.2, the carriers density in a semiconductor is several orders of magnitude lower against a metal electrode. The consequence of that is the creation of a SCL that extends over a certain range inside the semiconductor solid in order to generate the counter charge that neutralizes the charge in the electrolyte site ($\Delta\phi_{el}$). As previously mentioned, the formation of a SCL in this region opens up a completely new electrochemical view of the charge distribution across the electrode│electrolyte interface.

Within the next subsections, we will spend some paragraphs to descript the special charge distribution under different electrochemical conditions and how this SCL can ultimately determine the observed electrochemical redox behavior in semiconductor│electrolyte interfaces.

Basic concepts

The main picture of the band diagram of a solid semiconductor has been already depicted in figure 1.1. A quick look over this particular energy levels distribution shows that the ET through such electrodes during electrochemical reactions can only proceeds through specific pathways since only certain electronic energy levels are available. Electrons (e^-) can be then only injected at $E \geq E_{CB}$ and/or extracted at $E \leq E_{VB}$ (see Fig. 1.5), and no e^- exchange is then possible within the forbidden band gap in between (E_g=E_{CB}-E_{VB}). In the last case, when an e^- is extracted from the VB, the generated electron vacancy at the particular energy level is commonly called hole (h^+). This is a very used terminology in the solid-state physics jargon and it is usually said that the conduction in the valence band of the semiconductor proceeds

through h^+ injection which travel in the opposite direction to electrons (see Fig. 1.5). Of course, a h^+ vacancy can be occupied by an neighboring e^- of higher energy and therefore, after system relaxation, the generated h^+ will be located at the highest energy level of the VB. From a point of view of electrochemical reactivity, if the experimental conditions allow a h^+ concentration at the surface of the semiconductor electrode, they can act as power oxidizing agents of electrolytic species located in the vicinity of the semiconductor│electrolyte interface. With the same reasoning, interfacial species can be also oxidized on the electrode surface through e^- injection into the CB. The occurrence of one of previous mechanism will depend of course on the redox potential of the electro-active species in solution ($E_{F,redox}$ in Eq. 1.1). This particular electrochemical behavior found on semiconductor electrodes has ended in a variety of interesting applications like for example in electro-catalysis [45].

The e^- occupancy of the available electronic energy states ($N(E)$) in a semiconductor band diagram is given by the Fermi-Dirac distribution function:

$$f(E) = \frac{1}{1 + e^{\frac{E - E_F}{k_B T}}} \tag{1.19}$$

This expression describes the probability of a state of energy E to be occupied by an e^-, where k_B denotes the Boltzmann constant and E_F refers to the *Fermi energy level in the solid* ($E_{F,solid}$ in equation 1.4). It is important to highlight that the position of E_F relative to the bands of the solid is the dominant feature distinguishing a metal from a semiconductor (see Fig. 1.1). At T=0 K, the energy levels $E>E_F$ in a solid are empty of e^- ($f(E)$=0) while those levels $E< E_F$ are fully occupied ($f(E)$=1). Therefore, to describe the distribution of the electronic occupation in figure 1.5 at T>0 K through relation (1.19), the E_F level must be statistically located within de band gap region (see Fig. 1.5). In analogy with the expression (1.1), the applied electrochemical potential to the semiconductor electrode ($U_{electrode}$) will be related to this statistic E_F level in the solid through:

$$E_{F,solid} = -e \cdot U_{electrode} \tag{1.20}$$

In the next section, we will have the opportunity to check the electrochemical implications of the equality (1.20). In this sense, the most important feature will be the different SCL emerging profiles as $U_{electrode}$ is being modified.

Before tackling into this different SCL profiles, we find necessary to make a short incise here to describe some specific concepts concerning the semiconductor band diagram picture that will be used within forthcoming chapters. They correspond to:

- *Donors and acceptors*
- *Degeneration*
- *Crystallographic defects*

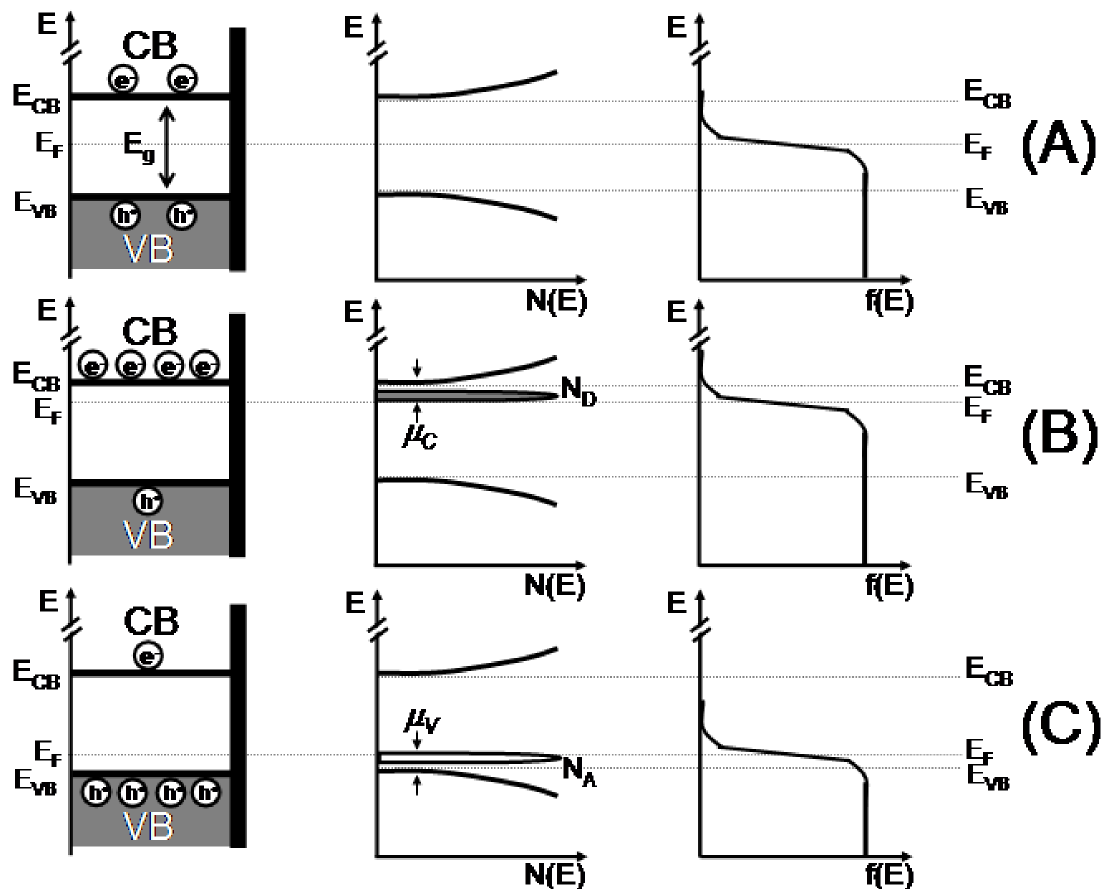

Figure 1.6: Band diagram, density of states and Fermi distribution for a: (A) *intrinsic*, (B) *p-type* and (C) *n-type* semiconductors.

The energy diagram represented in figure 1.5 corresponds to a chemically pure semiconductor, free of crystallographic defects. In the solid-state physic convention, it is usually denominated an *intrinsic* semiconductor. Semiconductor single crystals like Si(111) or Ge(111) can respond to this structure. However, in practice, there are some chemical and structural features that can induce a deviation of the original intrinsic semiconductor properties. The semiconductor is then called *extrinsic* or *doped*. It will be of special interest on passive films whose structure and chemical composition are rather complex (see section 1.3). The most common characteristic is the presence of chemical *impurities* within the semiconductor structure. Such impurities are no longer as part of the wave-function extending through the crystal and therefore, they introduce new energy levels within the forbidden gap. Of course, if such impurities are non-reactive and do not supply additional charge to the semiconductor interface, they can act as an isolated surface states (see concept at the end of this section). On the contrary, it is typically found that those impurities can strongly increase the conductivity of the semiconductor by forming **acceptor** levels (E_A near the VB) or **donor** levels (E_D near the CB). Since the quantities E_A - E_{VB} and E_{CB} - E_D are typically of a few tens of *meV*, at room temperature the e^- will flow from the VB to the acceptor level (h^+ injection) and from the donor level to the CB (e^- injection), respectively. The enhancement of the conductivity will be then proportional to the concentration of donor and acceptor impurities in the solid that give rise to proportional e^- or h^+ concentrations (n and p respectively). Figure 1.6 shows a summary of the different situations described above. Note that in order to preserve charge neutrality, E_F level must adjust itself toward the VB or the CB depending on

the kind of impurity (see Fig. 1.6B and C). The standard terminology in solid-state physics is such that if the semiconductor is dominated by acceptor impurities so that h^+ in VB outnumber e^- in CB, the solid semiconductor is termed *p-type* being h^+ the majority charge carriers. In the contrary case, it is termed *n-type* being now e^- the majority charge carriers. The energy differences between the Fermi level and the corresponding band are defined by the quantities:

$$\mu_V = E_F - E_{VB} = k_B T \cdot \ln \frac{N_{VB}}{N_A} \tag{1.21a}$$

$$\mu_C = E_{CB} - E_F = k_B T \cdot \ln \frac{N_{CB}}{N_D} \tag{1.21b}$$

for *p*-type and *n*-type semiconductors respectively (also indicated in figure 1.6). These quantities provide information on the doping level of the semiconductor where the term N denotes correspondingly the effective states densities. The lower the μ_V and μ_C values are, the higher the doping levels are and of course the higher the conductivity of the solid is. These properties were firstly employed in the silicon technology to quantitatively control the semiconductor conductivity by intentionally introducing small amounts of column-V elements in a Si-based device [46]. Within chapters 3 and 4, we will see that such characteristic doping levels are essential to explain the redox behavior of metal passive layers.

Following up with previous reasoning, when either N_A or N_D are very high, or in other words, when μ values in Eq. (1.21) are extremely low such that the Fermi level is almost buried in the main semiconductor band — either the valence or the conduction band (see Fig. 1.6) —, it is said that the semiconductor is **degenerated**. In this regime, the semiconductor behaves as a quasi-metallic solid with the corresponding sharp conductivity increase: either h^+ or e^- can easily access the corresponding main band. This particular regime will be especially useful when study metal-to-semiconductor transitions and *vice versa* that frequently occur on the electrode surface during electrochemical reactions.

Retrieving the previous concept of *semiconductor doping*, it is important to consider also other kind of doping elements in addition to chemical impurities (see above). In this sense, the crystallographic structure of the solid semiconductor can also play an important rule. Some specific **crystalline imperfections** can also act as donors or acceptors affecting the electronic properties of the semiconductor. Special mention has crystallographic defects like *vacancies, interstitials*, *dislocations* or *grain boundaries*. In the study of the electronic properties of the oxide passive films, this topic is crucial for a correct interpretation. For example, the iron passive film has a polycrystalline nature with a particular distribution of *cation* and/or *oxygen vacancies* and *interstitials* across the layer [12,13]. The final defects distribution will ultimately govern its electronic structure. To illustrate that, let us consider an ionic lattice for an oxide structure where VB electrons are in the orbitals close to the oxygen ions (O^{2-}). If a cation is removed from the lattice, electrons will be taken in order to keep the electro-neutrality. It results in an imperfection point susceptible of accepting electrons able to act as an acceptor level. If they are the unique doping element in the oxide structure, the concentration of *cation vacancies* will be equal to N_A. The contrary effect holds when an *anion vacancy* is formed giving rise to a donor level (N_D). Furthermore, if a foreign or a host atom of the lattice is trapped between the atoms of the crystal (*interstitial atom*), it can also

generate an acceptor or a donor level depending on whether it tends to give up or gain electrons. The transcendence of these defects is such that they can be used to explain phenomena like anodic oxidation and/or electrode corrosion, or to describe the particular diffusion profiles of the doping levels within the solid structure (see more details in section 1.2.3.2).

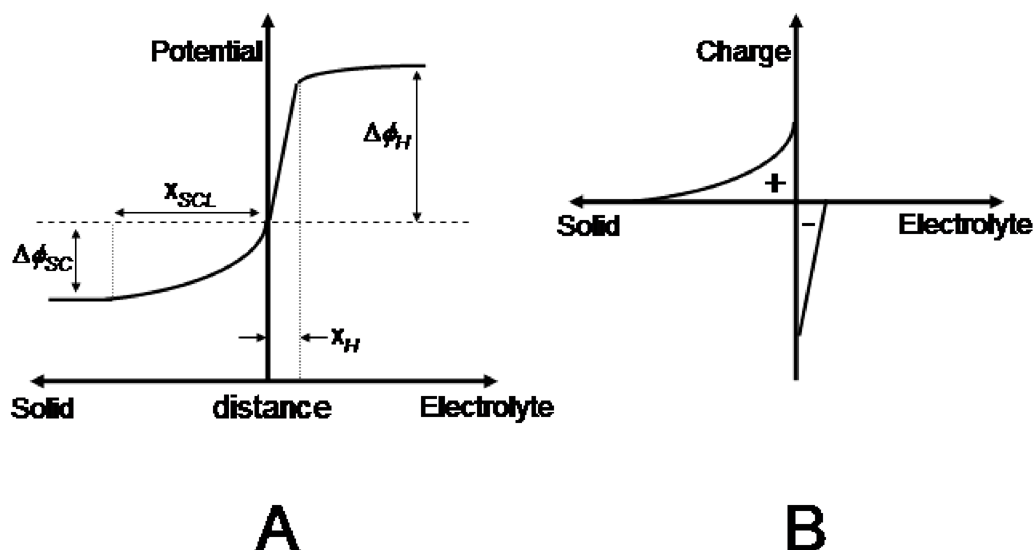

Figure 1.7: Potential (A) and charge distribution (B) at the semiconductor│electrolyte interface when the semiconductor is at depletion conditions (see discussion below). Note that the lower carriers density in the solid semiconductor $x_{SCL}>x_H$. After ref. [31].

When any of the previous defects is spatially located at the solid surface, they are assimilated to a *surface state* SS (see section 1.2.4.3) and same previous reasoning will hold as well.

Dislocations and grain boundaries constitute bulk defects that can also affect the electronic properties of the solid. They are indeed able to trap a significant amount of charge giving rise to different electrical double layers and independent reactive centers. Experimentally, these centers can be actually identified by local techniques (like SPM or electron microscopy) so that their complex electronic effects can be individually studied.

Charge distribution and Capacitance behavior in the semiconductor SCL

When a solid semiconductor is dipped into a certain electrolyte, the equalization of the Fermi levels at both sides of the semiconductor│electrolyte interface (Eq. (1.4)) is achieved through the transfer of majority carriers from the highest E_F phase to the lowest one. This process naturally occurs at open circuit potential (OCP, *i.e.* in the absence of an applied external voltage) and results in the formation of the SCL at the semiconductor surface. The chemical nature of this SCL corresponds to immobilized ions within the lattice near the solid surface mainly corresponding to ionized dopants. The local electric field created by these fixed charges determines the potential drop distribution across the SCL ($\Delta\phi_{SC}$) represented in figure 1.7. If consider a uniform density of immobile charges, the charge distribution across this layer can be evaluated by integrating equation (1.9) for each particular case. When considering the study of passive film formation under electrochemical control, we will be

especially interested on the effect of an external $U_{electrode}$ to the SCL distribution at the semiconductor surface. In semiconductor electrochemistry, this topic has become an unavoidable analysis since in most experimental conditions, i.e., high ionic strength and absence of specific adsorption and/or surface states, $U_{electrode}$ drops essentially across the SCL of the semiconductor: the dominant capacitive term in equation (1.7) corresponds to C_{SC}, being worthless the small contribution coming from the Helmholtz layer ($C_{SC} \ll C_{el}$).

Let us analyze the three main different situations of the SCL as a function of $U_{electrode}$ (see summary in Fig. 1.8 for *n*- and *p*-type semiconductor electrodes). First of all, let us introduce the concept of *Flat Band potential* (U_{FB}). If the external $U_{electrode}$ is such that the charge due to fixed ions within the solid lattice are balanced by the free charges at the surface, there is no potential drop across the SCL of the semiconductor so that the electron energy at the semiconductor surface is the same as in the bulk; the bands are then represented as *flat* bands like in figures 1.5 and 1.6, and now in figure 1.8A. In this situation and in the absence of storage charge in the form of surface states or adsorbed ions, the charge at the interface is zero:

$$Q_{Solid} = Q_{el} = 0 \quad \text{at} \quad U_{electrode} = U_{FB} \tag{1.22}$$

where $U_{electrode}$ is related to the solid Fermi level through relation (1.20). As a rule of thumb, when an anodic $U_{electrode}$ (lower $E_{F,solid}$) or a cathodic $U_{electrode}$ (higher $E_{F,solid}$) is applied to the semiconductor electrode, the entire band structure shifts to preserve the bulk electronic properties of the material while at the surface the SCL arises from the *bandedge pinning*: the energy of the bands at the semiconductor surface remains nearly constant (see Fig. 1.8). It is commonly said that at the semiconductor│electrolyte interface most of the applied $U_{electrode}$ is employed to bend the bands. In contrast, no SCL is developed at the metal│electrolyte interface and so all $U_{electrode}$ is dropped within the electrolyte double layer ($\Delta\phi_{el}$).

Now, depending on whether $U_{electrode}$ is above or below U_{FB}, the following three different profiles in the semiconductor SCL can be reached:

- *Depletion layer* ($U_{electrode} > U_{FB}^{n}$ *for n-type and* $U_{electrode} < U_{FB}^{p}$ *for p-type).*
- *Inversion layer* ($U_{electrode} \gg U_{FB}^{n}$ *for n-type and* $U_{electrode} \ll U_{FB}^{p}$ *for p-type).*
- *Accumulation layer* ($U_{electrode} < U_{FB}^{n}$ *for n-type and* $U_{electrode} > U_{FB}^{p}$ *for p-type).*

For simplicity, we will first consider the *n*-type case (first column in Fig. 1.8) and will later extend to the *p*-type case. If applying a discrete anodic $U_{electrode}$ over the U_{FB}, moderate amounts of majority charge carriers will be extracted from the surface. It is said that the surface is **depleted** or *exhausted* of both forms of mobile charge carriers thus producing an insulating layer represented by an upward band bending at the semiconductor surface (see Fig. 1.8B, first column). Integrating equation (1.9) in the depleted layer yields to a parabolic distribution of the potential drop of the form:

$$U(x) = \frac{eN_D}{2\kappa\varepsilon_0}(x - x_0)^2 \tag{1.23}$$

after applying the boundary conditions of zero field $dV/dx=0$ in the bulk where $U(x_0)=0$ being x_0 the actual thickness of the SCL in the semiconductor and $x=0$ representing the solid surface.

According to equation (1.23), the surface energy barrier seen by a bulk electron (see Fig. 1.8B, first column) takes the value:

$$U_S = \frac{eN_D x_0^2}{2\kappa\varepsilon_0} \tag{1.24}$$

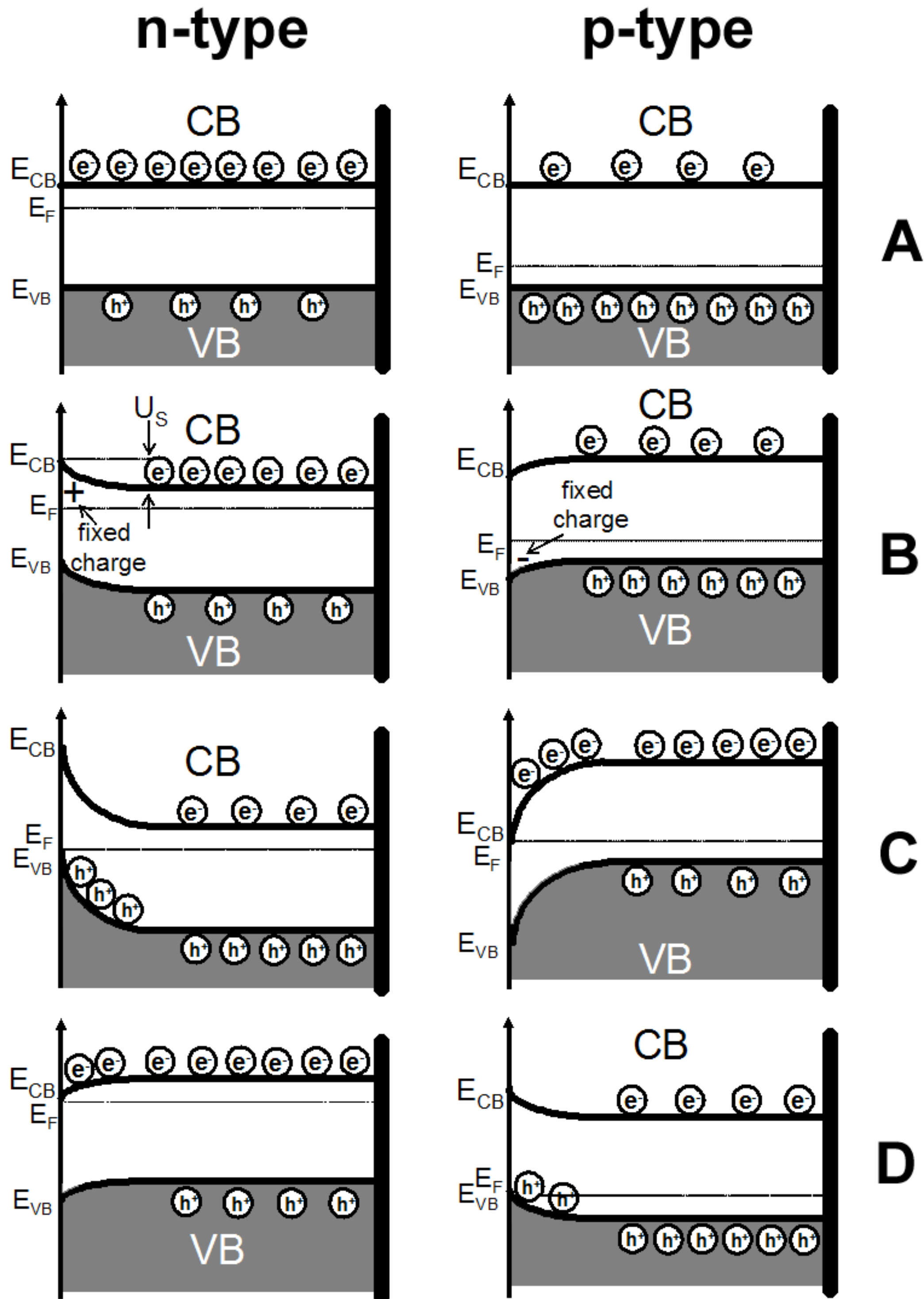

Figure 1.8: Band diagrams showing the SCL profiles of *n*-type (first column) and *p*-type (second column) semiconductor electrodes at different applied potentials ($U_{electrode}$). Four different situations are schematized: (A) Flat band (U_{FB}), (B) depletion, (C) inversion and (D) accumulation.

which is known as the *Schottky relation*. Indeed, this situation is comparable to the Schottky barrier traditionally studied on metal│semiconductor junctions [31,47], where the electrolyte, with an equivalent carriers density in the order of 10^{22} cm^{-3}, is here assimilated to the metal phase in the conventional Schottky junctions. To illustrate with an example, let us consider an *n*-type oxide passive film with U_S=1 V, a typical κ=10 and a donor density of N_D=10^{20} cm^{-3}. The resulting SCL thickness yields ~40 Å, much higher than the thickness of the Helmholtz layer at commonly used electrolyte ion strengths (~0.1 M). This SCL thickness corresponds to a highly doped semiconducting oxide, usually found on metal passive layers, so that a 2-fold decrease in the carriers density (typically 10^{18} cm^{-3} for an *n*-Si) yields a SCL thickness of hundreds of Å. It concludes that generally under depletion conditions, the interfacial electrical layer that dominates the ET will be the semiconductor SCL, being the $1/C_{el}$ term neglected in the partitioning equation (1.7). The total capacitance of the interface can be then evaluated through the differential capacitance $C_{SC}=dQ_{SC}/d\phi_{SC}$. The total charge in the SCL (Q_{SC} given in C/cm^2) is directly calculated through relation:

$$Q_{SC} = eN_D x_0 \tag{1.25}$$

It is common in the literature to include the contribution of the CB electrons in the derivation of the capacitance, which affect the calculated value of U_S by an amount equal to k_BT/e (0.025 V). Including this correction and introducing the relation (1.24) into (1.25), it yields:

$$Q_{SC} = \sqrt{2\kappa\varepsilon_0 eN_D}\sqrt{U_S - \frac{k_BT}{e}} \tag{1.26}$$

whose expression can be derived to obtain the differential capacitance:

$$C_{SC} = \sqrt{\frac{\kappa\varepsilon_0 eN_D}{2}} \cdot \frac{1}{\sqrt{U_S - \frac{k_BT}{e}}} \tag{1.27}$$

This expression is called *Mott-Schottky relation* and has been extensively used by experimentalists to get the basic electronic behavior of a semiconductor electrode immersed in a particular electrolyte. Under depletion conditions and in the absence of trapped charge at the surface, the potential drop within the SCL ($\Delta\phi_{SC}$) can be defined as:

$$\Delta\phi_{SC} = U_S = U_{electrode} - U_{FB} \tag{1.28}$$

Inserting equation (1.28) into (1.27), it can be rewritten in a more useful way:

$$\frac{1}{C_{SC}^2} = \frac{2}{\kappa\varepsilon_0 eN_D} \cdot (U_{electrode} - U_{FB} - \frac{k_BT}{e}) \tag{1.29}$$

Experimentally, the total capacitance (C_{Total}) of a solid│electrolyte interface can be reached by means of EIS (see 1.3.2) whose impedance data are adjusted to a simple electrical model (see upper inset of figure 1.9). This capacitance data is then measure as a function of the applied $U_{electrode}$ and represented in the form $1/C^2$ vs $U_{electrode}$ (so-called Mott-Schottky plot (MS)). The slope of the linear obtained behavior provides a measurement of the carrier

density (N_D or N_A values for *n*- or *p*-type respectively), and the intercept $1/C^2=0$ stands for the U_{FB} determination (see MS plot in Fig. 1.9). Note also that the slope sign determines the kind of doping species; *n*-dopants give a positive slope while *p*-dopants give a negative slope. It must be stressed that this MS plot holds under depletion conditions in the absence of other forms of interfacial stored charge than the SCL ($C_{Total} \approx C_{SC}$). Notwithstanding, more complex capacitance behaviors can be found if other capacitive elements (with $C \leq C_{SC}$) are also present at the interface, e.g., an adsorbed anion, effective SS or other sources of charge carriers. This case will be analyzed in more detail within the next sub-section.

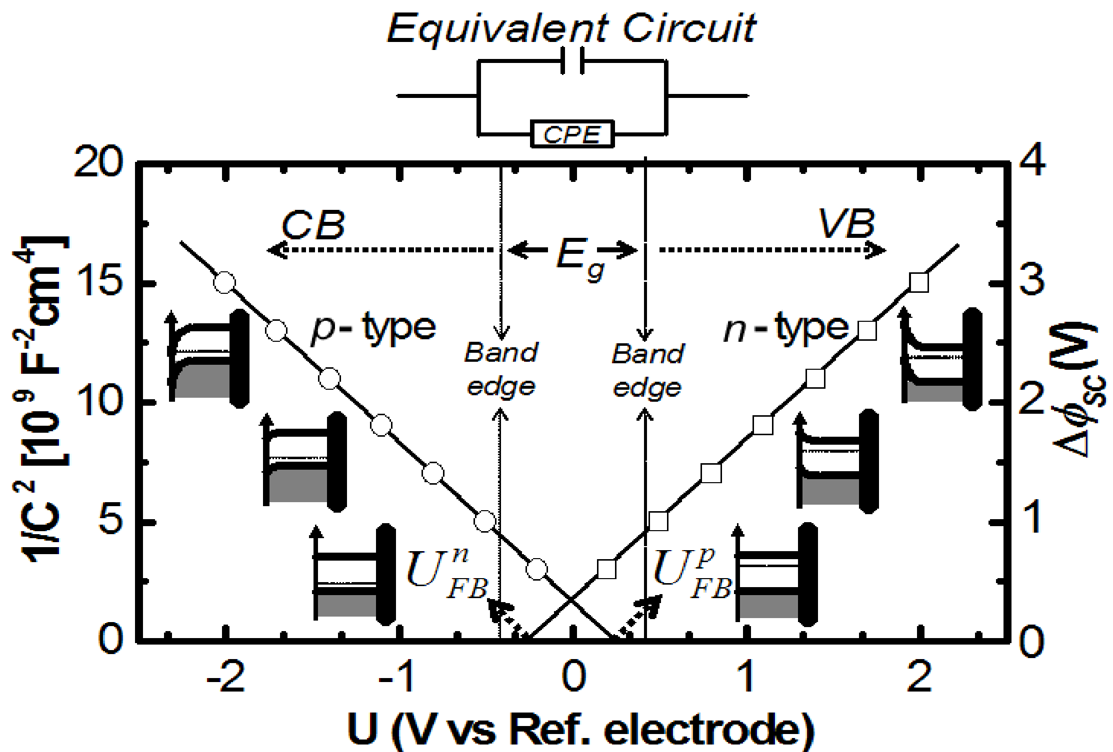

Figure 1.9: Mott-Schottky representation of the capacitance data for both *n*- and *p*-type semiconductors under depletion conditions. Insets at both sides represent the sequence of the band bending (*bandedge pinning*) as the electrode potential is decreased (*p*-type) or increased (*n*-type) from the Flat band situation. Upper inset shows the most employed equivalent circuit to fit the impedance data.

Let us continue with the $U_{electrode}$ excursion. Consider now the situation $U_{electrode} >> U^n_{FB}$ or $U_{electrode} << U^p_{FB}$ in a way that all the donor or acceptor species near the semiconductor surface have been ionized, i.e., the majority carriers have been completely extracted from surface resulting in an excessive band bending. Let us consider again the former case (*n*-type) for simplicity: the $E_{F,solid}$ level is now located in the lowest part of the band diagram near the VB edge (see Fig. 1.8C, first column). At this point, the e^- are not only depleted from the CB (the majority carriers band) but also from the VB in order to maintain the strong band bending imposed by the high external applied $U_{electrode}$. Following up with this reasoning, when e^- are extracted from the VB (h^+ injection), the n-type semiconductor conducts now through minority carriers (h^+ in the *n*-type case) and so that it experiences an **inversion** in the semiconducting behavior from an *n*- to a *p*-type at the electrode surface. The charge distribution within an inversion layer can be evaluated by considering a new space charge

layer of minority carriers near the surface. It can be equated by introducing a Boltzmann distribution (in analogy to the Gouy layer, see section 1.1.2.3) in the second term of the integrated Poisson's equation (1.9):

$$\left(\frac{dV}{dx}\right)^2 = \left(\frac{2}{\kappa\varepsilon_0}\right)\cdot\left(eU(x)N_D + p_b kT\cdot e^{\left(\frac{eU(x)}{kT}-1\right)}\right) \tag{1.30}$$

where the boundary condition of zero field dV/dx=0 ($U(x_0)$=0 in the bulk) has been again imposed. p_b represents the bulk density of holes. The first term of equation (1.30) corresponds to the fixed ionized species, so that the Boltzmann distribution representing the inverted layer in the second term will now determine the final potential profile at the interface. For the *n*-type case, the p_b term is very small and so high $U_{electrode}$ values (large band bending, see first column in Fig. 1.8C) will be required to make the second term in (1.30) comparable to the first one. A typical value of 10 nm is commonly obtained for the thickness of the inversion SCL [48]. If the charge density of minority carriers within the inversion layer is still lower enough such that the corresponding SCL thickness is orders of magnitude higher than the thickness of the electrolyte double layer and, therefore, the approximation $C_{Total} \approx C_{SC}$ in equation (1.7) is still valid, an inversion in the slope of the linear MS plot is then expected. An accurate analysis on that concern is presented in chapters 4 and 5.

To end with this block, let us consider the last case in which majority charge carriers are now injected into the semiconductor surface. For an *n*-type, it occurs when $U_{electrode} < U^n_{FB}$, i.e, when $E_{F,solid}$ overcomes the Flat band level. Since the band edges are pinned at the surface, the bands bend downward and the majority carriers (e^- in this case) accumulates at the surface ($n > n_b$ where n_b represents the e^- concentration in bulk) giving rise to a new SCL termed **accumulation layer** (see Fig. 1.8D, first column). Its potential distribution has of course opposite sign as compare to the depletion layer and it can be expressed as a contribution of the fixed dopant ions plus an excess of free accumulated charge. Following an equivalent procedure used in equation (1.30), the electric field in the accumulation layer yields:

$$\left(\frac{dV}{dx}\right)^2 = \left(\frac{2en_b}{\kappa\varepsilon_0}\right)\cdot\left(\frac{kT}{e}e^{\left(\frac{-eU(x)}{kT}-1\right)} + U(x)\right) \tag{1.31}$$

being now *U(x)* a negative potential. Again, previous boundary conditions employed in (1.30) are used. In analogy with equation (1.30), the first term in expression (1.31) accounts now for the excess of majority charge carriers at the semiconductor surface, and it gives comparable values for the SCL thickness (~10 nm [48]). It is important to stress here that when charge carriers accumulates on the surface, its density can approach the density in the electrolyte side (given by the ionic concentration) and C_{SC} becomes of the order of C_{el} which can not be now neglected in equation (1.7). The potential drop over the entire semiconductor│electrolyte interface is now partitioned between the semiconductor SCL and the electrolyte double layer [49,50]; the more negative $U_{electrode}$ is (heavier accumulation, see first column in Fig. 1.8D) the less the contribution of the SCL in the potential drop across the interface is. The extreme situation (at $U_{electrode} << U_{FB}$) yields to a degeneration state (see previous section) where the semiconductor electrode behaves as a metal and the interfacial potential drops almost completely within the electrolyte double layer. The capacitance behavior observed in the MS

plot under accumulation conditions can not be anymore used to extract quantitative information of the potential distribution within the semiconductor│electrolyte interface since C_{el} can not be now considered constant along the $U_{electrode}$ scan. As we will see in chapter 4, the accumulated charge on the semiconductor electrode surface usually involves the occurrence of redox processes that generate a current flown through the interface which are commonly accompanied by chemical transformations at the electrode surface.

The above forms/profiles of the SCL in the semiconductor side created under an external $U_{electrode}$ have been described within the mark of the thermodynamic equilibrium. This assumption requires that the generation of charge carriers at the semiconductor surface is faster than their flown into the electrolyte in order to completely develop the SCL formation. This condition mainly stands for the previously described situations for which a relatively high polarized electrode is required to build the surface carriers density up to the equilibrium values. However, at very high $U_{electrode}$, a **deep depletion** layer, which corresponds to a non-equilibrium configuration, can be often reached under standard electrochemical conditions. It was indeed outlined in figure 1.8C (first column); when a sufficiently high $U_{electrode}$ is applied such that an *inversion* layer is formed, but either minority carriers are not available at the surface or they are immediately consumed in an electrochemical reaction as fast as they generates at the electrode surface (the equilibrium is never reached), and then the second term of equation (1.30) can be considered negligible in the time of the experiment. As a result, we will have a continuous depletion situation as far as $U_{electrode}$ is increased and the $E_{F,solid}$ being buried into the minority charge carrier band. Under this regime, the potential distribution of the SCL is exclusively determined by the fixed ions and, therefore, the Schottky relation (1.24) will be again valid.

If now one takes holes as majority charge carriers and follows the above reasoning, it is possible to reach equivalent SCL profiles for a *p*-type semiconductor electrode (see second column diagrams in Fig.1.8A-D). Note that the shapes of the SCL for a *p*-type are inverted as compare to the *n*-type case, *i.e.* the depletion conditions for a *p*-type semiconductor in an electron energy scale are represented as a downward band bending (h^+ extracted from the surface).

Summing up, the most important factor to keep in mind when studying electrical double layers in a semiconductor│electrolyte interface (SCL), is that by modifying the external voltage. the experimenter can produce any form of charge distribution at the semiconductor surface. In successive chapters, we will see how electrochemical reactions are conditioned to the presence of available charge carriers at the electrode surface provided by the specific charge distribution profile in the semiconductor SCL. From a practical viewpoint, an accumulation layer in an *n*-type semiconductor electrode will allow cathodic current flow (with e^- flowing out of the semiconductor) if acceptors levels are available in the electrolyte (*e.g.* oxidized redox species). On the contrary, under depletion conditions those carriers will not be available for reaction and an effective energy barrier that blocks surface reactivity will be built up.

Surface States

In previous section 1.1.2.3, we introduced the concept of *surface state* (SS) as new energy levels that can be generated at the semiconductor│electrolyte interface. These SS can

exchange electrons with the main bands so that they can act either as donors, releasing an e^- to the conduction band and leaving a positive charge on the surface, or acceptors, by capturing an e^- from the valence band and resulting in a negatively surface charge. Therefore, SS can store net charge at the semiconductor surface thus modifying the SCL profile and, of course, the electrochemical electrode behavior. As previously stated, a variety of surface species can account for the formation of these additional surface energy levels. Probably, the most intuitive case corresponds to the so-called **intrinsic surface states** that have been largely approached in fundamental studies of semiconductor surfaces under vacuum conditions [51]. The nature of these intrinsic *SS* arises from the interruption of the covalent bonds of the lattice at the surface of the crystal, giving rise to half-occupied orbitals (so-called *dangling bonds*). These SS are commonly named *Shockley states*. Similarly, for semiconductors with ionic structures, ionic surfaces states or *Tamm states* are also found, again resulting from the surface truncation that leads cations or anions with lower coordination numbers at the solid surface. The energy of electronic levels at this sites will be higher that those in the bulk simply because of the lower electrostatic attraction, so they will energetically lie above the VB (within the gap region). If previous surfaces under vacuum conditions are transferred to an aqueous environment, the polar solvent molecules will immediately react with such high reactive SS species to form polar bonds (with a high dipole moment). These new bonds may act as new SS at the semiconductor│electrolyte interface, however, in the case of ionic oxide structures, the formation of hydroxyl groups (*-OH*) gives rise to energy levels that lie near or within the main bands and make them not detectable. For this reason, adsorption of large ions from the solution is in many cases the main source of SS generation at the semiconductor│electrolyte interface. Even non-adsorbed ions that are very close to the solid surfaces can induce SS.

In previous section, it was inferred the importance of SS on the electrode reactivity, because they can, to a certain extend, dominate the rate of the electrochemical reactions on a semiconductor electrode. To name a few electrochemical processes involving SS:

- Recombination (extinction) of minority carriers generated for example under inversion conditions (see previous sub-section) often occurs through SS thus preventing chemical reactions with ions in solution.
- SS can participate directly in the electrochemical reactions as intermediate states in the ET between the main bands and redox species in solution.
- The capture of charge carriers at the SS is of prime importance to explain electrochemical corrosion processes (this issue will be largely developed in chapter 5).

Despite their enormous impact on the semiconductor reactivity, the quantitative study of SS at the semiconductor│electrolyte interfaces is rather complex. As pointed in section 1.1.2.1, we can expect temporal energy fluctuation, described through Frank-Condon energy shifts, due to the presence of polar solvent molecules that surround the chemical specie associated to the SS. Lower λ values in equation (1.3) will be here obtained compare to the redox species in the electrolyte, since the SS see the solvent only in one hemisphere. These reasoning stands for either intrinsic or adsorbate SS cases exposed to the electrolyte, although the magnitude of the energy fluctuations can be different each case. Not only energy oscillations among empty

and occupied states are expected, but also more drastic chemical transformation can also take place. For example, upon capture or injection of an electron, surface chemical complexes that provide SS can be dissociated to either form a new chemical group with a completely different energy or dissolve into the solution disappearing from the solid surface. Another possible route, perhaps in part because of previous chemical transformations, may be when a SS is able to inject or capture carriers but not reversibly, fact that will impede to reach the equilibrium with the semiconductor Fermi level.

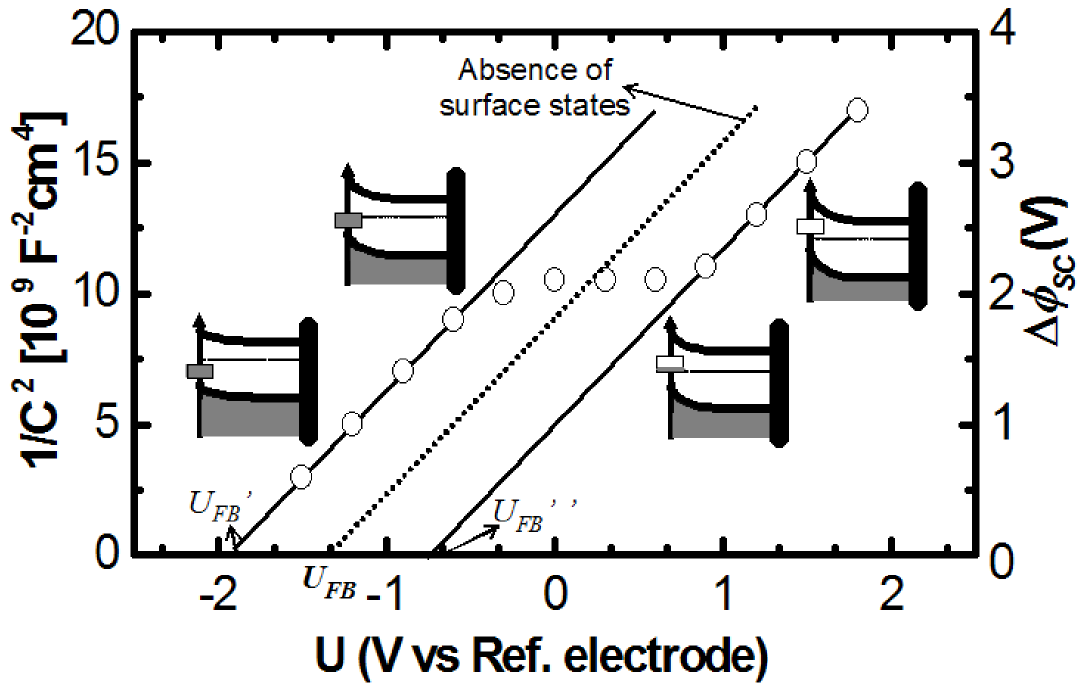

Figure 1.10: Mott-Schottky representation of the capacitance data showing the capacitance profile (opened circles) during the charging/discharging process of a *SS* on an *n*-type semiconductor | electrolyte interface. The dashed line represents the "ideal" curve in the absence of SS while solid lines represent the extrapolation of the capacitance behavior in the presence of charged and uncharged SS. The observed plateau in the curve corresponds to the bandedge shift (*bandedge unpinning*) that takes place when $E_{F,solid} = E_{SS}$ as shown in the sequence of pictures. Note that the SS is better represented as an ΔE_{SS} in the energy diagram (rectangle).

Hopelessly, all these features make difficult the experimental characterization of SS at semiconductor | electrolyte interfaces by conventional techniques. Some approaches can be found elsewhere [52,53]. It is especially interesting to analyze the expected capacitive response of a semiconductor electrode in the presence of SS under the application of an external potential $U_{electrode}$. Let us consider the simpler case of a chemically stable ion specifically adsorbed on the surface that has an energy level (E_{SS}) lying in the middle of the bandgap of an *n*-type semiconductor (see Fig. 1.10). Consider also that this SS can reversibly accept electrons with minor fluctuations in its energy levels and that the reduced an oxidized SS forms are negatively and positively charged respectively. Then, the charge stored in the SS (Q_{SS}) will depend on the position of $E_{F,solid}$ with respect to E_{SS} level through:

$$Q_{SS} = e \cdot f(E_F) \cdot N_{SS} \tag{1.32}$$

where N_{SS} denotes the density of SS given in cm^{-2}.

The function $f(E_F)$ is now referred to the E_{SS} energy level (see general form in expression (1.19)):

$$f(E_F) = \frac{1}{1 + e^{\frac{E_F - E_{SS}}{k_B T}}} \tag{1.33}$$

Taking equations (1.32) and (1.33), the differential capacitance of this SS yields:

$$C_{SS} = \frac{dQ_{SS}}{d(\Delta\phi_{SC})} = eN_{SS}\frac{d(f(E_F))}{d(\Delta\phi_{SC})} \tag{1.34}$$

indicating that the charge on SS depends uniquely on the potential drop across the semiconductor, which in turn, is given by the position of $E_{F,solid}$ in the solid. Equation (1.34) shows a maximum of C_{SS} at E_F=E_{SS}. The charge Q_{SS} has to be added to the charge provided by the SCL of the semiconductor (Q_{SC}) so that the interfacial charge represented in equation (1.5) ca be rewritten as:

$$Q_{el} = -(Q_{SS} + Q_{SC}) \tag{1.35}$$

The observed SS capacitance behavior points toward a simple electrical model for the semiconductor-*SS*│electrolyte interface that incorporates an additional C_{SS} term in serial contributing to the total capacitance in expression (1.7). However, as emphasized by Bard and coworkers [54], during the experimental filling/empting of a mono-energetic SS as the one represented in figure 1.10, the **Fermi level is pinned** at $E_{F,solid}$=E_{SS} and the interface capacity appears to be independent of $U_{electrode}$, displaying a plateau in the experimental MS plot (opened circles in Fig. 1.10); when $E_{F,solid}$ approaches the E_{SS} level, the potential drop is now employed in the SS charging/discharging process. During this process, the additional applied potential drops within the electrolyte Helmholtz layer and the band bending across the semiconductor ($\Delta\phi_{SC}$) remains unchanged. It means that the band edges must then shift an equivalent potential amount in the energy scale; the *band edges* are now *unpinned* and shift an amount equal to -Q_{SS}/C_H or +Q_{SS}/C_H (assuming a parallel capacitor model, equation (1.6)) respect to the situation of no SS presence (dashed line in Fig. 1.10). Once the SS are completely occupied or unoccupied, the band edges are again pinned and the bands bend linearly as a function of the $U_{electrode}$ following the MS relation in Eq. (1.29) (see Figs. 1.0 and 1.10). The extrapolation ($1/C^2$=0) of both linear ranges in the MS plot (Fig 1.10) results in two U_{FB} values shifted the same amount with respect to the no SS situation (U_{FB}*'* and U_{FB}*''*). They represent the hypothetical flat band positions plus the additional charge of negative (U_{FB}*'*) or positive (U_{FB}*''*) sign introduced by the filled or empty SS respectively.

The previously case describes the simplest SS picture at which we have a chemically stable SS at the electrode with an appreciable charge density N_{SS} (in the order of 10^{13} cm^{-3}), able to reversibly store charge and give a measurable capacitance response. However, we just pointed out at the beginning of this section that at the electrode│electrolyte interfaces the SS are commonly involved on electrochemical reactions that make SS undergo chemical transformations. The charge is then *not stored* and it is rather difficult to perform a direct measurement of the SS capacitance. In chapter 5, a more *practical* case with a SS that participates in the corrosion process of the electrode itself will be analyzed in detail.

1.1.2.5 Building up the diagram of the semiconductor│electrolyte interface

Briefly, we will bring all previous elements together to build up the experimental band diagram of the semiconductor│electrolyte interface (see Fig 1.11).

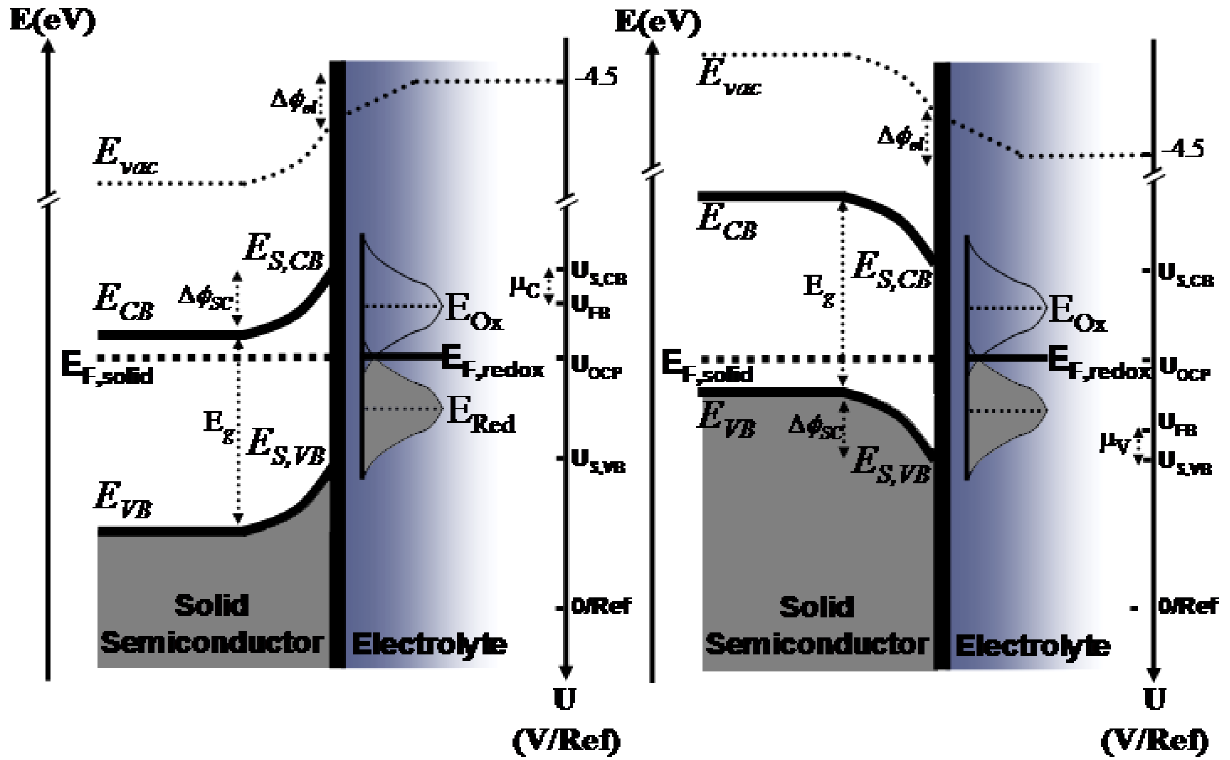

Figure 1.11: Construction of the energy diagram of the semiconductor│electrolyte interface for an n-type (left) and p-type (right) semiconductor electrodes.

The first required electrochemical parameter to be measured is the OCP value (U_{OCP}) which provides the equilibrium potential in the absence of an external applied $U_{electrode}$ (commonly named rest potential). Taking the previous equilibrium condition described in equation (1.4), it is possible to equate the correspondence:

$$-eU_{OCP} = E_{F,solid} = E_{F,redox} \tag{1.36}$$

and therefore, the potential drop across the SCL at the equilibrium is defined by:

$$\Delta\phi_{SC} = U_{OCP} - U_{FB} \tag{1.37}$$

where the U_{FB} can be experimentally determined under depletion conditions through the MS relation (Eq. (1.29)). Note that in the energy scale convention represented in figure 1.2, $\Delta\phi_{SC}>0$ when the bands are bent upward (see Fig. 1.11). The band edges of the majority carriers bands are then given by:

$$U_{S,VB} = U_{FB}^{p} + \frac{\mu_V}{e} \qquad (p\text{-type}) \tag{1.38a}$$

$$U_{S,CB} = U_{FB}^{n} - \frac{\mu_C}{e} \qquad (n\text{-type}) \tag{1.38b}$$

where the μ values have been described in expression (1.21). The edge of the minority carriers band results from the addition of the quantity E_g/e that can be obtained from the bulk electronic properties found on general handbooks [55].

To finish up with the energy diagram of the interface, the potential drop across the electrolyte ($\Delta\phi_{el}$) can be expressed in the scheme of figure 1.11 as:

$$\Delta\phi_{el} = \frac{\chi + \mu_C}{e} - U_{FB}^{n} \qquad \text{(n-type)} \qquad (1.39a)$$

$$\Delta\phi_{el} = \frac{\chi + E_g - \mu_V}{e} - U_{FB}^{p} \qquad \text{(p-type)} \qquad (1.39b)$$

where χ is the electron affinity (see Fig. 1.1).

This overall picture sketched in figure 1.11 is of major importance to predict the electrochemical behavior of the semiconductor electrode in the working electrolyte.

Along this section, we have analyzed the different electrical double layers present across the semiconductor│electrolyte interface with special emphasis on the semiconductor side. We have learnt that, opposite to metal electrodes where the potential drops entirely over the electrolyte double layer, in the semiconductor│electrolyte interface the potential drop is partitioned among both sides of the interface and that the dominating part on the charge transfer across the interface depends on the electronic properties of the semiconductor electrode and, more interestingly, on the imposed electrochemical conditions. Notwithstanding, within the forthcoming chapters we will see that the experimental quantification of this picture becomes now a days a difficult challenge.

1.1.3 Electron transfer at the semiconductor│liquid interface

1.1.3.1 General

In the early 1960s, various scientists started to develop modern theories of electron transfer between molecules in a homogeneous solution and between molecules and solid electrodes. Among them, the models proposed by Marcus [56] and Gerischer [57] have been the most extensively used. It is not the purpose of this section to give an extensive overview of these models, neither a description of the general *kinetic equations* of the ET on metal│electrolyte interfaces. Instead, we will focus the discussion only on those aspects that characterize the ET between a redox species in the electrolyte and a semiconductor electrode. For more extensive reviews, general bibliography is available [30,31,33].

Having the diagram of figure 1.11 in mind, let us first introduce the main features of the ET across the semiconductor│electrolyte interface. Departing from the equilibrium situation (OCP value in Eq. (1.36)), a net current density $j\neq 0$ (given in A/cm^{-2}) will flown across the interface when an **overpotential** η (being $\eta=U_{electrode}-U_{redox}$ where U_{redox} denotes the redox equilibrium potential of the species in the electrolyte which is frequently expressed in the standard conditions U^{0}_{redox}) is imposed through the application of an external potential. The $E_{F,solid}$ is then forced to shift from the equilibrium situation thus allowing electrons to flow out

or be injected into the electrode. Since these electrons are then collected or provided by the ions in solution, it usually implies chemical reactions at the electrode surface. Despite this is a very well-known concept in electrochemistry, the limited availability of charge carriers in the semiconductor electrode (e^- and/or h^+) implies that they have to be treated as individual reactants on interfacial reactions [57], in analogy with the reactant redox species in the solution. Let us consider the common redox couple Fe^{2+}/Fe^{3+} as the dominating redox reaction in the electrolyte. Then, the anodic electrochemical reactions at *positive overpotentials* [58] can proceed through the following reaction pathways:

$$Fe^{2+} \rightarrow Fe^{3+} + e^- \qquad (1.40a)$$

$$Fe^{2+} + h^+ \rightarrow Fe^{3+} \qquad (1.40b)$$

i. e. the anodic process corresponding to oxidation of the Fe^{2+}(aq) ion species can occur either through injection of an e^- or recombination (extinction) of a h^+ at the electrode surface (see Fig. 1.12). The reaction pathway for a given redox couple (*e.g.* Fe^{2+}/Fe^{3+}) depends then on the particular energy level distribution of the semiconductor electrode, and specially, on the *n*- or *p*- conduction type which ultimately determines the kind of majority charge carriers that govern the conductivity of the solid. Therefore, the measured current through our electrochemical set up corresponds essentially to the movement of majority charge carriers. Usually in practice, the observed current density is a contribution of several processes such as parallel reactions paths, reactions induced by minority carriers or absorption/desorption processes that generate capacitive currents.

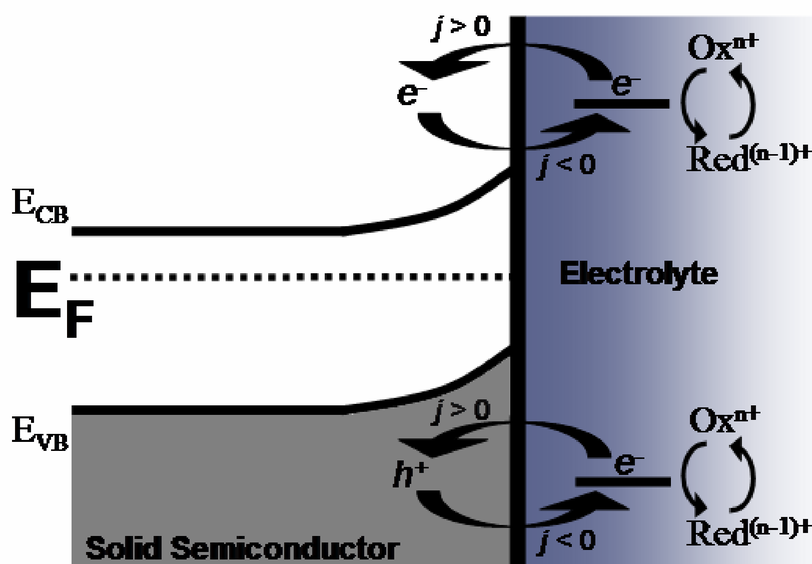

Figure 1.12: Different pathways involving electrons and holes transfer between the semiconductor electrode and the redox couple ox/red during the occurrence of the redox electrochemical reaction. Redox species are represented by a single energy level in the electrolyte (simplified representation). The standard electrochemical convention of the current sign has been used [58].

Previous to the development of modern ET theories [56,57], the current flow across electrode│electrolyte interfaces has been traditionally analyzed with classical models that

consider the electrochemical potential of the redox species using the so called absolute rate theory. They assume the existence an *"activated state"* which represents an energy barrier for the ET from the reduced (e.g. Fe^{2+}) to the oxidized (e.g. Fe^{3+}) form. In figure 1.13, the "activated state" is represented as the energy maximum in the potential curve resulting from both free energy curves of the oxidized and reduced species (ΔG_{red} and ΔG_{ox} represent respectively their *activation energies*). On the abscissa axis, the general reaction coordinate represents the energy fluctuation of the redox ion required to reach the "activated state" which will correspond to the reactive energy level in the semiconductor solid ($E_{F,solid}$, $E_{S,CB}$ or $E_{S,VB}$). Under these conditions, the rate constants of both oxidation (k_{ox}) and reduction (k_{red}) reactions are described by the Boltzmann distributions of the "activated state":

$$k_{ox} = k' e^{-\frac{\Delta G_{ox}}{k_B T}} \tag{1.41a}$$

$$k_{red} = k' e^{-\frac{\Delta G_{red}}{k_B T}} \tag{1.41b}$$

where *k'* is a pre-exponential factor. At first sight, one might expect from figure 1.13 that the application of an overpotential η has consequences uniquely on one barrier through lowering the activation energy of one of the redox species (depending on the η sign) while keeping the other constant. It would mean that when applying a positive η the anodic current would rise while the cathodic current would not be modified. Experimentally, this situation is unacceptable because η affects the total energy of the system so that it modifies the energy barriers of both redox forms (see Fig. 1.13B): when a $\eta > 0$ is applied we are simultaneously increasing the anodic current component and decreasing the cathodic one. As a first approximation, a linear relation between both activation energies and the applied η is then assumed:

$$\Delta G_{ox} = \Delta G^0 - \alpha z e \eta \tag{1.42a}$$

$$\Delta G_{red} = \Delta G^0 + (1-\alpha) z e \eta \tag{1.42b}$$

being α the so called *transfer coefficient*, ΔG^0 the activation energy at the equilibrium (see Fig. 1.13A) and z the number of e^- transferred in the reaction (in the following we will consider mono-electronic reactions, z=1). Equation (1.42) shows that if a $\eta > 0$ is applied, the activation energy ΔG_{red} rises in a fraction equal to $\alpha e \eta$. A simple trigonometric exercise (approximating the intersected curves in Fig. 1.13B to straight lines) yields to a complementary decrease in ΔG_{ox} equal to $(1-\alpha)e\eta$ (check ref. [59] for a more rigorous analysis). If consider now equilibrium conditions, rate constants on both directions are equal to:

$$k_{ox} = k_{red} = k_0 = k' e^{-\frac{\Delta G^0}{k_B T}} \tag{1.43}$$

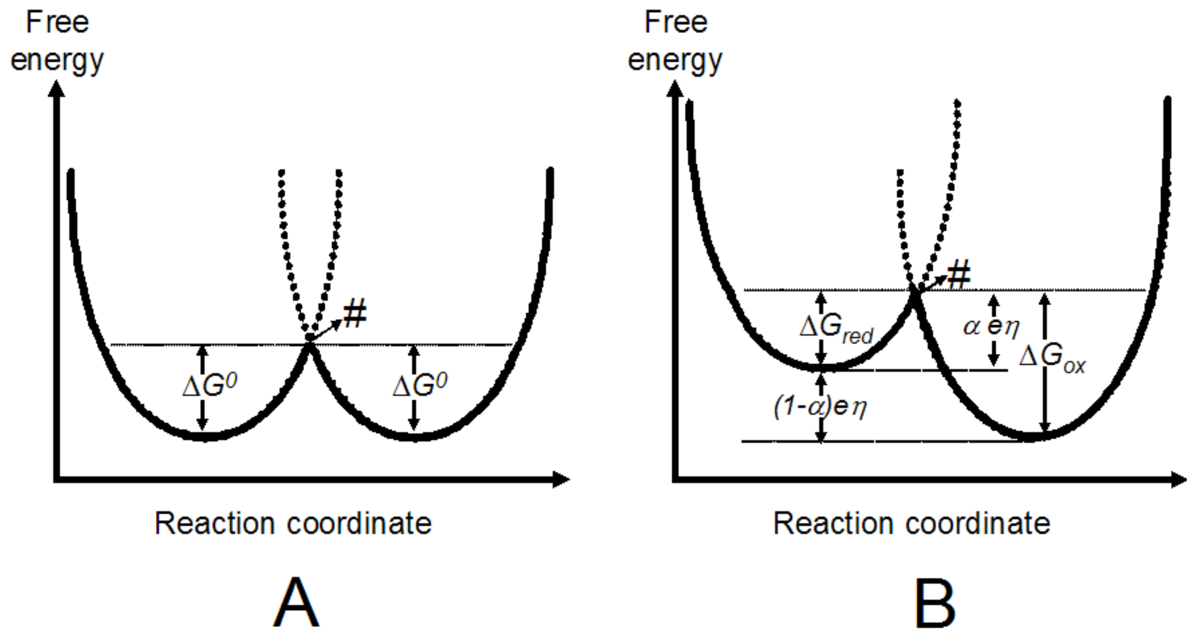

Figure 1.13: Free energy versus reaction coordinate under standard conditions at (A) equilibrium conditions and (B) under applied external potential. The sign of the imposed overpotential η will reduce the energy barrier of one of the redox species. In the used sign convention, a $\eta > 0$ decreases the energy barrier seen by the reduced form and increases the one seen by the oxidized form. # denotes the "*activated state*".

and k_0 is then defined as the rate constant at the equilibrium. Introducing equations (1.42) and (1.43) into (1.41), the rate constants can be rewritten as:

$$k_{ox} = k_0 e^{\frac{(1-\alpha)e\eta}{k_B T}} \tag{1.44a}$$

$$k_{red} = k_0 e^{-\frac{\alpha e\eta}{k_B T}} \tag{1.44b}$$

On the other hand, the total current (j_{Total}) flowing between the semiconductor electrode and the dominant redox couple in solution is the sum of the anodic and cathodic current components. Taking into account the sign convention [58], it yields:

$$j_{Total} = j_{ox} - j_{red} \tag{1.45}$$

The j_{ox} and j_{red} components are in turn proportional to the concentration of both redox forms in solution (c_{ox} and c_{red} respectively), the density of carriers at the semiconductor electrode surface (p and n respectively) and the corresponding rate constants (Eq. (1.44)):

$$j_{ox} = k_{ox} \cdot ep \cdot c_{ox} \tag{1.46a}$$

$$j_{red} = k_{red} \cdot en \cdot c_{red} \tag{1.46b}$$

Introducing equations (1.44) into (1.46), the equation (1.45) yields:

$$j_{Total} = k_0 \left(c_{ox} ep \cdot e^{\frac{(1-\alpha)e\eta}{k_B T}} - c_{red} en \cdot e^{-\frac{\alpha e\eta}{k_B T}} \right) \tag{1.47}$$

This is an extended form of the well-known Butler-Volmer relation (BV) that describes the kinetics of the ET across the electrode | electrolye interface as a function of the applied overpotential η. This equation is helpful to establish the major distinction between the ET on metals and on non-degenerated semiconductors electrode. In the former case, p and n parameters at the electrode surface are high enough to be considered as constants in the electrochemical reaction, and equation (1.47) simplifies into the BV equation for a metal | electrolyte interface:

$$j_{Total} = j_0 \left(c_{ox} e^{\frac{(1-\alpha)e\eta}{k_B T}} - c_{red} e^{-\frac{\alpha e\eta}{k_B T}} \right) \tag{1.48}$$

with the pre-exponential factor $j_0 = k_0 F$ that corresponds to the so called *exchange current*, the current that equally flows in both directions at the equilibrium ($j_{Total}=0$). The Faraday constant F is traditionally employed in electrochemistry instead of the elementary charge e. The typical current-potential curve deduced from equation (1.48) is illustrated in figure 1.14, and has been largely employed to quantitatively describe the empirical current-potential curves obtained from the metal | electrolyte interfaces.

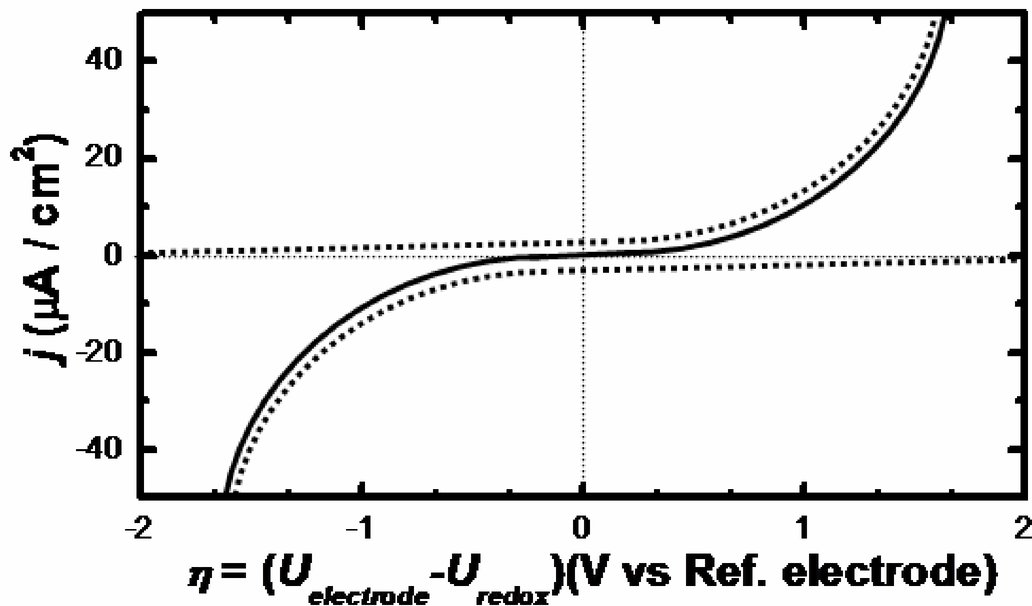

Figure 1.14: Current-potential profile according to the Butler-Volmer equation for α=0.5. Dotted lines correspond to the partial anodic and cathodic components given by each exponential term in equation (1.48). After ref. [31].

To make a simple comparison, in the metal case the applied potential arrives up to the solid surface (in the absence of a SCL) and, therefore, the potential-dependent parameter is the activation energy of the redox species in the electrolyte ΔG_{redox}. On the contrary, in the

semiconductor case the applied potential is eventually employed in bending the bands and, as consequence, the surface concentration of charge carriers is, in most cases, limited (see section 1.1.2.4). The potential-dependent parameter is now primarily the concentration of the charge carriers at the semiconductor surface (*n* and *p* terms in Eq. (1.47)). However, this assumption is valid only at certain conditions, since the electronic properties on the semiconductor surface strongly depends on the applied $U_{electrode}$ (or η). For this reason, within the next section we will analyze the main trends of the ET on the semiconductor electrode under the different SCL profiles described in section 1.1.2.4.

1.1.3.2 Electron transfer across the semiconductor SCL

The application of a quantitative formalism, like the BV type presented in Eq. (1.48), to a semiconductor electrode is complex because two potential-dependent parameters are mixed in the general kinetic equation (1.47): the activation energy of the electrolyte redox species relative to the energy levels in the solid and the concentration of the charge carriers at the electrode surface (*n* and *p*). The main assumption to be considered regarding a semiconductor electrode is that the ET proceeds via the main bands (CB and VB) either by direct transfer or through a SS (see *SS* in section 1.1.2.4). This fact implies that for a quantitative understanding of the redox processes, the analysis requires to treat each ET process individually. In chapter 4, a methodology to study ET at each individual band with a tunable redox probe in solution will be described.

Next, let us consider specific approaches for the kinetic treatment of the ET through the different SCL profiles in the semiconductor as a function of the applied overpotential η.

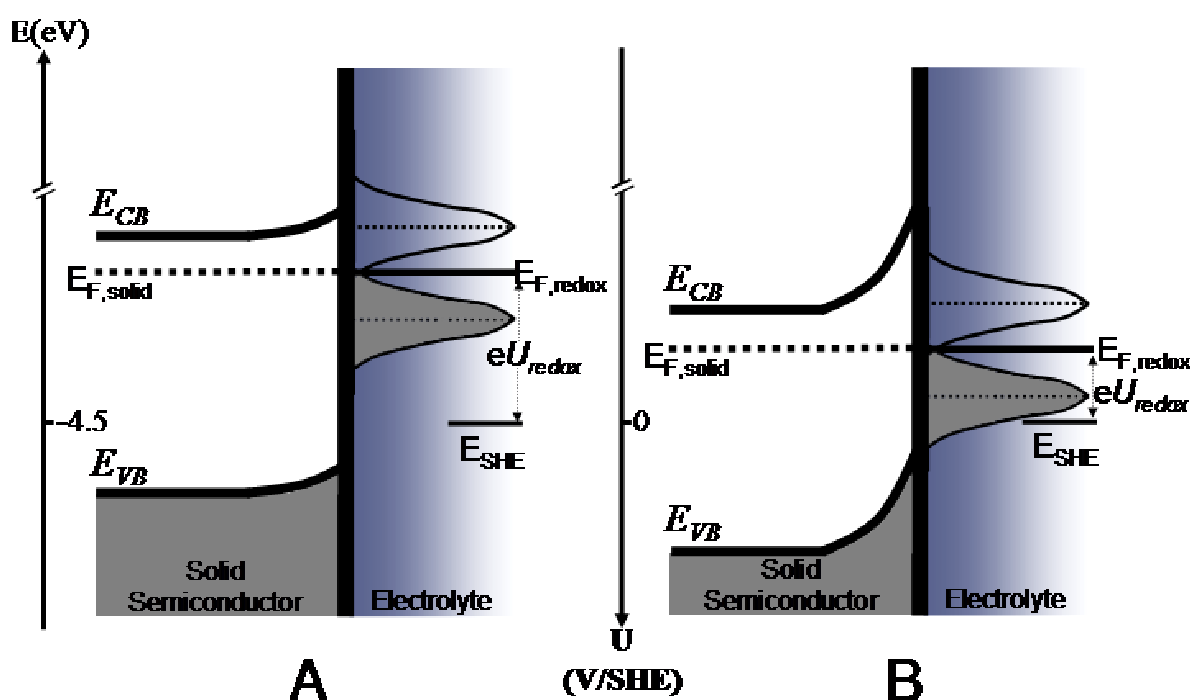

Figure 1.15: Energy diagrams of an *n*-type semiconductor | electrolyte interface for two different electrolyte redox couple: (A) a highly negative U_{redox} (CB process, see discussion) and (B) a positive U_{redox} (VB process).

Kinetics under depletion conditions

The ET through a semiconductor electrode under **depletion** conditions displays the most different electrochemical behavior as compare to the metal case. This behavior results in particular current-potential profiles that are actually being employed to explain outstanding electrochemical processes like metal corrosion or passivation as will be shown in chapters 4 and 5. As described in section 1.1.2.4, under depletion conditions the applied potential drops essentially in the semiconductor SCL ($\Delta\phi_{SC}$) through bands bending while the band edges remain pinned at the electrode surface. In this case, the relative position of the energy levels between the semiconductor band edges ($E_{S,VB}$ and $E_{S,CB}$) and the redox couple ($E_{F,redox}$) remains constant with the applied potential so that, in previous general equation (1.47), the key parameter that controls the ET is the density of charge carriers at the electrode surface (n or p depending on the semiconducting type). Although equation (1.47) contains *a priori* all the elements to explain the ET through any electrode│electrolyte interface, it is unspecific to quantify it when occurring at the semiconductor surface where it proceeds in general through one of the main bands as depicted in Fig. 1.15; diagram 1.15A corresponds to a rather negative (cathodic) U_{redox} which will favor a CB electrochemical process, while a more positive (anodic) U_{redox}, like the one in the diagram 1.15B, will favor the ET via VB. Since the ET process occurs horizontally, *i.e.* without electron energy lost (see Frank-Condon principle in section 1.1.2.1), it will be more convenient the use of the Gerischer's formalism [57] which considers a quantitative approach of the ET in terms of the position of the energy levels at both sides of the semiconductor│electrolyte interface. In the Gerischer's model some new premises are incorporated. Firstly, the reorganization energy parameter λ is again employed (see section 1.1.2.1) denoting the energy needed to accommodate the dipole solvent molecules of the solvation shell after the ET. The overall energy cycle of the oxidation-reduction process of a redox species in solution has been represented in figure 1.16. As also considered in other ET theories, the Frank-Condon principle also applies here and, therefore, the ET is expected to be very fast compared to the reorganization process of the solvation shell. According to these assumptions, the activation energies for the oxidized and reduced species take the form:

$$\Delta G_{red} = \frac{(e(U_{electrode} - U_{redox}) \; - \lambda)^2}{4\lambda} \tag{1.49a}$$

$$\Delta G_{ox} = \frac{(e(U_{electrode} - U_{redox}) \; + \lambda)^2}{4\lambda} \tag{1.49b}$$

where the empirical parameter of *transfer coefficient* α has been substituted by the more accurate λ term, assuming an harmonic oscillation for the fluctuations of the solvent molecules (for more detailed descriptions see refs. [31,57]). According to the energy cycle sketched in figure 1.16 and taking equation (1.41), the rate constant for ET within this model yields:

$$k = k' e^{-\frac{(\Delta G^0 + \lambda)^2}{4 k_B T \lambda}} \tag{1.50}$$

The pre-exponential factor *k'* includes the frequency of the nuclear motion ν through the transition state # (in the order of 10^{12}-10^{13} s^{-1}) and a transmission coefficient σ (ranging from 0 to 1) [31,57].

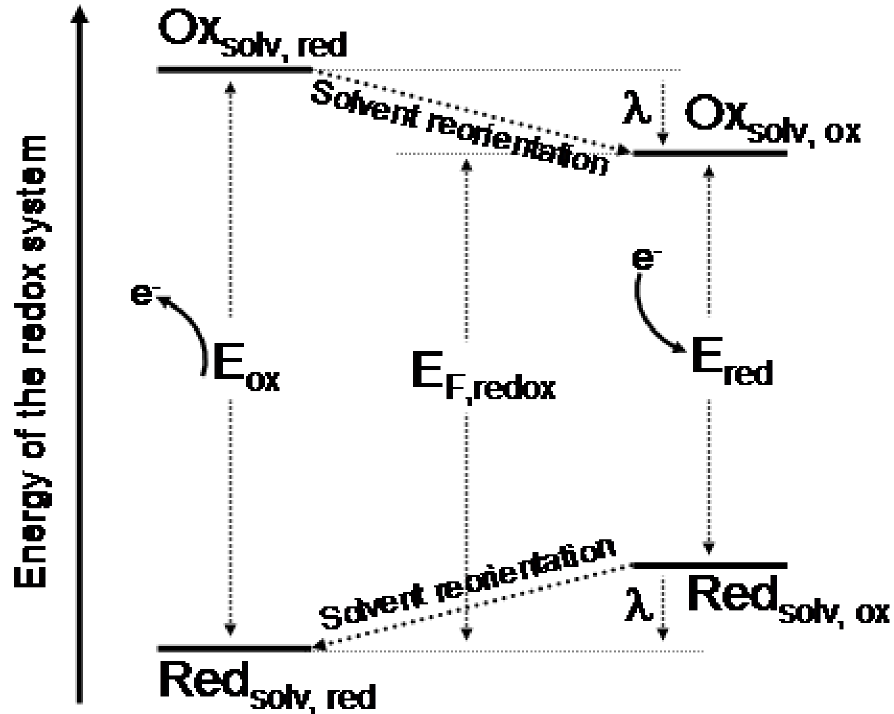

Figure 1.16: Energy levels of the redox system in both oxidized and reduced species. The sub-indexes *red* and *ox* denote the ion solvation shell corresponding to the reduced and oxidized forms respectively and λ is the reorganization energy (see text). From ref. [60].

In the Gerischer's model the ET occurs horizontally, *i.e.* at a constant energy from an occupied state in the solid to an empty state in the redox species and *vive versa*. Therefore, the ET rate will be proportional to the density of states at both sites of the interface as well as to the rate constant formulated in equation (1.50). Summing up, the kinetic equation, after introducing the boundary conditions for the specific case of the ET from an occupied state of the redox system to an empty state of the semiconductor CB, can be written as:

$$j_{CB}^{ox} = ek'_{CB}(1 - f(E_{CB}))\rho(E = E_{CB})c_{red} \cdot e^{\frac{-(E_{S,CB} - E_{F,redox}^{0} - \lambda)^2}{4k_B T\lambda}} \tag{1.51}$$

This j_{CB}^{ox} represents the current density component of the oxidation process for the reduced specie *[Red]* at the CB (see Fig. 1.17). The elements $f(E)$ and $\rho(E)$ are the Fermi distribution function of electrons (Eq. (1.19)) and the distribution of energy states in the solid, respectively, so that the product $f(E_{CB})\rho(E_{CB})$ represents the number of occupied states and $(1-f(E_{CB}))\rho(E_{CB})$ the number of empty states in the CB of the semiconductor, being the latter case commonly represented by N_{CB} (see Eq. (1.21)).

Equation (1.51) then holds:

$$j_{CB}^{ox} = ek'_{CB} N_{CB} c_{red} \cdot e^{\frac{-(E_{S,CB}-E_{F,redox}^{0}-\lambda)^2}{4k_B T\lambda}} \quad (1.52a)$$

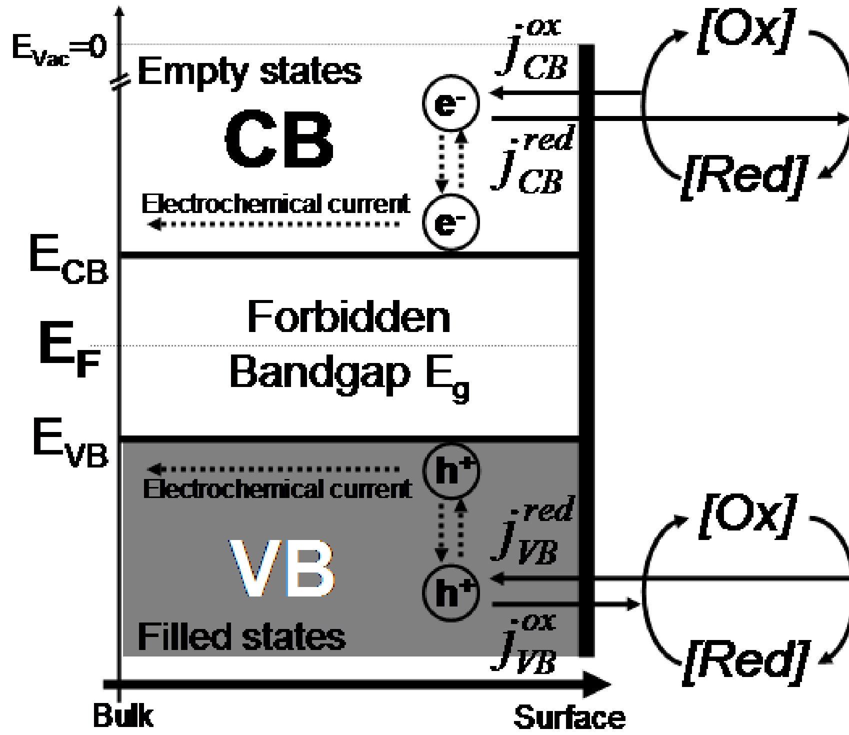

Figure 1.17: Different current densities originated as a result of the possible ET pathways between a redox couple in solution (*[Ox]/Red]* in the simplified representation) and the semiconductor electrode.

In analogy, the reversed current corresponding to the ET from the CB to the empty states of the redox system (reduction of the oxidized form *[Ox]* at the CB, see Fig. 1.17) can be then written as:

$$j_{CB}^{red} = ek'_{CB} n_S c_{ox} \cdot e^{\frac{-(E_{S,CB}-E_{F,redox}^{0}+\lambda)^2}{4k_B T\lambda}} \quad (1.52b)$$

where now the product $f(E_{CB})\rho(E_{CB})$ is equal to the number of free available electrons at the solid surface n_S. Following the same reasoning, it is possible to derive kinetic equations for the same anodic and current densities at the VB (see Fig. 1.17):

$$j_{VB}^{ox} = ek'_{VB} p_S c_{red} \cdot e^{\frac{-(E_{S,CB}-E_{F,redox}^{0}-\lambda)^2}{4k_B T\lambda}} \quad (1.53a)$$

$$j_{VB}^{red} = ek'_{VB} N_{VB} c_{ox} \cdot e^{\frac{-(E_{S,CB}-E_{F,redox}^{0}+\lambda)^2}{4k_B T\lambda}} \quad (1.53b)$$

being p_S the available hole density at the semiconductor surface. Note that only those current components j incorporating the terms n_S and p_S (Eqs. (1.52b) and (1.53a)) are dependent of the external applied potential through expressions:

$$n_S = n_0 e^{-\frac{e\Delta\phi_{SC}}{k_B T}} \tag{1.54a}$$

$$p_S = p_0 e^{\frac{e\Delta\phi_{SC}}{k_B T}} \tag{1.54b}$$

that relate n_S and p_S to the charge carrier densities in bulk (n_0 and p_0) through a Boltzmann distribution across the depleted SCL ($\Delta\phi_{SC}$). On the contrary, the current components j_{CB}^{ox} and j_{VB}^{red} remain independent of the electrode potential since N_{CB} and N_{VB} are constants and the exponential terms contain only fixed parameters for a given redox system.

The equations exposed in (1.52) and (1.53) are able to describe the experimental current-potential curves represented in figure 1.18 for *n*- and *p*-type semiconductor electrodes immersed in an aqueous medium.

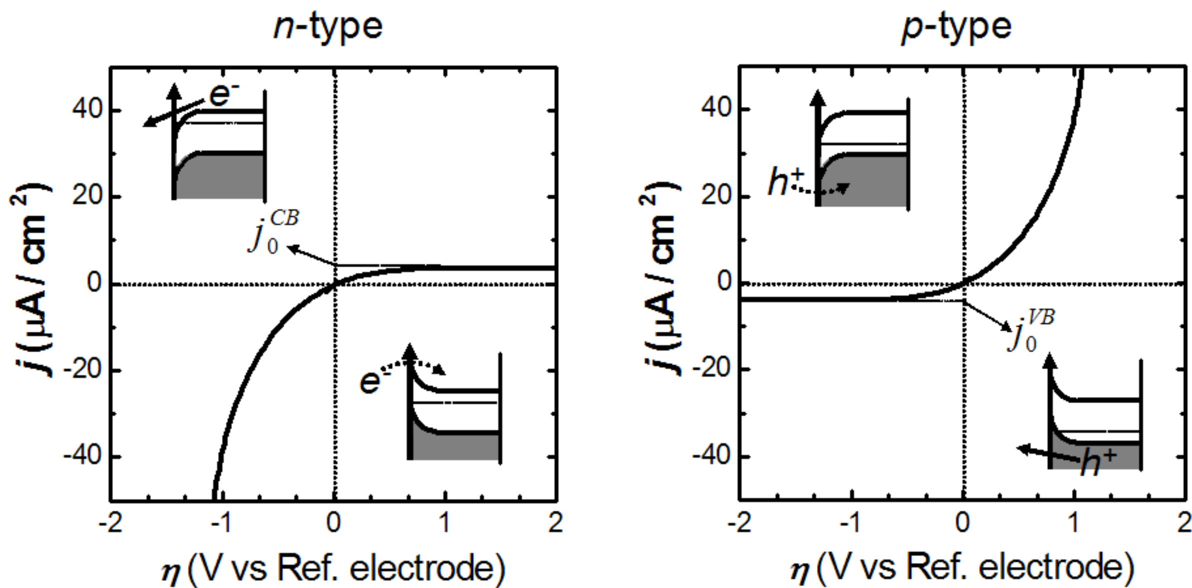

Figure 1.18: Current-potential curves for *n*- and *p*-type semiconductors in an aqueous electrolyte. j_0^{CB} and j_0^{VB} denote the exchange currents of the ET at the CB and VB respectively.

In analogy with the exchange current term introduced in equation (1.48), equations (1.52) and 1.53) can be also expressed in terms of equilibrium conditions so that two different exchange currents can be characterized on a semiconductor electrode:

$$j_{CB}^{ox} = j_{CB}^{red} = j_0^{CB} = ek'_{CB}\, n_{S,0} c_{redox} \tag{1.55a}$$

$$j_{VB}^{ox} = j_{VB}^{red} = j_0^{VB} = ek'_{VB}\, p_{S,0} c_{redox} \tag{1.55b}$$

being j_0^{CB} and j_0^{VB} the exchange currents for the ET at the equilibrium in the CB and VB respectively. Terms $n_{S,0}$ and $p_{S,0}$ denote the density of surface charge carriers under

equilibrium conditions. For simplicity, standard conditions are fulfilled as $c_{red}=c_{ox}=c_{redox}$. At this point, it is possible to define an overpotential for the depletion case as $\eta_{SC} = \Delta\phi_{SC} - \Delta\phi_{SC}^{o}$. Then, the overall processes at each band:

$$j_{CB} = j_{CB}^{ox} - j_{CB}^{red} \tag{1.56a}$$

$$j_{VB} = j_{VB}^{ox} - j_{VB}^{red} \tag{1.56b}$$

can be rewritten in a very simple form by introducing equations (1.55) and (1.54) into (1.52) and (1.53) at constant c_{redox}:

$$j_{CB} = -j_0^{CB}\left(\frac{n_S}{n_{S,0}} - 1\right) = -j_0^{CB}\left(e^{\frac{-e\eta_{SC}}{k_B T}} - 1\right) \tag{1.57a}$$

$$j_{VB} = j_0^{VB}\left(\frac{p_S}{p_{S,0}} - 1\right) = j_0^{VB}\left(e^{\frac{e\eta_{SC}}{k_B T}} - 1\right) \tag{1.57b}$$

Equations (1.57) are frequently compared to the BV relation (Eq. (1.48)). In comparison, an *apparent transfer coefficient* α' could be defined, taking values of 0 and 1 or *vice versa* for the electron exchange with the VB or CB respectively, in contrast to a value of 0.5 usually obtained in the metal case. The parameter α' has then no direct relation with the classical transfer coefficient α that accounts for the reversibility of the oxidation-reduction process on the electrode surface. If doing a simile of both α *and* α' parameters, the ET at the individual band appears to be possible in one way only, *i.e.* electron injection in the CB and hole injection (e^- extraction) in the VB. Moreover, the concept of *semiconductor overpotential* η_{SC} is also different from the commonly η employed in classical electrochemistry, since it does not describe the real overpotential reaction in the semiconductor case; under depletion conditions, the (majority) charge carriers are always transferred from and to the fixed band edges. In this sense, η_{SC} accounts exclusively for the availability of charge carriers at the electrode surface.

The total net current j_{Total} (Eq. (1.45)) flowing through the semiconductor│electrolyte interface will be the sum of both band contributions $j_{total} = j_{CB} + j_{VB}$, however, in practice, semiconductor electrodes present a certain doping density to improve their conductivity (*n*- or *p*-dopants, see *basic concepts* in 1.1.2.4) so that the total current will primary flow through the majority carriers band:

$$j_{total} \approx j_{CB} = -j_0^{CB}\left(e^{\frac{-e\eta_{SC}}{k_B T}} - 1\right) \quad (n\text{-type}) \tag{1.58a}$$

$$j_{total} \approx j_{VB} = j_0^{VB}\left(e^{\frac{e\eta_{SC}}{k_B T}} - 1\right) \quad (p\text{-type}) \tag{1.58b}$$

as it is observed in the experimental current-potential curves of figure 1.18 where the branch corresponding to the majority carriers band is uniquely displayed.

The previously argumentation is in general valid for reactions involving majority charge carriers, so the ET mainly occurs at the energy range corresponding to the majority carriers band. Nevertheless, it is still possible to have a participation of minority carriers thus generating new ET reactions on the surface electrode that would otherwise take place. For example, illuminating the semiconductor electrode with light of energy larger than the actual bandgap E_g, is probably the most common method to generate a certain hole population in the VB of an *n*-type semiconductor. Once created, this minority charge carriers concentration can participate in a parallel redox process (*e.g.* photo-corrosion on *n*-type semiconductors) giving rise to an additional photo-current component j_{ph} [61]. This is indeed a very interesting issue on the electrochemical passivation-corrosion field and some experimental details can be found elsewhere [30,31]. Notwithstanding, its accurate analysis is beyond the scope of this Ph.D. work.

Kinetics under accumulation: degenerated semiconductor

If the semiconductor electrode is brought to an accumulation situation (see section 1.1.2.4), the concentration of majority charge carriers at the surface (either n_S or p_S) is considerably raised until, at large applied $U_{electrode}$, $\Delta\phi_{SC}$ saturates and then most of the applied potential results in the change of $\Delta\phi_H$ (band edge unpinning). Under these conditions, the electrode behaves as a metal: the high carriers density at surface can be considered approximately constant as in the metal case. Under these conditions, the BV formalism is valid, *i.e.* equation (1.48) is accounted for the large overpotentials η values at which the accumulation layer is created at the semiconductor surface. *Tafel approximation*s [38] from equation (1.48) can be described for *n*- and *p*-type semiconductors as:

$$j_{total} \approx j_{red} = -j_0 c_{ox} e^{-\frac{\alpha e \eta}{k_B T}} \qquad (n\text{-type}) \qquad (1.59a)$$

$$j_{total} \approx j_{ox} = j_0 c_{red} e^{\frac{(1-\alpha) e \eta}{k_B T}} \qquad (p\text{-type}) \qquad (1.59b)$$

Equation (1.59a) stands then for an *n*-type semiconductor at $\eta \ll 0$ that allows accumulation of electrons at the surface and induces reduction of the redox species in solution (e^- are then transferred from the solid to the electrolyte). Equally, equation (1.59b) stands for a *p*-type semiconductor at $\eta \gg 0$ thus allowing accumulation of holes at the electrode surface and inducing oxidation of the redox species in solution (e^- are now transferred from the electrolyte to the solid). Note that Tafel equations are originally employed on metal electrodes with the particularity that while on the metal case they can be used in both anodic and cathodic directions, in the semiconductor case only the Tafel approximation that corresponds to the accumulation overpotential direction is valid (see Eq. (1.59)). The opposite corresponding approximation (reversed η) will bring the electrode to depletion conditions (previous section) where equations (1.59) are no longer valid.

In the accumulation situation, the kinetics of ET at *n*- and *p*-type semiconductor electrodes is then well described by expressions (1.59) which implies that the semiconductor

overpotential can be now expressed as $\eta = \Delta\phi_H - \Delta\phi_H^0$, equivalent to the original η described for a metal electrode.

The previous assumptions are extensive to a semiconductor electrode under **degeneration** conditions (see section 1.1.2.4). This state can be reached either by increasing the density of dopants in the solid (section 1.2.4.1) or by burying the Fermi energy $E_{F,\ solid}$ into the main band at high electrode potentials (high η). Under these conditions, the semiconductor behaves as a quasi-metallic solid, and Tafel equations are also applicable.

Kinetics at deep depletion

This non-equilibrium situation described in section 1.1.2.4 is in most cases accompanied by a charge transfer process at the semiconductor│electrolyte interface. When the semiconductor electrode is forced to a **deep depletion** situation at very high electrode potentials (either $U_{electrode}$ >>0 or <<0 depending on conduction type), two different ET processes can be described. On the one hand, since the SCL of the semiconductor electrode is in a continuous depletion state, same general kinetic equations (1.57) of ET involving majority charge carriers under depletion conditions, can be used ($E_{F,redox,1}$ in Fig. 1.19). On the other hand, at the high applied potentials, minority charge carriers are generated at the semiconductor surface (at either $E_{F,\ solid} << E_{S,VB}$ for an *n*-type or $E_{F,\ solid} >> E_{S,VB}$ for a *p*-type). In order to fulfill with the deep depletion conditions, these minority carriers have to be rapidly consumed in an electrochemical reaction as soon as they reach the electrode surface. Taking the *n*-type semiconductor example, at high anodic $U_{electrode}$, the generated holes at the electrode surface can act as a highly oxidizing agents of any redox couple in the electrolyte with a $E_{F,redox}$ level lying near the VB edge ($E_{S,VB}$). The electrochemical reaction then implies an ET from the redox occupied level to the VB of the semiconductor (h^+ annihilation) thus generating a j_{ox} ($E_{F,redox,2}$ in Fig. 1.19). These electrochemical reactions on the solid surface usually involve chemical reactions on the semiconductor electrode as we will see in section 1.2.4.4.

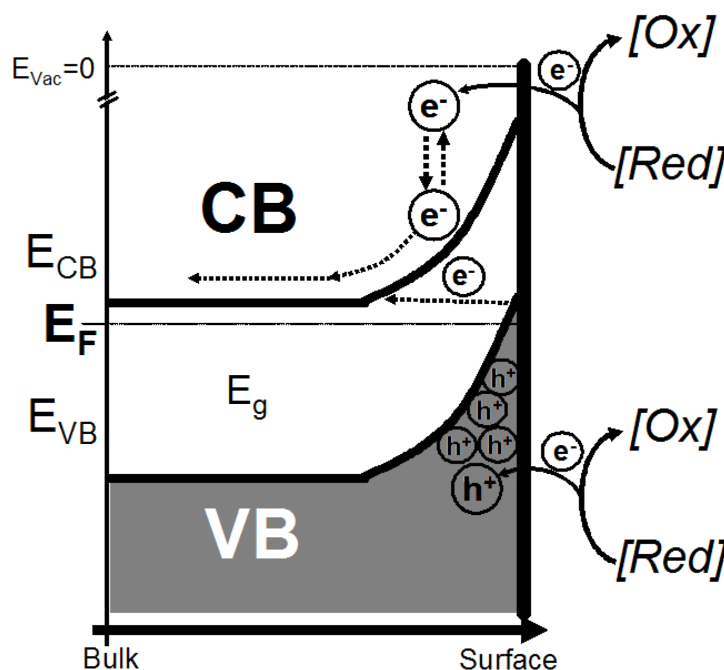

Figure 1.19: Energy diagram representation of the different ET pathways on an *n*-type semiconductor electrode under deep depletion conditions. Two different redox species $E_{F,redox,1}$ (up) and $E_{F,redox,2}$ (down) are represented in the simplified form.

1.1.3.3 Diffusion-controlled electron transfer

The kinetics of ET on a semiconductor electrode has been discussed in previous section assuming a *kinetic control* of the electrochemical process. It implies that the diffusion rate of redox species in solution is fast enough to maintain a concentration at the electrode surface equal to that in the solution bulk ($c_{S,redox}=c_{redox}$). In practice, the rate of ET is usually much faster than the diffusion rate of the ionic redox species from the electrolyte bulk to the electrode surface and *vice versa*. In this case, it is said that the electrochemical reaction is *controlled* or even *limited by diffusion*. This is particularly common on metal electrodes where the overlap between the electronic states in the electrode and in the electrolyte is good enough to assure a very fast ET (diffusion-controlled process). In most cases, the applied $U_{electrode}$ is sufficiently high that any redox species at the electrode surface is immediately consumed in the electrochemical reaction and thus, the surface concentration of the redox specie ($c_{S,redox}$) can be considered null.

Considering semiconductor electrodes, a poor overlap between the electronic states at both sides of the semiconductor│electrolyte interface is eventually found due to the presence of a particular SCL. Then, a pure kinetic control may be particularly more interesting on the semiconductor case. Nevertheless, as shown in section 1.1.2.4, under specific electrochemical conditions the semiconductor electrode may behave as a metal and, therefore, same current density j profiles resulting from the diffusion-controlled rate of the redox species across the electrolyte will be measured.

The quantitative information of the diffusion gradient for both oxidized *[Ox]* and reduced *[Red]* redox species in the electrolyte can be obtained by solving diffusion equations:

$$\frac{\partial c_{ox}}{\partial t} = D_{ox} \frac{\partial^2 c_{ox}}{\partial z^2} \tag{1.60a}$$

$$\frac{\partial c_{red}}{\partial t} = D_{red} \frac{\partial^2 c_{red}}{\partial z^2} \tag{1.60b}$$

where it is assumed that the solution is not disturbed and that the diffusion of molecules occurs only perpendicular to a planar electrode surface along the z-axis. D_{ox} and D_{red} designate the diffusion coefficients of the *[Ox]* and *[Red]* species. The analytical derivation of equation (1.60) can be carried out by applying the following boundary conditions: for an electrochemical oxidation process $Red \rightarrow Ox + 1e^-$, the initial *[Red]* concentration $c_{red,0}$ is constant and equal to the bulk concentration c_{red} whereas c_{ox}=0. The contrary situation holds for the reduction process $Ox + 1e^- \rightarrow Red$ (see refs. [62,63] for more details). Then, the result of the derivation at z=0 (electrode surface) yields the surface concentration profiles:

$$c_{S,red} = c_{0,red} \frac{\left(\frac{D_{red}}{D_{ox}}\right)^{\frac{1}{2}} \frac{c_{S,red}}{c_{S,ox}}}{1 + \left(\frac{D_{red}}{D_{ox}}\right)^{\frac{1}{2}} \frac{c_{S,red}}{c_{S,ox}}} \tag{1.61a}$$

$$c_{S,ox} = c_{0,ox} \frac{\left(\frac{D_{red}}{D_{ox}}\right)^{\frac{1}{2}} \frac{c_{S,red}}{c_{S,ox}}}{1+\left(\frac{D_{red}}{D_{ox}}\right)^{\frac{1}{2}} \frac{c_{S,red}}{c_{S,ox}}} \qquad (1.61b)$$

Since the ET is assumed to be very fast so that the *[Ox]* and *[Red]* species are always in equilibrium at the electrode surface (z=0), the surface concentrations ratio in (1.61) obeys the Nernst relation:

$$\frac{c_{S,ox}}{c_{S,red}} = e^{\left(\frac{e(U_{electrode} - U^0_{redox}}{k_B T}\right)} \qquad (1.62)$$

Equation (1.62) provides a relationship between the surface concentration of the redox species and the applied electrode potential.

The net current flowing through the electrode will be then proportional to the flux of material (commonly given in mol s^{-1} cm^{-2}) arriving to the surface (at z=0). If consider a general oxidation reaction, the flux can be described, in a first approach, by a linear concentration gradient of *[Red]* species diffusing toward the electrode surface:

$$flux = D_{red} \frac{c_{0,red} - c_{S,red}}{L_{diff}} \qquad (1.63)$$

Introducing (1.61a) in (1.63) and incorporating the charge conversion constant *F*, the current density for a diffusion-controlled electrochemical reaction yields:

$$j^{ox}_{diff} = c_{0,red} F \frac{D_{red} / L_{diff}}{1+\left(\frac{D_{red}}{D_{ox}}\right)^{\frac{1}{2}} \frac{c_{S,red}}{c_{S,ox}}} \qquad (1.64)$$

where the parameter L_{diff} is defined as the distance over which a linear concentration gradient produces the same flux during the electrochemical reaction course (also known as the thickness of the depleted layer of redox species, see Fig. 1.20A). As the *[Red]* species is consumed at the electrode surface, the concentration gradient changes with time and so $L_{diff} = L_{diff}(t)$. A more analytical approach gives a relation for this function of the form [62,63]:

$$L_{diff} = (\pi \cdot D_{red} t)^{\frac{1}{2}} \qquad (1.65)$$

showing that the distance L_{diff} increases with time as the *[Red]* specie is consumed in the electrochemical reaction (see Fig. 1.20A). If we consider now the limiting case of large applied overpotentials ($U_{electrode} >> U^0_{redox}$), $c_{S,red}$ is equal to zero and, after introducing Eq. (1.65), equation (1.64) simplifies to the form:

$$j_{\lim}^{ox} = c_{0,red} F \left(\frac{D_{red}}{\pi t} \right)^{\frac{1}{2}} \tag{1.66}$$

which is known as the *limiting current density*. Any further potential increase does not make the current any larger because it is limited by the diffusion rate of *[Red]* species going toward the electrode surface (Fig. 1.20B).

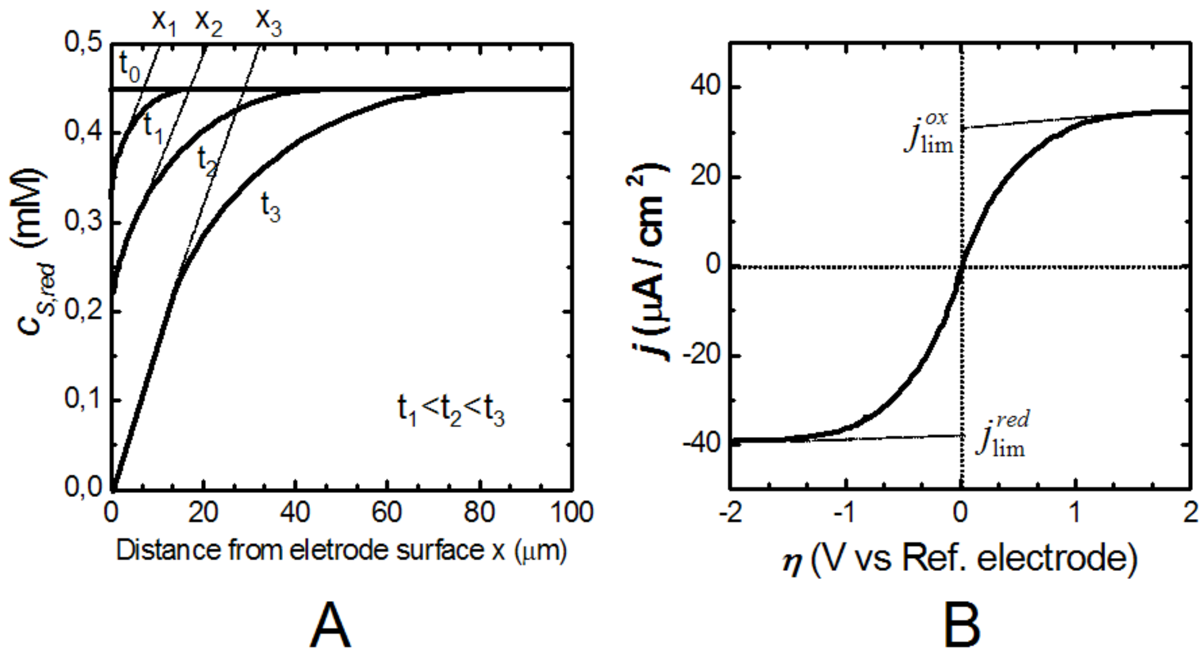

Figure 1.20: (A) Concentration profiles for the diffusion of a *[Red]* species to a planar electrode which is being consumed in the reaction *Red* → *Ox* + e^-. It has been represented for a constant current density *j* (constant flux) at different times departing from t_0=0s (x_0=0) and $c_{0,red}$ =0. Values x_1, x_2, and x_3 show the evolution of L_{diff} with time. (B) Current-potential curve for a diffusion-controlled electrochemical process.

The mass transport can be enhanced by disturbing the solution (under hydrodynamic conditions). Experimentally, it is commonly performed by rotating the solid electrode immersed in the electrolyte (named *rotating disc electrode* commonly employed on the electro-deposition technology). The best description was conducted by Levich *et al.* [64] who found a dependency of the L_{diff} with the rotation speed ω of the form:

$$L_{diff} = 1.61 D^{1/3} \omega^{-1/2} \nu^{1/6} \tag{1.67}$$

where ν is the kinematic viscosity of the solution and the rotation speed ω is experimentally given in rpm (rotations per minute). In this case, the $j_{\lim}^{ox}$ takes a constant value of:

$$j_{\lim}^{ox} = 0.62 c_{0,red} F \frac{D_{red}^{2/3} \omega^{1/2}}{\nu^{1/6}} \tag{1.68}$$

which is now independent of time. Both equations (1.66) and (1.68) can be similarly expressed for the reduction diffusion-controlled process $j_{\lim}^{red}$.

1.2 IMPACT OF THE SEMICONDUCTOR MODEL ON PASSIVE FILMS

1.2.1 General

Most outstanding technological materials like metals and metal-based alloys used in metallurgy, or semi-metals like Si and/or Ge largely employed in microelectronics, are subjected to surface chemical oxidation in the environmental conditions of operation (oxidizing atmosphere, aqueous media, etc.). This fact develops into the formation of a thin surface oxide layer that is present on the surface of these materials and that ultimately controls its reactivity. For that reason, surface oxide films play an important role in many disciplines such as electrochemical energy conversion, electrochemical analysis, electrocatalysis and corrosion protection [66,67]. Their particular properties depend on parameters such as stoichiometry, film thickness (d), applied electrode potential ($U_{electrode}$) or electrolyte composition (c_{redox}). The electrochemical environment has been largely employed to grow oxide layers in a controlled way, either by ramping or stepping the applied $U_{electrode}$ in a specific electrolytic medium (pH, c_{redox}). Finally, chemical and/or redox processes occurring at the oxide│electrolyte interface can decisively modify their physical-chemical properties and thus, the surface reactivity of the electrode.

As stated in the preface of this thesis, the largest amount of work concerning oxide films has been conducted for many years as an important part of the *Corrosion Science*. Undoubtedly, corrosion occurring on metal and metal alloys, when they are exposed to a fairly aggressive environment, is one of the most exciting matters in this field, where the surface oxide layer constitutes the only physical and/or electronic barrier hindering the corrosion reaction of the metal substrate underneath. This process is known as *passivation*, and despite the concept was formally introduced by the first time in 1836 [1] (see preface), it took several decades to figure out that the passivation state is based on the spontaneous formation of a highly protective oxide film (so-called *passive film*) of few nanometers thick at the metal surface. A wide description of the last experimental advances on the *in situ* analysis of some outstanding metal oxide systems will be presented in section 1.3. Of course this process is of an enormous technological significance, since the dissolution or corrosion rates determine in most cases the lifetime of many structural materials.

Generally speaking, corrosion processes do not involve the ion flux through the oxide layer only (so-called ion transfer reactions (*ITR*)) but also its electron transport properties (so-called ET reactions (*ETR*)). While *ITR* represent the ion migration through the oxide layer, which depends essentially on the local electric field and ionic diffusion, *ETR* represent a much more complicated processes affected by the distribution of electronic states at both sides of the oxide | electrolyte interface. Hence, it is of great interest to obtain information about the electronic properties of passive films.

In forthcoming sections, the previous semiconductor model (see section 1.1) is employed to describe the ET through a metal│passive film│electrolyte interface. Limitations and new concepts to better adapt the model to the passive oxide system are presented. A short review of the main models of ionic transport through passive layers is also included. Finally, previous background is used to briefly review the concept of passivity breakdown (electrode corrosion).

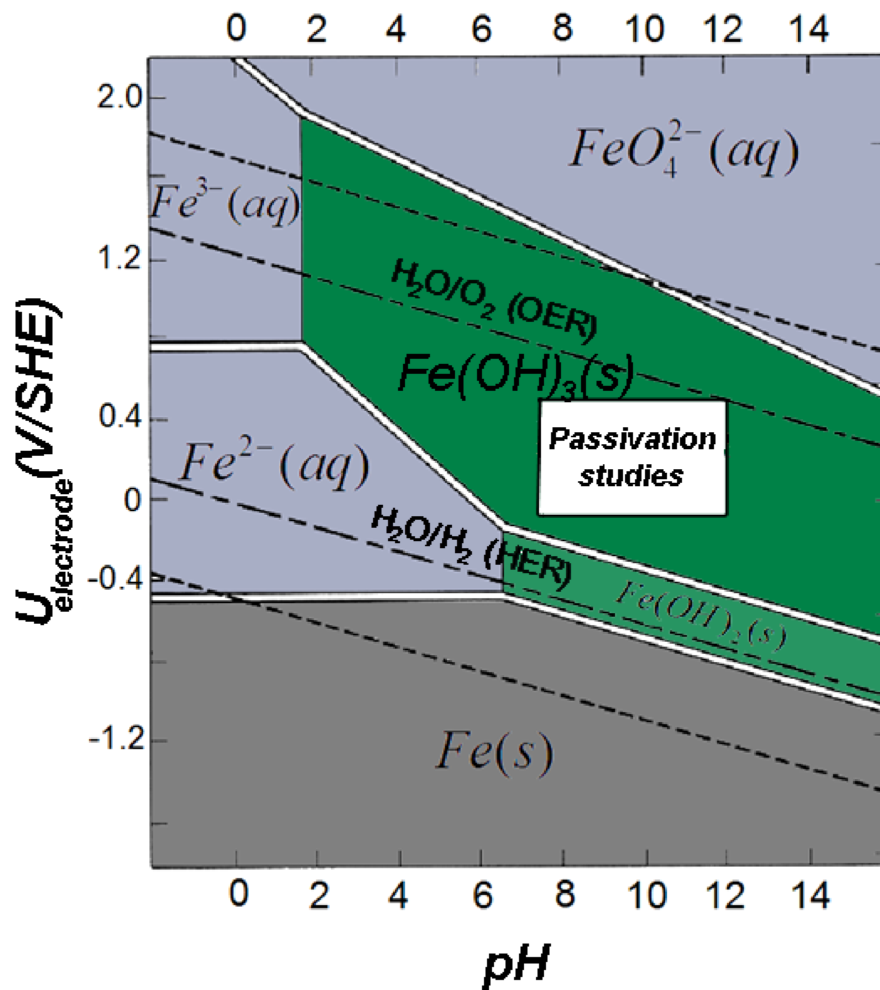

Figure 1.21: Simplified $U_{electrode}$ versus *pH* Pourbaix diagram for the Fe-water system at 25 ºC. Discontinuous lines denote Hydrogen Electrode Reaction (HER) and Oxygen Electrode Reaction (OER). The central white square area corresponds to the experimental conditions employed on fundamental studies of Fe passivity.

1.2.2 Thermodynamic aspects

The first consideration when studying oxide passive layers refers to their chemical stability in the electrolytic medium where they are formed. The result of calculations for the thermodynamic stability of metal oxide systems is frequently represented in the form of *pH* versus electrode potential ($U_{electrode}$) plots so-called Pourbaix diagrams [70]. Figure 1.21 represents the Pourbaix diagram of Fe in an aqueous environment. Blue areas in the Pourbaix diagram denote active regions where the material undergoes dissolution, while green areas indicate the formation of the corresponding oxides. This thermodynamic information is employed *a priori* to set up the oxide film growth conditions in the studies of passivity, *i.e.* electrolyte composition and passivation potential (U_P). It should, however, be pointed out that these diagrams does not give neither kinetic information of the oxide growth nor the exact composition and structure of the final passive layer. Since the data given in the Pourbaix diagram refers to the oxide bulk, the expected behavior for a thin passive layer may be significantly different and so the thermodynamic information is commonly used as a mere qualitative guidance. In the iron case, passive layers are typically formed within the *pH* range

of 7 to 12 and at U_P values among 0 and 0.4 V/SHE (see Fig. 1.2 for the electrode scale correspondence). Within these area in the Pourbaix diagram (Fig. 1.21), an Fe(III) oxide layer is thermodynamically expected to be present on the Fe electrode surface as the chemical entity responsible of electrode passivation (see experimental studies of this system in the next section 1.3).

1.2.3 The Band model on oxide films

1.2.3.1 Main trends

The description of the band model, as developed in the preceding sections, can be applied to improve our understanding of the ET through an oxide covered metal electrode in contact to an electrolyte. In general, crystalline bulk oxides may behave as metals, semiconductors or insulators [68]. Due to the chemical similarity between the crystalline bulk oxides and the amorphous oxide layers, similar characteristics of their electronic properties have been experimentally deduced [69], *e.g.* the *SCL*, photo-electrochemical behavior or the position of band edges. Figure 1.22 sketches the general band diagram for the metal | oxide | electrolyte interface, including all sources of energy levels arising after the interface formation. At a glance, we can observe the enormous complexity of the band diagram for this particular interface. The origin of this complexity is in general two-fold: (i) the nanometer-range thickness of these passive layers hinders, in many instances, the complete development of the oxide semiconductor *SCL*, fact that makes it questionable the establishment of an ideal band structure like the one described in previous section 1.1. And (ii) the amorphous nature of the passive layer also contributes to a non-ideal band structure since the energy distribution within its band diagram becomes less abrupt or poorer defined. A more extended list that better describes the picture represented in figure 1.22 is presented next:

- Passive films are often amorphous or have nano-crystalline nature giving rise to the formation of localized states near the band edges. In this case, the energy levels are not sharply defined and so the band gap E_g appears to be less abrupt than in the bulk crystalline case. This concept is so-called *mobility gap* (E_{mg}).

- Passive films are often non-stoichiometric so that new particular doping levels can be taken into consideration when constructing the band diagram.

- The passive layer grows by consuming the underlying metal so that it is not in thermodynamic equilibrium with the electrolyte. This fact develops into a characteristic depth profile of composition and structure within the oxide layer from the metal | oxide to the oxide | electrolyte interfaces.

- Formation SS at the oxide | electrolyte interface (section 1.1.2.4) bears a complex surface process commonly poor reproducible and not sharply defined due to the dynamic nature of the oxide surface. SS formation as well as intercalation of foreign ions may drastically modify the electronic properties of the oxide film.

- Under certain experimental conditions, passive layers may behave as mixed electronic/ionic conductors.

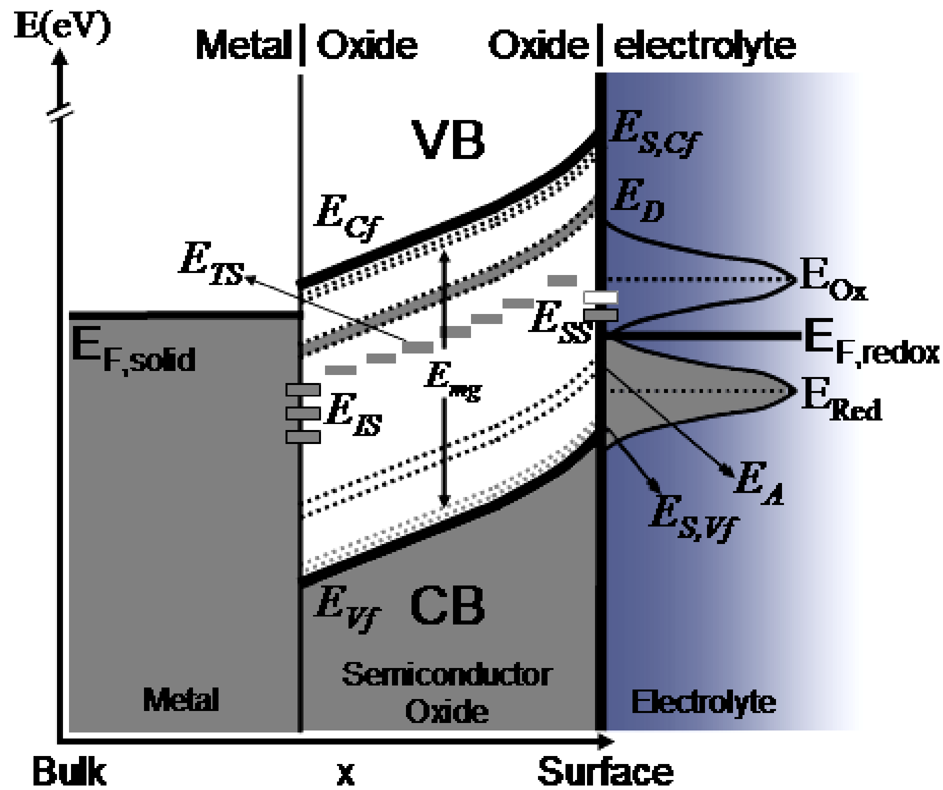

Figure 1.22: Proposed band model for the metal│oxide│electrolyte interface showing all sources of energy levels. Discontinuous lines indicate the poor definition of the energy levels due to the amorphous nature of the passive oxide layer (see text discussion).

Despite previous assumptions, the semiconducting nature of metal oxide layers has been demonstrated in many instances [30,65], although quantitative descriptions of their semiconductor band model have been poorly presented in the bibliography. Among the above points, the highly defective solid structure of the passive film is probably the main critical factor that makes indeed a quantitative analysis of its electronic properties difficult. Due to the dynamic nature of the metal│passive film│electrolyte interface, its quantitative band model is expected to be built up as long as the concentration profile of defects (*N(x)*) across the oxide film is constant. This fact implies that measurements of any physical-chemical properties of the passive layer should be done at steady state conditions, *i.e.* under conditions at which *ITR* can be neglected (see section 1.3 and chapter 2 for experimental methodologies). As a rule of thumb, the equilibrium of structural defects across the oxide layer will be maintained in thin semiconducting oxide films with low E_g value like, for example, Fe and Ni passive films. But for dielectric passive metal oxides like Ti or Al, the equilibrium can not be so easily reached and so that a more complex distribution function of defects $N(E,x,t)$ across the oxide film will be deduced.

Through the forthcoming sections, the new concepts listed above will be briefly reviewed. The band model picture sketched in figure 1.22 will be successively recalled along this section to illustrate the new appearing elements that characterize the metal│oxide│electrolyte junction.

1.2.3.2 Nature of the highly defective oxide structure

Passive film on metals present, as found experimentally, a high concentration of defects (N) that ranges between 10^{19} to 10^{21} cm^{-3} depending on parameters such as film thickness or applied potential ($U_{electrode}$). Vijh distinguishes up to 11 ways that oxide layers can become conductive, mostly associated to defects in the oxide structure [75,77]. These structural defects, so-called *point defects* [77], are mostly caused by either oxygen V_O^{2+} or metal V_M^{n-} vacancies, or their corresponding interstitials (O_i^{2-} and M_i^{n+}), as introduced in section 1.1.2.4. The lector not familiarized with these concepts is addressed to the basic representation of the main crystallographic defect types sketched in figure 1.23. Such defects within the oxide layer can act either as electron donors or acceptors levels (N_D and N_A respectively, see representation in Fig. 1.6) conferring a particular *n*- or *p*-type behavior respectively to the semiconducting oxide layer. In addition, the motion of such defects across the passive layer is responsible of the diffusion of metal and oxygen through the oxide film during, for example, the film growth process [77]. Note that a concentration of these defects in the order of 10^{20} cm^{-3} (an equivalent content of ~1 %) provides enough overlap between atomic orbitals for carriers to hop from one energy level to the next, thus allowing electronic conduction across the film. A list containing the main electronic parameters of some remarkable bulk metal oxides | electrolyte interfaces is presented in Table I. The chemical entity of such structural defects within the oxide lattice is usually associated to a metallic cation of an oxidation state different from stoichiometric structure in the bulk. Taking the Fe system as example, this passive film structure resembles a crystalline oxide structure which is in between the stoichiometric Fe_3O_4 and Fe_2O_3 spinel forms, where Fe(III) cations in the crystalline structure coexists with a percentage of Fe(II) species of up to ~10 %. These Fe(II) species have been commonly associated to the donor impurity (N_D) of the *n*-type Fe passive layer (see section 1.3 for further details).

Furthermore, intercalated foreign cations like H^+ or large anions like Cl^- and I^- may form localized states or *trap states* (E_{TS}) energetically located within the band gap of the oxide electronic structure. Low concentrations below 10^{18} cm^{-3} of these impurities may be sufficient to generate an efficient trap energy state that allows electron transport through the oxide film (see Fig. 1.22).

As previously mentioned, the thermodynamic equilibrium among both metal | oxide and the oxide | electrolyte interfaces depends on the migration behavior of ions across the oxide film. This ionic transport has been described by different models assuming a particular mechanism for the cation and/or anion vacancies transport through the oxide passive layer [71-74]. These mechanisms provide a detailed description of the *ITR* and they have been largely employed to model the kinetics of the oxide growth on metal electrodes, as we will review in section 1.2.4.2. In summary, a complete function that gathers both energy and spatial distributions of defects as a function of time $N = N(E, x, t)$ has to be considered. In figure 1.22, the observed energy profile within the *SCL* of the oxide film is caused by its particular distribution of defects.

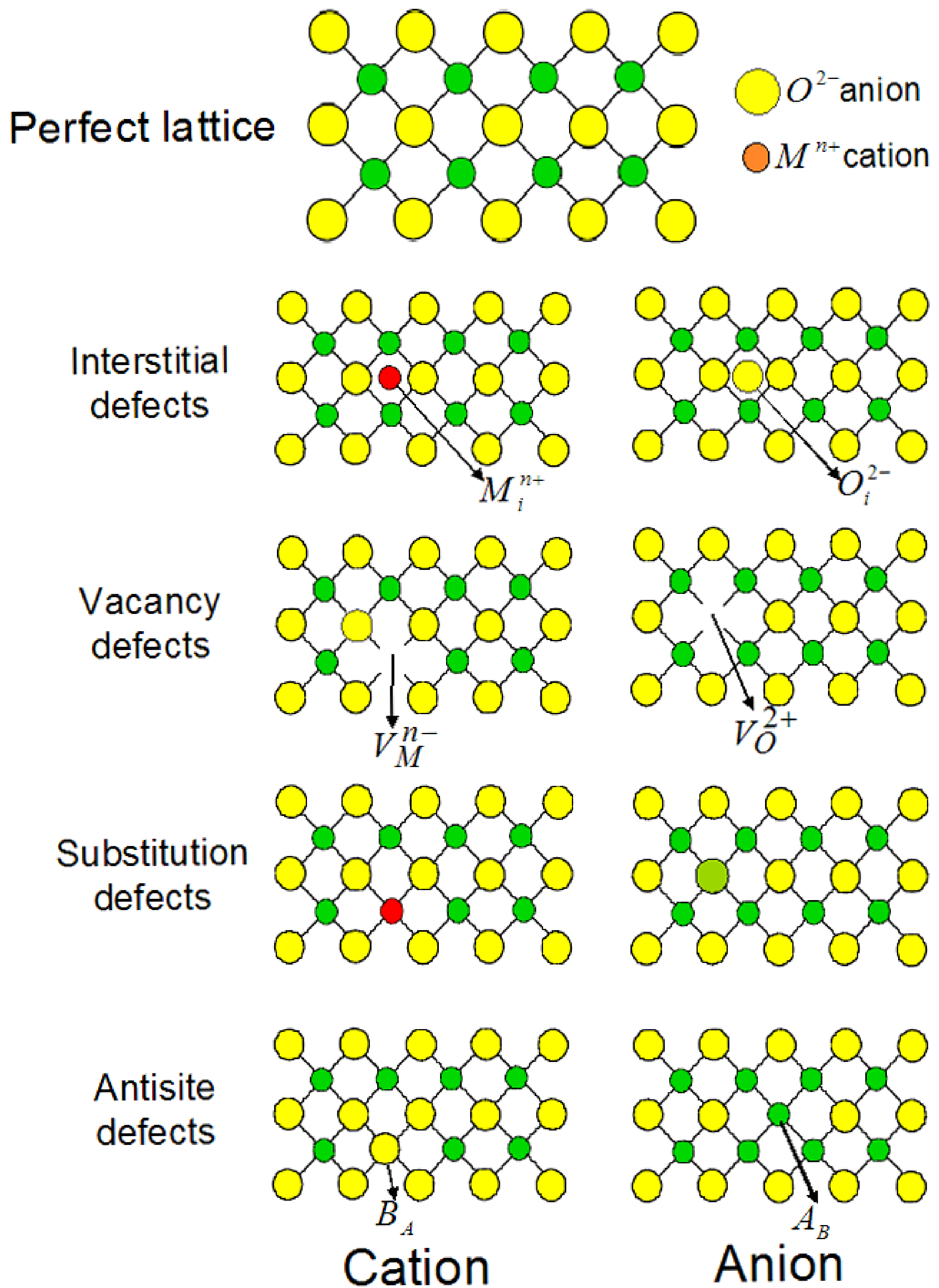

Figure 1.23: Schematic overview of the crystallographic point defects in the oxide lattice. Left and right column correspond to cation and anion defects respectively.

Table I. Main parameters corresponding to the electronic properties of bulk oxide Semiconductors|electrolyte interfaces. Last column (ε_{ox}) denotes the dielectric constant of the oxide layer. Data extracted from Refs. [30, 78].

METAL AND ALLOY	OXIDE FILM						
	Conduc. Type (*n*-, *p*- or i)	Bandgap (E_g/eV)	Doping density (N/cm^{-3})	Flat Band (E_{FB}/eV)	VB Edge ($E_{S,VB}$/eV)	CB Edge ($E_{S,CB}$/eV)	ε_{ox}
Cu	*p*	0.6-1.8	-	0.5	-	-	-
Fe	*n*	1.6-2.2	10^{20}	-0.1/0.15	2.2	0.2	10-35
Fe/Cr	*n*	1.9-2.1	10^{20}-10^{21}	-	-	-	10-30
Fe/Cr/Ni	*n*	1.9-2.3	10^{20}-10^{21}	-	-	-	10-30
Fe/Cr/Ni/Mo	*n*	2.3-2.8	10^{21}	-	-	-	10-30
Fe/Ni	*n*	1.9	10^{20}	-	-	-	10-35
Ni	*p* (*n*)	2.2-3.7	10^{20}	1.2	-	-	30
Al	*i*	4.5-9	-	-	-	-	7-20
Al/Cr	*n*	-	-	-	-	-	-
Cr	*p* (*n*)	2.5-3.5	10^{20}	-	-	-	10-50
Ti	*n*	3.2-3.8	10^{20}	-0.6	2.7	-0.3	7-114
Sn	*n*	3.5-3.7	10^{19}-10^{20}	-0.45/-0.3	3.8	0.1	-
Zn	*n*	3.2	10^{18}	-0.4/-0.85	2.6	-0.6	8.5
W	*n*	2.7-3.1	10^{17}-10^{18}	-0.5/0	-	-	23-57
Pb	*n*	2.8	-	0	-	-	-
Zr	*i* (*n*)	4.6-8	-	-1.8	2.5	-1.4	12-31
Cd	*n*	2.1	-	0	2.2	0.1	-
Nb	*n*	3.4	-	-0.75	-	-	-
V	*n*	2.75	-	0.9	-	-	-

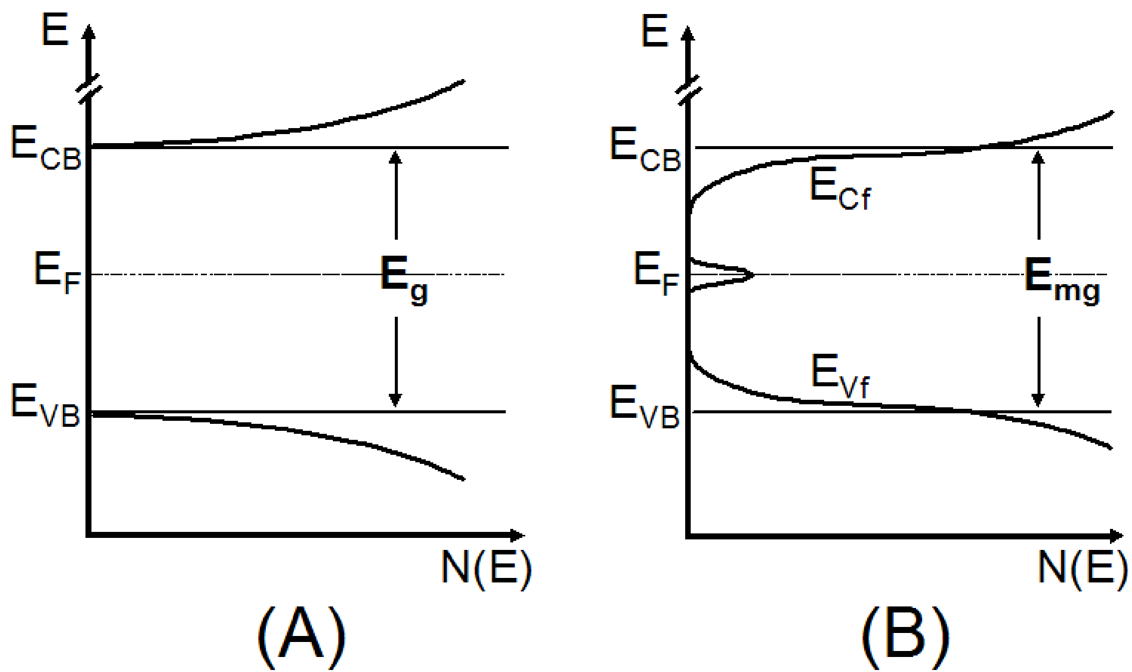

Figure 1.24: Density of state distributions in (A) an ideal and (B) an amorphous or defective semiconductor. The small tail at $E=E_F$ in (B) represents localized states accompanying the E_{Cf} and E_{Vf} levels. After ref. [76].

1.2.3.3 Mobility gap

The structure of amorphous oxides presents energy levels corresponding to valence electrons near the lattice anion (O^{2-}) as well as to the next excited energy state near the cation (M^{n+}). Therefore, *bands* (*CB* and *VB*) are expected to be in the passive oxide layer as they result from the solution of the Schrödinger's equation on a perfect three-dimensional periodic crystal. However, as each lattice site in the oxide amorphous structure is not identical with respect to its nearest neighbor, the energy levels may be not identical in the sense of *Pauli Exclusion Principle* [30]. It results in the appearance of somewhat unique bonding configurations of both cations levels (with slightly higher χ than most of the cation levels that conform the *CB*) and anion levels (with slightly lower E_I than most of the anion levels that conform the *VB*). These electron energy levels are represented in Fig. 1.22 as discontinuous lines below the *CB* and above the *VB* respectively. This particular electronic configuration gives rise to the concept of *mobility gap* (E_{mg}), that replaces the previous bandgap (E_g) definition and highlights the existence of an equivalent forbidden electronic gap whose energy limits appears to be more diffuse, *i.e.* less abrupt. This is better understood if represented in terms of density of states (see Fig. 1.24) where it is observed that a certain *band penetration* into the gap is allowed. Following up with this reasoning, the energy level above which orbitals have enough overlap for a conduction band electron to be transported through the film is defined as E_{Cf}. Equivalently, E_{Vf} will correspond to the lower E_{mg} energy limit below which holes can be transported through the film. At energies $E<E_{Cf}$ and $E>E_{Vf}$, the conductivity will progressively decrease (see Fig. 1.24) until carriers may eventually be trapped at the lowest *N(E)* energy levels.

In summary, from a practical electrochemical point of view, redox process on passive films involving semiconductor bands can take place in a certain potential range, and therefore, voltammetric peaks will be expected to broaden.

1.2.3.4 Surface and Interface states

The formation of localized states at the junction between two different phases has been a long standing issue in the fundamental studies of surfaces under UHV conditions [51]. In the metal│oxide layer│electrolyte contact, we have two different interfaces susceptible to become a source of *interface states* (IS). They have been also represented in figure 1.24 as a particular source of energy level in the amorphous oxide system. Note that the *IS* located at the oxide│electrolyte interface are then known as SS, as already introduced in the previous section 1.1.2.4, since they are located at the solid surface. *IS* are important at the semiconductor│oxide interface (*e.g.*, Si/SiO_2) where they arise because of the mismatch between the crystalline semiconductor structure underneath and the structure of the passive oxide on top. It commonly leaves dangling bonds or other nonbonding orbitals as occurs in the semiconductor│UHV interfaces [51]. However, the *IS* represented in figure 1.22 (E_{IS}) are rarely important in the role of ET across the metal│oxide interface since they can rapidly release or capture charge from the metal substrate thus loosing their charge storing capability. On the other hand, SS are expected to behave as it behaves in any semiconductor│electrolyte interface, as was inferred in section 1.2.1.4 (*Surface States* sub-section). SS at such an interface (E_{SS} in Fig. 1.22), and especially on an oxide semiconductor surface in contact to an aqueous environment, are dominated by the adsorption of ions like H^+ and OH^- that give rise to the formation of polar bonds on the solid surface [79]. More important is the adsorption of large anions as a source of SS, which will be treated in detail in chapter 5.

We can conclude that the general ET properties of the metal│oxide layer│electrolyte interface are dominated, if they are in sufficient density, by the presence of SS on the oxide surface.

1.2.4 Current transport through oxide films

1.2.4.1 General

As introduced at the beginning of this section, the total current flow through the oxide passive layers is the sum of two contributions: charge carriers transport (*ETR*) and ionic motion (*ITR*). The overall current density measured experimentally is then given by the sum:

$$j_{Total} = j_{cap} + j_{ITR} + j_{ETR} \tag{1.69}$$

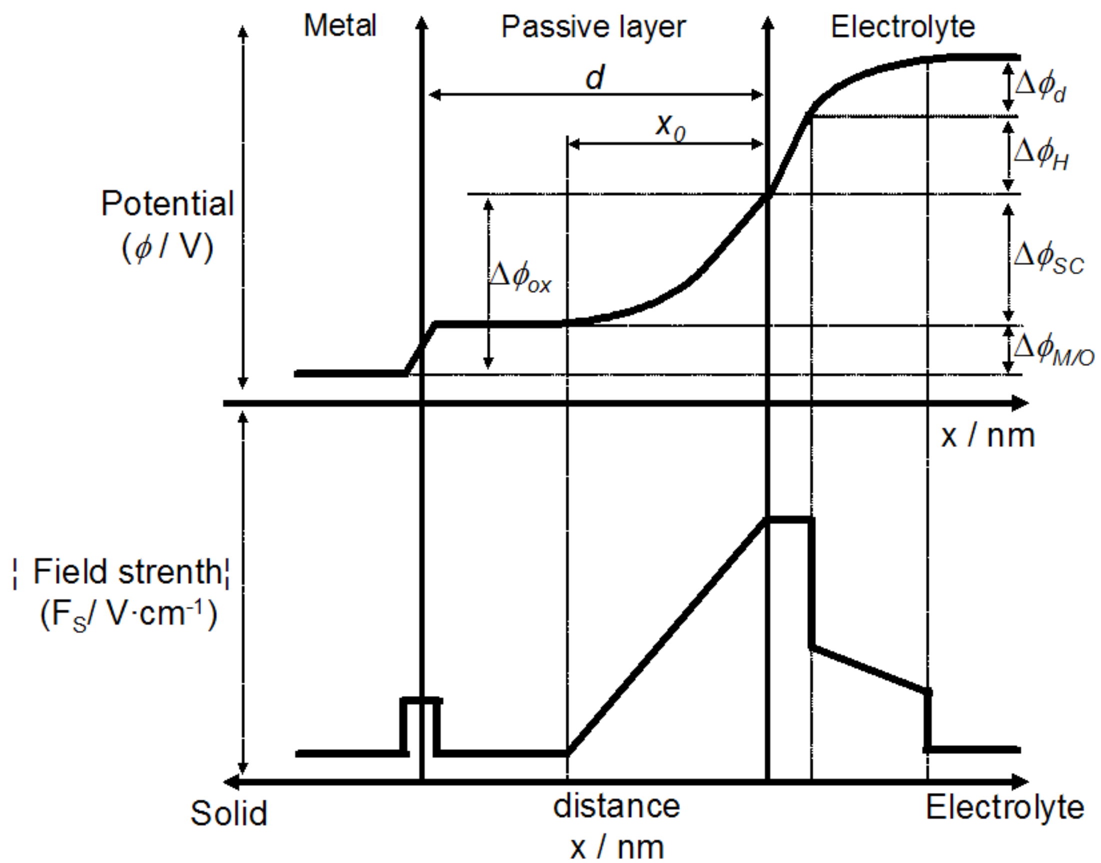

Figure 1.25: Potential (upper curve) and local field strength F_S (lower curve) at the metal│passive layer│electrolyte interface. *d* denotes the passive film thickness and $x_0=x_{SCL}$. Finally, $\Delta\phi_{ox}$ is the total potential drop within the oxide layer. After ref. [79].

where the last term of this equation refers to the charge carriers transport (e^- and h^+) through the oxide film and the two first terms have to do with the ionic movement. In previous section 1.2.3, a complete model of the general electronic structure of this interface was provided and can be employed, to understand the charge transport across the oxide film. Moreover, in this section, a short excursion through the principal models of ion transport across passive layers is provided. They refers directly to the term j_{ITR} in equation (1.69) which involves processes like the growth of the passive layer itself or the migration of defects within the oxide layer. The distribution of the potential across the interface will be of course determining as the driving force for ionic migration. Figure 1.25 sketches a first approximation of the potential drop and field strength, F_S (defined as dϕ/dx) at the metal│oxide layer│electrolyte interface. An additional potential drop ($\Delta\phi_{M/O}$), comparing to the simpler semiconductor│electrolyte interface (see distribution profile in Fig. 1.7), arises as a result of the metal│oxide contact. From an energetic point of view, it will suppose an extra potential barrier (see Field strength curve in Fig. 1.25) contributing to both ionic and majority carriers transport. Especially in the electronic transport case, the energy barrier at this interface may hinder the ET through the whole interface. Equally, point defects traveling toward the metal│oxide interface may feel the generated potential field at this contact. Fortunately, as the distribution of defects is not completely homogeneous within the oxide layer (see previous section), it is found in many passive films systems that a higher doping density is concentrated near the metal│oxide side thus acting as a natural ohmic contact for the passive layer (see experimental measurement in

section 1.3). The energy barrier at this interface is then minimized and so current transport is generally dominated by the energy barriers created at the oxide│electrolyte side.

Finally, the capacitive current component j_{cap} have to do with the charging-discharging process of the electrolyte double layers that were sketched in the figure 1.3. This is then produced by the movement of ions within the electrolyte coming to or from the electrode surface to shield the charge that is being generated there. Since ionic diffusion coefficients in the electrolyte are much higher than those within the oxide layer, these capacitive processes take place in a much lower time scale and can be easily separated in electrochemical experiments. However, in chapter 2 we will see how this current component becomes an enormous practical problem when measuring very low current flows through the interface.

1.2.4.2 Models for the passive film growth: ionic transport

The oxide growth during the formation of the metal passive layer, either at OCP or under an applied $U_{electrode}$, is the major evidence of the ion transport through the oxide film itself. At least one of the ionic species (M^{n+} or O^{2-}) has to diffuse or migrate through the oxide and accordingly the layer can grow usually either at the inner metal│oxide or at the outer oxide│electrolyte interface. Experimentally, it is found that the film growth kinetics may follow one of the following laws:

$$d = A + B \cdot \ln t \qquad \text{(logarithmic)} \qquad (1.70a)$$

$$\frac{1}{d} = C + D \cdot \ln t \qquad \text{(inverse logarithmic)} \qquad (1.70b)$$

being A, B, C and D constants.

Over the second half of the past century, several models have been proposed to explain the kinetic experimental equations (1.70). The evolution of these models has allowed to acquire an actual quantitative view of the oxide growth process in a fairly wide range of electrolytic media. Let us now give a quick review of the existing models by exposing their main assumptions and the main growth rate laws that are deduced for the passive film.

Mott-Cabrera model

The first quantitative description dates back to the work of Cabrera and Mott [71] in 1948. This model contains the following assumptions:

- Metal cations M^{n+} diffusion toward the oxide│electrolyte interface accounts for the film growth.

- Metal cations M^{n+} diffusion is assisted by the electric field strength existing within the oxide layer, which is assumed to be high and have a constant value equal to the quotient $\Delta\phi_{ox}/d$ (see Fig. 1.25).

- The value $\Delta\phi_{ox}$ is constant all along the oxide growth process, so it is independent of *d*.

- The rate limiting step is the transfer of a M^{n+} across the metal | oxide interface.

These assumptions lead to a rate law for the film growth of the form:

$$\left(\frac{dd}{dt}\right) = M\Omega\upsilon \cdot e^{\frac{\left(-E_a + \frac{na\Delta\phi_{ox}}{2d}\right)}{kT}} \quad (1.71)$$

where M, Ω and υ are the number of mobile ions per surface area unit, the molecular volume per cation M^{n+} and the vibration frequency, respectively. E_a and a are the activation energy for the rate controlling step (last model premise above) and the jump distance for the cation movement through the oxide, respectively. The integration of expression (1.71) gives rise to an inverse logarithmic rate law like the one represented in (1.70b).

Sato and Cohen's model

This model was developed in the sixties by Sato and Cohen [80] who performed an intensive study of the Fe passive film in borate buffers. They found an empirical exponential relationship among the measured j_{total}, the applied potential $U_{electrode}$ and the accumulated charge in the oxide layer Q_{ox}:

$$j_{Total} = k' e^{\left(m \cdot U_{electrode} - \frac{Q_{ox}}{n}\right)} \quad (1.72)$$

being *k'*, *m* and *n* empirical parameters. The authors then used a particular mechanism so-called "place exchange", which basically proposes that the passive layer grows by successively including mono-atomic layers of O^{2-} atoms into the metal phase as represented in figure. The process starts by a first adsorption of oxygen anions on the metal surface followed by an exchange of the atomic positions between the M^{n+} and O^{2-} atoms (from (i) to (iii) in Fig. 1.26). Previous steps are repeated resulting in the oxide film thicken (steps (iv) to (v)).

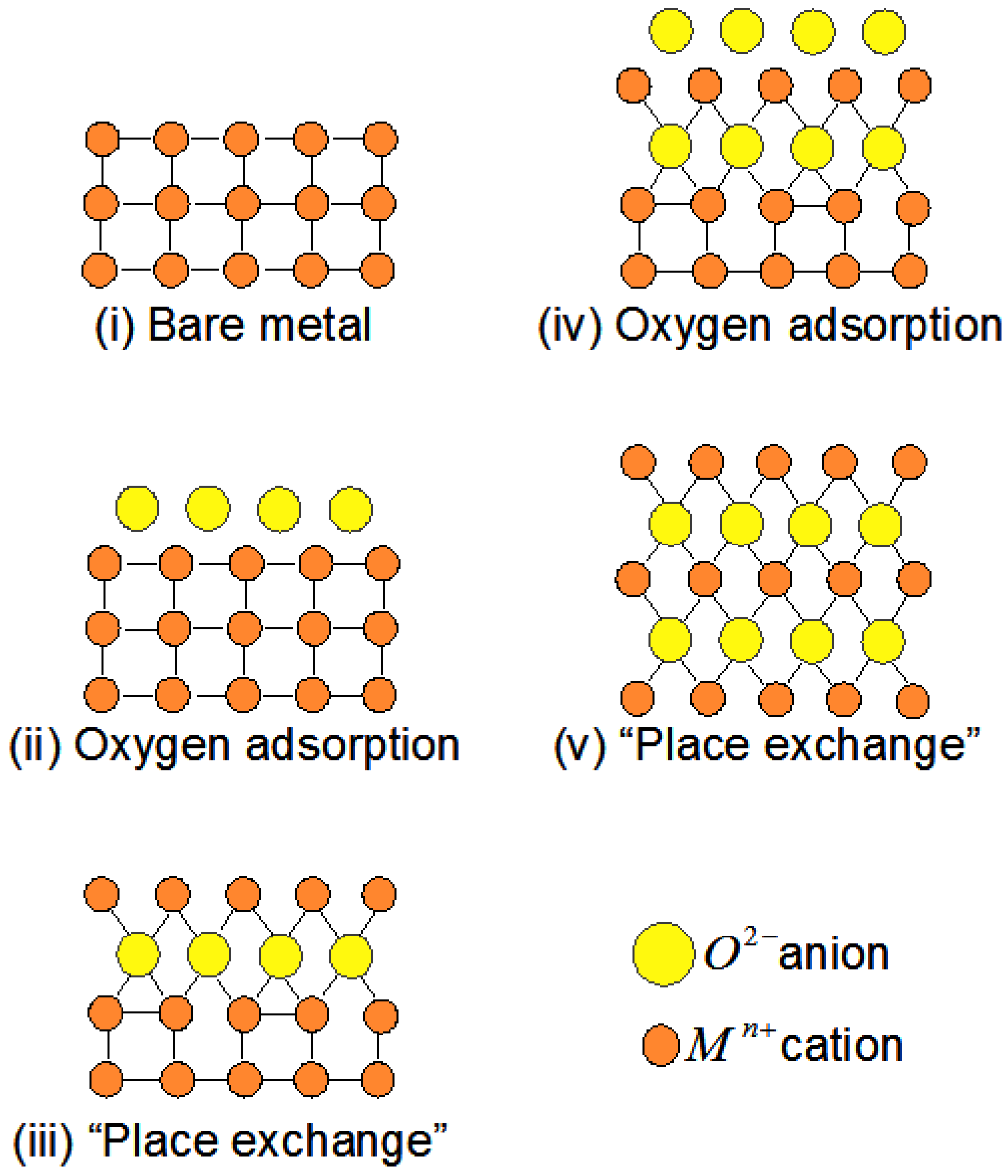

Figure 1.26: "*Place exchange*" mechanism for the oxide film growth: (i) Starting bare metal, (ii) first oxygen absorption layer, (iii) positions exchange between M^{n+} and O^{2-}, (iv) second oxygen adsorption and (v) "*place exchange*" between two *M-O* pairs.

Sato and Cohen used this model to obtain analytical expressions for the empirical parameters of equation (1.72):

$$k' = \frac{2FkT}{h}\sqrt{(N_{Site})^{\frac{n}{\upsilon}}(N_M^{ox})^{\frac{2}{\upsilon}}} \cdot e^{\left(\frac{nB_0F}{2\upsilon RT} - \frac{E_0 - E_1 + 0.5nE_{ox}}{\upsilon RT}\right)} \tag{1.73a}$$

$$m = \frac{nF}{2\upsilon RT} \tag{1.73b}$$

$$\frac{1}{n} = \frac{L^2 E_1}{4nRT} \tag{1.73c}$$

where E_0, E_1 and E_{ox} are the activation energies for the formation of the first oxide monolayer (step (ii)), subsequent monolayers (step (iv)) and incorporation of the absorbed oxygen atoms into the growing oxide film (steps (iii) and (v)) respectively. υ is defined as the number of times that a rate-controlling step takes place when the overall reaction occurs once. N_{Site} and N_M^{ox} are the total number of adsorption sites and the number of metal cations per unit area of oxide. B_0 is a constant and the rest parameters have their usual meaning.

After introducing equations (1.73) into (1.72), authors noticed out that under potentiostatic conditions, the final expression can be integrated to result in a logarithmic law of the form of Eq. (1.70a), where the activation energy (E_a) of the process appears to be a linear function of d (see ref. [81] for more details in the mathematic development).

Fehlner and Mott's model

In the early sixties, it was already quite established that a logarithmic mechanism for the oxide film growth could be assumed by any mechanism whose activation energy increased linearly with the film thickness as stated in the original and Cohen's model (see above). However, the "*place exchange*" mechanism did not provide a realistic description of the oxide growth for thick passive layers of more than few monolayers. Thus, in 1970, Fehlner and Mott [72] modified the earlier Mott-Cabrera model [71] to provide an alternative to the previous "*place exchange*" mechanism. The model assumes the following guidelines:

- Oxygen anion O^{2-} diffusion is responsible for the film growth.
- The rate limiting step is the transfer of an O^{2-} across the oxide│electrolyte interface into the growing passive layer.
- The field strength has again a constant value $\Delta\phi_{ox}/d$ and it is independent of film thickness d.
- As previously mentioned, the activation energy (E_a) of the rate limiting step increases linearly with *d whatever the mechanism of oxide growth is*.

In this model, the exact mechanism of the oxide film growth is not provided, and the model leans on the last premise which states:

$$E_a = E_a^0 + cte \cdot d \tag{1.74}$$

being E_a^0 constant.

Based on these new assumptions, previous equation (1.71) yields:

$$\left(\frac{dd}{dt}\right) = M\Omega\upsilon \cdot e^{\frac{\left(-E_a^0 - cte\cdot d - aF\right)}{kT}} \tag{1.75}$$

which gives rise to a logarithmic relationship after integration [72].

Point Defect Model (PDM)

This is the most recent model to describe the kinetics of the passive film growth on a metal surface. It was developed by Macdonald and *coworkers* in the early eighties [73,74,82] and probably provides the most quantitative and widest picture of the process which can be extended to any passive film (oxide or non-oxide) that grows on a metal electrode. The main assumptions of this model are:

- Whenever $U_{electrode}$ is over the Flade potential (U_{FP}), a continuous passive film, with general composition $MO_{n/2}$, exists on the metal surface, n denoting the oxide stoichiometry.

- The passive film contents a high concentration of point defects (see section 1.2.3.2). It is know that the major point defects existing within an oxide layer are cation and anion vacancies (V_O^{2+} and V_M^{n-} in Fig. 1.23), and also e^- and h^+ can be also found here as individual structural defects [77]. Same point defects types are considered to be within any passive layer.

- The passive film behaves as an "*incipient semiconductor*" and so the high field strength (F_S) across the oxide layer depends on the chemical and electrical properties (the *SCL* potential distribution). Therefore, it is independent of d even at potentiostatic conditions.

- Due to its semiconductor behavior, e^- and h^+ within the film matrix are assumed to be in their equilibrium states so that the electrochemical reactions involving these charge carriers are rate-controlling at both metal│oxide and oxide│electrolyte interfaces. When the electrochemical process involves the presence of V_O^{2+} and V_M^{n-} vacancies, the rate limiting step will be the diffusion of the vacancy through the oxide layer. This last assumption implies that they will be in their equilibrium states at both interfaces.

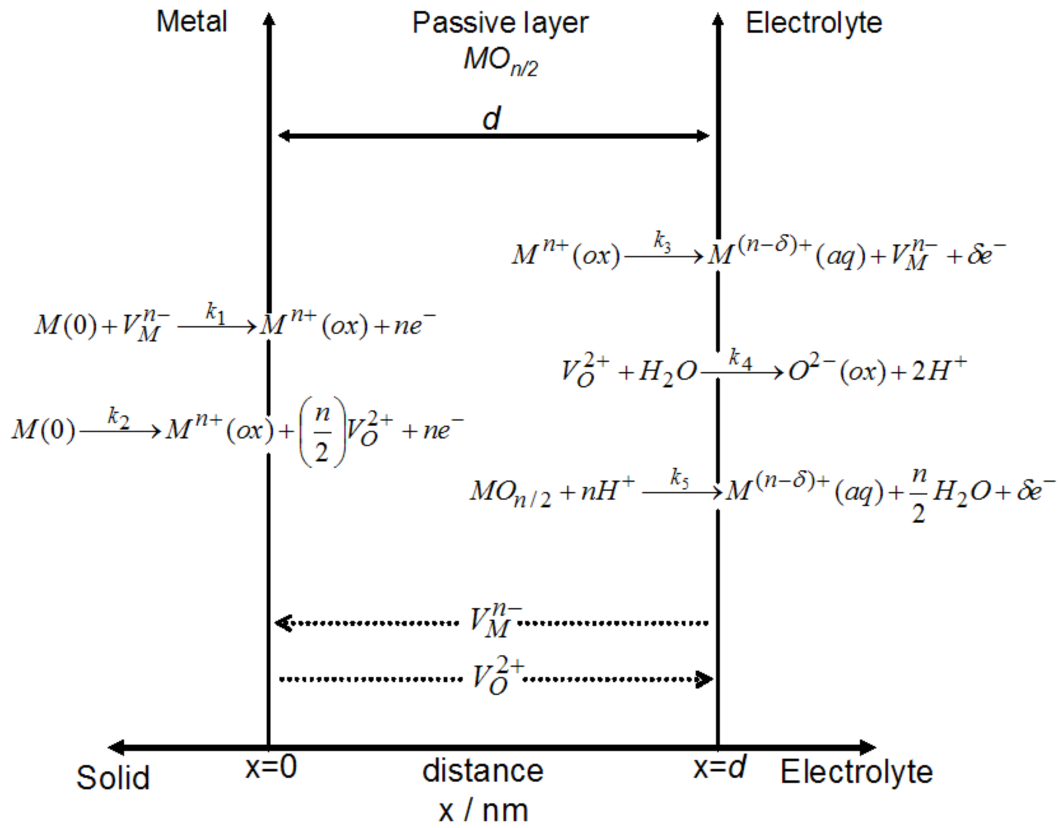

Figure 1.27: Scheme of the physicochemical processes occurring within the passive layer according to the PDM. Suffixes (aq) and (ox) indicate that the corresponding ion is in the *aqueous phase* or in the *oxide lattice* respectively. *M(0)* denotes the cation in the metallic state. Reaction 5 represents the electrochemical dissolution path of the passive film in acidic media. After ref. [82].

Figure 1.27 summarizes all the processes that involve generation and annihilation of point defects at both metal|oxide and oxide|electrolyte interfaces during passive film growth. Looking at this scheme in more detail, it is clear that the passive layer is formed as a result of the cation vacancies diffusion toward the metal|oxide interface (see reaction 4), whereas the diffusion of anion vacancies results in metal dissolution only (see reactions 3 and 5). Therefore, the calculation of oxide growth kinetics will reduce to the calculation of V_O^{2+} diffusion rate, *i.e.* transport of O^{2-} through the oxide layer. Hence, the film growth rate can be expressed as:

$$\left(\frac{dd}{dt}\right) = \frac{\Omega}{N_a} J_{V_O^{2+}} \tag{1.76}$$

where Ω is the molecular volume of the oxide and N_a is the Avogadro's constant. $J_{V_O^{2+}}$ represents the anion vacancies flux per unit area and time. The diffusion rate of a charged particle in the presence of both concentration and potential gradients can be calculated by using the generalized Fick's first law.

The V_O^{2+} flux then takes the form:

$$J_{V_O^{2+}} = 2KD_{V_O^{2+}} \left(\frac{c_{V_O^{2+}}(m\,|\,o) \cdot e^{2Kd} - c_{V_O^{2+}}(o\,|\,e)}{e^{2Kd} - 1} \right) \tag{1.77}$$

The constant K is equal to $F_S F/RT$ and terms $c_{V_O^{2+}}(m\,|\,o)$ and $c_{V_O^{2+}}(o\,|\,e)$ represent oxygen vacancies concentrations at metal│oxide and oxide│electrolyte interfaces, respectively. They constitute the anion vacancies gradients and essentially depends, in turn, on the corresponding potential drops across both interfaces ($\Delta\phi_{M/O}$ and $\Delta\phi_{O/E}$) through expressions:

$$c_{V_O^{2+}}(m\,|\,o) = \frac{N_A}{\Omega} e^{\left(\frac{2F\Delta\phi_{M/O} - (2/n)\Delta G_2}{RT} \right)} \tag{1.78a}$$

$$c_{V_O^{2+}}(o\,|\,e) = \frac{N_A}{\Omega} e^{\left(\left(\frac{\Delta G_4 - 2F\Delta\phi_{O/E}}{RT} \right) - 4.606\,pH \right)} \tag{1.78b}$$

which are deduced from the assumed equilibrium condition established for reactions 2 and 4 in figure 1.27 (check the above model assumptions). ΔG_2 and ΔG_4 are the standard Gibbs energies for reactions 2 and 4 respectively. At this point, an additional assumption must be introduced: the potential drop at the oxide│electrolyte interface $\Delta\phi_{O/E}$ is a function of the applied potential $U_{electrode}$ and solution pH (see reaction 4 in Fig. 1.27) through the expression:

$$\Delta\phi_{O/E} = aU_{electrode} + bpH + \Delta\phi_{O/E}^{0} \tag{1.79}$$

Moreover, the total potential drop across the metal│passive layer│electrolyte interface is related to the external applied potential as:

$$U_{electrode} + \Delta\phi_{ref} = \Delta\phi_{M/O} + \Delta\phi_{ox} + \Delta\phi_{O/E} \tag{1.80}$$

where $\Delta\phi_{ref}$ corresponds to the potential drop across the reference electrode│electrolyte interface. According to expressions (1.79) and (1.80), $\Delta\phi_{M/O}$ can be equated as:

$$\Delta\phi_{M/O} = (1-a)U_{electrode} + bpH - \Delta\phi_{O/E}^{0} + \Delta\phi_{ref} - \Delta\phi_{ox} \tag{1.81}$$

Introducing equations (1.78), (1.79) and (1.81) into (1.77), the rate law for the oxide film growth yields:

$$\frac{dd}{dt} = \frac{A(B-1)}{e^{2Kd-1}} \tag{1.82}$$

where:

$$A = 2KD_{V_O^{2+}}\, e^{\left(\frac{-2F}{RT}\left(aU_{electrode}+bpH+\Delta\phi^0_{O/E}\right)+\frac{\Delta G_4}{RT}-4.606\,pH\right)}$$

$$B = e^{\left(\frac{2F}{RT}\left(U_{electrode}+\Delta\phi_{ref}\right)-\frac{2\Delta G_2}{nRT}-\frac{\Delta G_4}{RT}-4.606\,pH\right)}$$

At potentiostatic conditions, equation (1.82) can be integrated and simplified into two different cases:

$$d = \frac{1}{2K}\left(\ln(2KA(B-1)) + \ln t\right) \qquad \text{for } d \geq 5\text{Å} \tag{1.83}$$

$$d = \left(\frac{A(B-1)}{K}t\right)^{1/2} \qquad \text{for d} \ll 5\text{Å} \tag{1.84}$$

Equations (1.83) and (1.84) have been successfully employed to quantify the passive film growth on an Fe electrode. The validation of this model as well as a rigorous mathematical development of the deduced oxide growth laws can be found in [73].

1.2.4.3 Electronic transport in passive films

From an experimental viewpoint, once the steady state is reached and the oxide film has completely grown at fairly high applied $U_{electrode}$, the conduction across the metal│oxide│electrolyte interface measured by means of the total current flow j_{total}, is mostly mediated by electronic transport. Indeed, this is one of the most important issues to understand the electrochemical behavior of such interfaces. However, and as an opposite face to the number of quantitative models existing on the ionic transport (previous section), there is a serious lack of information concerning quantitative models of the pure electronic conduction through passive layers and, hence, the reason why this matter constitutes the central subject of this Ph.D. work (see also the preface). Probably one of the major challenges that imposes experimental difficulties on the study of the ET through these interfaces is the use of proper experimental tools that allow a clear separation of the electronic current component from other components generated by ionic movement, oxide growth or surface electrochemical reactions. In this work, new methodologies have been designed for this purpose and will be extensively described in chapter 2.

In this section, the general mechanisms of the electronic conduction through passive layers are listed and briefly commented. A more detailed analysis on this emerging matter will be given in section 1.3 where the last advances on the measured electronic properties of passive films will be extensively treated.

As a mere guidance, it is possible to distinguish three different general mechanisms of electronic conduction, essentially depending on the film thickness (*d*) and on the intrinsic electronic properties of the oxides. Next, they are shortly reviewed.

Tunneling regime through thin passive films

When the thickness of the passive layer is within the range of 5 to 25 Å, *i.e.* several monoatomic planes of oxide, the electronic conduction is dominated by *direct electron tunneling* from the electrolyte to the metal phase underneath [30]. Therefore, the term *thin film regime* refers to the situation in which carrier transfer by direct tunneling is the dominant mechanism. This process can be better described by the *Fowler-Nordhiem tunneling* formalism which gives an analytical expression of the tunneling probability Θ of an electron being transferred through a triangular barrier in the presence of a high electric field F_S (see scheme in Fig. 1.28):

$$\Theta = e^{\left(\frac{-3}{4}\frac{\sqrt{2e \cdot m^*}}{\hbar}\frac{\phi_B^{3/2}}{F_S}\right)} \tag{1.85}$$

where $\hbar$ and m^* are the reduced Planck constant and the effective electron mass respectively. ϕ_B represents the energy barrier seen by the tunneled electron and constitutes the dominant parameter on the tunneling ET. The tunneling current (i_{tunnel}) can be then obtained from the product between the total carrier flux arriving at the tunnel barrier (ϕ_B) and the tunneling probability Θ:

$$i_{tunnel} = e v_R n \cdot \Theta \tag{1.86}$$

where v_R is the Richardson velocity, the velocity with which, on average, the charge carriers approach the barrier. n is again the density of available charge carriers.

Direct tunneling through passive films can be aided by the presence of energy levels in the bandgap of the oxide [83]. When the electron tunneling process across an energy barrier is done in the presence of available energy levels halfway in the barrier, they can act as a sort of stepping stone for e^- hopping, as it is represented in figure 1.28. This particular ET is called *resonance tunneling* and allows the tunneling mechanism to occur on thicker oxides films (~30Å), similarly to what has been reported for the long ET observed among redox centers in complex biomolecular systems [84].

In summary, whenever a pure tunneling process is the dominant electron conduction mechanism, *i.e.* electrons are always transferred from the metal E_F to the redox species in solution or *vice versa*, the overall metal│oxide│electrolyte interface will behave as a metal with the corresponding exchange current term j_0, which is now controlled by the tunneling probability Θ. This Θ parameter will be in turn a function of the oxide thickness d through equation (1.85); an increase of d means an increase of the barrier height ϕ_B from an energetic viewpoint.

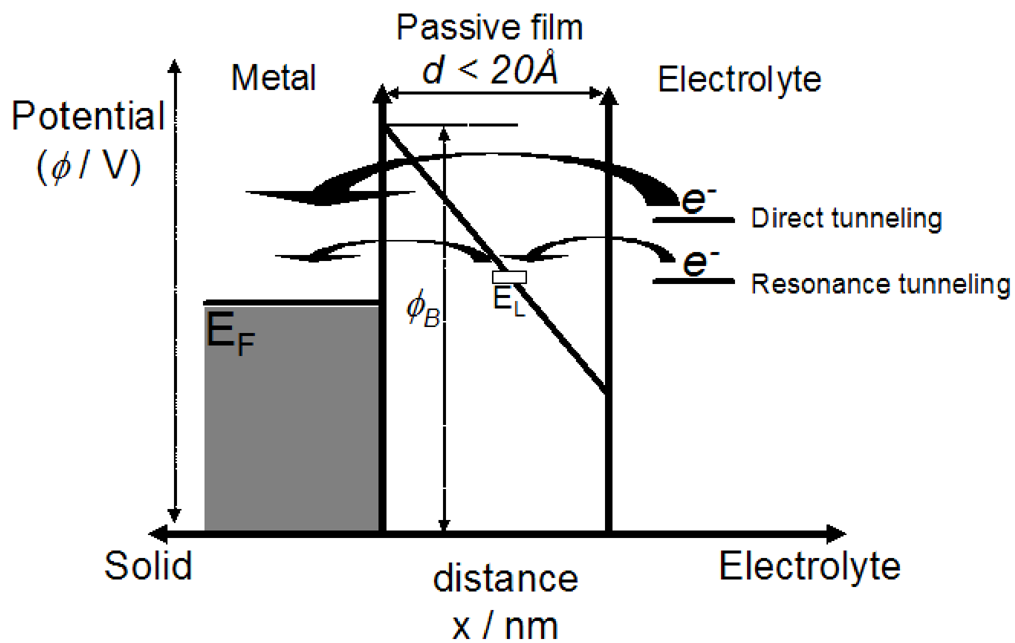

Figure 1.28: Potential distribution at metal│passive film│electrolyte interface with a thin passive film presenting a triangular energy barrier. Electron tunneling mechanisms for ET from the electrolyte (simplified representation) to the metal electrode are represented. E_L represents an empty localized state within the barrier.

Tunneling ET is commonly found on passive films formed on noble metal systems, *e.g.* Pt, Pd or Au, whose typical thicknesses do not exceed values of around a ten of amstrongs.

Electronic conduction through thick semiconducting passive films

In order to get a net electronic conduction through a *thick semiconducting passive layer*, two different conditions are required: (i) the charge carriers must be sufficiently energetic to reach the band, and (ii) they must be able to move through the oxide film without being trapped. We consider a *thick* semiconducting oxide layer when its thickness overcomes the thickness of the semiconductor *SCL* so that its semiconducting properties are completely developed (see Fig. 1.3). Since doping densities in semiconducting passive films are typically high (in the order of 10^{20} cm^{-3}, see table I), the *SCL* thickness decreases down to around 30Å depending on the applied $U_{electrode}$. Therefore, we can consider as a good approximation d > 40Å for a thick semiconducting passive films. It is also important to highlight here that when working with thick amorphous or nanocrystalline oxide layers, we may find surface regions with enhanced or blocked conduction due to different factors: the presence of conductive *grain boundaries*

(see section 1.1.2.4), the presence of regions with different stoichiometry of higher conducting or insulating nature, or film regions presenting lower thickness values that may give rise to a different mechanism of electronic conduction (*e.g.* tunneling ET). Concluding, the experimental approach to study electronic conduction through thick passive layers must take into account all these previous assumptions. Fortunately, the growth of passive films by electrochemical methods commonly presents wide electrochemical $U_{electrode}$ windows (passive region) in which thick coherent structures that efficiently block the surface redox activity of the electrode are reached. Therefore, within this electrochemical regime, the electrode redox behavior will be dominated by the electronic conduction through the thick oxide film.

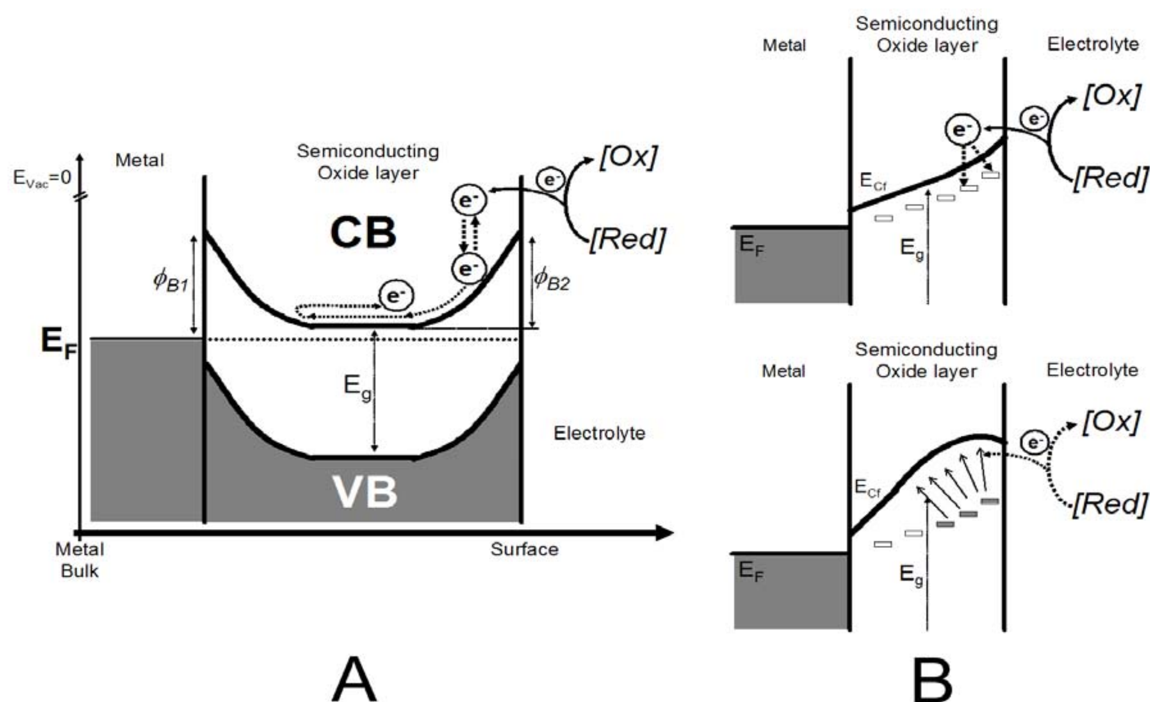

Figure 1.29: Electron transport blockage at the metal│passive film│electrolyte interface: (A) back-to-back diodes and (B) space-charge-limited current; before (upper scheme) and after (lower scheme) charge carriers trapping. Note that the barrier ϕ_{B2} is equal to $\Delta\phi_{SC}$ (see Fig. 1.11). The redox species are represented in its simplified form.

There are several examples showing that thick passive films, whose equivalent bulk oxides are semiconductors, present same semiconducting behavior when in the form of layers (*e.g.* passive films on Ni, Cu or Fe). Interestingly here is the example of the Fe passive layer that shows the same photocurrent spectra in solution when it is present either as a film or in the bulk form [85], thus corroborating their same semiconducting behavior. The study of these systems is then simplified to the analysis of the ET on an ideal semiconductor electrode. Section 1.1.3 gives a detailed overview of the charge transfer formalism across a semiconductor│electrolyte interface and, therefore, now we will introduce only a couple of new elements arising at the specific metal│semiconducting film│electrolyte interface. They refer to: (i) the so-called *back-to-back diode* and (ii) the *space-charge-limited current* effect. Let us consider the first case (i). This element was already introduced at the beginning of section 1.2.4.1; although the semiconducting properties of the passive layer are well evidenced by means of, for example, capacitance or photo-electrochemical measurements (see section 1.3), the metal│oxide interface may not provide an ideal back "*ohmic contact*"

resulting in the formation of an additional energy barrier at that interface (see Fig. 1.25 and discussion herein). Using the microelectronics terminology, if the energy barrier at the metal│oxide side is comparable to the barrier created at the oxide│electrolyte side when it is under depletion conditions (see section 1.1.2.4), two reverse-biased *Schottky diodes* as the one represented in figure 1.29A will be created. This particular energetic configuration prevents the e^- flow in either Bias directions due to the energy barriers ϕ_{B1} and ϕ_{B2} seen by an electron going from the metal and from the electrolyte to the semiconducting oxide respectively. This particular situation can outline problems in the data interpretation when studying redox behavior, because, for example, the ET from the electrolyte to the CB of the oxide film can be hidden by the impossibility to overcome the next barrier ϕ_{B1}. In any case, and as previously mentioned, the metal substrate under the passive layer usually provides a *natural* ohmic contact thanks to the defective nature of the metal│oxide junction itself, which provides additional energy states (see E_{IS} in Fig. 1.22) that aid the ET from oxide layer to the back metal and *vice versa*.

As for the (ii) case, there is a second reason that may account for the electron current blockage in a semiconducting passive layer. As pointed at the beginning of this section, even when sufficient energy is conferred to the charge carrier to be promoted to the corresponding band (at E_{Cf} and E_{Vf} levels), trapping of this carriers in the oxide lattice may also prevent from carriers motion and hence, from electronic conduction. When the density of trapped carriers, either below CB or above VB, is very high, the charge excess generated either by e^- or h^+ can build up an additional space charge layer (see Fig. 1.29B) as a result of the generated electric field near the surface. The presence of this additional SCL prevents, for example, the injection of more electrons thus blocking the current flow across the interface. In general, semiconducting oxide films containing a rather high density of such traps may present an insulator behavior due to the space-charge-limited current effect.

Electronic conduction through thick insulating passive films

One expects no electronic conductance through a thick insulating oxide layer, simply because charge carriers have insufficient energy to be promoted to either the CB or VB. These metal systems are commonly called *valve metals* and they usually form a coherent resistive film on the surface. To name a few: Al, Ti, Zr, Ta, Hf, Mo or V among the most important.

Since these systems are not the central part of this PhD. work, we will only mention a couple of cases in which electronic conduction may occur through an insulating passive layer. One refers to dielectric breakdown and it will be revised in the next section 1.2.4.4. The other relates to the high current that can flow at highly applied cathodic $U_{electrode}$ and which is mainly associated to cation ion diffusion through the layer more than to electronic reasons.

1.2.4.4 The role of the passive film in metal corrosion

Corrosion Science and, particularly, metal corrosion has developed a very extensive, interdisciplinary field (see preface), and obviously, it can not be treated here in depth. However, since chapter 5 of this thesis has been dedicated to the study of the abrupt transition

on the electronic properties of the Fe passive layer in an aggressive environment where it undergoes corrosion, we pretend to give here a plain revision of the main concepts that relate to metal corrosion in an aggressive ambient, paying special attention on the electronic aspects that finally produce the passive film disruption and lead to an unprotected metal surface.

Classical view

In general, the term *Corrosion* stands for material/metal deterioration or surface damage in an aggressive environment. In the metal case, it is essentially a chemical or electrochemical process that implies the oxidation of a metal which transfer electrons to the electrolytic environment and undergoes a valence change from zero to a positive value *n*. Commonly, this initial oxidation stage is coupled to a number of parallel electrochemical processes that result in material dissolution and/or eventual formation of secondary corrosion products. All this stuff makes *Metal Corrosion* a very complex process which can be approached from a huge variety of perspectives. From a very simplistic view, metal corrosion processes can be classified in two different blocks: the so-called *General Corrosion* that gathers those corrosion processes involving the entire surface area of the material, and *Localized Corrosion* which refers to a number of corrosion processes that are triggered at specifics sites on the material surface. Table II classifies the different forms of the most outstanding corrosion mechanisms and gives a short description of each one. For a more extended knowledge of all these processes, the reader is addressed to some comprehensive reviews of this field [86,87]. In any case, whichever the corrosion process is, the practical final result is the failure of the material operation.

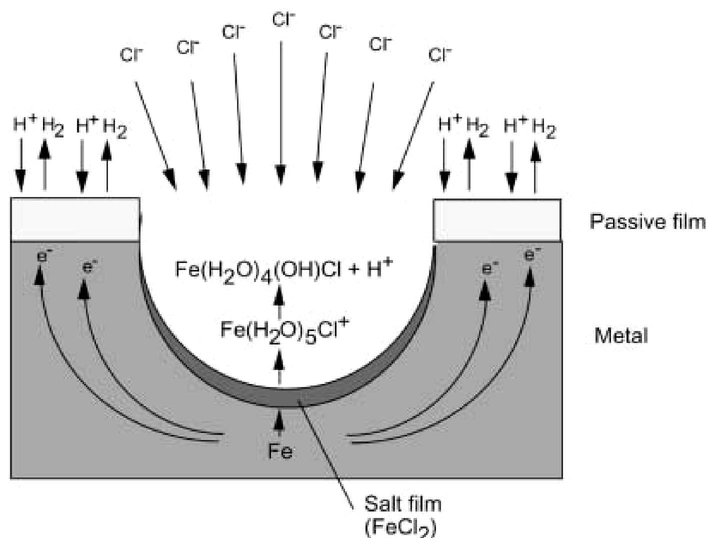

Figure 1.30: Schematic cross section of an active *pit* on an Fe electrode surface in the presence of chloride anions. Metal oxidation $Fe(0) \rightarrow Fe^{2+}(aq)+2e^-$ occurs at the pit while cathodic reduction $2H^+(aq)+2e^- \rightarrow H_2(g)$ takes place in the surrounding area. From ref. [78].

As stated in the introduction of this section, the presence of a surface passive film prevents the metallic substrate from further oxidation; the surface becomes *passivated*. However, the passive state of a metal can, under certain conditions, be susceptible to localized instabilities that prompt the corrosion of the metal electrode through the local dissolution of the passive

layer. This process is known as *pitting corrosion* (see Table II) and constitutes one of the most common mechanisms of corrosion of passivated metals [88-90]. Hereafter, we will focus our attention in the main aspects of this particular form of corrosion.

Pitting corrosion is a complex process taking place at passivated metal surfaces whose principal stage is the formation and growth of an active *pit*, like the one represented in Fig. 1.30, through which the effective dissolution of the metal occurs. Of course the details of the mechanisms depend on the metal itself, composition of the alloy and environmental conditions. For example, it is quite straightforward that these pits may easily generate at defective sites on the passive film surface, on sharp edges or sites where the oxide film is thinner. The essence of the pitting process relays in its anodic nature (metal dissolution) versus a passivated cathodic zone surrounding it (see Fig. 1.30), thus allowing the continuous flow of electrons to take place. Despite the complexity of the whole process, several consecutive stages have been distinguished [89]:

1. Breakdown of passivity.
2. Early stages of pit formation.
3. Pit growth.
4. Repassivation phenomena.

Table II. Forms of *General* and *Localized* corrosion processes [87].

GENERAL CORROSION		LOCALIZED CORROSION	
Corrosion type	**Description**	**Corrosion type**	**Description**
Atmospheric	Entire oxidation of the metal surface in a corrosive medium	Crevice	Oxidation at specific cavities or holes on the surface
Galvanic	Among dissimilar metal/alloys or phases in contact	Filiform	Crevice corrosion under protective films
High-Temperature	Formation of porous oxide structures	Pitting	Oxidation through formation of destructive pits
Biological	General oxidation catalyzed in the presence of bio-organisms	Biological	Damage produced by non-uniformly adsorption of micro-organisms
Stray-Current	Oxidation produced by external DC* sources	Selective leaching	Selective removal of a constituent metal in an alloy matrix

* DC denotes direct current.

It is well known that the presence of aggressive complexing agents like $Cl^-(aq)$ in the electrolytic medium is necessary to produce passivity breakdown and stable pit growth. Examples like Fe, Ni, Cu, or Al, or complex alloys like stainless steels, experience an abrupt transition from their passive state to the pitting corrosion when small amounts of Cl^- (in the order of μM) are added into the electrolyte. From a macro-scale view, it produces a sudden increase in the electronic conductivity of the electrode, which is detected by a sharp increase in the measured current flowing across the interface (see chapter 5 for the Fe case). Then, it turns out that the key point to better understand how the pitting process initializes relays on the quantification of the interaction process between the passive layer and the aggressive environment, *e.g.* the Cl^- anions, that may give rise to a particular energy levels distribution at the oxide | electrolyte interface.

As discussed by most authors, three main initiation mechanisms of passivity breakdown seem possible: the *penetration mechanism*, the *film breaking mechanism* and the *adsorption mechanism*. All three mechanisms are illustrated in figure 1.31. In the penetration mechanism [91], the main step involves the incorporation of Cl^- (or other pit promoting ion) through the oxide film until the metal | oxide interface where they start their specific action (Fig. 1.31A). The high F_S and the high defect concentration within the passive layer (see section 1.2.4.2) may presumably aid the Cl^- transport across the film. On the other hand, the film *breaking mechanisms* [92,93] requires a local film rupture, probably promoted by the existing stress among the oxide layer and the metal substrate, which gives direct access of the anions to the unprotected metal surface (Fig. 1.31B). And finally, the *adsorption mechanism* [94,95], which involves a first adsorption of the aggressive anions (*e.g.* Cl^-) on the oxide surface that catalytically enhances the removal of metal cations M^{n+} from the oxide layer to the electrolyte. This effect leads to a local thinning of the passive layer, which may trigger the formation of an active pit (Fig. 1.31C).

After passivity breakdown is produced, the next stages involving pit nucleation and growth will then proceed. The kinetics of these processes as well as their structural implications at the micro-scale have been also treated as the final stage of the pitting corrosion mechanism. In this Ph.D. work, we are especially interested on the first stages of passivity breakdown, however, a detailed analysis of sub-sequent pitting formation and growth can be found in several interesting reviews [87-89].

Semiconductor view

Previous classical models provide a general chemical and electrochemical picture of the passivity breakdown process. Nevertheless, it was stated at the beginning of this section that most metal passive layers present a semiconducting or insulating electronic behavior and, therefore, if one expects to obtain a quantitative picture of the initiation of the pitting corrosion process, it will be required to embed this semiconductor model into the actual classical corrosion mechanisms.

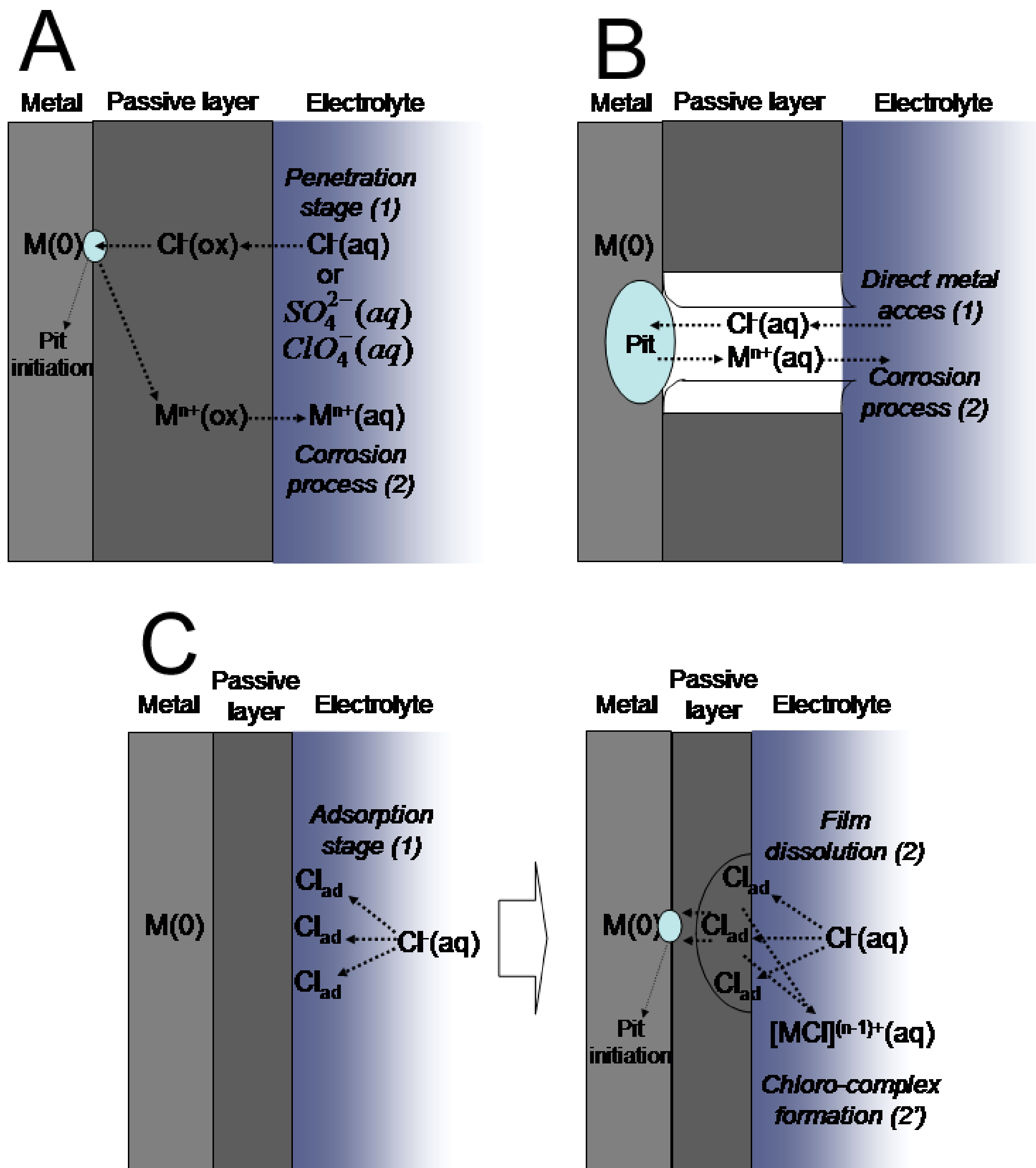

Figure 1.31: Schematic representation of the three mechanisms for the initiation of passivity breakdown (see text discussion): (A) penetration mechanism, (B) film breaking mechanism and (C) adsorption mechanism.

A well-described mechanism able to destroy the energy barrier created at the *SCL* of a semiconductor surface (see $\Delta\phi_{SC}$ term in section 1.1.2.4), is commonly referred as a *dielectric breakdown of the SCL*. It consists on the spontaneous generation of extra charge carriers in an electrically insulated region either by tunneling (*Zener breakdown*) or by collision (*avalanche breakdown*). Both mechanisms occur when a sufficiently high F_S is applied to the oxide layer thus producing high currents flowing across the interface. The former case refers to an excessive tunneling ET (see *Tunneling regime through thin passive films* in section 1.2.4.3) across the electrical *SCL*. Under a high F_S (either $U_{electrode}$ >>0 or $U_{electrode}$ <<0), the strong imposed depletion conditions may eventually equalize $E_{S,VB}$ and E_{CB} levels such that valence electrons can tunnel across the *SCL* into the CB, if the *SCL* thickness is in the tunneling range (<20Å, see Fig. 1.32). Note that the process generates *electron-hole pairs* (see Fig. 1.32) thus

allowing majority carriers (e^- in the *n*-type case) to move toward the solid bulk, while minority carriers accumulates at the electrode surface.

Electron-hole pairs can be also generated through the avalanche breakdown mechanism; when a charge carrier in an electric field can gain enough energy (E_g) to eventually excite a second carrier from the VB to the CB, a massive electron flow can occur. The typical distances that carriers travel before loosing its excess energy (named *mean free path* φ) is around 50-100Å, which implies that this specific mechanism usually takes place within thick oxide layer (with d= 50-100Å). The term *avalanche* denotes the autocatalytic nature of the process since an excited charge carrier can collide against another additional carrier and so successively thus generating high electric currents across the interface.

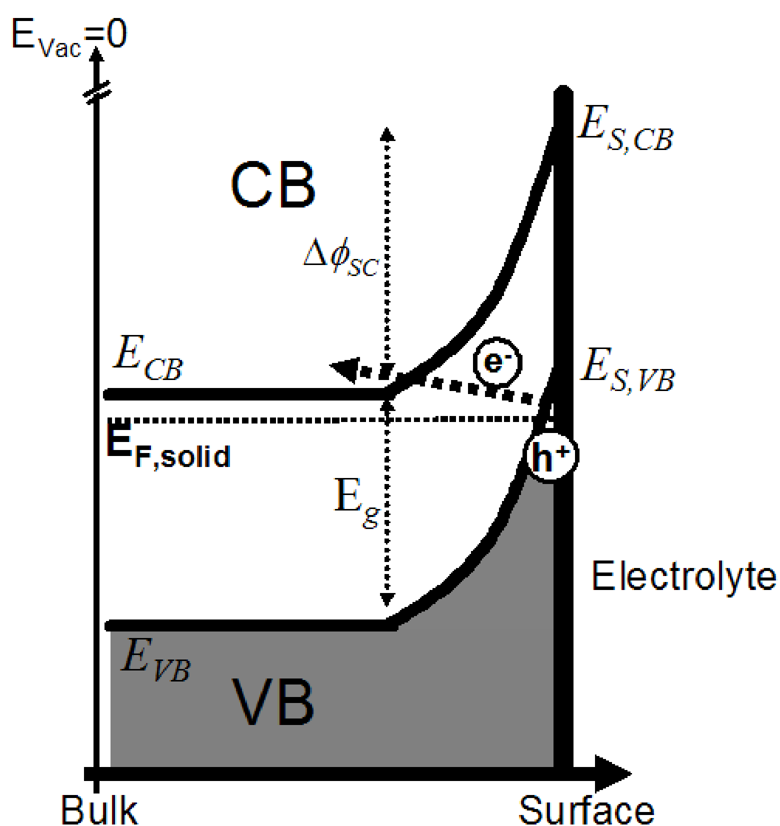

Figure 1.32: Zener breakdown process across the *SCL* of an *n*-type semiconducting electrode under strong depletion conditions.

The location of a carrier at the semiconductor solid surface is generally envisaged as the responsible of the lattice bond weakening which may ultimately take to the bond breaking and the corresponding electrochemical electrode corrosion (understood electrode dissolution). This process may proceed through different routes that involve either the movement of electrons to cationic SS or holes to anionic or covalent SS. The rate of these charge carriers (e^- and h^+) arriving to the particular SS will then determine the dissolution rate and, therefore, the material corrosion. Within this context, a flow of e^- traveling toward the semiconducting passive film surface will result in the interfering of the bonds between the M^{n+} compound and the neighboring O^{2-} anions of the lattice giving rise to cathodic removal of the oxide layer (so-called cathodic breakdown). In analogy, a h^+ flow going to the film surface will result in

direct surface bond oxidation giving rise to either a higher oxidation state phase or to anodic dissolution of the passive layer when the oxidation products are soluble in the working electrolyte. In this case, h^+ are generally envisaged as powerful oxidation agents. Corrosion involving holes are undoubtedly the primary corrosion route in semiconducting passive layers and it is thought to be also involved on the initial step of the passivity breakdown in the presence of aggressive anions. This extremely complex issue will be approached in depth in the forthcoming chapter 5. Nevertheless, some thermodynamic aspects of these processes will be given next. To this respect, general Gerischer's redox derivations concerning two simple decomposition reactions of a semiconductor compound of the form MX mediated either by e^- or h^+, are considered [96]:

$$MX + ne^- + solv \rightarrow M + X^{n-} \cdot solv \quad (1.87a)$$

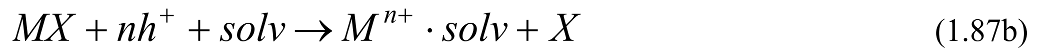

$$MX + nh^+ + solv \rightarrow M^{n+} \cdot solv + X \quad (1.87b)$$

where the term *solv* represents the solvent molecule surrounding the soluble species (see *solvation shell* concept in section 1.1.2.1). A redox potential can be defined for each of reactions in (1.87) with respect to a reference electrode. Considering the SHE reference scale (see Fig. 1.2), the counter reactions of (1.87) hold:

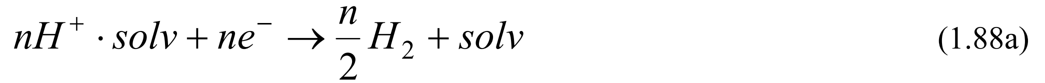

$$nH^+ \cdot solv + ne^- \rightarrow \frac{n}{2} H_2 + solv \quad (1.88a)$$

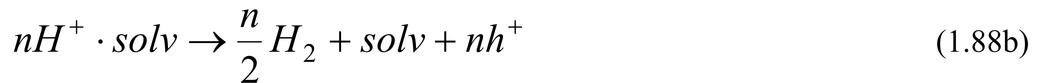

$$nH^+ \cdot solv \rightarrow \frac{n}{2} H_2 + solv + nh^+ \quad (1.88b)$$

The free energy differences ΔG_1 and ΔG_2 can be then evaluated from the corresponding combinations of (1.87) and (1.88) semi-cell redox reactions, yielding:

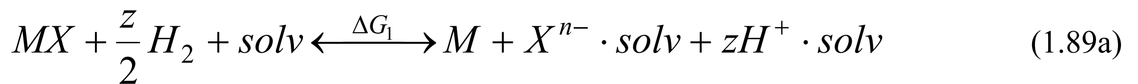

$$MX + \frac{z}{2} H_2 + solv \xleftrightarrow{\Delta G_1} M + X^{n-} \cdot solv + zH^+ \cdot solv \quad (1.89a)$$

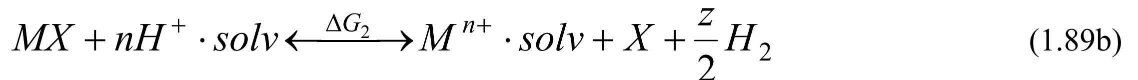

$$MX + nH^+ \cdot solv \xleftrightarrow{\Delta G_2} M^{n+} \cdot solv + X + \frac{z}{2} H_2 \quad (1.89b)$$

whose redox potentials can be determined through relations:

$${}_{n}U_{decomp} = \frac{\Delta G_1}{nF} \quad (1.90a)$$

$$ {}_pU_{decomp} = \frac{\Delta G_2}{nF} \tag{1.90b} $$

As seen in section 1.1.2.1, redox potentials in equations (1.90) can be equally described as the position of the Fermi levels in the electrolyte (see equation (1.1)).

Having characterized the thermodynamics of previous decomposition processes, it is then concluded that the decomposition reactions mediated by majority charge carriers in the semiconducting electrode can occur if [96]:

$$ {}_nE_{F,solid} > {}_nE_{decomp} \tag{1.91a} $$

$$ {}_pE_{F,solid} < {}_pE_{decomp} \tag{1.91b} $$

where ${}_nE_F$ and ${}_pE_F$ are the correspondingly the Fermi levels in *n*- and *p*-type semiconductors respectively. In practice, the position of ${}_nE_{decomp}$ and ${}_pE_{decomp}$ levels with respect to the band edges at the semiconductor│electrolyte interface will tell us, from a thermodynamic point of view, if the decomposition process becomes favorable, that is, when ${}_nE_{S,CB} > {}_nE_{decomp}$ or ${}_pE_{S,VB} < {}_pE_{decomp}$. These decomposition energy levels can be directly placed in the semiconductor band diagram for direct visualization of the process (see some examples in Fig. 1.33). Moreover, this discussion points out the importance of measuring the quantitative position of the band edges at the semiconductor│electrolyte interface as it will be showed in chapters 3 and 4.

The above thermodynamic data can be used to predict if a semiconducting oxide layer is susceptible of corrosion by determining the corresponding E_{decomp} level for reaction (1.89b), that would represent the anodic corrosion of the metal oxide surface (being *X*=O). Note that in reaction (1.89b) the presence of aggressive anions (*e.g.* Cl^-, SO_4^{2-}, *etc.*) can contribute to the decomposition potential through the term *solv*, for example, as a chelating agent of the dissolving metal ion M^{n+}. As it will be treated in chapter 5, more complex equilibria can be proposed if some information concerning the specific mechanism of the chloride action into the passive layer is known (see Fig. 1.31).

To end with this section, just to mention some of the limitations of the above described corrosion model for a semiconductor. First, equations (1.89) stand for decomposition processes induced by majority charge carriers, *i.e.* on large E_g semiconductors at room temperature and in the absence of illumination. Note, however, that under some experimental conditions (see section 1.1.2.4) a significant concentration of minority charge carriers can be generated at the semiconductor surface and might contribute to the decomposition equilibria in (1.89). And secondly, the above theoretical development serves to reasonably indicate whether the reaction is favorable or not, but since the whole corrosion process constitutes a very complex process with many steps, this thermodynamic picture fails in determining the activation complex that will dominate the kinetic mechanism. In conclusion, existing

theoretical models do not supply a quantitative view of the *realistic* (more than thermodynamic) energy levels where the SS involved in the decomposition reaction are, and ultimately determine the corrosion rate. Advanced technical approaches will be employed in chapter 5 to tackle into this issue.

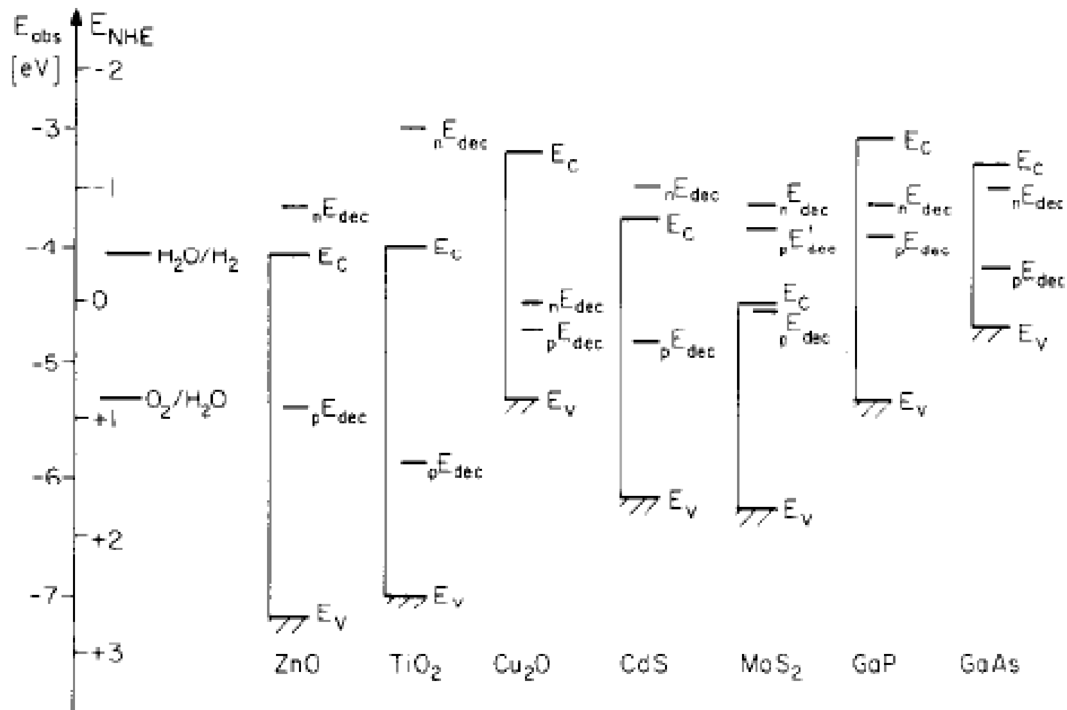

Figure 1.33: Position of band edges and decomposition Fermi energies of various semiconductor compounds and of water in the absolute (E_{abs}) and electrochemical (E_{NHE}) energy scales (see section 1.1.2.1). From ref. [96] (see also corresponding decomposition reactions herein).

1.3 *In situ* STUDIES OF METAL PASSIVE FILMS

1.3.1 Introduction

During the development of the previous section 1.2, we have seen that *passivation phenomenon* has its origin on metal systems whose outstanding practical applications prompted an immediate study of its fundamental understanding [97]. However, as in many other instances, the scientific comprehension of the process arrived some decades later, and since its early beginning, efforts have been focused on the study of the physicochemical properties of these metal passive films with the aim of elucidating the exact mechanisms that govern its surface reactivity and explain the nature of the passive state.

As it was stated in the preface, the electrochemical environment offers a perfect scenario for a fundamental approach of passive films [98-100]. Under a rigorous electrochemical control, their general properties such as chemical composition, film thickness, kinetics of the oxide growth and electronic properties can be accurately controlled. After oxide film formation,

relevant information concerning chemical composition and crystalline structure has been obtained *ex situ* by different means [101-103]. However, we pointed at the preface of this thesis that *ex situ* measurements assumed the possible artifacts inherent on the sample transfer stage from the electrochemical medium to the measuring chamber [101]. With these considerations, *in situ* measurements at the solid│liquid interface started to gain interest within the *"passivation community"*. Notwithstanding, its practical realization presented great experimental difficulties; the low thickness of passive films (ranging from few to a hundred nanometers, see section 1.2) and the necessity of an accurate electrochemical control in the aqueous medium in which they form, apply very strong technical constrictions on the use of the proper spectroscopy techniques able to *in situ* resolve its structure and chemical composition. In general, the obtained signal to noise ratio presents very low values, especially considering the presence of the surrounding liquid medium. Moreover, the required electrode potential control forces the electrochemical cell to be implemented in the measuring system.

Up to now, many of these experimental challenges have been overcome and the *in situ* measurements of solid│liquid interfaces under electrochemical control are now a reality. In the last decade, the synchrotron-based spectroscopic techniques [104] and the emerging SPM-based microscopies [14,105] have quantitatively increased our understanding of the crystalline structure, kinetics of the film growth and electronic properties of passive films in their native conditions.

This section seeks to review the most recent advances of *in situ* studies on metal passive films. The focus is again on the Fe system, as the target of this work, and also on Cu due to its widespread technological application and number of available studies. Moreover, Ni and Sn will be also briefly discussed. The discussion goes, however, beyond the particular analyzed system since the described methodologies are actually being employed on other more complex passive films systems. The whole discussion has been organized into a number of sections that present the different *in situ* approaches used to answer the main physicochemical questions of the passive film│liquid interface.

1.3.2 Recent advances on the electrochemical characterization

The electrochemical control is needed to guarantee a reproducible grown of the passive film on metal electrodes, but not uniquely with this purpose, the electrochemical techniques have also brought valuable information on the growth kinetics and electronic properties of the passive oxide film. Particularly, classical electrochemical techniques like cyclic voltammetry (CV) and EIS are still useful tools to answer some remaining questions on the passive film formation, surface chemical equilibria as well as film electronic properties.

Recent work on Fe passivity by Büchler *et al.* [106] constitutes an elegant demonstration of the co-deposition of a hydrated oxide layer on top of the so-called *natural* passive layer, presumably with a composition similar to FeOOH. This has been a long standing issue on Fe passivity that has put some difficulties in the interpretation of previous electrochemical results

like galvanostatic reduction experiments of the passive film [98,107,108]. The authors compare the cyclic voltammogram signal of an Fe electrode in borate buffer solution with that obtained from the electro-oxidation of Fe^{2+}(aq*)* on an inert Pt substrate in the same medium. In this manner, the peak of the semi-reaction redox process:

$$Fe^{2+} + 3OH^{-} \rightarrow FeOOH + H_2O + e^{-} \quad (1.92)$$

can be univocally assigned in the CV signal that characterizes the Fe passivation process (see Fig. 1.34A). The process described in equation (1.92) is further discussed by Ohtsuka *et al.* in the same medium by adding increasing amounts of Fe^{2+}(aq) [109]. The final thickness of the oxide film appear to be a linear function of the Fe^{2+}(aq) concentration being the growth rate independent of the applied potential. The passive film is thus composed by an inner compact layer (*natural* passive film) and an outer hydroxide layer that grows on top. In chapter 3, this duplex structure of the Fe passive film will be revisited and extended to different *pH* values. Equilibrium (1.92) ultimately governs the outer/inner layer ratio in the passive film during its electrochemical growth. Similar control of the duplex structure can be also achieved by introducing specific Fe(II)-chelating species, as studied by Rubim and more recently by Macdonald [110-112]. The CV signal within the Fe(II) electrochemical range (peak I in Fig. 1.34A) is enhanced by the presence of the Fe(II)-chelating species, like 2,2'-Bipyridine and Ethylenediaminetetraacetic acid (EDTA) that induce two effects on the electrochemical equilibria: (i) a shift toward the left hand side of the Fe(II) solubility product (Eq. (2) in section 3.2), thus enhancing the Fe(0)→Fe(II) oxidation process (peak I' in Fig. 1.34A). (ii) formation of a stable Fe^{2+}-chelant complex that prevents the electro-oxidation of Fe^{2+}(aq) (to form the outer layer, Eq. (1.91)) and will then occur at a higher electrode potential (out of the Fe CV which ranges from -1.1 to 1.2 V in the SCE electrode scale).

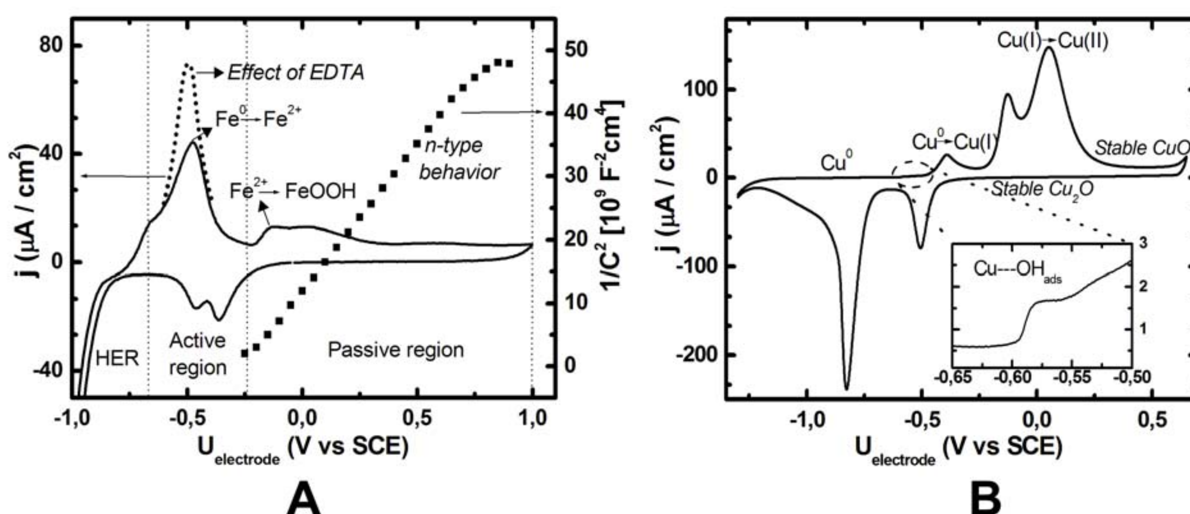

Figure 1.34: (A) CV of a polycrystalline Fe electrode in 0.3 M borate buffer solution of *pH* 7.5 at a scan potential rate of 5 mV/sec (left axis). Mott-Schottky representation of the capacitance data obtained by EIS (right axis). (B) CV of a polycrystalline Cu electrode in an aqueous 0.1 M NaOH solution at scan potential rate of 10 mV/sec. The inset figure corresponds to a detail of the electrochemical potential range within the OH^- adsorption region.

Although the semiconducting properties of the Fe oxides were soon discovered [85,113], recent studies have yielded a more quantitative understanding of its electronic behavior. Bojinov *et al.* analyzed the charge transport through the passive film electrochemically formed on Fe and Fe-Cr alloys using a particular EIS setup (so called Contact Electric Impedance and Resistance measurements; for experimental details of the set-up check [114,115]). They found that the ionic transport across the Fe│Fe oxide film│borate buffer interface proceeds via generation and transport of lattice point defects which, in turn, act as charge donors or acceptors in the oxide structure [114]. The Fe passive film thus behaves predominantly as an electronic conductor [115] so that the exact conduction mechanism requires to be treated from the viewpoint of the semiconductor electrochemistry [114] reviewed in previous sections. In this line, Buchler *et al.* have recently analyzed the semiconducting properties of the Fe passive film by comparing the EIS data of the passive film│borate buffer interface with a stoichiometric oxide│borate buffer one [116]. The capacitance data represented in the MS form (see Fig. 1.34A and ref. [30]) show that the *natural* passive film on Fe behaves as an *n*-type semiconductor with high doping density level (in the order of 10^{21} cm^{-3}) that slightly decreases as the formation electrode potential is increased within the Fe(III) range [116]. They also observed that the outer hydroxide layer has no significant effects on the general electronic properties of the whole Fe passive film [106]. However, in the presence of EDTA agents that suppress the deposition of the outer hydroxide layer [111], a slight increase in the doping concentration is observed and associate to the adsorption of EDTA on the interfacial oxygen vacancies. The control of the duplex structure of the Fe passive film is then of major importance to correctly interpret its electronic conduction and, therefore, its surface reactivity. Note that these semiconducting properties match with the previously redox process in (1.92). When an *n*-type semiconductor is under depletion conditions (see section 1.1), the available energy levels for charge exchange (band edges $E_{S,CB}$ and $E_{S,VB}$) appear to be pinned at the electrode surface and, therefore, the redox process represented in (1.92) is independent of the applied electrode potential [109].

The above works implicitly show that the thickness of the passive film plays also an important role in the measured electronic properties. To better dissect the semiconducting properties of the Fe passive film, its total thickness must be greater than the estimated SCL. In the example of Fe, in the Fe(III) potential range (see section 1.2.3.1), the SCL is about 3 nm [111] at $U_{electrode}$=0.5 V/SCE. In order to get Fe passive layers of $d \geq 3$ nm, more complex electrochemical procedures must be employed (see chapter 3).

The sharp duplex structure observed in Fe passive films does not occur on other metals because either they have been traditionally studied in alkaline media where the outer hydroxide layer formation is hindered (see section 3.2) or because the system presents an extremely low chemical solubility, *i.e.* high solubility products k_{SP}. This is the case of Sn passive films [117,118], which grow following a solid-state reaction with minimal release of ions into the solution. In chapter 3, an accurate analysis of the Fe passive film duplex structure is conducted by the use of well-oriented Fe substrates that allow higher resolution in the CV signal.

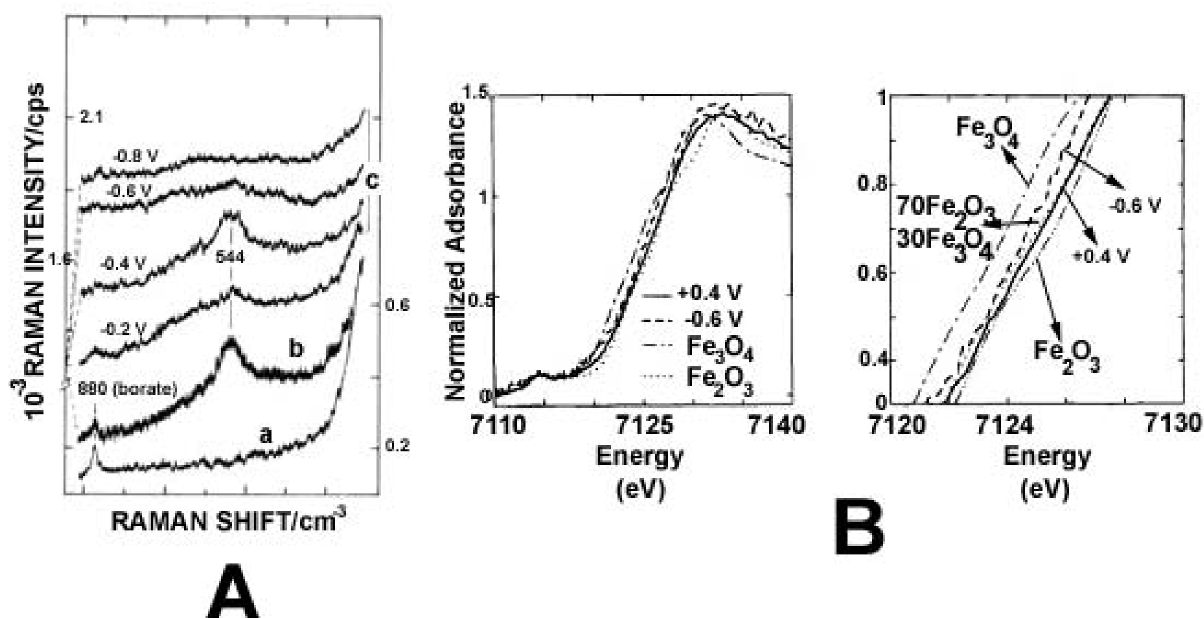

Figure 1.35: (A) *In situ* Raman spectra from a polycrystalline Fe electrode at open circuit potential before (a) and after (b) the deposition of a Ag particles film; (c) same as (b) but for different electrode potentials. From ref. [8]. (B) *In situ* XANES spectra from the Fe passive film immersed in a *pH* 8.4 0.136 M borate buffer. The electrochemical formation was performed by stepping the potential from -1.5 V/MSE to -0.6 V/MSE (dashed lines) or +0.4 V/MSE (solid line). Reference spectra of magnetite, maghemite and a calculated 30:70 mixture of the two are also included. After ref. [124].

1.3.3 *In situ* structural and chemical properties

One of the biggest challenges in the *in situ* study of passive films has been the quantitative analysis of its crystalline structure and chemical composition under electrochemical conditions. Early *in situ* optical studies allowed to probe the electronic structure through photo-electrochemical current measurements [119], or to estimate film thickness by ellipsometry [120], giving way to more structure-sensitive techniques like *in situ Surface Enhanced Raman Spectroscopy* (SERS). Rubim *et al.* reported the first *in situ* SERS studies on the passive film that forms on Fe electrodes in borate buffer media [8] (Fig. 1.35A). They found that at low applied potentials the Fe passive film is predominantly formed by a ferrous hydrated oxide film which was ascribed to an $Fe(OH)_2$ phase [8,110]. Later on, Devine and co-workers further analyzed this system using *in situ* SERS [9,121] and concluding that the Fe passive layer at low potentials in the passive electrochemical range (*passive region* in Fig. 1.34A) resembles a spinel Fe_3O_4 or a defective γ-Fe_2O_3 structure [121]. Despite the valuable *in situ* chemical information provided by this technique, *in situ* SERS measurements present some experimental limitations; in most systems, the poor Raman scattering collected from the oxide|solution interface is close to the noise level, as it is the case of Fe [8,9] and Sn [122] oxide films. In the last cases, the weak Raman scattering signal is usually enhanced by electrodepositing metallic particles of more novel metals (typically Ag or Au) on the electrode surface previous to passivation. After passive film growth, these particles act as enhancing centers of the SERS signal which is commonly amplified up to 3 orders of magnitude [10]. Although the authors have claimed that these particles are innocuous for the passive film

electrochemistry, it still remains unknown. An alternative to this experimental issue is presented in a recent contribution by Allongue *et al.* where the Fe passivation is studied on a thin Fe film electrodeposited onto a Au(111)-oriented substrate. They demonstrate that an amplification of 5 x 10^4 is achieved if both Fe film thickness and wavelength matching between the excitation signal and the plasmon resonance of the Au underneath are optimized [11]. In all these examples a general agreement exists concerning a local electromagnetic mechanism as the enhancing mechanism of the Raman signal that comes essentially from the passive film itself and not exclusively from the passive film region in contact to the enhancing metal. However, some controversy still exists on the peaks assignment, especially at early electrode potentials (*active region* in Fig. 1.34A), where the SERS peak around 550 cm^{-1} has been associated indistinctly to a ferrous $Fe(OH)_2$ phase [110] and to an unknown ferric oxide-hydroxide [121].

In the case of Cu passive films, *in situ* SERS was successfully applied to elucidate the chemical composition of the passive film grown in a wide electrochemical range (see CV signal in Fig. 1.34B) and in different *pH* media. Weaver and co-workers [123] identified the sequential formation of a first –OH adsorption at very negative potentials, followed by a Cu_2O and then a $Cu_2O/Cu(OH)_2$ duplex layer as the electrode potential is raised in the positive direction (see peaks assignation in CV of Fig. 1.34B). This success is in part due to the easy SERS-active surface preparation of the Cu electrode which consists on a simple electrochemical oxidation-reduction cycling procedure that generates a highly roughed electrode surface. Scarce *in situ* SERS results can be found on Ni and Sn passive films [118, 122].

Undoubtedly, *in situ* X-Ray adsorption and diffraction spectroscopies have greatly advanced the quantitative comprehension of passive film structure. In order to collect a significant amount of signal counts coming from the oxide│liquid interface, the use of synchrotron radiation sources is mandatory. The first high resolution *in situ* examination of Fe passive films in borate buffers were performed by Oblonsky *et al.* [124] using XANES (Fig. 1.35B). In this study, a close analysis of the small pre-edge peak of the passive film spectrum revealed that at high electrode potentials in the passive region (0.8 V/SCE in Fig. 1.34A) it is mostly composed by Fe(III) with a 7 % of Fe(II) content in its structure. This percentage gradually increases at more negative potentials, up to a 17 % at the onset of the passive region (-0.4 V/SCE in Fig. 1.34A), consistent with the model of the Fe passive film doped by Fe(II) species [116]. Moreover, the average valence of the final passive film was found to be independent of *pH* [125], despite a significant amount of electrode dissolution is observed at the lower *pH* value. More recently Virtanen *et al.* extended this investigation to alkaline and phosphate media [126] and found that the Fe passive layer is completely reduced to bare metal in both borate and phosphate buffers at nearly neutral *pH* through reductive dissolution and direct reduction respectively. However, an $Fe(OH)_2$ layer is the final reduction product in alkaline media.

Despite the vast collected amount of chemical information on the passivation process by *in situ* optical techniques, previous works do not give an exact crystalline structure for the passive film. Although ECSTM is a surface technique, it provided the first direct *in situ* proof of the crystalline nature of the Fe passive film [18]. Both triangular and *honeycomb*-like

arrays of atoms were simultaneously resolved, with spacing consistent with the outermost Fe(III) and O^{2-} ions of an oriented spinel structure (111)-face. The group of Marcus has extensively studied the passive film on Cu by using the same ECSTM technique and their most recent results offer a complete structural model for this system [19,20]. They used Cu(111) and Cu(001) to study the structure of the Cu passive film by direct *in situ* imaging of the atomic arrangements of the oxide layer at different oxidation potentials. At low passivation potentials (between -0.2 and 0 V/SCE in Fig. 1.34B) hexagonal and square atomic arrangements with a lattice periodicity of 0.3 nm is consistent with the expected low valence Cu(I) oxides of Cu_2O(111) and Cu_2O(001) forms respectively, showing a nice mismatch regarding the structure of the Cu substrate underneath. At higher passivation potentials (>0.75 V/SCE, Fig. 1.34B), same atomic lattices are measured on both Cu substrates, in good agreement with the in-plane nearest neighbor distance along the closest packed directions for a bulk CuO(001) structure. This common (001) oxide orientation on both Cu(111) and (001) electrodes is explained by the surface hydroxylation at the oxide│electrolyte interface necessary to stabilize the bulk termination of the late CuO phase. The identical phase on both substrates at high $U_{electrode}$ is further supported by the same measured step height of 0.25 nm that corresponds to one equivalent CuO(001) monolayer. All these findings on Cu passive films are in good agreement with previous *ex situ* spectroscopic measurements which propose a single Cu_2O passive layer at low electrode potentials and a duplex Cu_2O│CuO,$Cu(OH)_2$ layer at higher potentials. Other *in situ* measurements corroborate this duplex structure as for example those performed by *in situ* synchrotron far IR spectroscopy [127].

Similar studies have been conducted on Ni(111) passive films by the same group [128]. In this case, the passive layer is simply composed by an inner crystalline NiO layer that grows epitaxially with the metal substrate, *i.e.* Ni(111)│NiO(111) (both parallel or antiparallel oriented) and that is covered by a $Ni(OH)_2$ phase whose thickness varies depending on the experimental conditions.

Although SPM techniques have supplied direct crystalline information of the most important passive systems, they can not provide the whole 3-dimesional crystallographic view of the entire passive layer structure (defects, bulk information, etc). This crystallographic information can be accessed by *in situ* XRD. Special mention has the measurements conducted by Davenport *et al.* on Fe [12,13] and by Magnussen *et al.* on Ni passive films [129]. In the former case, the crystalline structure of the Fe passive film is definitively characterized; although it is related to Fe_3O_4 and γ-Fe_2O_3 structures, the Fe passive phase (so-called by the authors LAMM phase) presents a spinel structure with a fully occupied oxygen lattice, but with a notably different cation occupancy: 80% of the octahedral sites, 66% of the tetrahedral sites and 12% of octahedral interstitial sites. It is also found that the passive film has a nanocrystalline nature with numerous extended defects. In the second example, the *in situ* X-Ray scattering data corroborate the previously proposed NiO(111) structure for the Ni passive film with an exclusive antiparallel orientation. It is important to stress here that the XRD spectra result from the crystalline part of the passive layer only, which in most cases corresponds to the inner layer. This fact implies that the passive layer is usually grown under particular conditions to avoid further hydrated on-top layers, like step-potential electrochemical growth or solution flow after film formation.

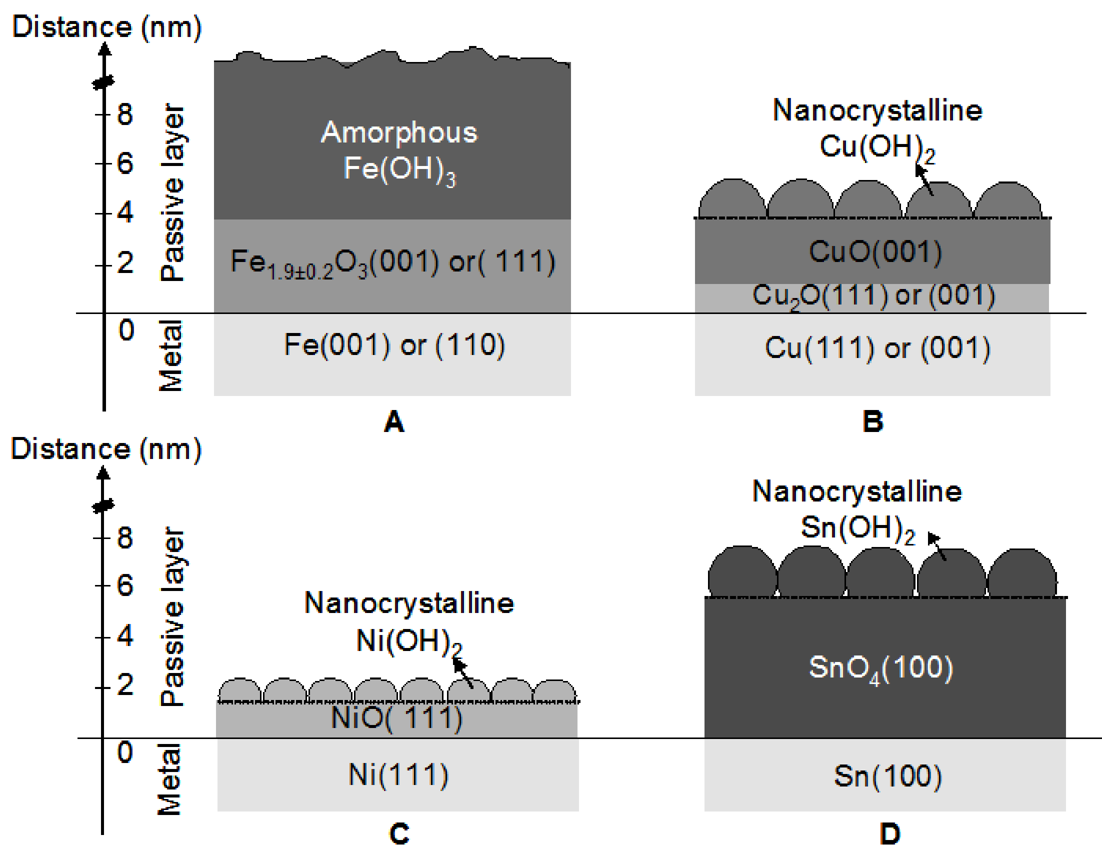

Figure 1.36: Summary of structural and chemical properties of the passive film on (A) Fe, (B) Cu, (C) Ni and (D) Sn. Darker color in the oxide film means higher oxidation state.

By way of summary, all the available crystallographic and chemical information about the passive films on Fe, Cu, Ni and Sn has been summarized in the figure 1.36A-D.

1.3.4 *In situ* studies of growth dynamics and electronic properties by SPM techniques

In situ SPM techniques have been demonstrated to be useful tools for the elucidation of the crystalline nature of the oxide passive layers (see previous section). However, the information provided by those techniques can give a much wider picture of the passivation process. The most remarkable demonstration is their capability to follow dynamic process on the electrode surface through time-resolved images [130]. For example, the group of Marcus has examined the dynamic processes of the passive film growth on Cu(111) and Cu(001) substrates in alkaline media [19,20]. At early electrode potentials prior to the passive film formation, a partially ordered OH^- monolayer is observed on both electrodes. This OH^- monolayer is ascribed to the precursor state of the Cu_2O film formation, in agreement with SERS results [123]. OH^- adsorption begins preferentially at the steps and proceeds until covering the entire surface, being the process faster as the potential increases. This is in contrast to Sn(100)

electrodes, where a clustered layer is evidenced at early stages of the passive film formation, and associated to a dissolution-precipitation process [118]. The early stages of Cu passive film formation (Cu_2O) are again observed as a quick nucleation followed by the complete surface coverage in the form of triangular crystallites, thus evidencing the crystalline nature of the passive layer [131]. The observed faceting of the oxide crystal is a common mechanism of stress release due to the large lattice mismatch with the metal substrate. It is important to note that the use of single crystal substrates allows high topographic resolution by ECSTM, but requires surface preparation methodologies that provides sufficiently large terraces. While Cu, Ni or Sn single crystals have been *in situ* imaged by ECSTM in many instances [19,20,,128,131], studies on Fe single crystals are rare [132].

The most popular SPM technique, the atomic force microscopy (AFM), has been also employed to follow *in situ* the passive film growth and dissolution. We wanted to mention here one of its latest applications conducted by Gewirth *et al.* [133] who combine CV and force spectroscopy by AFM to study the *in situ* the changes on the passive film surface as it is electrochemically grown and reduced in an alkaline medium.

The real capability of the SPM techniques in the field of passivity has been recently demonstrated with the *in situ* elucidation of the electronic properties of the oxide passive layers, which constitute the fingerprint of their redox behavior in solution. Although the redox behavior of semiconducting electrodes results directly from the availability of free charge carriers at the electrode | solution interface [30,31], few experimental studies have correlated the electronic structure of the oxide layer with the dynamics of film growth, dissolution and ET with redox species in the electrolyte. Early experiments with redox probes in solution have proven useful [134,135] but there are a limited number of probes with discrete available energies, and their different energy ranges and ET kinetics hinder a quantitative comparison between them. The tip of an ECSTM can be brought to tunneling distances of the electrode surface, thus acting as a probe of the local density of electronic states in the oxide film. In this case, the independent control of the tip potential provided by the ECSTM bi-potentiostatic control (see chapter 2, section 2.2) allows to tune the Fermi energy of the metallic probe over the entire electrochemical range. In short, the ECSTM technique allows to obtain a rapid and direct *in situ* view of the electronic charge transfer behavior of the electrode | electrolyte interface without the use of equivalent circuit models as in standard electrochemical methods like EIS. Recent reported data on Cu, Ni and Sn passive films demonstrate that it is possible to qualitatively locate the main energy levels of the oxide | electrolyte interface, by analyzing the stability of the STM image at different tunneling conditions (varying Bias and/or ECSTM tip potential, and tunneling current I_T (see section 2.2 for more details on STM parameters)) [118,128,131]. Concerning the duplex structures on Cu [20,131] and the Ni passive films [128] (see Fig. 1.36B and C), small changes in the ECSTM tip potential allow to electronically probe (and image) either the outer granular hydroxide layers ($Cu(OH)_2$ and $Ni(OH)_2$) or the inner crystalline films (CuO and NiO) [20,128] alternatively. In the former case, electron tunneling was attributed to electron *hopping* via empty localized states within the outer hydroxide layer at higher ECSTM tip potentials, while the inner crystalline phase can be imaged through lower energy empty levels that correspond, for Cu and Ni cases respectively, to: (i) a *subband* (*SB*) located in the middle of the band gap of the *p*-CuO film [131], and (ii) the presence of localized states of higher density near the VB of NiO [128]. At more positive

electrode potentials, the tunneling stability on the Cu passive film improves due to the possibility to inject electrons from the tip into the CB of the *p*-CuO phase [128].

In terms of the electronic structure, the ECSTM imaging conditions can be utilized to probe available electronic states in the oxide. However, a direct and quantitative determination of the oxide band structure would require real tunneling spectroscopy measurements in solution under potentiostatic control. ECTS provides a unique opportunity to direct probe the entire electronic spectrum of the passive film│electrolyte interface. In the mid-nineties, the first demonstrations of ECTS were presented on bare metallic surfaces of well-defined single crystals [24,136,137] as well as on Fe and Ti polycrystalline passive layers [138,139]. Schreyer *et al.* were the first to measure the local barrier height ϕ on polycrystalline Fe and stainless steel electrodes as a function of the electrode potential by recording I_T versus tip-sample (s) distance curves [138]. The observed decrease of ϕ as the Fe electrode is oxidized was explained by the introduction of localized Fe^{2+} electronic states acting as resonance centers for indirect tunneling. The authors suggest that such Fe^{2+} centers disappear at higher anodic (positive) $U_{electrode}$ leading to the loss of tunneling conductance. However, the large scattering in the ϕ values evidenced the need of a consensus on the initial tunneling conditions to obtain reliable ECTS data. These difficulties are also reflected in the work of Azumi *et al.* [139] where both I_T vs. s and I_T vs. tunneling Bias conditions are collected to measure ϕ values and tunneling spectra respectively, on Fe and Ti passive films. The authors outlined some important experimental limitations on these measurements: an accurate electrochemical control of the tip potential ramps (at constant substrate potential) and a better tip electrical insulation that allows to enlarge the working energy windows of the tunneling spectrum. All these technical difficulties obscured the interpretation of the ECTS results, and the subject was not recaptured until present time, mostly motivated by the fast development of the nanostructures fabrication and the necessity to find methods for their *in situ* characterization. Schindler and collaborators have recently revisited the ECTS methodology [140,141] and presented some important advances on the previous experimental limitations like the use of free oxygen atmosphere within the ECTS set-up or the application of fast tip potential ramps within the double layer electrochemical range to minimize the parasitic contributions to the tip current during the capture of the ECTS spectra [140]. However, the authors still claim the improvement of the tip electrical insulation methods in order to achieve a better resolution of the ECTS curves by minimizing the tip double-layer capacitance current. All these technical questions will be answered in chapter 2 (sections 2.3 and 2.4), where a complete description of the tip preparation procedure as well as of the ECTS performance to obtain reliable tunneling spectra of the passive film│electrolyte interface, will be provided.

1.3.5. *In situ* measurements of passivity breakdown in chloride media

As treated in section 1.2.4.4, passivity breakdown in chloride-containing media is one of the most outstanding processes in corrosion protection of technical materials. Although the final effects of chloride corrosion extend to the material bulk, the early stages of this phenomenon

constitute a surface process which usually implies a first Cl^- adsorption step on the oxide passive surface (among the different mechanism described in section 1.2.4.4), followed by the (electro)chemical corroding processes [5]. In order to elucidate the mechanism of this process, a number of *in situ* methods have been used with the aim of detecting and characterizing the earliest presence of adsorbed Cl^- and the corrosion precursor M-Cl complex in a wide electrochemical range. Evidence of Cl^- adsorption was firstly reported by SERS on Cu [123]. In the Cu(I) electrochemical range (see Fig. 1.34B), the complex CuCl acts as a competitor with the Cu_2O oxide phase formation on the surface. This process was recently analyzed by the group of Marcus using ECSTM on a Cu(111) electrode [142]. During the electrochemical oxidation of Cu in alkaline medium, surface Cl^- competition is observed at potentials corresponding to the ordered OH^- adsorption range prior to Cu(I) formation (Fig. 1B). At higher chloride concentrations, the preferential reaction of hydroxides at the step edges of the Cu surface is fully blocked by the formation of a non-ordered CuCl complex. However the final structure of the Cu_2O passive layer in chloride media is not modified besides the observed rougher edges. At lower *pH* values, the surface chemical equilibrium:

$$Cu_2O + 2H^+ + 2Cl^- \rightarrow 2CuCl + H_2O \qquad (1.93)$$

is shifted toward the right hand side thus undergoing electrode corrosion [123]. This rich surface speciation on Cu caused by Cl^- does not occur on other metallic systems like Ni or Fe. ECSTM studies of the passivation of Ni(111) in the presence of chloride revealed that even in acidic sulphuric media, the NiO(111) lattice and the observed 2-dimensional oxide dissolution are independent of chloride at electrode potentials below the passivity breakdown potential (U_B) [143] (see revision of the concepts in chapter 5). However, in more alkaline media, the group of Macdonald has recently found by EIS that the presence of increasing concentrations of Cl^- produces a linear increase of the doping density (N_A) on the *p*-NiO passive layer at electrode potentials under U_B [144]. They concluded that the cation vacancies (majority defect in the *p*-type semiconductor oxide) are promoted by the presence of Cl^- through Ni-chelating process: Cl^- interacts with the vacancies at the oxide|electrolyte interface thus promoting their generation at the metal|oxide interface and increasing the cation vacancy density within the oxide layer. Passivity breakdown of Ni is then explained by the enhanced flux of those vacancies across the oxide passive layer, as postulated in the PDM developed by the same authors [73,74].

The first direct *in situ* studies concerning the presence of chloride on Fe passive layer surfaces were performed by ellipsometric measurements [145] whose final conclusions suggest, besides some controversy, that no pre-absorption of chloride takes place in nearly neutral *pH* at electrode potentials previous to U_B. As for the imaging of the process, the most spectacular results have been reported by Punckt *et al.* who managed to *in situ* monitor the surface of a stainless steel electrode at the micrometer scale while it is undergoing metastable pitting in an aqueous chloride medium [146]. Micro-pit formation and subsequent passivation were resolved using a contrast enhanced optical microscope developed by the same group improved with a lateral resolution down to 2 μm. The current generated by the observed metastable pit formation was simultaneously recorded so that they could collect both image and activity of an individual pitting event.

Chapter 2

Experimental developments

2.1 GENERAL

This chapter is dedicated to the description of the main characterization techniques employed in this Ph.D. work. It is not intended to be a mere description of all employed experimental techniques, but it focuses the attention on the most important technical developments that will show their relevance in the forthcoming chapters 3, 4 and 5. This part constitutes an important contribution of this thesis since the implemented methodologies go beyond the scope of passivity, as it will be exemplified in the Appendix A. The results of this chapter are structured in three different parts: the first section 2.3 deals with the description of the ECSTM technique with special emphasis on the design of the 4-electrodes configuration of the electrochemical ECSTM set-up, and settles the basis of the classical preparation methods to prepare ECSTM probes. The second part (section 2.4) goes deeper into the methodologies of the STM probes elaboration and describes a new developed procedure that allows the use of these STM probes on *in situ* electrochemical tunneling spectroscopy applications. As a short summary, this simple described procedure results in the elaboration of Pt/Ir tips with residual electrochemical currents of less than 1 nA when the tip potential is scanned a very high rates up to 20 V/s. Finally, the last section 2.5 of this chapter deals with the description of the designed protocol to record *in situ* tunneling spectra from the electrode│electrolyte interface. Special care is placed on choosing suitable initial tunneling conditions to obtain comparable *in situ* tunneling data along the electrode oxidation. As will be demonstrated, these particular conditions can be found out through measurements of the barrier height at different electrode and tip potentials.

Although standard instrumentation has been additionally employed at different characterization stages throughout this work, they are not described in this chapter. A short explanation will be provided when corresponds at each corresponding section.

The detailed results of this chapter are presented in the following publications:

- Electrochemistry in *Scanning Probe Microscopy: Basic Concepts and Applications*. Phantoms Report (2003) 75.
- *Preparation of Reliable Probes for Electrochemical Tunneling Spectroscopy* Anal. Chem. **76** (2004) 5218.
- *Electrochemical Tunneling Spectroscopy to fingerprint electrode electronic structure*, Anal. Chem. **78** (2006) 7325.

2.2 FUNDAMENTALS OF STM

Since this thesis arises within the frame of the electrochemistry, before tackling into the specific results, we consider necessary to firstly provide a short introduction to the STM technique as well as to the tunneling formalism which is inherent in any of their related working modes.

2.2.1 Origin and operation mode

The STM technique was firstly developed by Binnig and Röhrer in 1982 [161] and constituted the initial shoot for the field of *Nanoscience*. After its discovery, a number of different related techniques were appearing in the subsequent years giving rise to a family of techniques actually known as SPM (see preface). These techniques are characterized by their high spatial resolution on both vertical and lateral directions, which allow the visualization of crystalline surfaces at atomic level (see section 1.3). But undoubtedly, the most outstanding feature of these techniques is their capability to work under any environmental conditions (UHV, air or liquid). All SPM techniques have the same *modus operandi*; the studied surface is scanned by a low dimensional probe at very small distances in the order of few amstrongs. Next, by measuring a particular magnitude that depends on the sample-to-probe distance (s), a 3-dimensional map of the surface can be then built up. In the specific case of the STM, the measured parameter is the tunneling current (i_{tunnel}) flowing between the probe and the sample surface as a result of the voltage difference applied between them (so-called V_{Bias} in electronics jargon). The STM probe corresponds to a very sharp tip usually made of W or other noble metal like Au, Pd or Pt/Ir (see next two sections of this chapter). The accurate positioning of the STM probe over the studied surface is achieved by attaching the probe to a piezo-electric tube which allows movements in all three spatial directions with an amstrong accuracy.

As it will be deduced from this chapter, the SPM techniques are, at the present time, still subjected to a continuous technical development.

2.2.2 Tunneling formalism

2.2.2.1 General models

As pointed in the previous section, the operation of an STM microscope is based on the measured tunneling current flowing between the STM tip and the sample surface through the insulating gap s under an applied V_{Bias}. The first model that gave a simple analytical tunneling expression assumed the simplification of the 3-dimensional metal│insulator│probe junction into a one-dimensional metal│insulator│metal contact [162] (see Fig. 2.1). The deduced equation that relates the applied V_{Bias} with i_{tunnel} and s, yields:

$$i_{tunnel} = i_0 \frac{V_{Bias}}{s} \cdot e^{-k\sqrt{\phi_B \cdot s}} \tag{2.1}$$

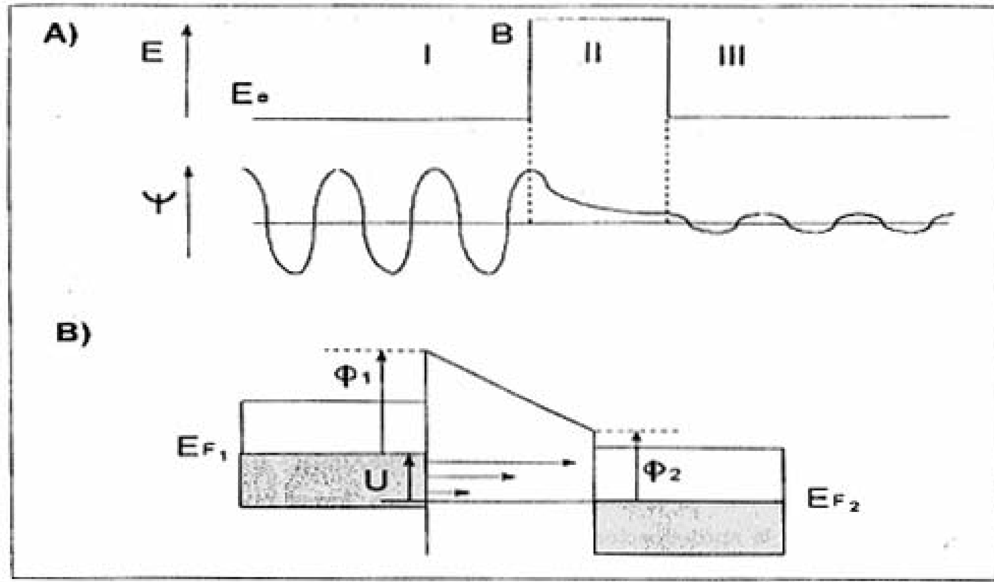

Figure 2.1: (A) Schematic energy diagram for the tunnel process on a one-dimensional tunneling junction; energy barrier (up) and wave function (down) representations. (B) Band diagram representation for the electron tunnel process through a metal│insulator│metal junction. Longer arrow represents higher tunneling probability.

This expression is valid for the case of low V_{Bias} values for which the density of electronic states do not vary significantly with this magnitude. In expression (2.1), i_o is a constant, ϕ_B is the local electronic barrier height seen by the tunneled electron, and k is a constant equal to 1.025 $Å^{-1}eV^{-1/2}$. It is important to stress here that the tunneling barrier height ϕ_B measured by STM is a local property of the analyzed surface which should not be confused with the general work function (Φ) of the material that is an averaged parameter over the entire crystalline lattice. Expression (2.1) has been largely employed to get the tunneling parameters in UHV-STM. However, this model fails to explain those phenomena where the tip geometry can play an important rule. Later on, Tersoff and Hamann proposed a 3-dimensional model for the STM tunneling junction, giving rise to a more accurate tunneling expression of the form [163]:

$$i_{tunnel} = i_0 \cdot N_S(V_{Bias}) \cdot e^{-k\sqrt{\phi_B \cdot s}} \quad (2.2)$$

where N_S denotes the *local density of states* (LDOS) evaluated in the centre of the tip curvature. From expressions (2.1) and (2.2), it is deduced that the high lateral resolution of the STM technique resides in the exponential dependence of i_{tunnel} versus s. The final implication of this dependence is such that the major percentage of the tunneled electrons takes place through the last atom of the tip apex which is closer to the surface. A simple calculation using (2.1) and, taking a typical ϕ_B value of 4 eV, yields that an atom which is 2 Å closer than the neighboring atoms will bring the 99 % of the tunneling current. Another conclusion deduced from equation (2.2) is the direct relation among the applied V_{Bias} and the surface LDOS. In short, it means that the STM image actually represents the density of states per volume unit in a localized surface point at the energy level given by V_{Bias}. This fact has been experimentally evidenced by imaging semiconductor surfaces like Si or Ge at different Bias conditions. The particular electronic structure of these substrates (reviewed in chapter 1) eventually displays localized SS that can be individually imaged by STM at atomic scale (see Fig. 2.2).

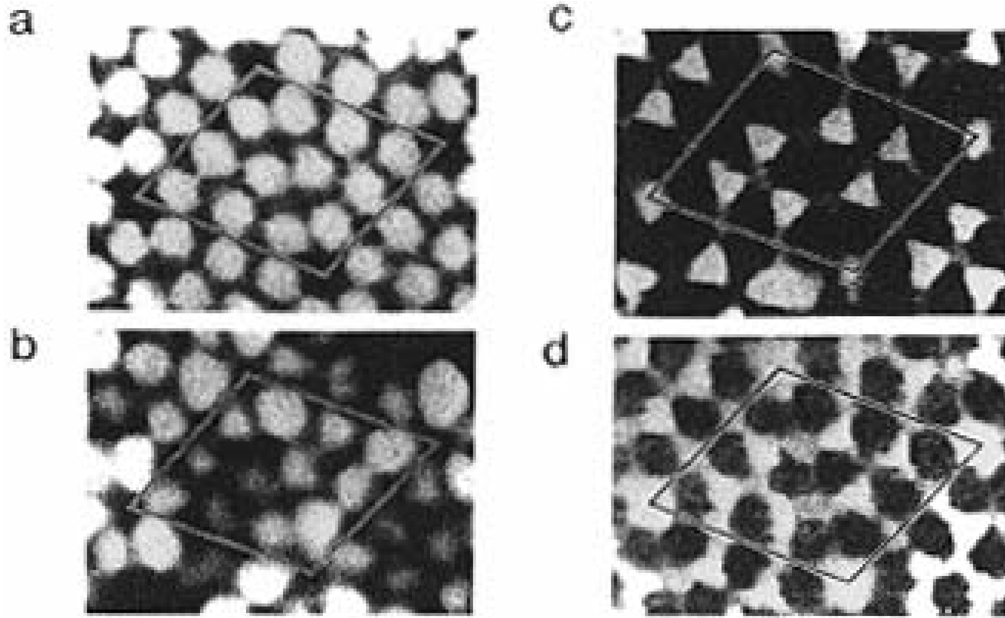

Figure 2.2: Individual probed SS at the reconstructed Si(111)-7x7 by UHV-STM. Image recorded at V_{Bias} of (a) +2 V, (b) -0.35 V, (c) -0.8 V and (d) -1.8 V.

From equation (2.1), a simple relation for the barrier height ϕ_B determination can be directly expressed as:

$$\phi_B = 0.952\left(\frac{d \ln i_{tunnel}}{ds}\right)^2 \tag{2.3}$$

and has been probed to reasonably match on experimental STM junction under different working environments [136].

2.2.2.2 The ECSTM model

The mechanism of tunneling conduction for an STM operating in an electrochemical environment is still poorly understood. Although the exponential i_{tunnel} decay with the sample-to-probe distance s applies also in these systems (Eq. (2.2), the obtained barrier height ϕ_B values appears to be significantly lower than in UHV or air STM junctions. As a consequence, a number of models were proposed to explain this phenomenon. With some particularities, all these models propose an electron tunneling process where the electrons do not cross directly the liquid gap, but rather momentarily stay at low energy intermedium states existing within the liquid gap. These states have been associated (see for example the model of Gimzewsky *et al.* [162]) to a metastable solvation configuration of the tunneled electron that, in average, allows to decrease the observed effective tunneling barrier.

2.3 ELECTROCHEMISTRY IN SCANNING PROBE MICROSCOPY: BASIC CONCEPTS AND APPLICATIONS

Reference: I. Díez-Pérez and F. Sanz, Electrochemistry in *Scanning Probe Microscopy: Basic Concepts and Applications*. Phantoms Report (2003) 75-81.

INTRODUCTION

The Electrochemical Scanning Tunneling Microscopy (EC-STM) technique is a STM based technique used for the study of electrolyte-electrode interfaces. Therefore, the same elements as in a standard STM experimental set up can be found in the case of an EC-STM equipment. The tunneling current flowing between a metallic tip and a conductive sample will be again used to obtain topographical information as well as the electronic structure of a determined electrode surface immersed in the corresponding electrolyte. Although the fundamentals of both techniques are then essentially the same, 2 different elements must be introduced in a conventional STM set up in order to operate as an EC-STM: a 4-electrodes electrochemical cell and the development of suitable EC-STM probes.

EC-STM probes

Since the EC-STM technique will be employed for the study of electrolyte-electrode interfaces, the EC-STM probe, that will scan the surface at a few amstrongs distance, will be of course immersed in the same liquid environment. This fact adds an additional current component to the tunneling current flowing through the tip, known as the electrochemical current. The figure 1 shows I/V curves for both W and Pt/Ir tip, recorded far from the surface in order to evaluate only the electrochemical current term. These curves are typically called cyclic voltammograms when recorded in a conventional electrochemical cell. As observed in the curves of figure 1, the tip electrochemical behavior strongly depends on the material used for the tip. As in the STM technique, the tunneling current will be used here again as the feedback signal, which means that it will be indispensable to minimize the electrochemical tip current at the level of less than 10 % of the set point tunneling current, that is typically less than 0.1 nA. For this purpose, the electrochemical tip potential range selected to apply a determined EC-STM Bias voltage must be within the range of minimum electrochemical current observed in the voltammogram (see plateaus for W and Pt/Ir delimited by the arrows in the curves of figure 1). Within this potential range, only electrochemical current due to charge-discharge processes of the surface electrode in contact with the electrolyte takes place (pure capacitance current), while no electrochemical reaction associated to the water dissociation or other species accounts. The current associated to the charge-discharge processes directly depends on the tip area exposed to the electrolyte, for this reason, the EC-STM probes are commonly isolated, just exposing the very end tip apex to the electrolyte.

Many tip-manufacturing and tip-isolating methods have been extensively described in the bibliography [1-5]. Here we give a short overview of the most commonly used ones for EC-STM operation.

Electrochemical tip etching methods

The electrochemical etching procedure has become the most used method for EC-STM tips manufacturing, due to the low cost, the achieved proper tip geometry and also the easy-way experimental set-up from the electro-chemists point of view. The figure 2 shows a scheme of the standard set up for the electrolytic cell used for the electrochemical sharpening of the EC-STM tips. It consists on a 2-electrode electrolytic cell configuration, being the counter electrode (cathode) a platinum wire and the working electrode (anode) a wire of the tip material. The chosen material for the EC-STM probe manufacturing and then, the preparation method depends on the specific application. Well-known and commonly used tungsten (W) wire for general STM applications are also used for applications on EC-STM imaging, mainly on metals or other systems, where the employed STM Bias values are relatively low (i.e. lower than 300 mV). For electronic spectroscopy applications or semiconductor imaging, where a wide STM Bias range is required, more noble materials are used like for example Au, Pd metals or Pt-Ir and Pd-Rh alloys. In table I, the experimental conditions for the electrochemical manufacturing of EC-STM tips are shown. By means of comparison, in the case of more noble metals and alloys, higher applied voltages as well as more reactive chemical agents are generally required as compare to the common W. Even in the case of more stable materials like Pt/Ir alloys, more complex electrochemical methods with programmed potential waves must be employed to etch the material and obtain the EC-STM probe. For further information, additional bibliography can be reviewed [6].

Tip-isolating methods

As was pointed above, the electrochemical charge associated to the charging-discharging process of an electrode in contact with a specific electrolyte depends directly on the exposed area of the electrode itself. For this reason, the EC-STM tips must be isolated from the electrolyte, in the way that just the very end tip apex remains in contact with the electrolyte. With this isolation process, the electrochemical current measured through the STM preamplifier must be better than 10 % of the tunneling set point current, that is, typically less than 0.1 nA. This electrochemical noise current corresponds to a nominal exposed area of $<500\ \mu m^2$. Table II shows a summary of the most relevant tip-isolating methods. In general, the tip isolation is performed by covering the entire surface of the probe with a specific polymer. The difficulty of the covering procedure will lay on leaving a small uncovered area at the end of the tip. In the case of low melting point polymers like the most commonly used Apiezon wax, the uncovered area is controlled by the temperature and thereby, the viscosity of the wax. In this sense, in the case of varnishes the viscosity control and then the exposed area, is controlled by the concentration of the organic solvent before the application. On the other hand, in the case of electrophoretic paints, this control is achieved by the final thermal treatment.

4-electrodes electrochemical cell

In a conventional electrochemical cell, the electrochemical potential applied to the sample (U_S) is controlled by a 3-electrode configuration: a working electrode (sample, U_S), a reference electrode (U_R) and an auxiliary electrode (U_C). The connections between these 3 electrodes are as follow: the applied and measured potential of the sample is measured versus the reference electrode. Then, in general terms, the electrochemical potential of the sample can be expressed as $U_S = V_{SR} - U_R - IR_{el}$, being V_{SR} the voltage between the sample or working electrode and the reference electrode, and IR_{el} the ohmic drop in the electrolyte when a current I is flowing between both electrodes through the electrolyte. The last term can be minimized just by using conductive electrolytes and by reducing the separation gap between both electrodes. Since the reference electrode is an ideally non-polarizable electrode, its electrochemical potential (U_R) will keep constant independently of the current flowing through it. It means that any change in the V_{SR} value will corresponds to a change in the U_S electrochemical potential. This is true when low currents I are being measured but for currents in the order of μA or higher, the use of a third electrode, the auxiliary electrode (U_C), is needed. When a voltage V_{SR} value is applied, the U_S is measured versus the U_R through a high impedance voltmeter to avoid the current flow, while the current is measured between the U_S and the U_C. The element used for the entire electrochemical control described above is the potentiostat.

For years, the most extensively used reference electrode was the Calomel electrode (Hg / Hg_2Cl_2 / KCl) but for sustainability during the past 10 years the Silver Chloride electrode (Ag / AgCl / KCl) became the most universal. On the other hand, a Pt wire or another inert material is commonly employed as the auxiliary electrode.

The electrochemical cell for EC-STM applications will be essentially the same, and the same components can be also found inside, however, the mechanical stability needed for EC-STM measurements require firstly, very low dimensions and secondly, a special geometry suitable for the implementation on a STM microscope head. This special design makes difficult the implementation of a real reference electrode as those described previously. For this reason, quasi-reference electrodes have been introduced in the designs of EC-STM electrochemical cells. They consists on a Pt, Pd or Pt/Ir wire immersed in the electrolyte and although their electrochemical potential is pretty unstable and electrolyte composition-dependent, they can be previously calibrated versus a standard reference electrode, also allowing an easy incorporation in the small EC-STM electrochemical cell. Although no current passes through this quasi-reference electrode, their stability is only available for some hours. Alternatively, when aqueous solutions are used, Pd-H loaded electrodes are used as reference. These electrodes are based on the H_2 / H^+ equilibrium as in the case of the universal Normal Hidrogen Electrode (NHE) [7]. In the last years, real reference electrodes are being miniaturized in order to introduce them in the EC-STM cell. Figure 3 shows a specific design of an EC-STM electrochemical cell for a commercial STM microscope head.

As we pointed in the previous section, the EC-STM tip immersed into the working electrolyte must be isolated in order to minimize the electrochemical current that will be

measured through the STM tip preamplifier. This current will also depend on the potential applied to the tip for a desired STM Bias potential, and therefore, the tip electrochemical potential (U_{tip}) have to be also controlled. Then the implementation of a bipotentiostat instead of the standard potentiostat allows an independent control of the U_S and U_{tip} versus the same reference electrode in the cell. In this configuration the STM Bias potential yields to $V_{bias} = U_S - U_{tip}$. Figure 4 presents a scheme of the final 4-electrodes configuration for a conventional EC-STM cell.

Table I. Materials and methods used for electrochemical etching of EC-STM tips.

Wire material	Electrolyte	Voltage Type
W	1-4 M KOH, NaOH	DC or AC
Au	30 % vol HCl	DC or AC
Pt (Pt/Ir)	20 % vol KCN	AC
	60 % $CaCl_2$ / 4 % HCl / 36 % H_2O	AC
	4 M NaCN / 1 M NaOH	AC

Table II. Summary of the most common methods of EC-STM tips isolation.

Material	Application	Characteristics
Apiezon wax	Wax melting + Vertical tip covering	Resistent Inert
Varnish	Dissolved varnish + Vertical tip covering	Can contaminate Easiest preparation
Electrophoretic Paint	Electrophoresis + Vertical tip thermal Annealing	Clean Lowest tip area Complex exp set up

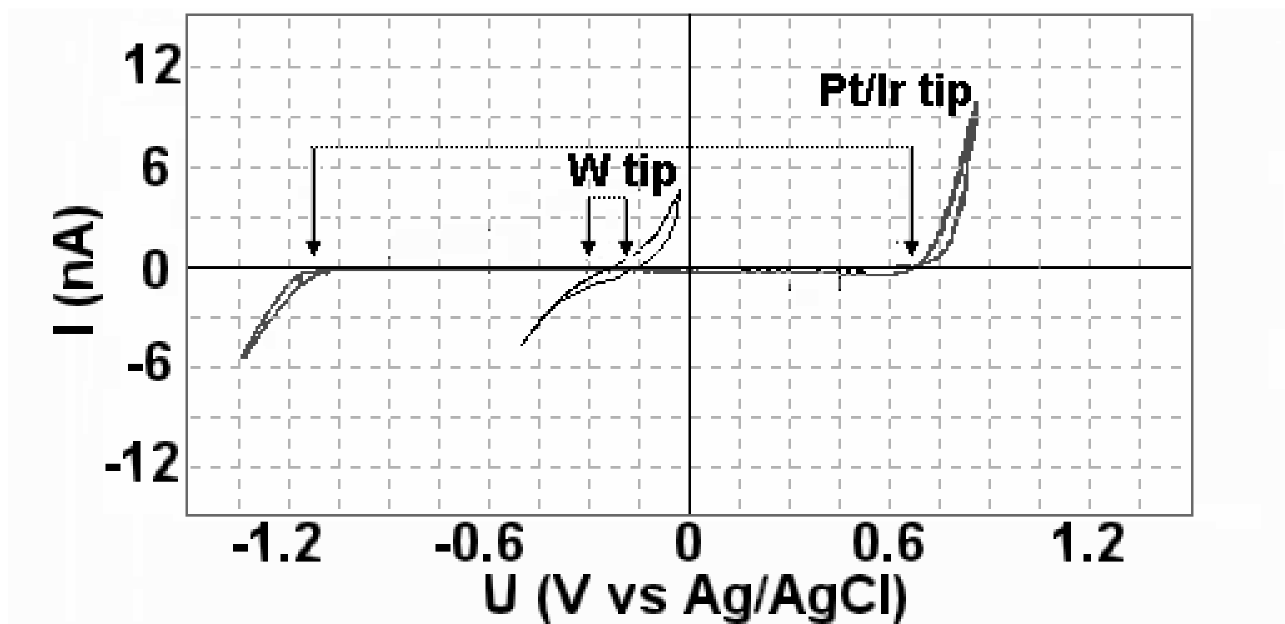

Figure 1

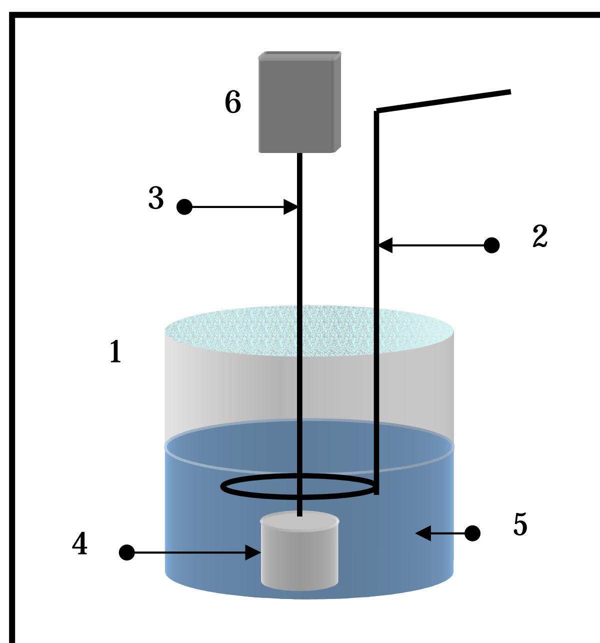

Figure 2

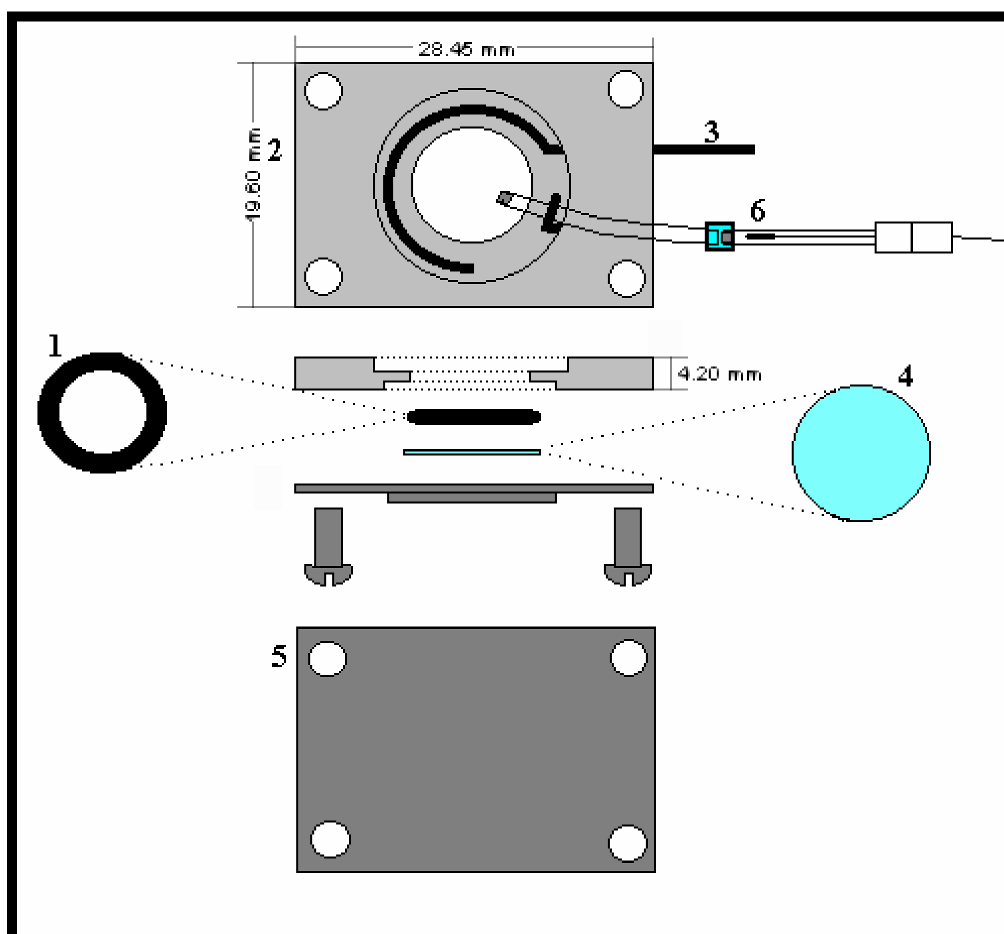

Figure 3

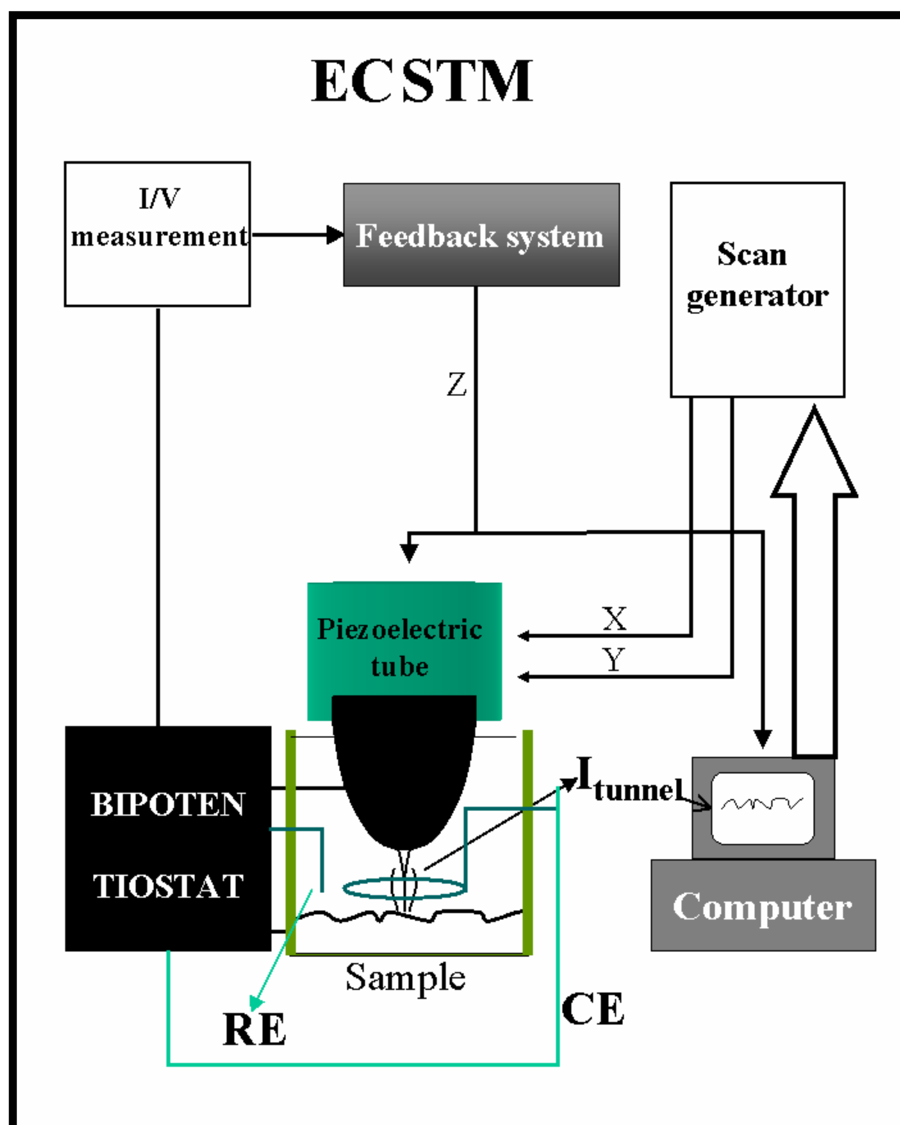

Figure 4

Figure captions

Figure 1. I/V curves for W and Pt/Ir tips inside the electrolyte recorded far from the sample surface. The arrows indicate the electrochemical potential range with just charging-discharging capacitance current contribution.

Figure 2. Scheme of an electrolytic cell designed for EC-STM tips manufacturing. (1) Pyrex glass, (2) Anode, Pt wire, (3) Cathode, tip material wire, (4) Tip holder, (5) Working electrolyte, (6) Micrometric screw.

Figure 3. Specific design of an EC-STM electrochemical cell for a commercial STM microscope head. (1) Viton O-ring, (2) Teflon cell base, (3) Auxiliary electrode Pt wire, (4) Sample working electrode, (5) Stainless steel holder plate, (6) Ag/AgCl reference electrode.

Figure 4. General scheme of a 4-electrodes configuration for a conventional EC-STM cell.

References

[1]. Mircea Fotino, *Rev.Sci. Instrum.* 64 (1) January 1993, 159-167.

[2]. R.M. Penner, M. J. Heben, T.L. Longin, N. S. Lewis, *science*, vol 250, Nov.1990, 1118-1121.

[3]. C.E.Bach, J. Nichols, W.Beckmann, H. Meyer, A. Schulte, J.O.Besenhard, P.D. Jannakoudakis, *J. Electrochem. Soc,* 140 (5) 1993, 1281 – 1984.

[4]. A. Schulte, R.H.Chow, *Analytical Chemistry*, 1996, 68, 3054 – 3058.

[5]. A. Garcia-Guell, I. Diez-Perez, P. Gorostiza, F. Sanz*, J. Electrochem. Soc*., submitted.

[6]. Colton, Engel, Frommer, Gaub, Gewirth, Guckenberger, Heckl, Parkinson, Rabe, “Procedures in Scanning Probe Microscopies”, John Wiley, Chichester, England, 1998.

[7]. John O'M. Bockris and Amulya K. N. Reddy, “Modern Electrochemistry”, Vol 1, Plenum: New York, 1998.

2.4 PREPARATION OF RELIABLE PROBES FOR ELECTROCHEMICAL TUNNELING SPECTROSCOPY

Reference: A. G. Güell, I. Díez-Pérez, P. Gorostiza and F. Sanz, *Preparation of Reliable Probes for Electrochemical Tunneling Spectroscopy* Anal. Chem. **76** (2004) 5218-5222.

© American Chemical Society, direct link access:
http://pubs.acs.org/cgi-bin/article.cgi/ancham/2004/76/i17/pdf/ac035150h.pdf

2.5 CONDUCTANCE MAPS BY ELECTROCHEMICAL TUNNELING SPECTROSCOPY TO FINGERPRINT THE ELECTRODE ELECTRONIC STRUCTURE

Reference: I. Díez-Pérez, A. G. Güell, P. Gorostiza and F. Sanz, *Electrochemical Tunneling Spectroscopy to fingerprint electrode electronic structure*, Anal. Chem. (2006) in press.

© American Chemical Society, direct link access:
http://pubs.acs.org/cgi-bin/article.cgi/ancham/2006/78/i20/pdf/ac0603330.pdf

Chapter 3

Fe passivity: electrochemistry and ECSTM

3.1 GENERAL

In this chapter, the passivation process on iron polycrystalline substrates is studied by means of electrochemical and ECSTM techniques. The aim is to go deeper into those kinetic aspects of the process that still remain unknown. Firstly, in section 3.2, CV is largely used to analyze the duplex structure formation of the Fe passive layer at different *p*Hs. The process is studied at both active and passive electrochemical ranges where the pre-passive and passive layers are respectively formed. The expected electrochemical pathways within the different electrochemical ranges are proposed, with special emphasis on how parallel chemical equilibria play on the final structure and thickness of the passive oxide layer. Farther in this section, ECSTM is employed to *in situ* follow the early stages of the pre-passive film growth in the active range. The general mechanism of the growth process is determined at the nanometer scale. Moreover, by the analysis of the ECSTM image and additional *ex situ* measurements, some new parameters like the rate of the oxide growth or the film thickness achieved are also provided.

The cathodic electrochemical reduction of the Fe passive layer is treated in section 3.3. Again, obscure aspects of this process are the main target. In short, new well-oriented Fe substrates are specially prepared for this study. Their ultra-flat surface structure produces a delay in the hydrogen electrode reaction that allows the characterization of the whole cathodic reduction of the passive layer, which appears to be hidden on polycrystalline electrodes.

The detailed results of this chapter are presented in the following publications:

- *First Stages of Electrochemical Growth of the Passive Film on Iron*, J. Electrochem. Soc., **148** (2001) B307.

- *The cathodic reduction of the iron passive film grown on ultra-flat iron thin films*, (2006) submitted to J. Phys. Chem. B.

3.2 FIRST STAGES OF THE ELECTROCHEMICAL GROWTH OF THE PASSIVE FILM ON IRON

Reference: I. Díez-Pérez, P. Gorostiza, F. Sanz and C. Müller, *First Stages of Electrochemical Growth of the Passive Film on Iron*, J. Electrochem. Soc., **148** (2001) B307.

Reprinted from the above publication, © The Electrochemical Society 2001, with permission from The Electrochemical Society.

Journal of The Electrochemical Society, **148** (8) B307-B313 (2001) B307
0013-4651/2001/148(8)/B307/7/$7.00 © The Electrochemical Society, Inc.

First Stages of Electrochemical Growth of the Passive Film on Iron

I. Díez-Pérez,* P. Gorostiza,* F. Sanz,,z and C. Müller**

Laboratory of Electrochemistry and Materials, University of Barcelona, 08028 Barcelona, Spain

The first stages of electrochemical growth of passive film on iron have been studied electrochemically by *in situ* electrochemical scanning tunneling microscopy (ECSTM). A freshly polished iron surface has been cathodically reduced in a borate buffer solution (pH 7.5) to get an oxide-free surface, and the passive film has been subsequently formed by applying short anodic potential steps. ECSTM has been used to follow the evolution of the oxide starting with growth on the surface at very negative potentials. We associate the changes observed on the surface to formation of iron hydroxides from Fe^{2+}(aq). The growth rate and film thickness have been measured from scanning tunneling microscopy images and compared with literature values. Cyclic voltammetric results obtained at pH 7.5 were compared with those in commonly used borate buffer pH 8.4. X-ray photoelectron spectroscopy measurements provide additional information about the oxidation state of the iron passive film formed potentiostatically.
© 2001 The Electrochemical Society. [DOI: 10.1149/1.1381073] All rights reserved.

Manuscript submitted June 2, 2000; revised manuscript received October 10, 2000. Available electronically June 29, 2001.

Corrosion protection of materials like steels and iron is a subject of longstanding technological interest. However, to date only a few reports have studied the process at the nanometer level.[1,2] One difficulty in making this kind of experiments on iron is the necessity for electrochemical control. In this context, a variety of new analytical tools such as scanning probe microscopy (SPM) offers new avenues of exploration. The electrochemical oxidation and reduction behavior of the passive films on iron has been extensively studied in some electrolytic media.[3-5] In particular, borate buffer solutions have been used for this purpose because it is easy to obtain a stable, reversible oxide film under potentiostatic control. Recently, a great number of studies have been focused on the chemical composition of the iron oxide film formed in the classic borate buffer solution of pH 8.4 by using a variety of techniques: electrochemistry,[6] ellipsometry,[7] *in situ* X-ray absorption near edge structures (XANES),[8,9] laser reflection,[10,11] and surface enhanced Raman spectroscopy (SERS).[12,13] All of them have been designed to work *in situ* under potentiostatic control, which allows for investigating the chemical composition of the electrochemically formed iron oxide films. Early work by Nagayama and Cohen[14] suggests that the passive film has a layered structure consisting of an inner layer of Fe_3O_4 and an outer layer of γ-Fe_2O_3. In addition, ferrous ions were found in the solution following the first stages of film formation. These suggestions are in good agreement with a recent work reported by Oblonsky and Davenport[8] who observed by *in situ* XANES a strong material loss on iron electrodes at the early potentials of passivation. In this way, the existence of Fe(II) oxides/hydroxides at the first stages of the oxide film formation has been characterized by *in situ* SERS in different electrolytic environments.[12,13] Recently, we have studied the electrodeposition of Zn in this media in order to produce highly adherent protective thin films. By using a borate buffer solution of pH 7.5,[15] the impact of the iron passive film on the initial stages of the Zn deposition mechanism was investigated. Unfortunately, no electrochemical studies of the oxidation-reduction processes on iron have been reported at this pH, apart from XANES measurements[8] on an iron electrode at pH 7.4 which indicate that stronger iron dissolution takes place in this media as compared to pH 8.4, although no changes in the final chemical composition of the oxide were observed.

Despite all the chemical information about iron passive films, morphological changes associated with oxidation-reduction processes on the iron surface in this media remain largely unexplored. Recently, an atomic force microscopy (AFM) study[16] of oxide growth formed on an iron electrode by applying oxidation-reduction cycles (ORC) to high anodic potentials was described. The authors reported that defect sites still remain on the grown iron passive film allowing localized corrosion to occur. Previous studies of iron passive film by STM[17] revealed a well-ordered phase at high anodic potentials and an arrangement of both Fe^{3+} ions and hydroxyl groups were proposed for the outermost region of the film.

In the present contribution we investigate the effect of decreasing pH upon the electrochemical response of an iron electrode and how it can influence the oxidation-reduction processes as compared to the classical borate buffer solution at pH 8.4. The surface changes observed by *in situ* STM during the first stages of iron passive film formation, that is, in the Fe(II) dissolution potential range (active-passive transition) are also presented, giving new information about the growth mechanism of iron oxide.

Experimental

Mechanically polished iron polycrystalline disks (0.3 mm thick and 10 mm in diameter) were used as working electrodes in our investigation. The polishing procedure begins with grid silicon carbide polishing papers (30, 9, 5, 3, and 1 μm particle size, successively) followed by finishing with 0.3 μm aluminum oxide powder. Between each polishing step, the iron surfaces were sonicated in Milli-Q water and ethanol. With this treatment we obtained a mirror-like surface with a roughness typically less than 2 nm in 1 μm^2 scans as measured by AFM/STM.

Electrochemical scanning tunneling microscopy (ECSTM) studies were performed using a Discoverer STM Topometrix 2010 with a DM 1000 bipotentiostat. The STM electrochemical cell was made of Teflon and exposed a sample area of 0.34 cm^2 to the solution through an O-ring. A Pt wire is used as a counter electrode, and we incorporate a true Ag/AgCl reference electrode with a double membrane to avoid chloride contamination (Modified Molecular Imaging (Phoenix, AZ, USA) Ag/AgCl electrode). All potentials presented in this work are quoted with respect to this electrode. STM tips were prepared by electrochemical etching of a Pt/Ir 80:20 wire in an acidic $CaCl_2$ solution and covered with Apiezon wax. Figure 1 shows the potential window of these Pt/Ir tips. Before each experiment the samples were thoroughly rinsed in different solvents in order to remove organic contamination from the surface, followed by a final rinse in Milli-Q water. The usual imaging conditions were a tip potential of 400 mV more positive than the sample potential and a setpoint current of 3-5 nA. All STM images were recorded in the constant current mode and at constant applied potential. The *XY* sample drift rates were controlled during the experiments.

Ex situ AFM studies were conducted in air at room temperature using an extended multimode AFM head with a Nanoscope IIIa controller. (Digital Instruments Veeco Metrology Group, Santa Barbara, CA, USA). All AFM images were performed in tapping mode

* Electrochemical Society Student Member.
** Electrochemical Society Active Member.
z E-mail: f.sanz@qf.ub.es

B308 Journal of The Electrochemical Society, **148** (8) B307-B313 (2001)

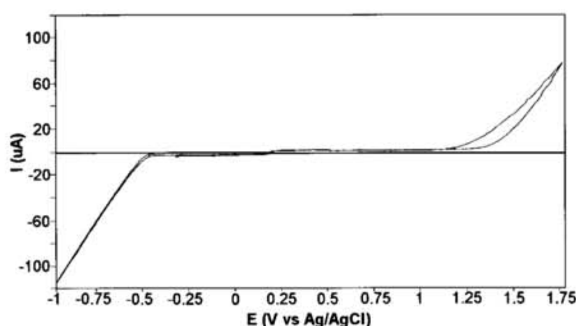

Figure 1. Cyclic voltammogram of a Pt/Ir tip in a borate buffer solution at pH 7.5. The scan rate was 5 mV/s.

with silicon cantilevers of 60 N/m spring constant (Nanosensors, Wetzlar-Blankenfeld, Germany).

A classical electrochemical study was performed with a Solartron electrochemical interface SI 1287 model with maximum ranges of ±14.5 V and ±2 A in voltage and current, respectively. Cyclic voltammetry was performed under static hydrodynamic conditions and allow us to study the electrochemical processes occurring at the pH 7.5.

The supporting electrolyte was a borate buffer solution of pH 7.5 made from 0.3 M H_3BO_3 and 0.0375 M $Na_2B_4O_7 \cdot 10H_2O$. All the solutions were made with pro analysis purity grade chemicals and Milli-Q water of 18 MΩ cm.

X-ray photoelectron spectroscopy (XPS) measurements were carried out using a Perkin-Elmer PHI 5500 model. The samples were excited with an Al kα source which provides an energy resolution of 0.42 eV. An Ar^+ ion gun was used to acquire depth profiles of the iron samples. All samples to be studied by XPS were freshly prepared, dried with N_2, and transferred to the ultrahigh vacuum chamber.

Results and Discussion

Cyclic voltammetric study.—Figure 2 compares the cyclic voltammograms of iron substrate in borate buffer solutions at pH 8.4 and 7.5. Clear differences are observed, although the peaks can be assigned to the corresponding oxidation-reduction processes on the iron surface. An important current increase in the active-passive region (peak I in Fig. 2) is registered at pH 7.5. This correlates well with the previous XANES measurements at this pH,[8] where a strong

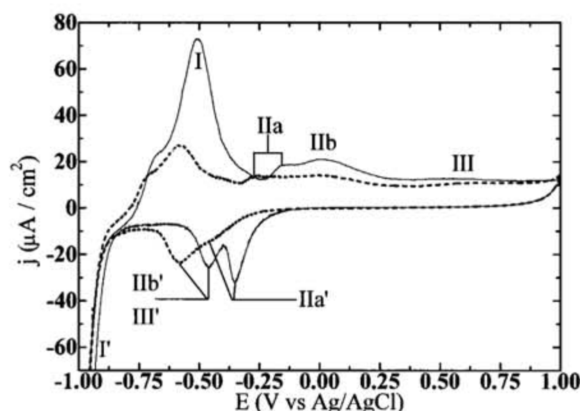

Figure 2. Cyclic voltammograms of an iron electrode in a borate buffer solution at pH 7.5 (——) and 8.4 (– – –). Scan rate was 5 mV/s.

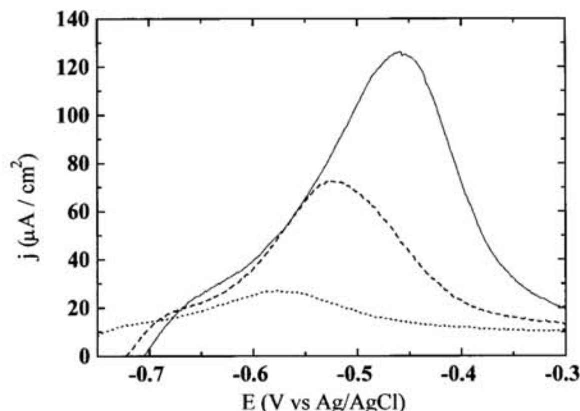

Figure 3. Evolution of the so-called anodic peak I in Fig. 2 as a function of different pH: 8.4 (· · · ·), 7.5 (– – –), and 7 (——).

material loss from iron electrodes was registered at early potentials of passivation, so a higher dissolution rate of Fe(II) at this pH is expected against pH 8.4. The processes that take place in this potential range, are described by Eq. 1 and 2

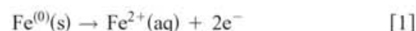

$$Fe^{(0)}(s) \rightarrow Fe^{2+}(aq) + 2e^- \quad [1]$$

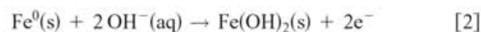

$$Fe^0(s) + 2\,OH^-(aq) \rightarrow Fe(OH)_2(s) + 2e^- \quad [2]$$

Bardwell and MacDougall[18] suggested that in this potential range, it takes significantly more time of anodization for the passive film to reach a "well-formed" state through which Fe^{2+} ions cannot be transported. That was clearly observed in the *in situ* STM study presented below and how that fact can influence the final film thickness.

Still lowering the pH value (curve at pH 7 in Fig. 3), cyclic voltammograms show a further increase in the iron dissolution rate. The processes involved in peak I are discussed in more detail in the ECSTM study section.

The subsequent oxidation process (peak IIa in Fig. 2) and the corresponding reduction process (peak IIa′) have been reported[10] as an iron(III) hydroxide formation on the surface described by the heterogeneous reaction in Eq. 3

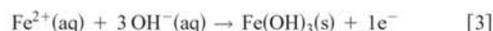

$$Fe^{2+}(aq) + 3\,OH^-(aq) \rightarrow Fe(OH)_3(s) + 1e^- \quad [3]$$

At pH 7.5 (see Fig. 2), a clear current increase of both peaks IIa and IIa′ have been registered. This indicates a higher concentration of $Fe^{2+}(aq)$ nearby the electrode, induced by the lower OH^- anion concentration, with respect to the classical pH 8.4. Thus, the $Fe^{2+}(aq)$ oxidizes to $Fe^{3+}(aq)$ and precipitates as hydroxide (see Eq. 3) because of its low solubility product[19] $\{K_{sp}[Fe(OH)_3] = 1.58 \cdot 10^{-39}\}$. This $Fe^{2+}(aq)$ is generated in the previous process (peak I), as it has already been reported,[8,20] and accumulates progressively in each oxidation-reduction cycle. This process was also observed at pH 8.4 as a progressive current increase of peaks IIa and IIa′ after each electrochemical cycle (see Fig. 4). This, of course, will produce an increase in the iron film thickness.[10] Larger reduction times at the cathodic potential of -0.97 V[6] are needed to reduce all iron to metallic Fe^0.

The broad peak IIb (and its associated reduction peak IIb′) corresponds to the oxidation of the iron(II) oxide/hydroxide layer formed on first stages of passivation, to an Fe(II)/Fe(III) oxide film,[6,12] as described by Eq. 4

Journal of The Electrochemical Society, 148 (8) B307-B313 (2001) B309

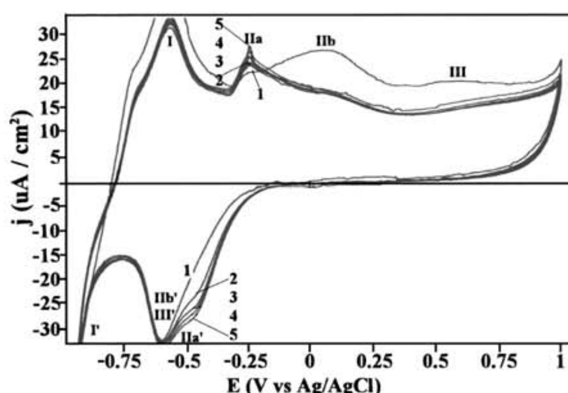

Figure 4. Consecutive cyclic voltammograms of an iron electrode in a borate buffer solution at pH 8.4. Scan rate, 5 mV/s.

$$5FeO(s) + 2H_2O \rightarrow Fe_3O_4/Fe_2O_3(s) + 4H^+(aq) + 4e^- \quad [4]$$

The final composition of this iron oxide film at anodic potentials of $+0.3\ V < E < +1\ V$, current plateau III in Fig. 2, has been determined by XANES measurements[8] and contains mostly Fe^{3+} ions with around 7% of Fe^{2+}, depending slightly on the applied potential. Such anodic oxide films present remarkable semiconducting properties,[10] which have been compared with sputter-deposited iron oxides.[22] An important current increase of peaks IIb and IIb′ is observed at pH 7.5 in Fig. 2, so a thicker film is formed here at early potentials of passivation (peak I) as compared to pH 8.4.[10]

The oxidation-reduction processes corresponding to peaks IIa, IIa′, and IIb′ exhibit a clear shift of +0.11 V in their potential position at pH 7.5, with respect to pH 8.4. Taking a value of $1.26 \cdot 10^{-15}$ for the $Fe(OH)_2(s)$ solubility product,[19] a decrease of $OH^-(aq)$ concentration in one order of magnitude corresponds to an increase of $Fe^{2+}(aq)$ concentration in two orders of magnitude. This $Fe^{2+}(aq)$ concentration change generates a variation of +0.11 V in the Nernst potential, which coincides with the potential increase measured for this oxidation-reduction processes. For this reason, and because borate anion concentration was almost constant for all pH buffers, because only the boric concentration is varied, we assign this potential shift to the pH change and not to the borate anion concentration, as it was suggested elsewhere.[8]

Consecutive cyclic voltammograms presented in Fig. 5 show that the peaks of the redox processes at pH 7.5, are the same as those observed above for pH 8.4 (Fig. 4). In cycles 1 to 8, the upper potential vertex has been increased progressively. It is observed that achieving the peak of an oxidation process, its corresponding reduction peak appears through the cathodic scan. A point that should be highlighted here is the current growth of peak IIb′ in cycles 6, 7, and 8, which means that a weak oxidation of Fe(II) to Fe(III) takes place through the current plateau III (see Fig. 5). These two well-defined peaks in the cathodic scan indicates the bilayered nature of the final iron passive films, composed by an inner layer of Fe(II)/Fe(III) oxide (corresponding to peak IIb′) and an outer layer of hydrated Fe(III) hydroxide (peak IIa′). This structure is the same as the one proposed for classical pH 8.4, although a clear increase in the thickness of both layers is observed at pH 7.5.

Ex situ XPS measurements.—Figure 6 shows two depth profiles of the XPS iron signal of a native iron passive film (Fig. 6a) and of an iron passive film formed in a borate buffer solution at pH 7.5 by applying an anodic potential step from the metallic iron region to 0.8 V for 15 min (Fig. 6b). The XPS Fe signal consists of a doublet corresponding to $2p_{1/2}$, $2p_{3/2}$ electronic states (13.1 eV separation between the peaks). Both peaks exhibit a clear shift depending on

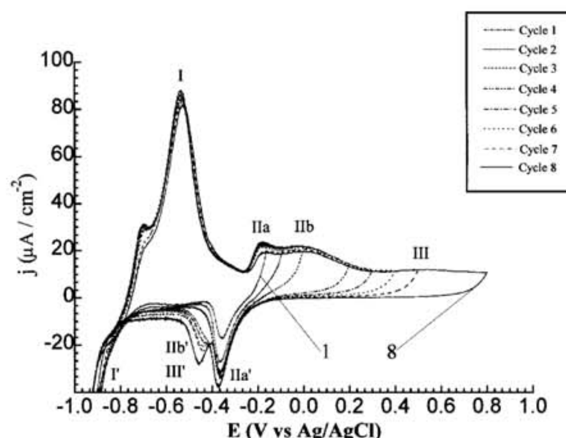

Figure 5. Consecutive cyclic voltammograms of iron in a borate buffer solution of pH 7.5. From cycles 1 to 8, the upper limit potential was increased progressively: cycle (1) −0.16, (2) −0.09, (3) 0, (4) 0.2, (5) 0.3, (6) 0.4, (7) 0.5, and (8) 0.8 V.

the oxidation state for Fe, labeled in Fig. 6b. Since the nature of passive film on iron can change its composition when it is removed from the cell, these results must be interpreted carefully. However, some interesting points can be analyzed from XPS data. A clear lowering of the iron valence through the oxide film until metallic iron is observed because the Fe 2p electron energy of the XPS spectra changes with each sputtering cycle (see Fig. 6b). Therefore, an Fe(III) oxide layer will be expected in the outermost region of the passive film; this is in good agreement with the electrochemical results.

A thicker oxide film exists in the case of the electrochemically formed film, since one more sputtering cycle is needed to remove it completely. The final thickness of the electrochemically formed oxide film was previously evaluated by the galvanostatic cathodic polarization method[11] and resulted in 3.1 nm, which is practically the same as the passive film formed in borate buffer at pH 8.4[10,11] at the same potential. Therefore, assuming from the XPS results that the electrochemical film is twice the thickness of the air-formed film, we estimated the thickness of the air-borne oxide film as less than 2 nm.

ECSTM study.—In Fig. 7, two STM images of a freshly polished iron surface in air and in borate buffer solution pH 7.5, respectively,

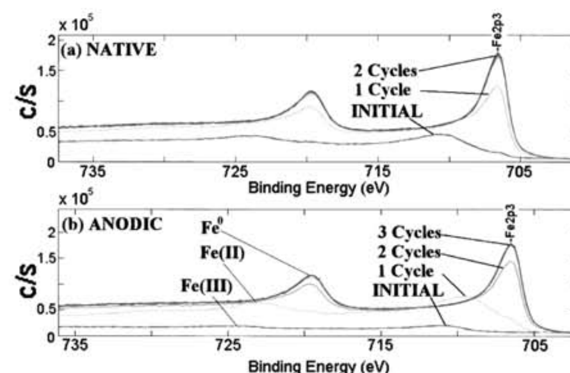

Figure 6. Depth profiles of the XPS signal of iron surface (a) freshly polished and (b) polished and oxidized electrochemically in a borate buffer solution at pH 7.5.

B310 Journal of The Electrochemical Society, 148 (8) B307-B313 (2001)

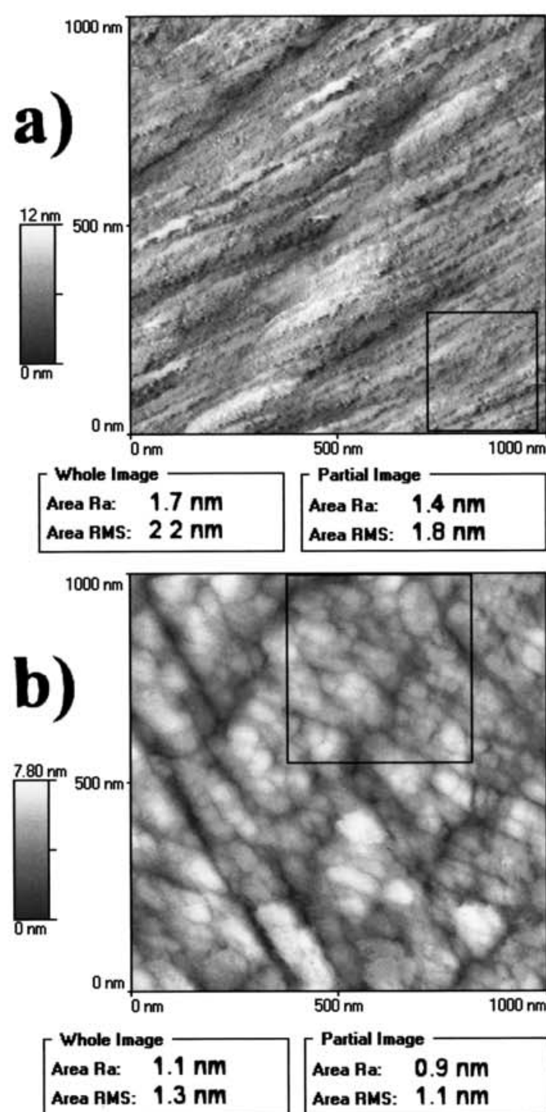

Figure 7. STM images of freshly polished iron surfaces (a) in air and (b) in a borate buffer solution of pH 7.5 at potential of +100 mV, where no faradaic current was registered.

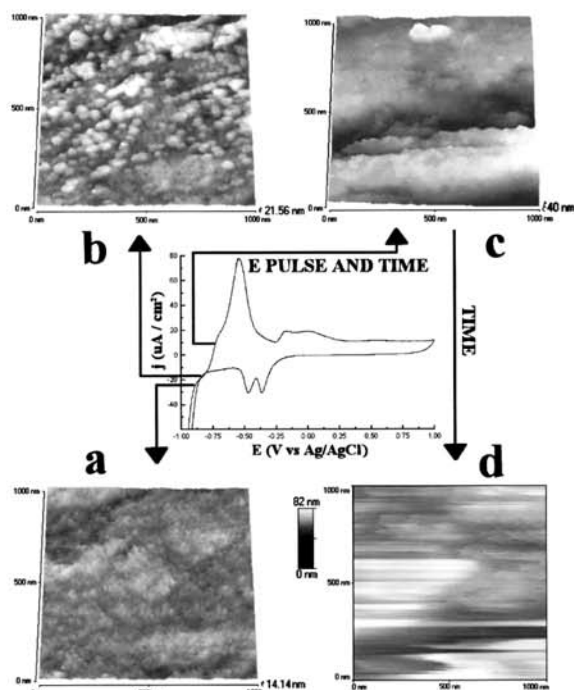

Figure 8. STM images of the same scanned area (1 μm^2) of an iron electrode at several stepped potentials in a borate buffer solution of pH 7.5: (a) −880, (b) −800, and (c) and (d) −700 mV. A cyclic voltammogram of the electrode in the same solution has also been inserted in order to visualize the electrochemical region under study.

are presented. Both morphologies are very similar presenting some scratches across the images because of the previous mechanical polishing. These scratches were clearly observed at larger scans. The average roughness achieved at scans of 1 × 1 μm was less than 2 nm as indicated in the same figure.

Figure 8 shows the morphology of an iron electrode surface in borate buffer pH 7.5 at different potentials in the active-passive region (see the voltammogram in Fig. 8). Image 8a shows the iron surface at −880 mV after setting the potential to −1 V for 30 min so that all the iron oxide film was reduced to Fe^0. In the potential range from −1 to −880 mV, no changes in the topography were registered, although some occasional instabilities in the tunneling current were observed at more cathodic potentials, due to hydrogen bubbles. Therefore, this surface corresponds to the topography of oxide-free iron with an average roughness of 1.5 nm, very similar to that measured for native oxide films (Fig. 7). It indicates the very low thickness of the oxide film formed on air as obtained by XPS measurements, so the average roughness at this large scan does not really change in the presence of the oxide. A short potential step from −880 to −800 mV produced the beginning of the iron dissolution followed by a quick nucleation process observed all over the surface (image 8b). These nuclei presented heights between 6 and 7 nm. Note that this process occurs under cathodic current flow, so a current component of the hydrogen evolution reaction still exists when iron oxidation starts. As was discussed in the cyclic voltammetry section, the first oxidation of Fe^0 to Fe(II) starts at this potential, so we associate this nucleation with the formation of $Fe(OH)_2(s)$ on the iron surface according to the equilibrium given by Eq. 2. However, at this pH 7.5 and according to the value of the equilibrium constant[19] [$K_{sp}(Fe(OH)_2) = 1.26 \cdot 10^{-15}$], a concentration around 10^{-2} M $Fe^{2+}(aq)$ will exist in solution near the iron surface and will precipitate at more anodic potentials (peak IIa) as was described in the cyclic voltammetry section.

In order to follow the evolution of this Fe(II) hydroxide completely, we increased the sample potential from −800 to −700 mV, where it was observed that the hydroxide film grows until it covers the whole surface (image 8c). In addition, the oxidation rate was relatively slow at this potential and allowed us to follow the evolution by STM in real time (Fig. 9). At this point, it is important to highlight that tunneling through a Fe(II) oxide layer has been reported previously,[21] although the corresponding mechanism is not fully understood at present. Image 9a is the same image as 8b. The registered sample current at this image was still highly cathodic, which indicates that the hydrogen evolution reaction has not finished and iron oxidation rate is still very low. As sample potential was stepped to −700 mV (image 9b), Fe(II) hydroxide nuclei start to

Journal of The Electrochemical Society, 148 (8) B307-B313 (2001) B311

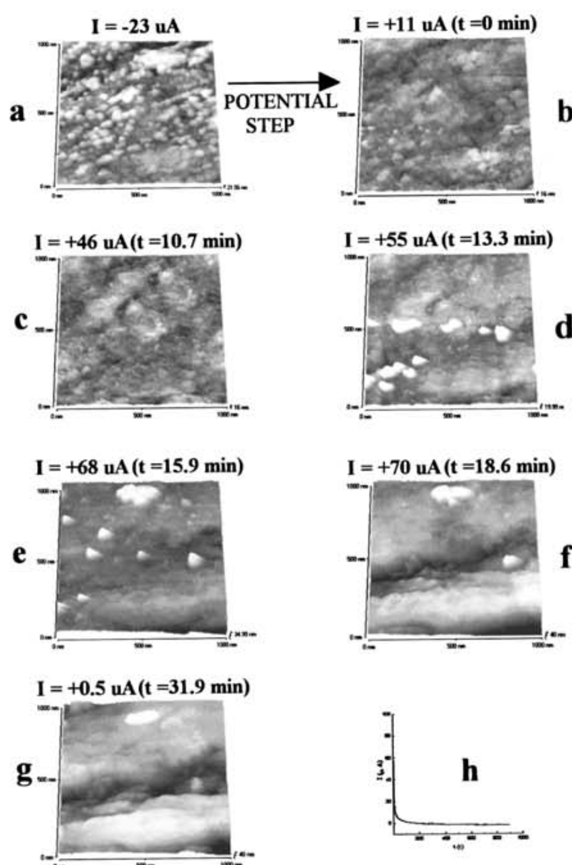

Figure 9. STM image of real-time sequence of the same scanned area of the iron surface in borate buffer at pH 7.5. The sample potential was stepped from −800 mV (image a) to −700 mV (images b-g). Time and current are shown on top of each image. Curve (h) corresponds to a *I vs. t* transient at an applied constant potential of −700 mV.

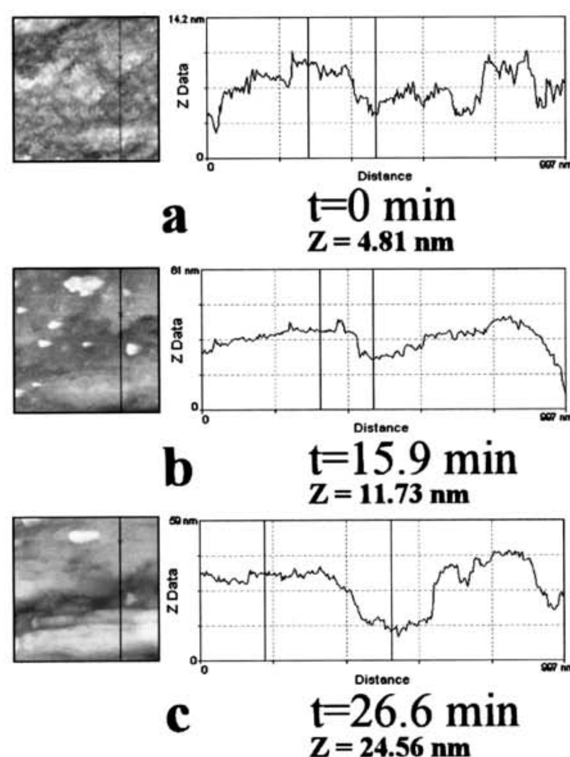

Figure 10. Topographical section of the previous STM images 9a, 9e, and $9f_2$ (not included in Fig. 9). Height of hydroxide film has been measured at different times: (a) 0, (b) 15.9, and (c) 26.6 min.

coalesce because of lateral growth. The sample current becomes anodic (see on top of the STM images in Fig. 9), which indicates a sharp increase in the iron oxidation rate. The initial hydroxide nuclei have almost completely coalesced in 11 min (see image 9c). This is followed by nucleation of a different structure as shown in the next image, 9d. This change from "two-dimensional" to three-dimensional growth of the film indicates that the coated surface is still incompletely passivated at this stage and iron continues to dissolve and precipitate at those sites where the surface was not well covered or had a higher number of defects. Figure 9e shows how new nuclei appear on the surface and are again covered until a homogeneous oxide film is once again observed (images 9f and g). Obviously, in the images 9d and e the frequency of nucleation is now lower than that observed at image 9a. This well-formed film (image 9g) is followed by a fall in the current to a value close to zero, which indicates that the passivation of the iron surface has been achieved. At this point, instabilities in the tunneling current started to appear, producing poor imaging conditions (see image 8d) and indicating the low conductivity of such oxide film.

A detailed analysis of the images allows the thickness and the growth rate of this iron hydroxide film to be evaluated. Figure 10 shows topographic profiles of the same section taken from some images in Fig. 9. As we have previously observed by *ex situ* AFM (see Fig. 11), the anodic oxide layer grows preferentially on scratch-free areas of the surface, as can be also observed in the *in situ* STM images (upper and lower halves of Fig. 10c). In contrast, it seems clear that hydroxide film growth is practically nonexistent at certain surface defects. Taking the cross section in image 10a as a reference, because it corresponds to the morphology of the oxide-free iron surface, we measured a final thickness of 20 nm. To corroborate that this thickness is not due to an artifact of the STM image, we covered a half of an iron electrode with an Apiezon mask and grew the oxide film on the uncovered part of the electrode in contact with the solution. This electrochemical growth of the film was made under the same electrochemical conditions as those used in the previous *in situ* STM experiment. Next, the mask was dissolved in an Ar-bubbled trichloroethylene solution and then dried under nitrogen atmosphere. Then, the height of the oxide film was measured by *ex situ* AFM taking the covered part of the electrode as the reference plane. The value measured this way was between 16 and 18 nm (see Fig. 12). Taking into account that the air-borne oxide was not reduced from the covered part of the electrode, the real thickness of the film will be around 2 nm thicker than the thickness to measured here (see XPS measurements section), so it is quite consistent with the value obtained previously by *in situ* STM. This value is much higher than that measured from laser reflectance techniques[10] for an electrochemical iron oxide film formed at pH 8.4 by simply scanning the sample potential to high anodic values. In the previous electrochemical study at pH 7.5 also scanning the potential, we observed that a thickness value of 4.1 nm, as estimated by integration of cathodic peaks IIa′ and IIb′ in Fig. 2 (2.4 mC/cm^2 at pH 7.5), is much lower than that obtain by a constant potential experiment. So it seems clear that the final thickness of the iron oxide film depends strongly on the electrochemical potential sequence applied on the iron sample to grow it up.

B312 Journal of The Electrochemical Society, 148 (8) B307-B313 (2001)

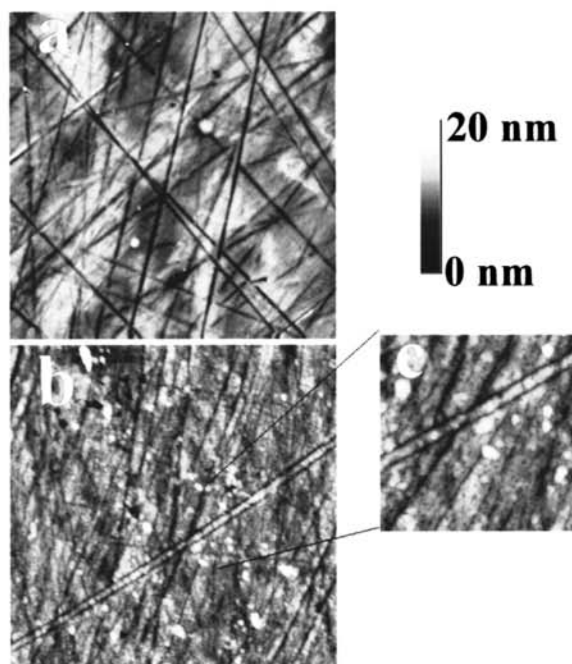

Figure 11. *Ex situ* AFM images: (a) 5 × 5 μm image of a freshly polished iron surface, (b) 5 × 5 μm image of an iron oxide surface electrochemically grown in borate buffer solution of pH 7.5 by stepping the potential from −1 to +0.9 V (passive region) where the electrode was kept for 15 mins, (c) 1.7 × 1.7 μm image of a zoomed area of image b.

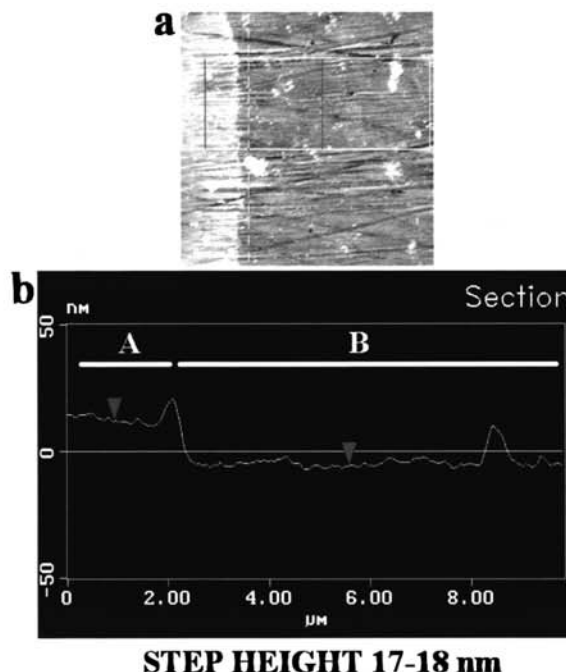

Figure 12. (a) 10 × 10 μm *ex situ* AFM image. The lighter left part of the image corresponds to the uncovered part of the electrode during the film formation process. Maximum *Z* range, 50 nm. (b) Averaged topographical section taken from the square in image 12a. A and B in the profile correspond to uncovered and covered part of the electrode surface, respectively.

By taking all topographical profiles of the images in Fig. 9, we have calculated a value of 0.74 nm/min for the iron hydroxide growth rate during the first stages of passivation at this potential.

In Fig. 13 a schematic model of the iron hydroxide growth has been represented. Figure 13a represents the high energy sites on the surface where the oxidation starts at lower potentials. Figure 13b shows the global or generalized surface oxidation at higher potentials in the peak I region (active-passive region). At more positive potentials than −0.4 V, iron(III) oxidation processes are involved. When a complete hydroxide layer is formed (diagram d), the anodic current drops to practically zero, indicating the passivation of the iron electrode.

Conclusions

The electrochemical results for the iron oxide film formation in borate buffer solution at pH 7.5 reveal some differences with respect to the pH 8.4 solution. These differences are attributed exclusively to pH change and not to the anionic concentration, in contrast to reports for phosphate media where anions play an important role in the passive film formation.[20] At lower pH, a higher dissolution rate of Fe^{2+}(aq) is observed.

No changes in composition have been reported for the iron oxide films formed at pH 7.5[8] as compared to pH 8.4, although a clear increase in the final thickness of the iron oxide film is deduced from the voltammetric study performed under the same electrochemical conditions. A bilayered structure is observed for the oxide film grown under these conditions.

Morphological evolution during the first stages of the iron passive film formation has been followed by *in situ* STM. From the analysis of STM images, we propose a mechanism of ion Fe^{2+} dissolution and iron(II) hydroxides formation on the iron surface at early potentials of passivation. This process begins at very low iron

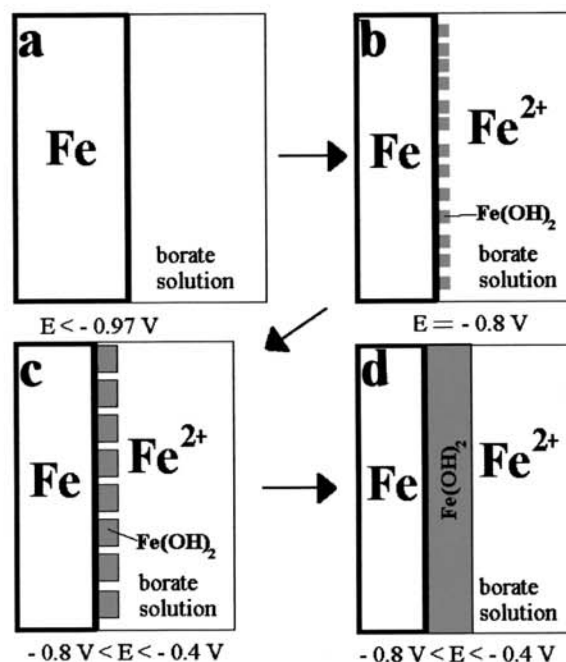

Figure 13. Schematic model of iron(II) hydroxide film growth.

Journal of The Electrochemical Society, **148** (8) B307-B313 (2001) B313

oxidation potentials. Rapid nucleation indicates that the iron cation concentration near the most active sites will be over the saturation point at this pH, so Fe(II) hydroxide is formed. Iron dissolution and formation of its corresponding hydroxide is able to proceed over the whole surface at higher potentials in the active-passive region. This process continues until all the surface is covered, thus producing effective protection of the iron electrode. These results show that passivation of the iron surface can be achieved at early cathodic potentials just by allowing the Fe^0 to Fe^{2+} oxidation process to be completely finished. In this case, the measured thickness in the STM images was much higher than that obtained for passive film formed by scanning the potential at a given speed.

Further investigations about topographic changes over the active-passive region of iron passive film and about how it can be related to its semiconducting properties, are being performed in our laboratory.

Acknowledgments

The authors are grateful to J. C. Ferrer for the XPS measurements and to "Serveis cientifico-tècnics" of the University of Barcelona for the technical assistance. Financial support of the present work comes from the CYCIT under research project MAT 97-0379.

The University of Barcelona assisted in meeting the publication costs of this article.

References

1. A. R. Despic and M. G. Pavlovic, *Electrochim. Acta,* **27**, 11 (1982).
2. M. Nakamura, A. Aratama, A. Yamagishi, and M. Taniguchi, *J. Electroanal. Chem.,* **446**, 227 (1998).
3. J. Benzakour and A. Derja, *J. Electroanal. Chem.,* **437**, 119 (1997).
4. O. Khaselev and J. M. Sykes, *Electrochim. Acta,* **42**, 2333 (1997).
5. R. C. Bhardwaj, A. González-Martin, and J. O'M. Bockris, *J. Electrochem. Soc.,* **138**, 1901 (1991).
6. V. Jovancicevic, R. C. Kainthla, Z. Tang, B. Yang, and J. O'M. Bockris, *Langmuir,* **3**, 388 (1987).
7. F. C. Ho and J. L. Ord, *J. Electrochem. Soc.,* **119**, 139 (1972).
8. L. J. Oblonsky, A. J. Davenport, M. P. Ryan, H. S. Isaacs, and R. C. Newman, *J. Electrochem. Soc.,* **144**, 2398 (1997).
9. P. Schmuki and S. Virtanen, *Electrochem. Soc. Interface,* **6**(2), 38 (1997).
10. M. Büchler, P. Schmuki, and H. Böhni, *J. Electrochem. Soc.,* **145**, 609 (1998).
11. M. Büchler, P. Schmuki, and H. Böhni, *J. Electrochem. Soc.,* **144**, 2307 (1997).
12. J. C. Rubim, *J. Electrochem. Soc.,* **140**, 1601 (1993).
13. J. Gui and T. M. Devine, *J. Electrochem. Soc.,* **138**, 1376 (1991).
14. M. Nagayama and M. Cohen, *J. Electrochem. Soc.,* **109**, 781 (1962).
15. I. Díez-Pérez, P. Gorostiza, F. Sanz, and C. Müller, To be published.
16. J. Li and D. J. Meier, *J. Electroanal. Chem.,* **454**, 53 (1998).
17. M. P. Ryan, R. C. Newman, and G. E. Thompson, *J. Electrochem. Soc.,* **142**, L177 (1995).
18. J. A. Bardwell and B. MacDoudall, *J. Electrochem. Soc.,* **135**, 2157 (1988).
19. R. M. Smith and A. E. Martell, *Critical Stability Constants*, Vol. 4, Plenum, New York (1976).
20. S. Virtanen, P. Schmuki, M. Büchler, and H. S. Isaacs, *J. Electrochem. Soc.,* **146**, 4087 (1999).
21. A. Schreyer, L. Eng, and H. Böhni, *J. Vac. Sci. Technol. B,* **14**, 1162 (1996).
22. M. Büchler, P. Schmuki, H. Böhni, T. Stenberg, and T. Mäntylä, *J. Electrochem. Soc.,* **145**, 378 (1998).

3.3 THE CATHODIC REDUCTION OF THE IRON PASSIVE FILM GROWN ON UNTRA-FLAT IRON THIN FILMS

Reference: I. Díez-Pérez, P. Gorostiza, M.-C. Bernard, P. Allongue and F. Sanz, *The Cathodic Reduction of the Iron Passive Film Grown on Ultra-Flat Iron Thin Films*, (2006), submitted to J. Phys. Chem. B.

THE CATHODIC REDUCTION OF THE IRON PASSIVE FILM GROWN ON UNTRA-FLAT IRON THIN FILMS.

I. Díez-Pérez[a,b], P. Gorostiza[a], M.-C. Bernard[b], P. Allongue[b,*], F. Sanz[a,+]

[a]*Laboratory of electrochemistry and materials (LCTEM), University of Barcelona, Martí i Franquès 1, 08028 Barcelona, Spain*

[b]*Laboratoire de Physique de la Matière Condensée, CNRS - UMR 7643, Ecole Polytechnique, 91128 Palaiseau, France*

Abstract

Low-roughness epitaxial Fe thin films on Au(111) surfaces have been used as a model Fe substrate to study the cathodic processes of the passive film on Fe by means of electrochemical techniques and Rutherford Back Scattering (RBS). After passivation of the surface at +0.6 V/Ag/AgCl, negative going scans of potential reveal a new reduction process that is not observable with anodic films grown on polycrystalline iron. This reported cathodic peak occurring at –1.0 V is related to the last reduction process Fe(II) $\rightarrow$ Fe(0). A detailed study of this feature as a function of solution pH, solution stirring, passivation potential and time is performed. Upon this process is presented and discussed in terms of the bilayer model of the iron passive film. Understanding the process occurring at the electrode allows full control on the experimental conditions to obtain a desired oxide bilayer structure. Rutherford Back Scattering (RBS) measurements were also performed to quantitatively determine mass losses upon passivation/depassivation cycles, which allow us to analyze the Fe dissolution kinetics in the different electrolytic media. Considerations of the Fe passive film bilayer structure on the electronic properties of the whole passive layer will be done.

* Permanent address: Laboratoire de Physique de la Matière Condensée (UMR CNRS 7643), Ecole Polytechnique, F-91128 Palaiseau (France).

+ Correspoding author: f.sanz@qf.ub.es

Introduction

The growth mechanism, structure, chemical composition of the passive film on iron have been investigated for several decades[1,2,3]. The final goal of these studies is to understand the corrosion mechanism on Fe and Fe-based materials, and to gain *know how* in their efficient corrosion protection. In this sense, the electrochemical formation and reduction behavior of passive films on iron has been extensively studied in some electrolytic media[4-6], in particular borate buffer solutions where it is easy to obtain a stable, reversible oxide film under potentiostatic control. Recent studies have been focused on the chemical composition of the iron oxide film grown on polycrystalline iron in the classical borate buffer solution of pH 8.4 by using a variety of techniques: electrochemistry[7], ellipsometry[8], *in situ* XANES[9,10], laser reflection[11,12] and SERS[13,14]. All of them have been designed to work *in situ* under potentiostatic control. In most of these studies, rough polycrystalline Fe surfaces have been used, since they constitutes similar systems than those employed on industrial applications. To get a more fundamental view of the oxidation-reduction processes on the Fe passive film, more ordered, better controlled surfaces should be required. In this way, electrochemical and spectroscopic information on Fe single crystal or well-defined thin iron layers are scarcely available[15-17].

As the general structure of the Fe passive film, Nagayama and Cohen[2] early suggests that the anodic oxide presents a bilayer structure consisting of an inner Fe_3O_4 layer and an outer layer made of γ-Fe_2O_3. On the other hand, ferrous ions were found in the solution following the first stages of iron passive film formation. These conclusions agree with the recent work reported by L. J. Oblonsky and A. J. Davenport[9] who observed by *in situ* XANES a strong material loss on iron electrodes at the early potentials of passivation. In this sense, the existence of Fe(II) oxides/hydroxides at the first stages of the oxide film formation has been characterized by *in situ* SERS in different electrolytic environments[13,14].

To avoid the preparation of an iron single crystal electrode, we propose a new strategy based on the use of well defined electrodeposited epitaxial Fe(110)/Au(111) thin films[18] as a model substrate. Such films, primarily grown for magnetic purpose, prove to be very useful to investigate the reduction mechanism of the iron passive layer. In fact, after anodic oxidation of the iron deposit at +0.6 V in borate buffer solution, a new cathodic process is observed at –1.0 V upon scanning the potential towards negative values. This peak is not observed with polycrystalline iron for it merges with the hydrogen evolution reaction (HER). The relation of this peak with the overall structure of the Fe passive film, together with the oxide film dissolution kinetics studied by electrochemical and RBS measurement, are presented. As a result, a more detailed and completed model of the Fe passive film cathodic reduction in borate media at nearly-neutral pHs is proposed.

Experimental

• *Electrodes* : Fe/Au(111) electrodes, hereafter designated as Fe thin film electrodes, were obtained by electrodepositing iron on 80 nm-thick Au films evaporated on mica substrates. Highly textured Au(111) films were obtained using evaporation conditions (substrate temperature 300°C, deposition rate 3-5 Å/s). After flame annealing Au films consist in large flat top grains on the µm-scale. On the atomic scale the reconstruction of the Au(111) surface is visible by STM[18]**.** Iron thin films were electro-deposited onto freshly fame annealed Au(111) substrates at –1.2 V/AgAgCl from a 1 mM $FeSO_4$ solution in 10^{-2} M K_2SO_4 + 10^{-4} M KCl + 10^{-3} M H_2SO_4[18]. Films grow epitaxially as seen by *in situ* STM[18]. The first 2-3 ML consist in γ-Fe(111) but deposits thicker than 5 ML consist in bcc Fe with a (110) texture as derived from EXAFS and XRD. Left image in figure 1 shows a large scale AFM image of a 60 ML thick film. The grain structure with flat tops of ca 500 nm in width is typical of polycrystalline Au(111) films evaporated on mica. Zooming (right image in Fig. 1) reveals that the iron layer is very smooth with a rms of 0.29 nm measured on the top of gold grains. This smoothness is consistent with epitaxial growth[18]. Such sample will be referred to as Fe/Au or Fe(*N*)/Au sample in the following, with *N* the initial iron thickness expressed in ML.

Polycrystalline iron samples (99.99 %), hereafter designated as poly-Fe electrodes, were mechanically polished disks 10 mm in diameter. Mechanical polishing was performed down to 0.3 µm alumina to obtain a mirror finish of the surface. Prior to each experiment the samples were thoroughly rinsed in different solvents (trichlorethilene, acetone, ethanol successively) to remove organic contamination. A final rinse with Milli-Q water was then performed. The mean rms of such substrates was typically < 2 nm[19].

• *AFM observations* : *ex situ* imaging was conducted in air at room temperature using an Extended Multimode AFM head with a Nanoscope IIIa controller (Digital Instruments, Veeco Metrology Group, Santa Barbara, California, USA). All AFM images were acquired in tapping mode using silicon cantilevers (spring constant 60 N/m) purchased from Nanosensors (Wetzlar-Blankenfeld, Germany).

• *Electrochemical measurements* : we used a conventional three electrode electrochemical cell made of Teflon connected to a computer controlled potentiostat PGSTAT12 Autolab (Eco Chemie, Utrecht, The Netherlands). A Pt wire served as counter electrode and a Mercury Saturated Sulfate Electrode (MSE) or a Ag/AgCl as reference electrode. In the following all potentials are quoted against Ag/AgCl. The sample holder exposed a sample area of 0.2 cm^2 through a Viton O-ring. Unless otherwise specified, all measurements were performed under static hydrodynamic conditions and the electrolyte volume was fixed to 20 ml. Dissolved oxygen was removed from the solution by bubbling nitrogen prior to measurements.

•*Solutions* : Buffer solutions of different pH (7.5, 8.4 and 9.2) were prepared by mixing different concentrations of H_3BO_3 and $Na_2B_4O_7{\cdot}10\ H_2O$ and keeping the ionic strength of all solutions to 0.3 M. The solution of pH 12.2 was prepared from a 10^{-2} M of NaOH. All the solutions were made with pro analysis purity grade chemicals (Merck, Germany) and Milli-Q

water of 18 MΩ·cm. The pH was measured using a calibrated pH-meter from Metrohm (Herisan, Switzerland).

• *Rutherford Back Scattering (RBS)* : The surface density of iron atoms on the Au/mica substrates (D_{Fe}) was measured using Rutherford backscattering (RBS) with the 2 MeV Van de Graaf accelerator at the Groupe de Physique des Solides (University Paris 7). The backscattered alpha particles were detected at 165° off the incident beam with a silicon detector. The method may detect much less than an equivalent monolayer of iron. The conversion between Fe counts obtained directly from the Fe RBS peak integration and the Fe atomic surface density is made through a Bi/Si reference sample with a perfectly known surface density, and taking into account a value of 0.09910 for the effective section ratio of the Fe/Bi system. Fe/Au sample used for RBS analysis were 10 and 15 ML thick deposits to optimize sensitivity. Half of the sample was kept as reference sample (density D_{Fe}^0) while the other half was used for oxidation / reduction experiments. The difference $\Delta = D_{Fe}^0 - D_{Fe}$ measures the total amount of Fe atoms eventually lost per passivation / reduction cycle. Before RBS measurements, the sample was kept under N_2 atmosphere in order to avoid further Fe oxidation and/or contamination. Each measurement was checked from two independent experiments.

Results and discussion

Cyclic voltammetry: poly-Fe vs Fe/Au samples. Figure 2 presents both cyclic voltammograms of a poly-Fe electrode and a Fe(60)/Au surfaces in the classical borate buffer of pH 8.4. Both electrodes display essentially, the same structure of peaks, which have been labeled with the same notation previously presented elsewhere[19]. As main differences between both signals, it can be noticed that the passive current density (i_{pass}) measured in the passive electrochemical potential range ($U \geq 0$ V) is slightly lower in the case of the Fe/Au, thus indicating the lower density of defects[20] as compared to the polycrystalline case. The onset of the oxygen evolution reaction (OER) is also found at higher potentials in the Fe/Au (inset of figure 2). In the cathodic branch, the same structure of peaks is again observed. The reduction processes corresponding to peaks IIa' and IIb' corroborate again that we have the same bilayer structure for the passive film grown on Fe/Au[11,19]. The main feature of the Fe thin film electrochemical signal is the appearance of a new cathodic peak labeled I' at a sample potential $U_S = -0.91$ V. This peak is located close to the onset potential for hydrogen evolution reaction (HER). It is generally not observed on poly-Fe because the HER starts at less negative potentials. In some instance a shoulder may however be detected in the rise of the cathodic current at poly-Fe.

The reduction of the last Fe(II) hydroxide layer into metallic Fe has been previously proposed to take place together with the HER, as concluded by *in situ* Raman measurements[13,21]. Other studies by Light Reflectance Techniques[11,12] support also these results. All these works were performed on poly-Fe surfaces so the Fe(II) film reduction

process itself has not been individually studied. In this sense, the Fe/Au studied here allows individual and univocal assignment of the peak I' (see figure 2) to the solid phase reaction:

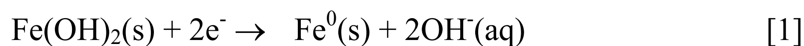

$$Fe(OH)_2(s) + 2e^- \rightarrow Fe^0(s) + 2OH^-(aq) \quad [1]$$

in borate buffers of intermediate-high pHs, despite the mention of a reductive dissolution mechanism proposed in these media[22], which supports a complete dissolution of the Fe passive film during the cathodic reduction corresponding to peaks IIa' and IIb' in the voltammogram. The presence of the peak I' indicates the low-roughness and good orientation of the Fe/Au since a shift of around 100 mV in the HER as well as in the OER allows the peak I' to be clearly distinguished. This property makes thin films preferable to polycrystalline substrates as models to study Fe passivity. In the next section, the behavior of peak I' at different experimental conditions is presented, which reveals the existence of a $Fe(OH)_2$ layer after the cathodic reduction of the Fe_2O_3 passive film formed at high anodic potentials[11,12,19,22,23].

Investigations of parameters influencing peak I'. The clear occurrence of peak *I*' at Fe/Au electrodes prompted a detailed study as a function of experimental parameters. The following procedure was used. The freshly prepared Fe/Au electrode was pre-polarized at –1.1 V for 1 minute to reduce the eventual native oxide formed during transfer of the electrode from the deposition solution to the borate solution; the sample potential was then stepped into the passive region (between +0.6 V and +0.8 V depending on pH). After one minute the potential was scanned negatively at 5 mV/s towards –1.3 V. Stepping the potential instead of scanning minimizes the release of soluble Fe(II) species to the solution[23,24], thus avoiding the complete dissolution of the iron thin film electrode. Peak I' will be characterized by its potential U_P and integrated charge Q_P.

Effect of pH. Figure 3A shows cathodic curves corresponding to the Fe(20)/Au samples at different pHs. In addition and as a checking of the dissolution of the Fe thin film, blanks of the electrochemical Au signal in the same experimental conditions were recorded in the different working media. Figure 3B compares the electrochemical signal corresponding to an Fe/Au electrode and a bare Au substrate as the blank signal, both at pH 8.4. As we will analyze in the last section, it is easy to distinguish when the Fe thin film has been partially dissolved after a number of oxidation-reduction cycles, since the cathodic signal of the iron thin film progressively approaches that of the bare Au surface (see figure 3B).

As it is shown in the inset of figure 3A, the potential shift observed for the peak I' as the pH media is increased, agrees perfectly with a Nernst potential shift expected for the redox reaction proposed in the equation [1]. The only soluble species generated in that reaction corresponds to OH^- anions, which would give a Nernst potential shift of 59 mV per pH unit[25]. The experimental slope of $U_{I'}$ versus pH value indicates the good agreement between experimental and calculated values, thus corroborating the previous proposed mechanisms for the cathodic reduction of the Fe passive film corresponding to the peak I'.

Effect of the hydrodynamic conditions on peak I'. Another way to test whether the layer reduced in the peak I' is formed by $Fe(OH)_2$ (see equation [1]) is to study its solubility. For that purpose, we play with the hydrodynamic conditions of the liquid environment in order to increase the diffusion of Fe^{2+}(aq) into the bulk of the solution, thus displacing the equilibrium toward the right side (soluble species):

$$Fe(OH)_2(s) \leftrightarrow Fe^{2+}(aq) + 2OH^{-}(aq) \qquad [2]$$

Taking the value of $1.26 \cdot 10^{-15}$ for the $Fe(OH)_2$(s) solubility constant (K_{ps})[26], it is possible to estimate the maximum concentration of Fe^{2+}(aq) that can be dissolved at a given pH. In our working buffers, we obtain the following values for the Fe^{2+}(aq) concentration: $2 \cdot 10^{-4}$ M, $3.16 \cdot 10^{-6}$ M and $5.02 \cdot 10^{-12}$ M for pHs 8.4, 9.3 and 12.2 respectively (see table I). These values give us a good estimate of the maximum amount of material that can be removed from the proposed $Fe(OH)_2$ layer at the low electrochemical potential range corresponding to the peak I' at every pH. This, in turn, allows to estimate the film thickness of the $Fe(OH)_2$ layer that remains on the surface. In table I, the result of the thickness for the $Fe(OH)_2$ layer has been estimated by integration of peak I' at the different pHs. This thickness value is expressed in terms of Fe^0 monolayers (ML). Using preliminary X-ray diffraction of these Fe/Au films[27], we can calculate the atomic surface density and thus, the amount of Fe (expressed as number of Fe ML) corresponding to the $Fe(OH)_2$ layer. In order to do that, the crystallographic parameters for the surface Fe-O bond in the $Fe(OH)_2$ oxide structure are needed, but we have approximated it by a layer of pure Fe^0, bcc packed and (110)-faced orientation (unit cell of 2.02 Å)[27]. The expression of the $Fe(OH)_2$ layer in ML of pure Fe^0 gives an estimate of the real $Fe(OH)_2$ thickness and suffices to compare the amount of dissolved Fe at different pHs and hydrodynamic conditions. With the Fe unit cell, we can get an atomic surface density for our Fe thin film of $2.45 \cdot 10^{15}$ cm^{-2}, which in turn can be used to calculate the number of Fe ML that correspond to the integrated charge of the peak I' at the different pHs (see table I), for a 2 e^- transfer reaction as defined by the equation [1]. As should be expected for a $Fe(OH)_2$ layer, the charge corresponding to the peak I' progressively diminishes as the medium pH decreases (see figure 3A), indicating the major solubility of the film at the lower pHs. The charge of the peak I' at the higher pH of 12.2 corresponds to the maximum thickness that can be reached by the $Fe(OH)_2$ layer, since in this medium, the anodic-cathodic processes on the iron surface progress through solid state reactions with practically no dissolution of the oxide film[22,28]. The amount of Fe^{2+}(aq) dissolved at pH 12.2 (calculated from the solubility values of table I) corresponds to $8.71 \cdot 10^{-8}$ ML which indeed indicates that practically no material-loss of the $Fe(OH)_2$ layer will take place in this medium. With this assumption, in the last column of table I we show the values of the Fe^{2+}(aq) concentration according to the lost Fe amount from the $Fe(OH)_2$ layer in static hydrodynamic conditions during the time corresponding to the scan potential from the peaks IIa' and IIb' where the $Fe(OH)_2$ layer is formed, to the peak I' itself (see figure 3A). Although a correlation between the quantity of Fe-loss and the pH value (8.4 and 9.3) exists, the Fe^{2+}(aq) concentrations reached in the solution are still far below the solubility values. In order to avoid limitations in the dissolution rate of the $Fe(OH)_2$ layer by Fe^{2+} diffusion, the experiment was repeated at dynamic hydrodynamic conditions. For that purpose, the passive film was grown in the same fashion as described above. Once the film is formed, the sample potential was again scanned back from the passive film formation potential, between 0.6 and 0.8 V, to a value in the potential range corresponding to the

existence of the $Fe(OH)_2$ layer, between peaks IIb' and I'. Once this cathodic potential is reached, the scan potential is stopped and the solution stirred by nitrogen bubbling for 10 minutes. The hydrodynamic conditions allow the equation [2] to completely reach the equilibrium. Figure 4 shows the results of such experiments obtained at the different pHs. At the lower pH 8.4, the complete disappearance of the peak I' after the solution stirring (see figure 4A) indicates that the $Fe(OH)_2$ layer has completely dissolved in this pH. The Fe^{2+}(aq) concentration reached by the total amount of Fe corresponding to the whole 4.8 Fe ML of $Fe(OH)_2$ layer will be equal to $1.5\cdot10^{-7}$ M, which is at this pH still well below the Fe^{2+}(aq) solubility limit. Similar behavior is also observed for the case of pH 9.3 media (see figure 4B). In this case, the Fe^{2+}(aq) solubility value is close to the Fe^{2+}(aq) concentration generated by the total dissolution of the $Fe(OH)_2$ layer. As a result, the peak I' after the 10 minutes stirring treatment is still visible, although the associated charge is, at this point, very low, (equivalent to less than 1 Fe ML), thus indicating that the Fe^{2+}(aq) concentration at the end of the dissolution process is close to the saturation point and therefore, longer stirring times will be needed in order to dissolve completely the $Fe(OH)_2$ film. In both cases, a second cycle of step + cathodic scan (see beginning of this section) after the stirring stage again at static hydrodynamic conditions was performed in order to check that the Fe/Au film was not completely removed during the passive film dissolution. For the sake of comparison, the step + cathodic scan of a freshly prepared Fe/Au film at purely static hydrodynamic conditions have been included for each corresponding pH. To corroborate that this behavior indeed corresponds to the dissolution of an $Fe(OH)_2$ film, exactly the same experiment was repeated at pH 12.2. In this conditions, the Fe^{2+}(aq) solubility product is low enough (see table I) to practically block the dissolution of the $Fe(OH)_2$ layer (see figure 4C). The charge of peak I' recorded at static hydrodynamic conditions and after the stirring, is very similar, $3.90\cdot10^{-3}$ and $3.83\cdot10^{-3}$ C / cm^2 respectively, in agreement with the existence of an $Fe(OH)_2$ film as the final stage of the passive film cathodic reduction.

Structure of the Fe passive film. It is interesting to investigate the role of the $Fe(OH)_2$ layer in relation to the bilayer structure of the Fe passive film[11,19], in order to elaborate a complete model of the oxide film reduction mechanism. In previous work, different cycling electrochemical potential experiments were performed at nearly neutral pHs[11,19], thus observing that the so-called outer layer generated on the outermost part of the passive film in contact to the electrolyte grows progressively in each cycle, as evidenced by the current increase of the peak IIa'. This outer layer is composed by an Fe(III) deposit layer formed by the electro-oxidation of the Fe^{2+}(aq) species generated at earlier potentials. On the other hand, the inner layer, also known as the natural passive film (Fe_3O_4)[10], is nicely reversible under the same conditions, as observed by the constant height of the peak IIb' in every cycle[19]. Figure 5 shows cycling experiments on Fe/Au film, similar to those presented elsewhere with poly-Fe[11,19] , with an Fe thin film. The previous anodic step + scan back stage was successively repeated several times in the pH 8.4 medium, following the same procedure described above. Although the step potential method has been commonly employed to grow the Fe passive film with the minimum material dissolution[23,24,29,30] , here the experiment was performed with an Fe^{2+}(aq) concentration of 10^{-4} M in order to minimize the Fe/Au film dissolution during electrochemical cycle and also to have available Fe^{2+}(aq) ions in the solution for the outer layer formation. The increase of the peak IIa' current (see inset in figure 5) indicates the quick growth of the outer layer as consecutive electrochemical potential cycles are applied. On the

other hand, the peak IIb' corresponding to the inner layer or natural passive film decreases progressively, indicating that this layer is being dissolved during every cycle and its subsequent formation gives a progressively thinner inner oxide film. Taking into account that this inner Fe passive film forms through a solid phase reaction[20], the thickness of this oxide film is defined by the potential drop across the layer, which can be assumed to be a linear function of the applied potential[31,32]. As consequence, we associate the decay of the peak IIb' current to the progressive lowering of the Fe thin film coverage onto the Au substrate, thus decreasing the effective area of the inner Fe passive layer after its formation, and also indicating that the dissolution of the Fe passive film during cathodic reduction cycles takes place in an inhomogeneous way giving rise to an islands-like structure of the Fe/Au film. Total disappearance of peak IIb' may eventually occur with these Fe/Au films because the Fe can be completely dissolved from the Au substrate (see figure 5). This situation is of course impossible on poly-Fe where peak IIb' never vanishes. This result is consistent with the roughening process observed on Fe bulk electrodes after electrochemical cycling in nearly neutral pHs[6,11,33] , where Fe dissolution occurs. The direct relationship between the peaks IIb' and I' (see inset of figure 5) indicates that the $Fe(OH)_2$ layer analyzed in the previous sections and reduced in peak I', corresponds to the lower oxidation state of the natural passive film or inner layer, while the outer layer forms all over the surface and completely dissolves during its cathodic reduction in the peak IIa'. The higher negative slope for the peak I' respect to IIb' in the inset of figure 5 (slopes ratio of around 2:1) agrees with the fact that the cathodic process occurring on I' is a 2-e^- process compare to the 1-e^- process on IIb'. With all this parameters, in figure 6 we propose a complete model of the cathodic reduction process of the Fe passive film in nearly neutral pHs. Fe/Au films electrodeposited from acidic media are very useful model systems to study Fe passivity. An interesting feature is the possibility to control the exact ratio *outer layer/inner layer* by cycling the electrochemical potential and measuring the charge ratio between peaks IIa' and IIb'. The aim of this application is focused on future investigations on separating both contribution of each layer on the electronic properties of the passive film on Fe and compare them with those obtained on the complete bilayer structure of the Fe passive film[11,34,35].

Quantitative RBS analysis.

Fe dissolution kinetics during the passive film reduction. We analyzed by RBS the total Fe amount of a freshly prepared Fe thin film before and after the passivation-reduction procedure, in order to correlate it with the previous electrochemical data on dissolution kinetics of the passive film. The experiments were performed on passive films grown at pH 8.4 and pH 12.2. Figure 7 shows a typical RBS spectrum of a fresh Fe(10)/Au film. Plateaus observed for channels below 220 correspond to mica (elements : Si, Al and K) and the main peak at channel 350 to the Au film. The small peak at channel 250 corresponds to the iron layer. Its integration gives D_{Fe} the surface density of iron atoms/cm^2. When comparing the RBS signals before and after the anodic step + cathodic scan stage in the pH 8.4 buffer, the amount of lost Fe is $6.21 \cdot 10^{-15}$ and $6.33 \cdot 10^{-15}$ Fe atoms/cm^2, for two independent experiments. The experimental complexity of the sample preparation and subsequent RBS measurement prevents to have a wide statistics for these results, however, the reproducibility between the

different independent experiments seems to be adequate. The Fe material lost after the passivation and reduction process will correspond, of course, to the dissolved Fe^{2+}(aq) during the passive film formation/reduction. Taking an average of the Fe RBS densities lost at pH 8.4, and transforming it into Fe ML, we obtain an equivalent total lost Fe amount of 2.56 ML, in excellent agreement with the 2.6 ML obtained electrochemically from the charge of peak I' at pH 8.4 (see table II). The same experiments were performed for passive films grown at pH 12.2, resulting in a lost Fe amount of $0.94 \cdot 10^{-15}$ and $1.05 \cdot 10^{-15}$ Fe atoms/cm^2. This corresponds to an equivalent total lost Fe amount of about 0.4 ML or about 8 % of the total film thickness. As stated above, the Fe^{2+}(aq) generated at this pH is practically zero, so we associate this slight Fe material lost to mechanical removal during the stirring stage.

These results validate the method proposed above to use the charge of the peak I' corresponding to the Fe passive film formed in different buffer media to quantitatively monitor the oxide film dissolution.

Effect of the passivation time and potential on peak I'. As the final stage of this study, we looked at the effect of the passivation potential and anodization time on the thickness of the inner layer by analyzing the peak I'. Figure 8A shows a serie of cathodic scans of different Fe passive film formed on fresh Fe(15)/Au films at different passivation potentials, while in figure 8B, peaks I' of the passive film formed at the same anodic potential of 0.8 V but at different anodization time, are presented. It is observed that the main influence on the inner layer comes from the passivation potential, while the anodization time does not practically change the charge and position of the peak I'. Paying attention in the former case, as the passivation potential is stepped toward more anodic values, the charge of the peak I' increases, keeping the same potential position. Although it is well-known that a slight thickening of the inner layer occurs as the potential formation is increased in the passive plateau III[11], the main inner layer thickening takes place in the active region I (see figure 2), as previously observed[19]. Therefore, the observed difference in the inner layer thickness estimated again by the peak I' charge (see figure 8), 2.3 ML and 0.9 ML respectively for 0.8 and 0.1 V of anodic formation potentials, can only be explained by an additional passive film dissolution when it is formed at the lowest anodic potentials in the passive plateau. RBS measurements again corroborate the dissolution kinetics differences between low and high anodic potentials for the passive film formation. For this purpose, the lost amount of Fe of two different Fe(15)/Au films passivated by stepping the potential to 0.1 and 0.8 V, was measured. The obtained RBS results were $3 \cdot 10^{-15}$ and $0.13 \cdot 10^{-15}$ Fe atoms/cm^2 respectively for each anodic potential which corresponds to equivalent Fe lost amounts of 1.2 and 0.05 ML respectively. It is clear that there is a certain dissolution of Fe passive film when stepping at the lower anodic potential of 0.1 V, while practically no Fe lost is detected at 0.8 V. If we take the previously 2.6 ML of dissolved Fe during the cathodic reduction at the same pH 8.4 (see previous section), we obtain a total of 3.8 ML of dissolved Fe for the complete stage of anodic step to 0.1 plus the cathodic scan back. The difference between this value and the 4.8 ML corresponding to the total inner passive film thickness previously estimated (see table II), gives a value of 1 ML for the remaining passive film, which is again in good agreement with the cathodic peak I' charge at this potential (see inset 8A). This additional dissolution detected during the anodic polarization at low anodic potentials of 0.1 V in the passive region can be explained from the point of view of the electronic structure for the Fe passive film at the

different anodic potentials in the passive plateau (Fe(III) oxide region). Previous studies in the last years have determined that the Fe(III) passive film behaves as a n-type semiconductor with a high doping concentration[23,34 ,36]. It is well established that this doping concentration decreases as the sample potential is increased in the passive region due to the progressive oxidation of the Fe(II) n-type doping species[36], which has a direct implication on the surface electronic barrier of the semiconducting oxide. Thus, although a linear growth of the passive film thickness with formation potential could be attributed to oxygen diffusion mechanisms[31,32]. Passive film thickening is indeed true when measuring the total oxide film thickness including inner and outer layer. Here we go further and are able to analyze separately the evolution of the natural inner layer ($Q_{I'}$), connecting it with the small Fe amounts that dissolve during passivation. In that sense, we think that electronic effects may play a role. The lower the anodic potential in the passive plateau, the higher the doping concentration in the oxide film, and the thinner the space charge layer. This results in a higher electron concentration in the film, coming from the metal and/or possibly from redox species in solution. In any case a higher electron concentration would allow to reduce Fe(III) to Fe(II), thus displacing the equilibrium:

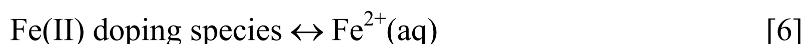

$$\text{Fe(II) doping species} \leftrightarrow Fe^{2+}(aq) \qquad [6]$$

toward the soluble specie, and giving a higher dissolution rate of the film at the lower anodic potentials in the passive plateau. These results are in agreement with the almost linear behavior of the donor density versus anodic potential presented in previous works[36,37], which saturates at high potential values (>0.5 V). Same behavior can be observed for the peak I' charge (see inset of figure 8A), indicating that dissolution of the passive film decreases in the same manner as the donor concentration of the Fe(III) passive layer. These results suggest that the formation of a lower doping semiconductor at high anodic potentials and the development of a depletion layer, reduce the availability of electrons at the oxide/electrolyte interface thus producing a two-fold effect: first, by preventing further oxidative reactions with the electrolyte as discussed elsewhere[34], but also by preventing reduction (and subsequent dissolution) of the layer itself, by electrons *from the solid electrode*. In this way, the absence of electrons in the space charge layer could "latch" the film oxidized, which adds a new aspect to the passivation of iron and other transition metals.

In view of these results, we can speculate that the inner layer forms a "native ohmic contact" for the outer n-Fe_2O_3 layer, much in the way that electron donors such as phosphorus are implanted at high concentrations into silicon, in order to make n++ ohmic contacts to metal layers (usually Au)[38]. The energy diagram that arises from the model of figure 8 is then essentially the one presented elsewhere[34], with the inner oxide layer providing an ohmic junction between the metallic Fe and the outer n-Fe_2O_3 layer and hence preventing the buildup of an energy barrier at the metal/oxide interphase. The rectifying contact is instead built up at the n-Fe_2O_3/electrolyte interphase, as was quantitatively discussed before[34]. Interestingly, the flatband potential of n-Fe_2O_3 is about -280mV/SSC[34], almost concurrent with the reduction peak IIa' corresponding to the outer layer. Our interpretation is that as the energy barrier is lowered when scanning the potential towards negative values (increasing U_{fermi}), electrons are forced to flow to the *surface* of the outer layer where they are trapped and cause the reduction of the layer itself by the solid-state reaction:

$$Fe(III)(s) + e^- \rightarrow Fe(II)(s) \quad [7]$$

followed by dissolution of the Fe(II) species as described by equation [6].

On the other hand, the effect of the anodization time gives a remarkable current increase of the peak IIa', which means an increase in the outer layer thickness, but seems not to have any significant effect on the inner layer as observed by the same charge and position of I'. Long anodization times can then be used to produce thicker anodic layers consisting mainly of a semiconducting Fe_2O_3 outer layer[11,12,34] , in a similar manner as the 2-step procedure described elsewhere[19,34].

Conclusions

The structure of the passive film on iron and its cathodic reduction dynamics have been studied by cyclic voltammetry and RBS analysis in Fe thin films prepared on Au(111) substrates. A voltammetric peak corresponding to the last reduction stage of the passive film into metallic Fe^0 is reported for the first time. These films also allow to control the amount of Fe in the electrode. Together the setup offers the opportunity to study the reduction of the passive films in exquisite detail. We have observed that Fe(II)-like film that it is thought to exist in the potential range previous to the HER in high pH media, behaves as an $Fe(OH)_2$ layer which in addition, is present in a wide pH range from nearly-neutral values to very high ones. In short, the cathodic peak I' position and thickness of this $Fe(OH)_2$ layer as well as the dissolution behavior at the different pH media have been studied, observing that indeed the larger thickness and lower dissolution kinetics as well as the shift of the peak I' toward more cathodic values as the pHs media is increased, behaves in a way that corroborates the existence of a $Fe(OH)_2$ passive layer in this potential range.

The relationship between the $Fe(OH)_2$ layer and the complete structure of the Fe passive film indicates that this $Fe(OH)_2$ film corresponds to the last stage of the inner layer cathodic reduction. Moreover, these results together with the comparison between polycrystalline and thin film Fe surfaces, shows that these Fe thin films electrodeposited from acidic solutions on well-oriented Au substrates are ideal systems for fundamental studies of the structure and kinetics of the oxide passive film on Fe.

From the present structural model and the previously studied electronic properties, an electronic model of the Fe passive film bilayer is proposed. The inner layer is thought as a "native ohmic contact" of the hydrated n-Fe_2O_3 outer layer, which in turn forms a rectifying contact in the oxide/electrolyte interphase. The absence of electrons on the oxide surface prevents Fe(III) $\rightarrow$ Fe(II) reduction, thus *latching* against film dissolution. Further work are being developed on our lab to elucidate the implication that the different types of Fe oxide grown on the surface at different potential ranges, have on the electronic properties of the film.

Acknowledgments

The authors are grateful to Scientific-Technical Services of the University of Barcelona for the use of facilities. Financial support of the present work comes from the CYCIT under research project MAT2000-0986.

References

1. N. Sato, T. Noda, K. Kudo, *Electrochim. Acta.*, **19**, 471 (1974).

2. M. Nagayama, M. Cohen, *J. Electroanal. Chem.*, **109**, 781 (1962).

3. T. Chen, B. D. Cahan, *J. Electroanal. Chem.*, **129**, 17 (1982).

4. J. Benzakour, A. Derja, *J. Electroanal. Chem.*, **437**, 119 (1997).

5. O. Khaselev, J. M. Sykes, *Electrochimica Acta*, **42**, 2333 (1997).

6. R. C. Bhardwaj, A. González-Martín, O'M. Bockris, **138**, 1901 (1991).

7. V. Jovancicevic, R. C. Kainthla, Z. Tang, B. Yang, O'M. Bockris, *Langmuir*, **3**, 388 (1987).

8. F. C. Ho, J. L. Ord, *J. Electrochem. Soc.*, **119**, 139 (1972).

9. L. J. Oblonsky, A. J. Davenport, M. P. Ryan, H. S. Isaacs, R. C. Newman, *J. Electrochem. Soc.*, **144**, 2398 (1997).

10. P. Schmuki, S. Virtanen, *The Electrochemical Society Interface*, **2**, 38 (1997).

11. M. Büchler, P. Schmuki, H. Böhni, *J. Electrochem. Soc.*, **145**, 609 (1998).

12. M. Büchler, P. Schmuki, H. Böhni, *J. Electrochem. Soc.*, **144**, 2307 (1997).

13. J. C. Rubim, *J. Electrochem. Soc.*, **140**, 1601 (1993).

14. J. Gui, T. M. Devine, *J. Electrochem. Soc.*, **138**, 1376 (1991).

15. M. Seo, M. Chiba, K. Suzuki, *J. Electroanal. Chem.*, **473**, 49 (1999).

16. M. Seo, M. Chiba, *Electrochim. Acta.*, **47**, 319 (2001).

17. De-Sheng Kong, Shen-Hao Chen, Li-Jun Wan, Mei-Juan Han, Langmuir, **19**, 1954 (2003).

18. A. L. Cagnon, C. Gomes, A. Morrone, J. Schmidt, P. Allongue, Phys. Chem. Chem. Phys, 3, 3330 (2001).

19. I. Díez-Pérez, P. Gorostiza, F. Sanz, C. Müller, *J. Electrochem. Soc.*, **148**, B307 (2001).

20. Patrick Schmuki, *J. Solid State Electrochem.*, **6**, 145 (2002).

21. J. C. Rubim, J. Dünnwald, *J. Electroanal. Chem. Interfacial Electrochem.*, **258**, 1376 (1991).

22. P. Schmuki, S. Virtanen, *The Electrochemical Society Interface*, **2**, 38 (1997).

23. L. J. Oblonsky, A. J. Davenport, M. P. Ryan, H. S. Isaacs, R. C. Newman, *J. Electrochem. Soc.*, **144**, 2398 (1997).

24. M. F. Toney, A. J. Davenport, L. J. Oblonsky, M. P. Ryan, C. M. Vitus, *Phys. Rev. Lett.*, **79**, 4282 (1997).

25. The Nersts relationship for the bielectronic redox reaction defined by equation [4] holds: $U = U^{0'} - (2.303 \cdot R \cdot T / F) \cdot pH$, being R the gas constant, T the temperature equal to room temperature of 293 K, F the Faraday constant and $U^{0'}$ the formal potential of the reaction. Then the expression reaches: $U = U^{0'} - 0.058 \cdot pH$.

26. R. M. Smith, A. E. Martell, *Critical Stability Constants*, Vol. 4, Plenum, New York (1976).

27. P. Allongue *et al*, to be published.

28. S. Virtanen, P. Schmuki, M. Büchler, H. S. Isaacs, *J. Electrochem. Soc.*, **146**, 4087 (1999).

29. A. J. Davenport, L. J. Oblonsky, M. P. Ryan, M. F. Toney, *J. Electrochem. Soc.*, **147**, 2162 (2000).

30. E. E. Rees, M. P. Ryan, D. S. McPhail, *Electrochemical and Solid-State Letters,* **5**, B21-B23 (2002).

31. D. D. Macdonald, *J. Electrochem. Soc.*, **139**, 3434 (1992).

32. L. Zhang, D. D. Macdonald, E. Sikora, J. Sikora, *J. Electrochem. Soc*., **145**, 898 (1998).

33. J. Li, D. J. Meier, *J. Electroanal. Chem.*, **454**, 53 (1998)

34. I. Díez-Pérez, P. Gorostiza, F. Sanz, *J. Electrochem. Soc.,* **150**, B348 (2003).

35. M. Bojinov, T. Laitinen, K. Mäkelä, T. Saario, *J. Electrochem. Soc*., **148**, B243-B250 (2001).

36. M. Büchler, P. Schmuki, H. Böhni, T. Stenberg, T. Mäntylä, *J. Electrochem. Soc*., **145**, 378 (1998).

37. J. Liu, D. D. Macdonald, *J. Electrochem. Soc*., **148**, B425 (2001).

38. S.M. Sze, *VLSI Technology*., chapter 9, McGraw-Hill, Editors International (1988).

Figure captions

Figure 1. (10x10) μm^2 AFM image of a Fe(60)/Au film electro-deposited from acidic media onto an Au(111) oriented substrate. A (2x2) μm^2 zoomed image and the corresponding roughness analysis are also included. 5 nm of Z scale.

Figure 2. Cyclic voltammograms corresponding to signals of Fe polycrystalline (dotted) and Fe(60)/Au film (solid) electrodes. 5 mV/s of scan potential rate.

Figure 3. Influence of pH: (A) negative going scans from 0.8 to –1.3 V of a 20 ML Fe thin film at pHs of 8.4 (——), 9.2 (·····) and 12.2 (----). The passive film was previously formed by stepping the potential to an anodic value between 0.5 and 0.8 V depending on the working pH. (B) Blank negative going scan of the Au substrate in the same pH 8.4 media. For comparison, previous Fe passive film signal in the same conditions is included. 5 mV/s of scan rate in all cases.

Figure 4. Influence of solution stirring: cathodic branches of the Fe passive film reduction on a Fe(20)/Au film at pHs 8.4 (A), 9.3 (B) and 12.2 (C). In every graph, curves were presented as follow: (·····) same curve as figure 3A, under static conditions, (——) curve recorded under static conditions upon stirring the solution for 1 min at the potential marked by the arrow (see same graph), and (----) consecutive curve recorded again at same static conditions than those on figure 3A (omitted in graph C). 5 mV/s of scan rate in all cases.

Figure 5. Consecutive negative going scans of the same Fe passive film grown on a Fe(20)/Au film (see number of cycles in the graph). Inset figure, normalized charge of every cathodic peak as a function of number of cycles. 5 mV/s of scan rate.

Figure 6. Schematic model of the passive film cathodic reduction in nearly-neutral borate buffer media.

Figure 7. Typical RBS spectrum obtained with Fe/Au electrode. The different elements identified are indicated in the figure. The peak related to Fe (see also inset) is integrated to determine D_{Fe}.

Figure 8. (A) Effect of passivation potential: same as Fig. 3A for a Fe(20)/Au electrode. The passive film was grown at the potentials: (——) 0.8V, (----) 0.4 V and (·····) 0.1 V. Inset: variations of $Q_{peak\ I'}$ as a function of $U_{passivation}$. (B) Influence of passivation time: same as Fig. 3A for a Fe(20)/Au electrode. The passivation time is indicated in minutes in the figure.

Table I. Comparison of Fe^{2+} solubility and $Fe(OH)_2$ layer dissolution at the different pHs (analysis from voltammetry of figure 3A).

pH	Fe^{2+} solubility (M)	Peak I' charge (C)	Fe film ML	dissolved Fe(M)
8.4	$2\cdot10^{-4}$	$1.77\cdot10^{-3}$	2.2	$8.32\cdot10^{-8}$
9.3	$3.16\cdot10^{-6}$	$2.54\cdot10^{-3}$	3.2	$6.41\cdot10^{-8}$
12.2	$5.02\cdot10^{-12}$	$3.77\cdot10^{-3}$	4.8	—

Fig. 1

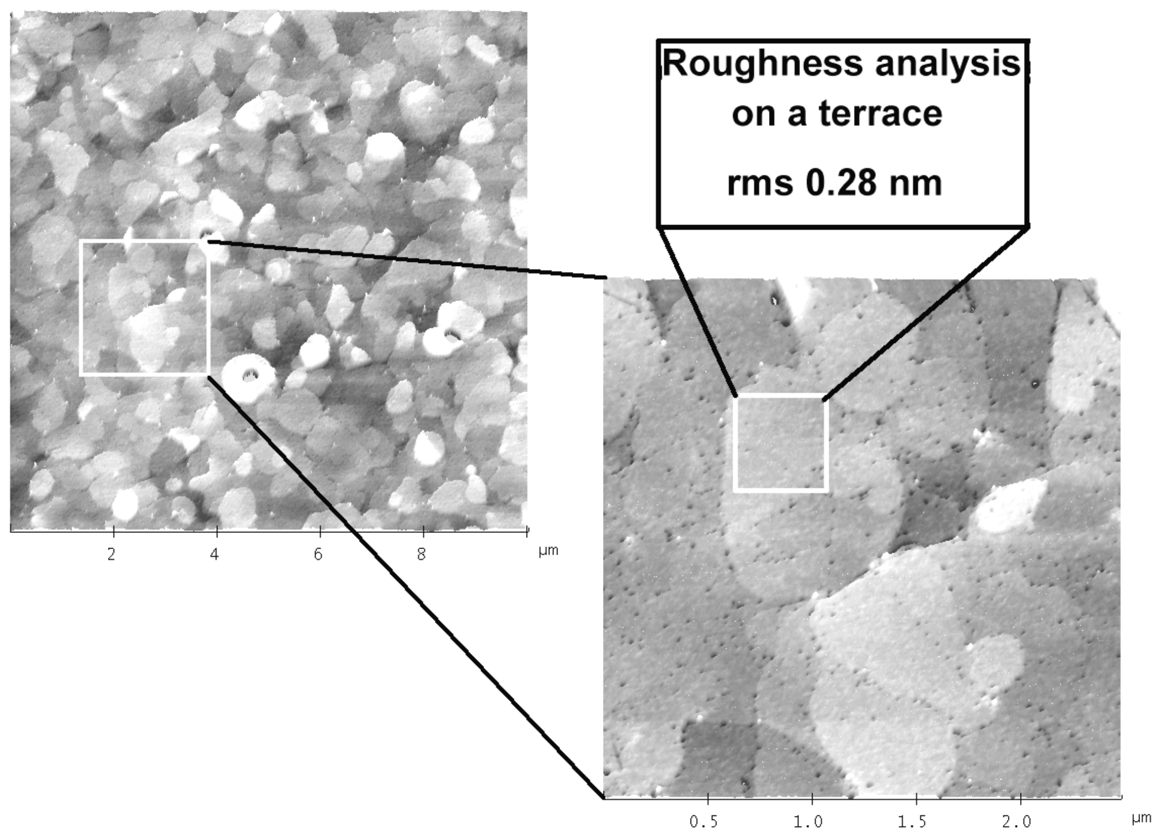

Fig. 2

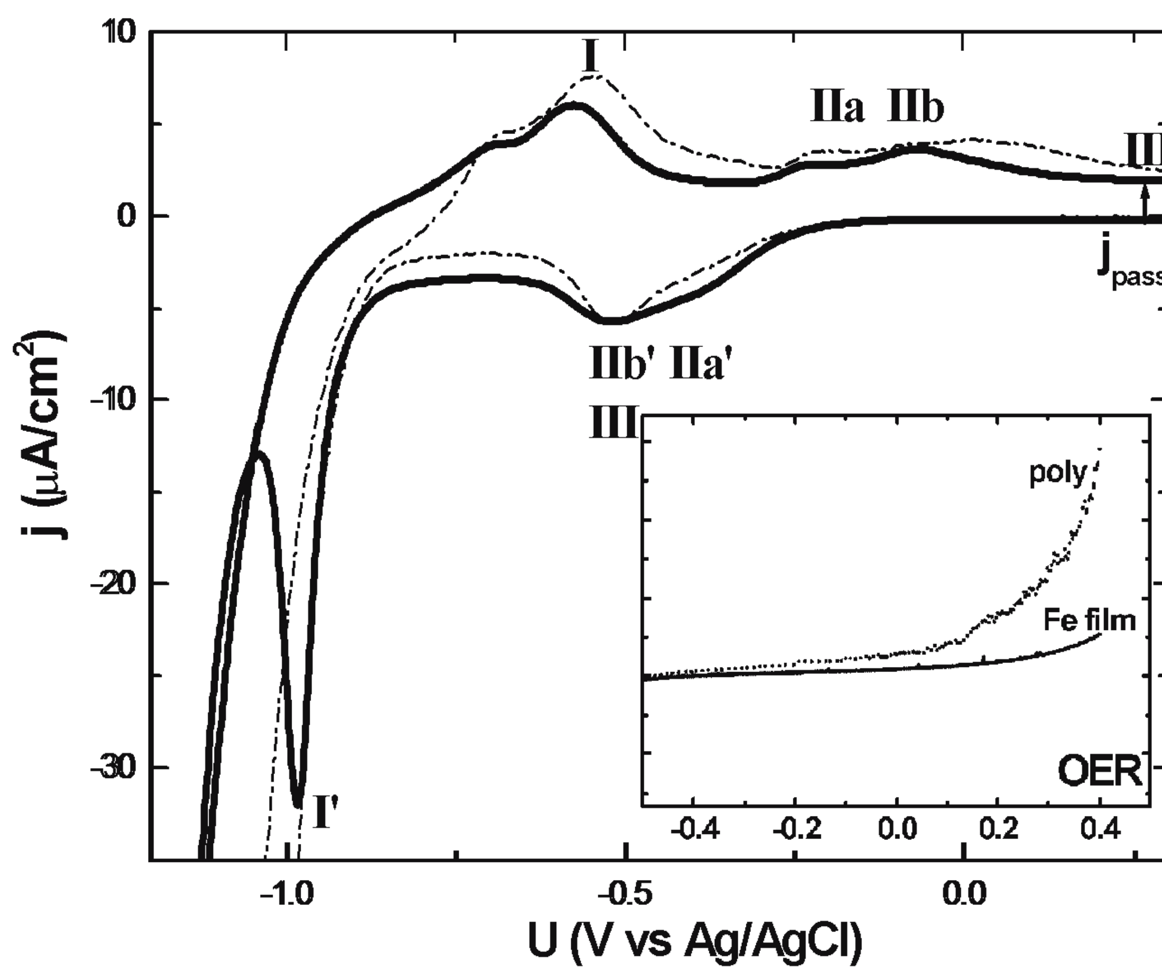

Fig. 3

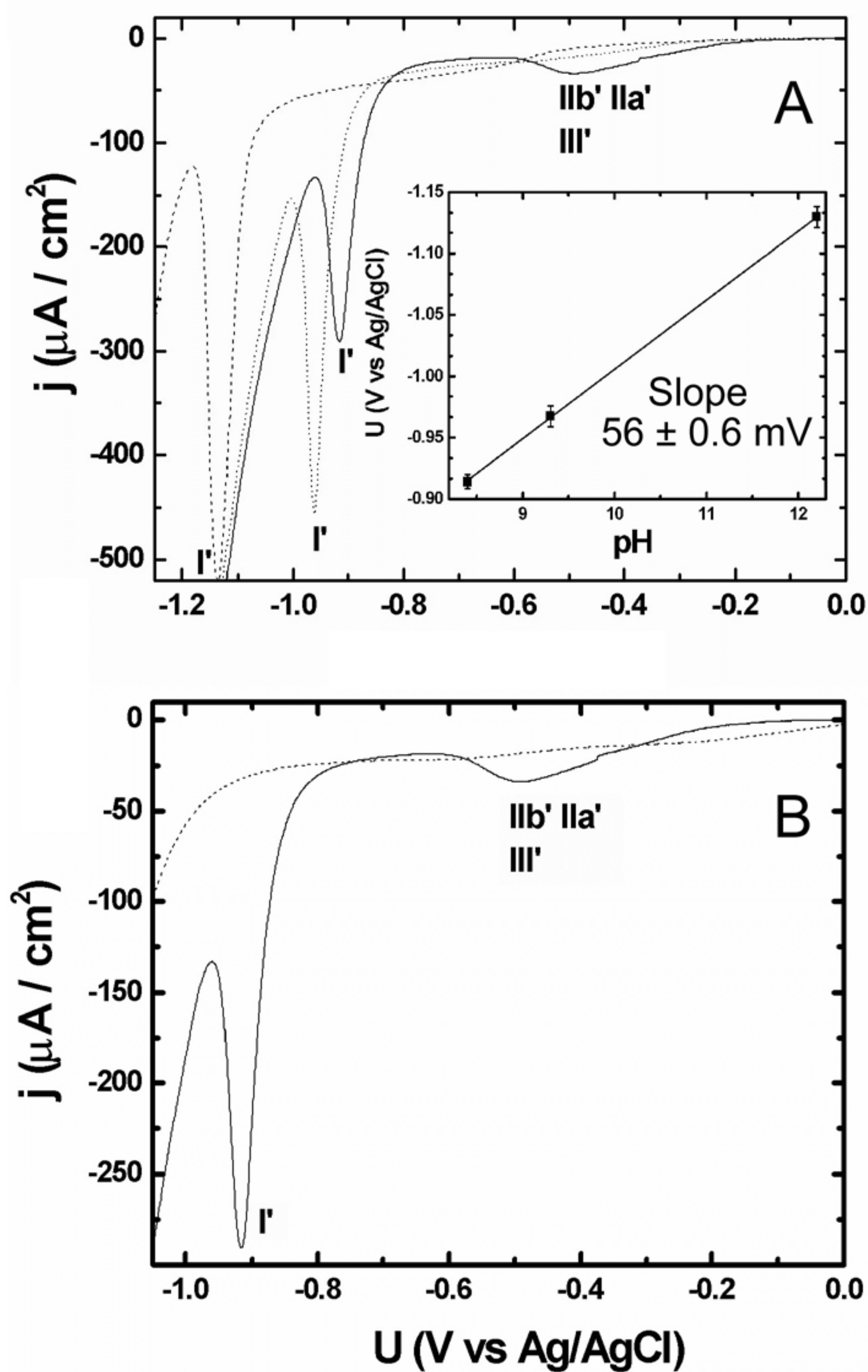

Fig. 4

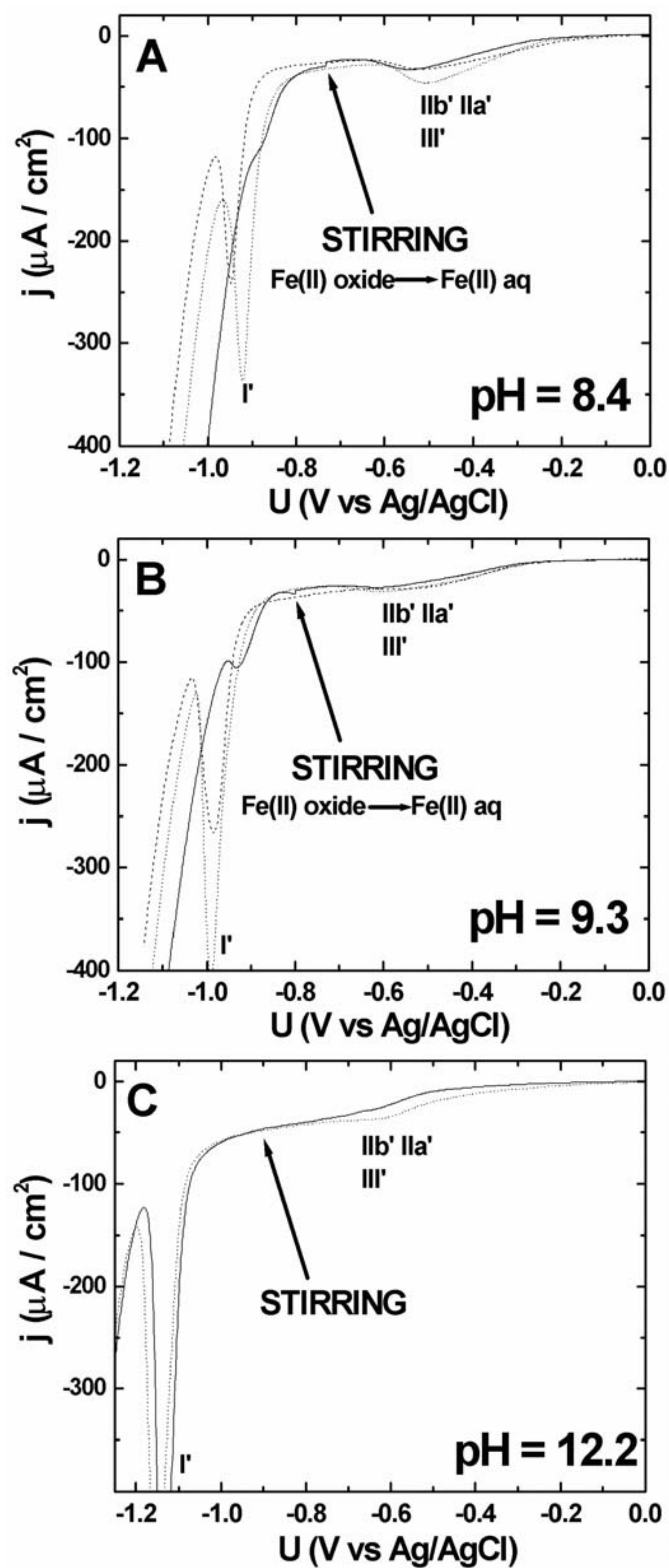

Fig. 5

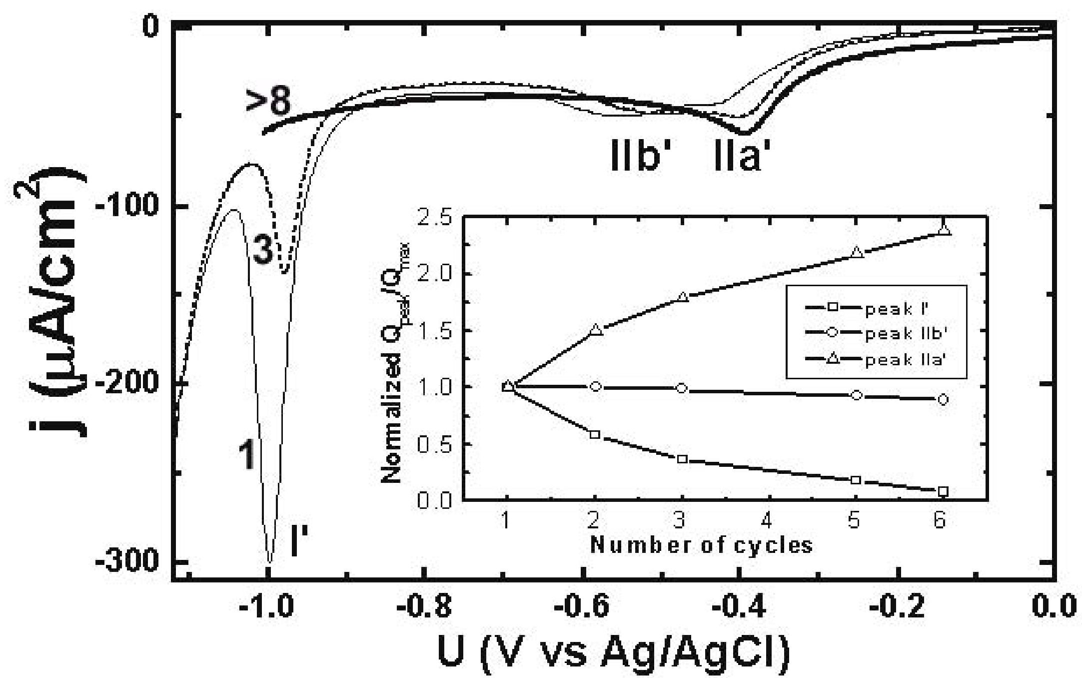

Fig. 6

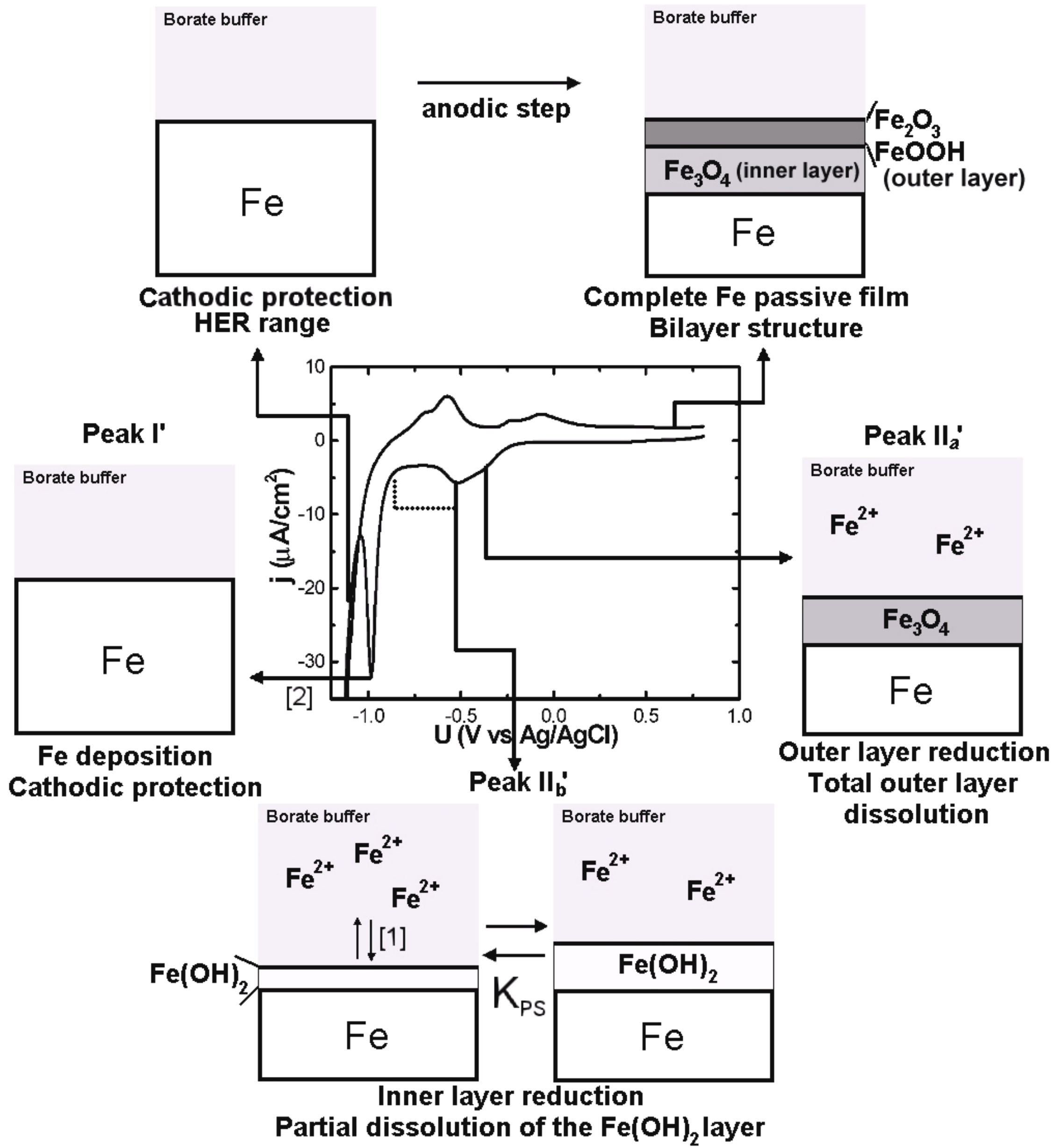

Fig. 7

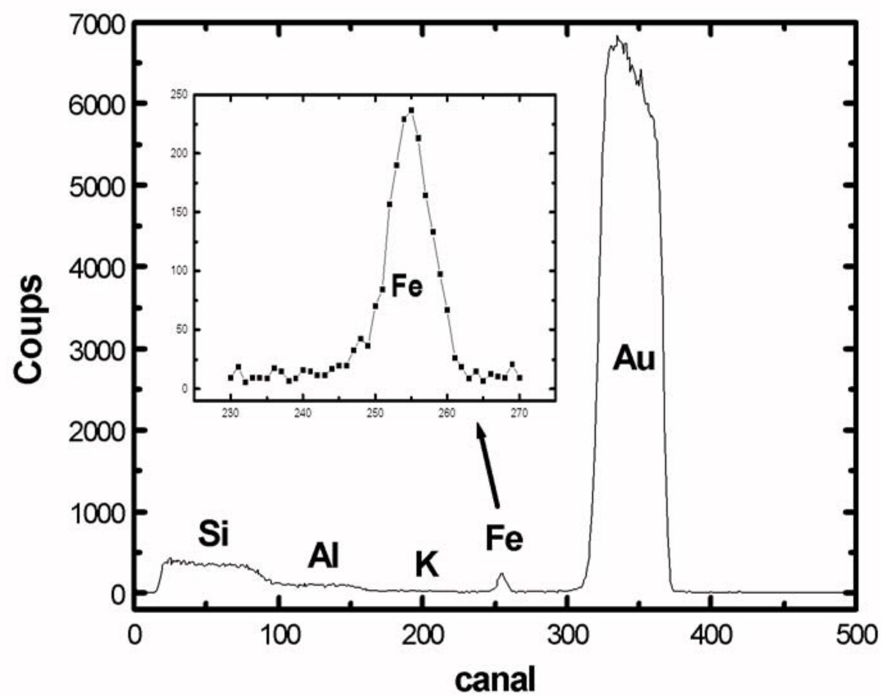

Fig. 8

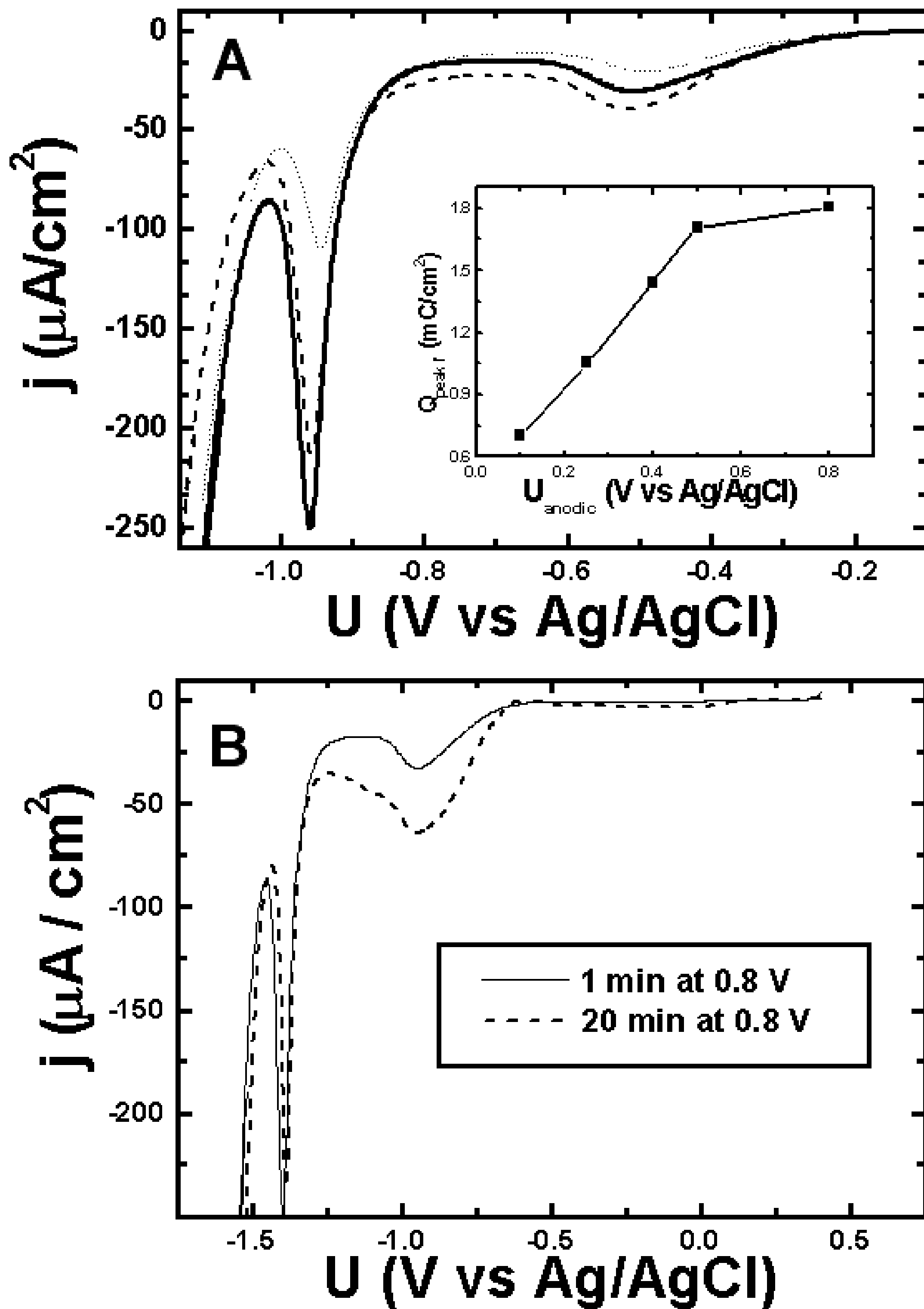

Chapter 4

Fe passivity: *in situ* electronic structure

4.1 GENERAL

In this chapter, the passivation process on iron polycrystalline substrates is studied by means of EIS ECSTM and ECTS techniques. The aim of this study is to sketch an energy diagram as complete as possible for the Fe electrode│electrolyte interface within its entire electrochemical potential range. Firstly, in section 4.2, the suitability of the ECSTM technique to probe the principal pathways of the electronic conduction through the Fe electrode│electrolyte interface within the different electrochemical potential ranges is shown. The main fundamental parameters of the ET through the Fe oxide film in the passive state are presented, together with the first quantitative band diagram of the interface. Next, in section 4.3, individual *in situ* tunneling spectra are recorded from Fe electrode│electrolyte interface within the different electrochemical potential ranges and fitted to a simple double-exponential kinetic model. The electronic structure of the Fe oxide as a function of its oxidation state can be then *in situ* and quantitatively analyzed. The concept of *electronic passivity* is then revisited in view of the obtained electronic structure within the passive region, and the process is also analyzed as a function of medium *p*H and electrode potential, giving rise to a complete and consistent description of the electrode redox behavior.

From the use of conductograms described in the previous chapter 2, the main transitions on the Fe electrode surface can be observed, as well as the reversibility in the electronic properties when the electrode is electrochemically oxidized and reduced in the borate buffer. Brighter areas in the conductogram represent active redox energy levels that can act as the electronic pathways for further redox reactions with electro-active species in solution. Anodic oxidation and cathodic reduction of the Fe passive layers take place when the Fermi level of the solid electrode approaches a high conductance region. A dynamic band diagram of the entire process is ultimately provided.

The detailed results of this chapter are presented in the following publications:

- *Direct Evidence of the Electronic Conduction of the Passive Film on Iron by EC-STM*, J. Electrochem. Soc., **150** (2003) B348.

- *Electronic barriers in the iron oxide film govern its passivity and redox behavior: Effect of electrode potential and solution pH*, Electrochem. Commun., **8** (2006) 1595.

4.2 DIRECT EVIDENCE OF THE ELECTRONIC CONDUCTION OF THE PASSIVE FILM ON IRON BY ECSTM

Reference: I. Díez-Pérez, P. Gorostiza and F. Sanz, *Direct Evidence of the Electronic Conduction of the Passive Film on Iron by EC-STM*, J. Electrochem. Soc., **150** (2003) B348.

Reprinted from the above publication, © The Electrochemical Society 2003, with permission from The Electrochemical Society.

B348 Journal of The Electrochemical Society, 150 (7) B348-B354 (2003)
0013-4651/2003/150(7)/B348/7/$7.00 © The Electrochemical Society, Inc.

Direct Evidence of the Electronic Conduction of the Passive Film on Iron by EC-STM

I. Díez-Pérez, P. Gorostiza, and F. Sanz*[z]

Laboratory of Electrochemistry and Materials, Department of Physical Chemistry, University of Barcelona, 08028 Barcelona, Spain

The electronic conduction mechanism through the electrochemically formed passive film on an iron polycrystalline surface was studied by *in situ* electrochemical scanning tunneling microscopy (EC-STM) and electrochemical impedance spectroscopy (EIS). *In situ* STM imaging conditions of the iron oxide layer in the different electrochemical potential regions [Fe(II) and Fe(III) oxide] were determined and successfully compared to their semiconducting properties evaluated by EIS. As a result, a quantitative explanation for the highly stable STM images of a thick iron oxide formed at high anodic potentials can be obtained. This experimental data allows us to present a quantitative energy diagram of the iron|passive film|electrolyte interface as well as to give first estimates of some electronic parameters of the passive film on iron. These results suggests that the so-called passivity of iron electrodes may arise from the buildup of an energy barrier at the oxide|electrolyte interface.
© 2003 The Electrochemical Society. [DOI: 10.1149/1.1580823] All rights reserved.

Manuscript submitted October 15, 2002; revised manuscript received January 30, 2003. Available electronically May 30, 2003.

It is well established that electronic and ionic transport through the so-called passive oxide films is directly connected to the corrosion processes that take place on these interfaces. The understanding of the mechanism of these processes would have a large impact in many technological fields where strong investments are focused on the corrosion protection of metals and their alloys. One of the key elements for the accurate understanding of these processes is to get a detailed energy level distribution of the passive film surface in contact with the environmental electrolyte. Iron passive films constitute one of the most extensively studied systems in this field due to the wide technological applications of iron and iron-based alloys. Most of these studies are being carried out in borate buffer media at nearly neutral pH. In this media, highly stable, reversible iron oxide films can be electrochemically formed on the surface under potentiostatic control. The oxidation state of the iron oxide film can also be controlled by selecting the suitable potential range.[1] A considerable amount of work on iron passive film has been focused on its structure and chemical composition in the different electrochemical potential ranges. For this purpose, a new group of *in situ* spectroscopic techniques mainly based on synchrotron radiation, was recently developed to be able to perform structural measurements of the oxide films under electrochemical control. Among them, we can find some works on iron oxide films using a variety of the following *in situ* techniques: X-ray scattering,[2] laser reflectance technique,[3] ellipsometry,[4,5] Surface enhanced Raman scattering (SERS),[6-10] extended X-ray absorption fine structure (EXAFS),[11-13] and X-ray absorption near edge (XANES).[14,15] The results extracted from these structural studies show that at early anodic potentials in the potential range corresponding to the first electrochemical oxidation process, an Fe(II) oxide/hydroxide appears on the surface.[6-10] In previous work developed in our laboratory, we show that this Fe(II) oxide grows under potentiostatic conditions within this potential range until it completely passivates the surface.[1] On the other hand, the electrochemically formed iron oxide at high anodic applied potentials in the so-called passive region has been largely studied. The proposed structure corresponds to a spinel-like nanocrystalline structure of an Fe(III) oxide doped with a high concentration (around 7%) of Fe(II) species.[15,16]

Despite all this available chemical and structural information about electrochemical iron oxide films, there are few reports explaining the quantitative relationship between the oxide crystalline structure and the electronic-ionic conduction mechanisms through the film. Among these, the contributions by Büchler *et al.*,[17,18] deserve to be highlighted in which the semiconducting properties of the passive anodic iron film grown in borate buffer at pH value of 8.4 are compared to those of different sputter-deposited iron oxides. Their results indicate that the iron oxide film formed in the passive region behaves as an n-type semiconductor with the Fe(II) species acting as electron donors. The doping concentration extracted from these measurements agrees with the expected Fe(II) concentration in the oxide film extracted from structural measurements.[14] In addition, it is important to point out the contact electric impedance (CEI) measurements carried out by Bojinov *et al.*[19,20] The authors provide quantitative measurements of the ionic and electronic diffusion coefficients (D_i and D_e, respectively), showing that $D_i \ll D_e$ by several orders of magnitude and hence concluding that the passive film on iron behaves predominantly as an electronic conductor.

Electrochemical scanning tunneling microscopy (EC-STM) is a powerful tool for investigating the electronic structure and conduction mechanism through the iron oxide films, since it can be used alternatively as an *in situ* imaging tool or as an *in situ* spectroscopic technique.[21] In the last case, the main advantage is that the tuning probe can provide direct electronic information of the interface, not needing *a priori* electrical model. To date, few studies have dealt with tunneling through the iron oxide film by EC-STM. Ryan *et al.*[22] have shown images of an iron oxide passive film electrochemically formed over a sputtered iron thin film for electrode potentials more anodic than the Fe(II) existence potential range, but the measurements were only addressed to structural elucidation. On the other hand, Schreyer *et al.*[23] performed measurements by EC-STM of the observed local barrier height on a polycrystalline iron surface when the applied sample potential is increased within the Fe(II) potential region, observing for the first time the breakdown of the tunneling signal at electrode potentials over this region. These results were explained by the authors assuming that the tunneling mechanism is based on the Fe^{2+} species as the resonance centers of the electrons tunneling through the oxide film and that these centers are oxidized to Fe(III) at potentials more anodic than 200 mV *vs.* Ag/AgCl.

In this paper we report for the first time highly stable EC-STM conditions for imaging thick iron oxide films electrochemically formed on a polycrystalline iron surface at high anodic potentials in the so-called passive region. These results allow us to propose a quantitative model of the electronic structure of the iron oxide film as well as to give the first characterization of some fundamental parameters of these semiconducting electronic properties. Furthermore, electrochemical impedance spectroscopic (EIS) measurements on these electrodes are also presented and successfully compared to the electronic model proposed for the iron oxide film.

Experimental

The samples used in this study were mechanically polished polycrystalline iron disks (99.99%), 0.3 mm thick and 10 mm in diam-

* Electrochemical Society Active Member.
[z] E-mail: f.sanz@qf.ub.es

Journal of The Electrochemical Society, **150** (7) B348-B354 (2003) B349

eter. The chemical purity of this surface was previously checked *ex situ* by X-ray photoelectron spectroscopy (XPS).[1] The polishing procedure involved a first step of grinding by silicon carbide polishing papers (30, 9, 5, 3, and 1 μm particle size, successively) and then finishing with 0.3 μm aluminum oxide powder. Between each polishing step, the iron surfaces were sonicated in Milli-Q water and ethanol. Before each experiment the samples were thoroughly rinsed in different solvents in order to remove organic contamination from the surface, followed by a final rinse in Milli-Q water. With this treatment we obtained a mirror-like surface with a mean roughness of typically less than 2 nm[1].

EC-STM studies were performed at room temperature by using a Molecular Imaging microscope head (Phoenix, AZ, USA) controlled by a Nanoscope IIIa electronics (Digital Instruments, Veeco Metrology Group, St. Barbara, CA, USA). The STM electrochemical cell was made of Teflon and exposed a sample area of 0.42 cm^2 to the solution through an O-ring. A Pt wire was used as a counter electrode and a homemade true Ag/AgCl reference electrode with a double membrane to avoid chloride contamination was incorporated. All potentials presented in this work are quoted with respect to this electrode. STM tips were prepared by the electrochemical etching of a Pt/Ir 80:20 wire in an acidic $CaCl_2$ solution and covered with Apiezon wax. Tips prepared with this method present a broad working potential range in our working electrolytic media.[1] The measured tip current at potentiostatic conditions was less than 0.1 nA. All STM images were recorded in the constant current mode at typical tunneling set-point currents ranging from 1 to 3 nA.

The electrochemical impedance measurements were performed at room temperature with a Solartron Instruments electrochemical interface (SI 1287 model, Hampshire, England) coupled to a Solartron HF frequency response analyzer, SI 1255 model. All impedance measurements were done with an excitation signal of 10 mV amplitude and frequencies ranging from 1 Hz to 5 kHz. The impedance data were analyzed with the software package Zview, 2.3+ version. The supporting electrolyte was a borate buffer solution of pH 7.5 made of 0.3 M H_3BO_3 and 0.0375 M $Na_2B_4O_7 \cdot 10\ H_2O$. All solutions were prepared with pro analysis purity grade chemicals from Merck (Darmstadt, Germany) and Milli-Q water of 18 MΩ cm.

Results and Discussion

EC-STM measurements.—Figure 1 shows a set of EC-STM images of an iron electrode surface at different applied potentials in borate buffer at pH 7.5. Figure 1a was taken at a potential of −750 mV after running cathodic reduction at −1.05 V for 15 min. A flat metallic iron surface was observed, whose roughness was given by the previous mechanical treatment.[1] A short potential step into the Fe(II) potential region produces the appearance of small grains at some points of the surface (see upper half of Fig. 1b) and the process can be visualized by EC-STM within the entire Fe(II) potential range.[1] However, when the sample potential is shifted to the Fe(III) potential region while keeping constant tunneling bias, unstable tunneling conditions are obtained and the EC-STM image is eventually lost (lower half of Fig. 1b). Note that Fig. 1a, b, and upper half of d were registered at approximately the same sample bias potential, between 200 and 250 mV. It is important to denote that in the conditions corresponding to the lower half of Fig. 1b and the upper half of Fig. 1d, we observed STM tip crashing on the iron oxide surface, often resulting in the removal of the Apiezon isolating layer. This effect was first reported by Schreyer *et al.*[23] who found that the tunneling signal breaks down at a sample potential close to the Fe(III) potential region. Recent advances in the characterization of these layers by EIS measurements (see next section) and other *in situ* spectroscopic techniques[2-16] have revealed that a high concentration of Fe(II) divalent centers remains in the iron passive film at anodic potential within the Fe(III) potential region. To take these results into account, the breakdown of the tunneling regime can be attributed to the buildup of an electronic energy barrier at the interface, due to the development of an n-type space-charge region (SCR), which would be depleted of electrons at potentials more

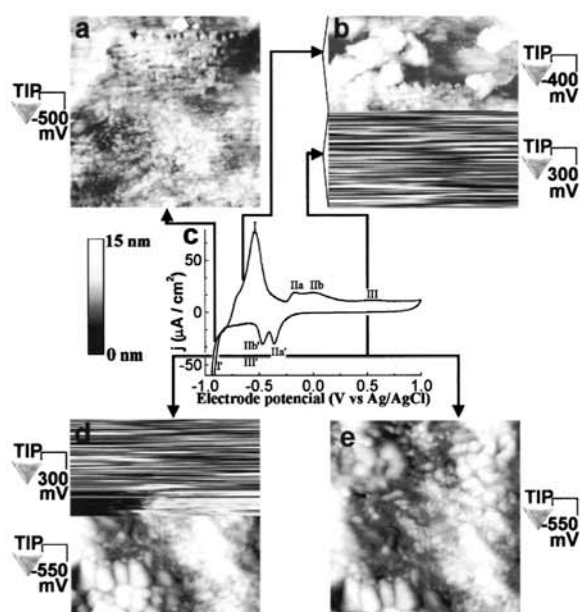

Figure 1. EC-STM images of the iron oxide film formation in borate buffer at pH 7.5 and at sample potentials of: (a) −750 mV, (b) upper half −650 mV and lower half +500 mV, (d) and (e) +500 mV. Image scan size: 400 × 400 nm^2. Tip potential is indicated next to the corresponding image. In the case when two different tip potentials were used in the same image, the values have been specified next to each corresponding part. (c) Cyclic voltammogram of the electrochemical system. Scan sample potential rate, 5 mV/s.

positive than U_{FB}. If this was the case, stable *in situ* STM image within the passive region would still be possible by transferring electrons directly from the tip to the conduction band (CB) of the semiconducting oxide film. Indeed, this is shown in the lower half of Fig. 1d, where an EC-STM image can be recovered again at higher anodic potentials in the Fe(III) region by simply applying a high enough tip cathodic potential. In this view, the tip potentials commonly used for Fe(II) oxide imaging, correspond to energy levels within the forbidden bandgap of the Fe(III) oxide semiconductor,[1,23] being the absence of electronic states responsible for the observed unstable tunneling conditions. In order to restore the stable tunneling conditions, the tip potential must be set to more negative values (see lower half of Fig. 1d and e). The stability of the tunneling current and, what is more important, the stability of the surface topography as we scan the oxide surface keeps constant for hours.

A more accurate study of the *in situ* tunneling behavior as a function of the tip potential in the Fe(III) oxide region allowed us to quantitatively locate the transition potential that we attribute to the conduction bandedge (Fig. 2): the EC-STM images were collected at a sample potential of +500 mV. In order to have a thick (20 nm[1]) oxide layer where a deep space-charge region (SCL) could be completely developed, the oxide film was formed following a two-step procedure. Before oxidation, the air-born oxide was removed by applying a potential of −1.05 V for 15 min. The first oxide-forming step was made by scanning the potential from −1.05 to −0.55 V at 5 mV/s rate, where the Fe(0) to Fe(II) process takes place. Then, the potential was held for 10 min in order to let the Fe(II) oxide film grow completely, as previously reported.[1] Finally, the potential was scanned again from −0.55 V to a selected potential in the passive region [Fe(III) oxide range] and held there for 30 min, until a residual current of 0.5 μA was reached. Of course, with this treatment, a bilayer structure for the iron passive film will be obtained as

B350 Journal of The Electrochemical Society, 150 (7) B348-B354 (2003)

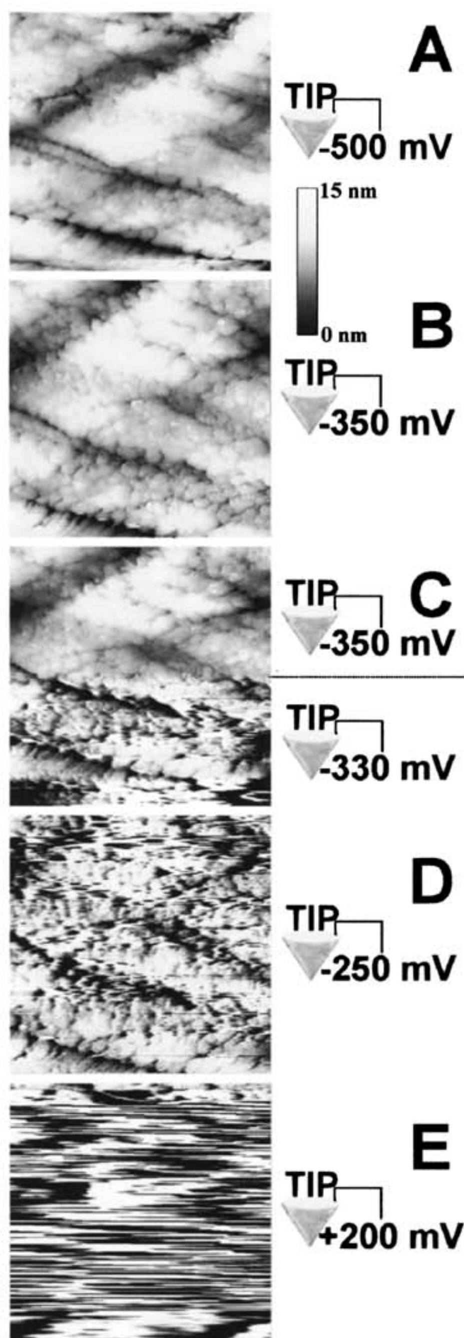

Figure 2. Set of EC-STM images taken on the same surface area of the iron oxide film formed in a pH 7.5 borate buffer and at a fixed sample potential of +500 mV. Images were recorded at increasing tip potentials as indicated on the right side. Image scan size: $400 \times 400\ nm^2$.

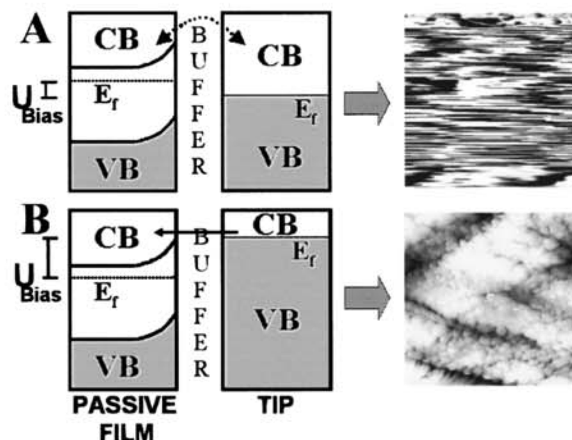

Figure 3. Mechanism scheme of the electron tunneling between the STM tip and the iron oxide film at high anodic potentials in the passive region: (A) nontunnelable conditions and (B) stable tunneling conditions.

previously explained elsewhere.[1,17] Next to the oxide growth, the tip potential was stepped from −500 to +200 mV at intervals between 10 and 20 mV and *in situ* STM images were being registered immediately after each potential step.

It was found that for tip potentials more positive than −350 ±20 mV, stable tunneling conditions are no longer possible. The accurate evaluation of the tunneling regime can be done through the measured tunneling current flowing between the tip and the sample directly taken from the STM current preamplifier. We observed that a tip potential step over a more positive value than −350 mV, results in the beginning of slight instabilities in the measured tunneling current which can be detected in the STM image as a clear distortion of the surface topography (see Fig. 2c). This situation is sketched in Fig. 3. We interpret the abrupt increase in tunneling current when the tip potential was stepped to be due to the overlap between tip electronic states and the semiconductor conduction band. Beyond $U_C = -350 \pm 20$ mV, the energy level of the conduction band-edge can be reached, and, consequently, it is possible to inject electrons from the tip into the oxide film (see Fig. 3B) and to get stable EC-STM images of the semiconducting iron oxide film. On the other hand, at tip potentials lying under the conduction band level and/or in the semiconductor bandgap, the electron injection and thereby the stability of the EC-STM images are no longer possible (see Fig. 3A). The uncertainty of ±20 mV is in agreement with electrons overcoming the low energy barrier at these potentials ($\leq kT$) by thermal excitation at room temperature, which still allows STM imaging. Remarkably, the CB edge that we obtain is much sharper than is expected for amorphous or noncrystalline materials, whose density of states has tails extending into the so-called mobility gap.[24] It is important to highlight here that, in spite of the general image noise and distortion observed at tip potentials more positive than −350 mV, the actual surface topography observed at a tip potential values of −500 and −350 mV (Fig. 2A and B) can still be recognized at tip potentials of −330 and −250 mV (Fig. 2C and D). At potentials higher than −250 mV, complete image loss was observed and consequently the surface topography can no longer be distinguished (Fig. 2E). In order to interpret the different observed transitions of the tunneling regime as the tip potential is shifted through the conduction bandedge (Fig. 4), several points must be taken into account. The stable tunneling regime obtained for Fig. 2A and B has been represented in the image A of Fig. 4, where a high density of empty states on the iron oxide surface is accessible to electrons coming from the STM tip. The tip-sample distance is defined by the fixed current set point and the difference between both sample and tip Fermi levels (bias potential) through the classical STM exponential current-distance(s) dependence $I \propto V \exp(-As\sqrt{\Phi})$ described elsewhere,[25] where Φ is the mean local tunneling barrier height and A is a constant. In our case, this

Journal of The Electrochemical Society, **150** (7) B348-B354 (2003) B351

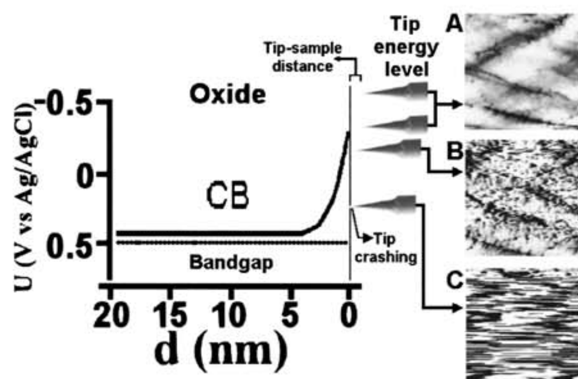

Figure 4. Detailed scheme of the three different tunneling regimes recorded at +500 mV sample potential and at different tip potentials around the conduction bandedge of the semiconducting iron passive film. Tip potential values of: (A) −550 and −350 mV, (B) −250 mV, and (C) +200 mV. Inset of selected EC-STM images from Fig. 2.

barrier Φ arises in part from the development of a SCL in the semiconducting material. At tip potentials more positive than the conduction band level (see Fig. 4B), the density of states on the surface starts to decrease as corresponds to the forbidden bandgap of the semiconducting oxide,[26] and the barrier experienced by electrons on the tip increases. However, this barrier can also be tunneled under certain conditions, such as at the sample potentials in the passive region, the semiconducting oxide is in strong depletion (see Fig. 4 and the next section for the measurement of the flatband potential), and therefore, at energies near the conduction bandedge the SCL is still thin enough so that electrons can still tunnel through the energy barrier of the oxide directly into the conduction band. In terms of the tunneling mechanisms, the local energy barrier has increased with respect to the situation in which the tip energy level lies directly within the conduction band (no barrier at the oxide, see Fig. 4A). As a result, at a fixed tunneling current set point, the tip-sample distance(s) has to be decreased by the STM feedback system, according to the previous exponential relationship. Now this situation produces a lower overlap between the tip electronic states and the conduction band, as well as the possibility of tip-sample physical contact due to their closer proximity, in agreement with the observed EC-STM image distortion (see Fig. 4B). As the tip potential is progressively shifted to more anodic values, the energy barrier increases and the tip-surface distance decreases, until at potentials more positive than −250 mV, the SCL becomes thick enough (approximately over 1 nm) to be nontunnelable. At this point the complete image loss as well as tip crashing were observed during the experiment (see Fig. 4C).

This particular tunneling behavior is observed for all potentials applied to the sample within the passive region. Figure 5 shows same EC-STM images (a and b) at two different sample potentials in the passive region by keeping the tip potential at the same value in the conduction band level. As can be observed, the stability of the tunneling regime is independent of the applied sample potential in agreement with the represented band model (the same Fig. 5). Moreover, we observe that there are no dynamic surface processes occurring for the potential range corresponding to the passive region, in contrast to what happens at early potentials in the active region of iron.[1] The image is again lost at more anodic tip potentials (Fig. 5c). At this point it is important to highlight that tip-induced modifications of the oxide film are never observed, even in the case in which we would achieve to inject electrons through the valence band (which is not the case). We need not forget that we are fixing the electrochemical potential in the Fe(III) passive region, which means

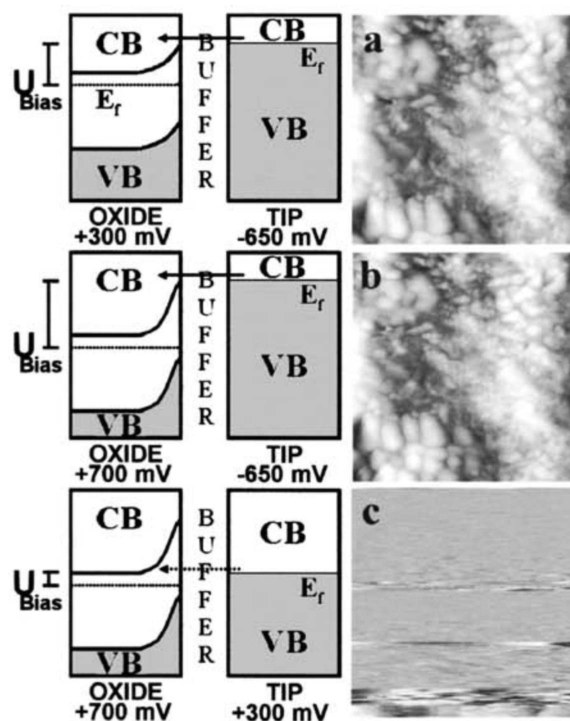

Figure 5. EC-STM images taken on the same area of the iron passive film formed in pH 7.5 borate buffer where both tip (U_{tip}) and sample potentials (U_S) were changed. Tunneling mechanism and U_{tip}, U_s values are included for each image. 400 × 400 nm^2 scan size and 15 nm z scale.

that the tip-reduced Fe(II) would reoxidize quickly to the Fe(III) form.

With the aim of applying this technique as a spectroscopic tool on this system, we attempt to differentiate the type of iron oxide electrochemically grown on the surface, by studying the behavior of the tunneling regime as a function of the potential applied to the tip. For this purpose, we repeated the experiment summarized in Fig. 2, but this time with an iron oxide grown at a potential in the Fe(II) region. The results are presented in Fig. 6, showing that the behavior of the tunneling current is completely different from the Fe(III) region, which indicates a different electronic structure. In this particular case, the Fe(II) oxide film can be visualized even at very positive tip potentials (see Fig. 6) when the Fe(III) oxide in the passive region shows a clear image loss. An interpretation from the point of view of the electronic structure for the Fe(II) oxide is still unclear due to the lack of information on its electronic properties, although it is generally agreed that the structure of the film is an Fe(II) oxohydroxide probably hydrated.[6-10,26] Our results (Fig. 6) show that the film is conductive either due to a highly defective structure or to a very narrow mobility gap.[24] No evidence is found for the formation of an electron barrier in the material at these potentials. In case a highly defective structure would be created on the Fe(II) oxide surface, the resulting new surface energy levels could act as a resonance center for the electron tunneling to the conduction band of the Fe(II) oxide. With this qualitative model, the slight differences that can be observed in the surface topography registered at lower and higher tip potentials (see Fig. 6a and c, respectively) could be explained in the same manner as Zuili *et al.*[27] accounts for the different topography of the passive nickel oxide film obtained at different tip potentials. These results were interpreted as tunneling through different localized states in the oxide bandgap associated with different oxide structures in the nickel passive film.

B352 Journal of The Electrochemical Society, 150 (7) B348-B354 (2003)

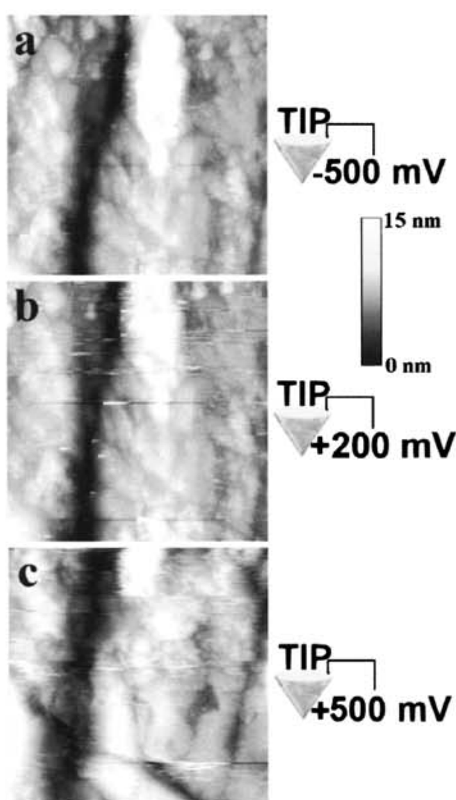

Figure 6. EC-STM series of images taken on the same passive film surface area formed in pH 7.5 borate buffer at the same $U_s = -690$ mV. Different U_{tip} indicated next to the image. 600 × 600 nm^2 scan size.

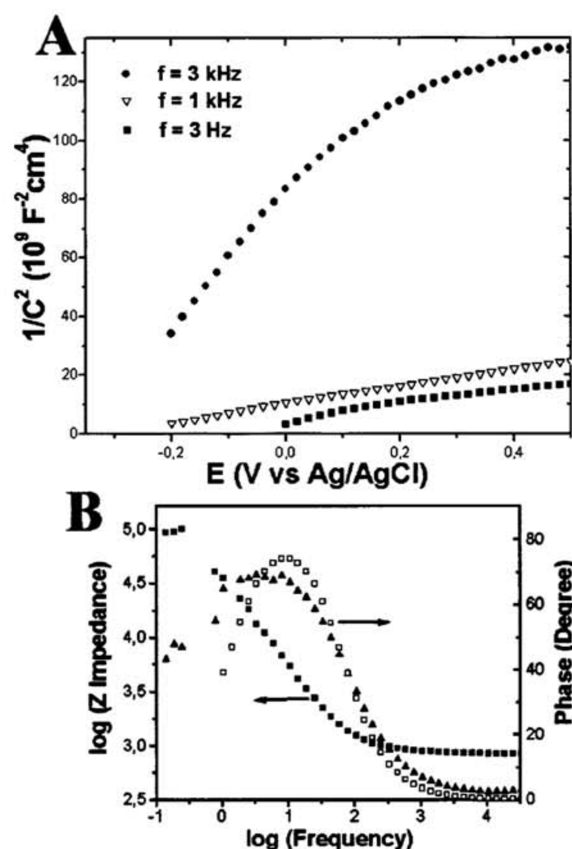

Figure 7. (A) Mott-Schottky plots calculated from the pure capacitance values for the iron oxide film grown at +700 mV in pH 7.5 borate buffer. (B) Bode plot representation of the impedance for the same passive film. Filled symbols correspond to the total impedance of the oxide‖electrolyte interface and open symbols correspond to the same signal with electrolyte resistance subtraction.

It must be stressed that our EC-STM results provide a direct experimental measurement of the conduction bandedge energy, not addressing an electrical model as when EIS data occurs (see the next section). In addition, these results make it possible to characterize *in situ* the topography of the iron oxide film at high anodic potentials in the passive region as well as studying dynamic electrochemical processes that can take place on this surface. Further quantification and the validation of the quantitative band model deduced by EC-STM for the iron passive film is carried out in the next section.

Capacitance measurements.—Figure 7 shows the results of the capacitance measurements of an electrochemically formed iron oxide film at +700 mV in borate buffer solution at pH 7.5. The oxide film was grown following the same electrochemical procedure detailed above. Impedance measurements were then performed at different frequencies and the electrode capacitance was computed assuming a classical resisto-capacitor (RC) parallel equivalent circuit. A constant phase element (CPE) was accounted for in the electrical model for the correction of the capacitance response of the semiconducting oxide film, although as it was found by other authors,[17] the contribution to the final extracted semiconducting parameters was very small. The flatband potential (U_{FB}) was determined by extrapolating the curves $1/C^2$ *vs.* U at $1/C^2 = 0$ using the Mott-Schottky relationship and assuming an $\varepsilon = 10$ for an Fe_2O_3 film.[16] The doping concentration N_D was calculated from the slope of the linear part, where a positive slope indicates n-type behavior of the layer.[28]

Figure 7A shows that there is a dispersion of the Mott-Schottky behavior as a function of the working frequency. In order to fit the classical model of a parallel RC equivalent circuit to the iron oxide film, it is necessary to work at a frequency for which the film presents a purely capacitive behavior (90° phase angle). A study of the capacitance response as a function of the working frequency for the oxide‖electrolyte interface formed at +700 mV in pH 7.5 borate buffer is presented in Fig. 7B. Subtraction of the uncompensated electrolyte resistance at higher frequencies than 100 Hz was also applied in order to get the pure interfacial impedance (open symbols in Fig. 7b). The capacitance behavior observed by the negative slope of the log (impedance) *vs.* log (frequency) curve ranges from 30 Hz to 1 kHz, the former one corresponding to the maximum phase angle (see Fig. 7b). The Mott-Schottky plots measured in this frequency range (see Fig. 7a) give similar values of U_{FB} and N_D, as observed in Table I. At the highest phase angle, the $U_{FB} = -280$ mV and the

Table I. Values of U_{FB} and N_D from Mott-Schottky plots at different frequencies.

Frequency (Hz)	N_D (cm^{-3})	E_{FB} (V *vs.* Ag/AgCl)
5000	9.4×10^{19}	−0.430
3000	1.7×10^{20}	−0.380
1000	1.3×10^{21}	−0.290
30	2.0×10^{21}	−0.280

Journal of The Electrochemical Society, **150** (7) B348-B354 (2003) B353

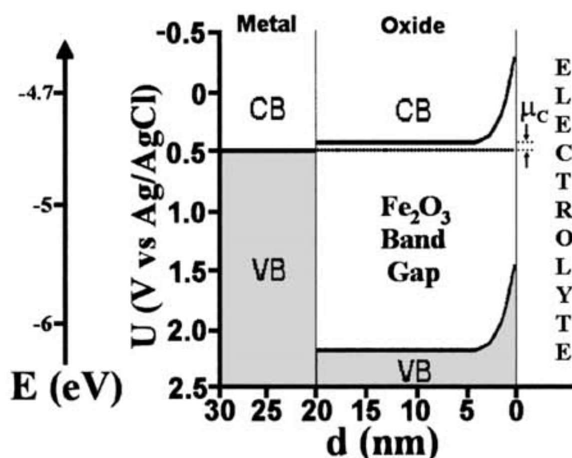

Figure 8. Scheme of the quantitative band model for the Fe^0||iron passive film||electrolyte interface at an anodic $U_s = +500$ mV.

obtained N_D value are in good agreement with the CB edge found by EC-STM at slightly more negative potentials than U_{FB} (-350 mV). When using frequencies higher than 1 kHz, the phase angle is very low, indicating the inadequacy of the equivalent circuit model. In addition, at these higher frequencies, the extrapolated FB values are not consistent with the CB edge observed directly by EC-STM and were therefore disregarded.

The experimental data obtained in this study are combined in Fig. 8 to sketch a quantitative energy diagram for the iron|iron passive film|electrolyte interface. The stability of the oxide films is often attributed to ion-selective layers,[24] but electronic effects can also play an important role. It was recently reported[19,20] that the passive film on iron behaves predominantly as an electronic conductor. Here we have shown that the anodically formed film is a highly doped, quasi-degenerated n-type semiconductor, whose passivity may arise from the ~5 nm thick SCL, depleted of electrons and nontunneable at far anodic potentials. Such SCL produces an electronic energy barrier at the oxide|electrolyte interface that can be overcome by tunneling electrons from an EC-STM tip at sufficiently negative potentials, but that would be insurmountable for most oxidative processes at the interface. This band model should be useful for the understanding and prediction of the (electro)chemical reactions taking place on the oxide surface and/or for the better understanding of the corrosion mechanism of this system.

We further attempt to estimate some electronic parameters of the Fe(III) oxide, which to our knowledge, have never been reported. The difference $\mu_C \equiv U_{FB} - U_C \approx 70$ mV indicates that the semiconductor is highly doped but still far from degeneration.[29] [Although $\mu_C < 4k_BT/e$ is not the purely nondegenerative case, at $\mu = 70$ mV the semiconductor is still far from degeneration ($\mu_C \leqslant 0$), and the error in assuming Maxwell-Boltzmann statics is low (electron density overestimated by a factor of 1.02).] If all donor impurities are ionized, the electron density is equal to the net dopant density (*i.e.*, N_D assuming that the density of donors is much larger than the density of acceptors). The following relationship then holds[28]

$$U - U_C = (k_BT/e)\ln(N'_C/N_D) \qquad [1]$$

which is expressed in terms of the electrode potential U (corresponding to the Fermi energy level), the bandedge potential U_C, and the effective density of the conduction band states N'_C. At the flatband potential ($U = U_{FB}$), considering $\mu_C = 70$ mV measured by EC-STM, and $N_D = 2 \times 10^{21}$ cm^{-3} obtained by EIS,[17,30] an estimate of $N'_C \sim 2.5 \times 10^{22}$ cm^{-3} can be provided for the Fe(III) oxide layer. This is a very high value but includes the contribution of the different conduction band minima υ (*i.e.*, $N'_C = \upsilon N_C$). We have not found data for υ of Fe_2O_3 or Fe_3O_4 in the bibliography. In any case, the following expression allows the calculation of the density-of-states effective mass of electrons for Fe(III) oxide

$$N'_C = 2(2\pi m^*_{dn}k_BT/h^2)^{3/2} \qquad [2]$$

which yields $m^*_{dn}/m_0 = 0.01$, m_0 being the free electron mass and again including the contribution of the different band minima. Moreover, having the μ_C value, the surface potential barrier created at the semiconductor|electrolyte interface for each sample potential can be directly estimated and hence, the thickness of the SCL can be calculated[28] (*e.g.*, 5 nm at $U = +500$ mV). Note that this is considerably lower than the total thickness of the film[31] formed in these conditions (20 nm[1], see Fig. 8).

Conclusions

Whole-electrode impedance spectroscopy together with local EC-STM imaging and investigations about the stability of EC-STM tunneling regime have been addressed to obtain, for the first time, well-defined imaging conditions for the thick iron oxide film electrochemically formed on an iron polycrystalline surface at the potentials of the anodic plateau corresponding to the so-called passive region. We propose a quantitative band model for the oxide film that accounts for the obtained results and allows the measurement of the energy barrier at the oxide/electrolyte interface, and the ability to give the first estimates of some electronic parameters of the Fe(III) oxide film. It is suggested that the passivity of iron electrodes arises from the buildup of the nontunnelable energy barrier at the oxide|electrolyte interface. Work is underway in our laboratory to elucidate the avalanche electrochemical processes involved in the onset of conduction when the anodic plateau is broken, the so-called transpassive region.

The use of the STM tip as a tunable energetic probe provides direct information about the electronic structure of the interface and does not require any electrical model to be assumed. Furthermore, it allows the validation and complements the EIS data. The study of the tunneling regime stability as a function of the probe (STM tip) potential can be applied to the recognition of different iron oxides formed on the surface under electrochemical control. This allows the performance of *in situ* tunneling spectroscopy on the basis of differences in the electronic properties of these materials, and could therefore be extended to many other systems.

Acknowledgments

The authors are grateful to Scientific-Technical Services of the University of Barcelona for the use of facilities. Financial support of the present work comes from the CYCIT under research project MAT2000-0986.

University of Barcelona assisted in meeting the publication costs of this article.

References

1. I. Díez-Pérez, P. Gorostiza, F. Sanz, and C. Müller, *J. Electrochem. Soc.*, **148**, B307 (2001).
2. M. F. Toney, A. J. Davenport, L. J. Oblonsky, M. P. Ryan, and C. M. Vitus, *Phys. Rev. Lett.*, **79**, 4282 (1997).
3. M. Büchler, P. Schmuki, and H. Böhni, *J. Electrochem. Soc.*, **144**, 2307 (1997).
4. N. Sato and K. Kudo, *Electrochim. Acta*, **16**, 447 (1971).
5. V. Jovancicevic, R. C. Kainthla, Z. Tang, and J. O'M. Bockris, *Langmuir*, **3**, 388 (1987).
6. J. C. Rubim and J. Dünnwald, *J. Electroanal. Chem.*, **258**, 327 (1989).
7. J. Gui and T. M. Devine, *J. Electrochem. Soc.*, **138**, 1376 (1991).
8. J. C. Rubim, *J. Electrochem. Soc.*, **140**, 1601 (1993).
9. J. C. Rubim, *Trends Corros. Res.*, **1**, (1993).
10. V. Schroeder and T. M. Devine, *J. Electrochem. Soc.*, **146**, 4061 (1999).
11. M. Kerkar, J. Robinson, and A. J. Forty, *Faraday Discuss. Chem. Soc.*, **89**, 31 (1990).
12. G. G. Long, J. Kruger, D. R. Black, and M. Kuriyama, *J. Electroanal. Chem.*, **150**, 603 (1983).

B354 Journal of The Electrochemical Society, **150** (7) B348-B354 (2003)

13. R. W. Hoffman, in *Passivity of Metals and Semiconductors*, M. Froment, Editor, p. 147, Elsevier Science Publishers B.V., Amsterdam (1983).
14. L. J. Oblonsky, A. J. Davenport, M. P. Ryan, H. S. Isaacs, and R. C. Newman, *J. Electrochem. Soc.*, **144**, 2398 (1997).
15. S. Virtanen, P. Schmuki, M. Büchler, and H. S. Isaacs, *J. Electrochem. Soc.*, **146**, 4087 (1999).
16. A. J. Davenport, L. J. Oblonsky, M. P. Ryan, and M. F. Toney, *J. Electrochem. Soc.*, **147**, 2162 (2000).
17. M. Büchler, P. Schmuki, H. Bühni, T. Stenberg, and T. Mäntylä, *J. Electrochem. Soc.*, **145**, 378 (1998).
18. M. Büchler, P. Schmuki, and H. Böhni, *J. Electrochem. Soc.*, **145**, 609 (1998).
19. M. Bojinov, G. Fabricius, T. Maitinen, K. Mäkelä, T. Saario, and G. Sundholm, *J. Electrochem. Soc.*, **146**, 3238 (1999).
20. M. Bojinov, T. Laitinen, K. Mäkelä, and T. Saario, *J. Electrochem. Soc.*, **148**, B243 (2001).
21. I. Díez-Pérez, P. Gorostiza, F. Sanz, and C. Müller, *Scanning Probe Techniques for Materials Characterization at Nanometer Scale*, D. C. Hansen, H. S. Isaacs, and K. Sieradzki, Editors, PV 2000-35, p. 122, The Electrochemical Society Proceedings Series, Pennington, NJ (2000).
22. M. P. Ryan, R. C. Newman, and G. E. Thompson, *J. Electrochem. Soc.*, **142**, L177 (1995).
23. A. Schreyer, L. Eng, and H. Böhni, *J. Vac. Sci. Technol. B*, **14**, 1162 (1996).
24. N. F. Mott and E. A. Davis, *Electronic Processes in Non-crystalline Materials*, 2nd. ed., Clarendon Press, Oxford (1979).
25. *Scanning Tunneling Microscopy I*, H. J. Güntherodt and R. Wiesendander, Editors, p. 7, Springer-Verlag, Heidelberg (1992).
26. M. Sakashita and N. Sato in *The Passivity of Metals*, R. P. Frankenthal and J. Kruger, Editors, p. 479, The Electrochemical Society Corrosion Monograph Series, Princeton, NJ (1978).
27. D. Zuili, V. Maurice, and P. Marcus, *J. Electrochem. Soc.*, **147**, 1393 (2000).
28. S. R. Morrison, *Electrochemistry at Semiconductor and Oxidized Metal Electrodes*, p. 68, Plenum Press, New York (1980).
29. See, e.g., S. S. Li, *Semiconductor Physical Electronics*, Plenum Press, New York (1993).
30. P. Schmuki and S. Virtanen, *Electrochem. Soc. Interface*, **6(2)**, 38 (1997).
31. E. Sikora and D. D. Macdonald, *J. Electrochem. Soc.*, **147**, 4087 (2000).

4.3 ELECTRONIC BARRIERS IN THE IRON OXIDE FILM GOVERN ITS PASSIVITY AND REDOX BEHAVIOR: EFFECT OF ELECTRODE POTENTIAL AND SOLUTION pH

Reference: I. Díez-Pérez, P. Gorostiza and F. Sanz, *Electronic barriers in the iron oxide film govern its passivity and redox behavior: Effect of electrode potential and solution pH*, Electrochem. Comm., **8** (2006) 1595.

Reprinted from the above publication, © Elsevier 2006, with permission from Elsevier.

ELSEVIER

Available online at www.sciencedirect.com

Electrochemistry Communications 8 (2006) 1595–1602

electrochemistry communications

www.elsevier.com/locate/elecom

Electronic barriers in the iron oxide film govern its passivity and redox behavior: Effect of electrode potential and solution pH

I. Díez-Pérez [a], F. Sanz [a,b,*], P. Gorostiza [b,*]

[a] *Laboratory of Electrochemistry and Materials (LCTEM), Department of Physical Chemistry, University of Barcelona, Martí i Franquès 1, 08028 Barcelona, Spain*

[b] *Centre de Referència en Bioenginyeria de Catalunya, Parc Científic de Barcelona, Josep Samitier 1-5, Barcelona 08028, Spain*

Received 20 June 2006; received in revised form 7 July 2006; accepted 11 July 2006
Available online 17 August 2006

Abstract

We have measured *in situ* the electronic conductance spectra of the passive film formed on an Fe electrode immersed in a borate buffer solution using electrochemical tunneling spectroscopy (ECTS) and electrochemical impedance spectroscopy (EIS) techniques, and we have followed their changes as the electrode is electrochemically oxidized and reduced. We demonstrate that pre-passive Fe(II) oxide and the passive Fe(II)/Fe(III) film, behave as p- and n-type semiconductors, respectively and that their reversible inter-conversion is mediated by the availability of free charge carriers on the electrode surface. ECTS spectra have been also modeled to obtain the main electrochemical kinetic parameters of the electron transfer through both p-Fe(II) and n-Fe(III) oxides at different sample potentials and pHs values. We find that the electronic energy barrier in the oxide and its dependence with electrode potential and solution pH, determine the reactivity and passivity of iron.

© 2006 Elsevier B.V. All rights reserved.

Keywords: Electrochemical tunneling spectroscopy; Fe passivity; Electronic energy barriers; pH effect on passivity

1. Introduction

The phenomenon of passivity is based on the spontaneous formation of a surface oxide layer that prevents a metallic electrode from corroding [1]. However, the detailed mechanism of the passive film growth and the electronic effects responsible for the electrode protection, are still poorly understood. Fundamental work on passive films on metallic electrodes has been based on conventional electrochemical techniques, typically in neutral and alkaline media. The chemical composition and structure of passivated surface electrodes have been recently investigated by *ex situ* structural methods like microscopy and spectroscopy in vacuum [2,3]. *In situ* techniques have been the key to understand the chemical composition and structure of passive film on metals and steels in solution [4–7]. The introduction of scanning tunneling microscopy (STM) and its application to electrochemistry (ECSTM) [8] has allowed further insights into the structure and electronic properties of the passive film in the solution of interest [9,10], including the recent applications of ECTS [11–14].

The passive film on iron and other transition metals present a semiconducting character [15]. The complete model proposed for the Fe passive film structure in most of the experimental conditions (static hydrodynamic conditions and potential scanning) consists on a structure that resembles a spinel Fe_3O_4 or a defective γ-Fe_2O_3, being $Fe_{1.9\pm0.2}O_3$ the closest measured stoichiometry (mostly Fe(III)) [4]. The outer interphase of the passive layer

* Corresponding authors. Address: Laboratory of Electrochemistry and Materials (LCTEM), Department of Physical Chemistry, University of Barcelona, Martí i Franquès 1, 08028 Barcelona, Spain. Fax: +34 93402 1231.

E-mail addresses: fsanz@ub.edu (F. Sanz), pau.gorostiza@ub.edu (P. Gorostiza).

1388-2481/$ - see front matter © 2006 Elsevier B.V. All rights reserved.
doi:10.1016/j.elecom.2006.07.015

1596 I. Díez-Pérez et al. / Electrochemistry Communications 8 (2006) 1595–1602

(the oxide/electrolyte side) is suggested to have a higher concentration of cation interstices (Fe(III) form is predominant) [4], eventually terminated by a hydrated Fe(III) hydroxide film [10,15], while at the inner metal/oxide interphase an excess of Fe(II) vacancies is expected. The presence of this particular outer interphase confers a fairly ideal n-type behavior to the Fe passive film that is named Fe(III) passive film for simplification. In general, the Fe passive film presents an n-type behavior with the Fe(II) centers acting as electron donors [15,16]. The excess of vacancies close to the metal/oxide interphase may serve as an ohmic contact between the metal and the n-Fe(III) outer interphase, as suggested by the increase in conductance when the outer film is dissolved [17]. This is analogous to heavily doped metal/n^{++}/n and metal/p^{++}/p ohmic contacts used in microelectronics. On the other hand, the properties of the Fe pre-passive oxide that forms at low electrochemical potentials ($\leqslant -0.3$ V vs. reference electrode and Fe(II) called oxide again for simplification) [10,18,19] have not been well defined, although they can strongly influence the properties of the final passive film. As relevant information of this Fe(II) pre-passive layer, its partial solubility in nearly neutral media has been demonstrated in some instances [10,20]. Although several general models of the Fe passive film were proposed 15 years ago [21,22], the implications of its electronic properties on the electrode redox behavior are not yet completely understood.

In this study, we show reproducible local *in situ* electrochemical tunneling spectra of the iron electrode/borate buffer interface while it is reversibly oxidized and reduced under electrochemical control. The experimental ECTS spectra are presented in the form of conductograms [23] that allow to analyze the observed transitions in the electronic properties of the electrode during the electrochemical processes. Our EIS results confirm the n-type properties of Fe(III) and reveal the p-type character of Fe(II). The electrochemical oxidation and reduction of Fe to form and dissolve its surface passive film can be then explained by the interconversion of p-Fe(II) to n-Fe(III) oxides and *vice versa*, at the electrode surface. The availability of charge carriers on both semiconducting surfaces gives rise to the oxidation of p-Fe(II) and the reduction of n-Fe(III) when the Fermi level (E_F) approaches the corresponding Flatband values. The electronic properties of Fe(II) and Fe(III) oxides (Flatband potential, doping type and concentration) are combined with ECTS data to elaborate a band diagram model of the electrochemical processes. The electrochemical kinetic parameters of the electron transfer through the Fe passive film at different sample potentials and pH values are quantitatively obtained by fitting the ECTS curves to a double exponential Butler–Volmer relation. It is found that electrode reactivity and passivity are coupled to the availability of free charge carriers in the semiconducting Fe passive film, as given by the electrode potential and solution pH.

2. Experimental

2.1. Sample and electrolyte

Mechanically polished iron polycrystalline disks were used as working electrodes and prepared as previously described [10,18]. The working electrolyte consists on a pH 7.5 borate buffer solution prepared from 0.3 M H_3BO_3 and 0.0375 M $Na_2B_4O_7 \cdot 10H_2O$. In all cases pro-analysis purity grade chemicals from Merck (Darmstadt, Germany) and Milli-Q water of 18 MΩ cm, were used.

2.2. Electrochemical measurements

Cyclic voltammetry and capacitance measurements were performed at room temperature using a Solartron Instruments electrochemical interface (SI 1287 model, Hampshire, England) connected to a Solartron HF frequency response analyzer (SI 1255 model). All impedance measurements were done with an excitation signal of 25 mV amplitude (~kT) and frequency of 1 kHz. Thick Fe oxide films were growth by applying a 2-step electrochemical procedure [10,18]. A standard electrochemical cell with a large area Pt counter electrode and a Ag/AgCl reference electrode (SSC) provided with a Luggin capillary, was used. All measurements were made with deaerated borate solutions and under nitrogen atmosphere.

2.3. ECTS measurements

ECTS spectra of almost 2 V amplitude at scan rates up to 20 V/s were recorded, so extremely well insulated STM tips are required to minimize electrochemical noise currents. A detailed explanation of our ECTS set up, complete experimental methodology and preparation procedure of STM probes, have been presented elsewhere [23,24]. Briefly, ECTS curves were acquired at the different Fe oxidation states (U_S) and they were differentiated numerically to obtain the conductance vs. U_S curves. 3D conductance maps (conductograms) were built by stacking conductance curves with the tip potential (U_T) or electron energy (E) represented in the *Y*-axis, the Fe oxidation state in the *X*-axis and the electrode conductance encoded in a vertical gray scale. Tunneling junctions are fixed along the entire conductogram by adjusting the corresponding initial current setpoint at the different initial voltage biases [23]. However, individual ECTS curves are shown without tunneling junction compensation for simplicity. Sample and tip potentials were independently controlled vs. the same reference electrode. ECTS data were captured using a STM system (Pico-SPM, Molecular Imaging, USA) which incorporates a modified STM electrochemical cell with a double-membrane SSC reference electrode and a large platinum wire as counter electrode. All electrochemical potentials presented in this work are quoted vs. the SSC electrode and converted to the vacuum electron energy scale (E) using the relation $E(\text{eV}) = -(U_S + 4.7)$ [25].

I. Díez-Pérez et al. / Electrochemistry Communications 8 (2006) 1595–1602 1597

3. Results and discussion

3.1. Capacitance measurements

EIS was employed to obtain capacitance data of the Fe passive film [15–18] at the different potential regions during anodic oxidation in borate buffer pH 7.5. In order to grow thick and well-controlled Fe oxide films, we follow a 2-step electrochemical procedure as in previous works [10,18], being the final U_S value located within the upper limit of the corresponding Fe(II) and Fe(III) ranges, respectively. Once the electrode is passivated (transient constant current $I_S < 0.5$ μA) the impedance measurements are started. The impedance of the oxide/electrolyte interface is then measured while U_S is scanned back toward the lower limit of the Fe(II) or Fe(III) electrochemical ranges, respectively. Fig. 1a shows the Mott–Schottky (M–S) representation of the capacitance (C) data in both Fe(II) and Fe(III) electrochemical ranges. The Fe(III) oxide presents a n-type behavior within the entire Fe(III) passive region as indicated by the positive slope of the linear M–S relation, and yields a donor density (N_D) of 10^{21} cm^{-3} and a Flat-band potential (U_{FB}) of −280 mV, in agreement with previous works [15–18]. Besides, within the Fe(II) range, the oxide film was grown following the procedure employed in [10] (see also Section 2) to assure a sufficiently thick oxide layer (~20 nm) that preserves it from its chemical dissolution [20]. The oxide presents a negative slope in the M–S plot, corresponding to a p-type behavior with a high acceptor density (N_A) of 10^{22} cm^{-3} and U_{FB} of −200 mV. It must be noted that the transition Fe(II) → Fe(0) occurs concurrently with the hydrogen evolution reaction (HER) [10,19], so the narrow potential range used to measure the M–S of Fe(II) prevents reduction of the film. In view of these results, at least three different behaviors can be expected in the tunneling spectra of the Fe electrode: metallic Fe(0), p-Fe(II) and n-Fe(III) oxides.

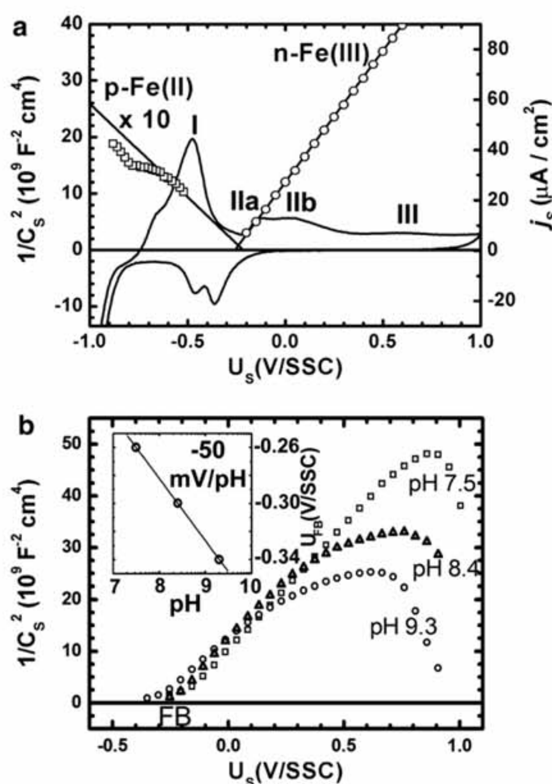

Fig. 1. Mott–Schottky (M–S) representations of the capacitance data of different Fe|oxide|electrolyte interfaces: (a) The M–S plots of Fe(II) and Fe(III) oxides grown in borate of pH 7.5 indicate p- and n-type behavior, respectively. The cyclic voltammogram of the Fe electrode in this medium is added in order to locate the corresponding electrochemical ranges. U_S scan rate of 5 mV/s. (b) M–S plots of the n-Fe(III) oxide grown in borate buffer at different pHs. The inset plot shows a nearly Nernstian shift of the U_{FB} values extrapolated from the M–S plots as a function of pH.

We have also measured the evolution of the capacitance behavior of the n-Fe(III) passive film grown in borate buffer at different working pHs (Fig. 1b). The fit of the M–S linear ranges yield N_D values of the same order of magnitude, ~10^{21} cm^{-3} for all three pHs, while U_{FB} values shift at a ratio of ~50 mV/pH (inset plot in Fig. 1b). This is in agreement with a nearly Nernstian dependence of the band edge position as function of pH, as found in other semiconductors like silicon [27,28]. This indicates that the potential difference across the Helmholtz layer is essentially determined by an acid–base equilibrium [28]. As the pH is increased, the M–S plots of the n-Fe(III) film/borate interface presents a shorter linear range followed by a quadratic dependence at higher U_S. This behavior is explained by the different passive film thicknesses achieved when they are grown at different pHs. Following the 2-step procedure to grow a thick passive film [10,18], the first thickening stage in the active electrochemical range (peak I in Fig. 1a, see also supporting data) gives rise to a progressively thinner Fe(II) film as the pH increases, due to the lower Fe^{2+}(aq) solubility at higher pH [10]. As a result, the expected final thickness of the Fe(III) film grown within the passive electrochemical range (peak III in Fig. 1a) will be the lowest at the highest pH and vice versa. In previous work, we measured a thickness of ~20 nm for the n-Fe(III) passive film at pH 7.5 [10], which is well above the estimated thickness value for the space charge region (SCL) of the semiconducting oxide layer: ~5 nm at $U_S = 500$ mV band bending [17,18]. Therefore, the SCL can be completely developed within the n-Fe(III) passive film formed at pH 7.5 in the entire electrochemical passive range at depletion conditions (M–S of Fig. 1b and left inset of Fig. 3c). At higher pHs, the thickness of the passive film is expected to be in the range of few nm because the oxide film growth takes place essentially through a field-assisted ion transport mechanism [21,27] and less through dissolution–precipitation process in the active range. At pH 8.4, the thickness of the passive film is ~4 nm [15]. At $U_S = 500$ mV, the 5 nm of SCL [17,18] surpasses the oxide thickness and causes

1598 I. Díez-Pérez et al. / Electrochemistry Communications 8 (2006) 1595–1602

the M–S plot to deviate from linear behavior into a quadratic one beyond $U_S = 400$ mV (pH 8.4 in Fig. 1b). The quadratic dependence of the M–S corresponds to a constant C–U characteristic which is due to complete electron depletion of the n-Fe(III) oxide film giving rise to a metal/dielectric/electrolyte interface (see the right inset of Fig. 3c). Further increase of U_S displays the capacitance behavior of this new interface: lowering E_F within the metal does not result in the increasing of the SCL [27], giving rise to a nearly constant capacitance behavior vs. U_S (Fig. 1b). This metal/dielectric/electrolyte interface displays a deep depletion capacitance profile; majority charge carriers are completely depleted and minority carriers (holes h^+ in the n-Fe(III)) are not available until E_F approaches the valence band (VB) edge [27]. When U_S is further increased, E_F approaches the VB edge and minority carriers become available. An inversion layer is then formed [27,30] as observed in all pH conditions (Fig. 1b).

The short linear range displayed in the M–S plot of the n-Fe(III) passive film grown at the highest pH 9.3, shows the lowest thickness value that can be estimated from the linear-to-quadratic threshold to a value of ~2.5 nm, thus indicating that the n-Fe(III) oxide grows purely through a field-assisted ion transport mechanism at a rate of 1–3 nm/V [21], based on the inward oxygen diffusion from the electrolyte.

3.2. ECTS study

In previous works, we reproducibly measured the energy barrier between an ECSTM tip located above the conduction band (CB) edge and the Fe electrode at potentials spanning the entire Fe electrochemical range [23,30] (-1.1 V $< U_S <$ 1 V). We used these results to set stable initial tunneling conditions in order to obtain reproducible ECTS spectra when Fe is reversibly oxidized and reduced within the three main electrochemical ranges (Fe(0), Fe(II) and Fe(III)). The ECTS spectra were collected in the form of tip current vs. potential $I_T(U_T)$ characteristics every 50 mV of U_S (sample oxidation state) and differentiated to obtain the local conductance dI_T/dU_T which directly depends on the density of states at the different electron energies. These conductance curves are then stacked together into two different conductograms (see Section 2) corresponding to the anodic processes (increasing U_S branch, Fig. 2a) and cathodic processes (decreasing U_S branch, Fig. 2c). The cyclic voltammogram of the Fe electrode in this medium has been aligned in Fig. 2b as a mere guidance to aid the interpretation. Three main electrochemical ranges can be distinguished during both oxidation and reduction processes in terms of their conductance behavior:

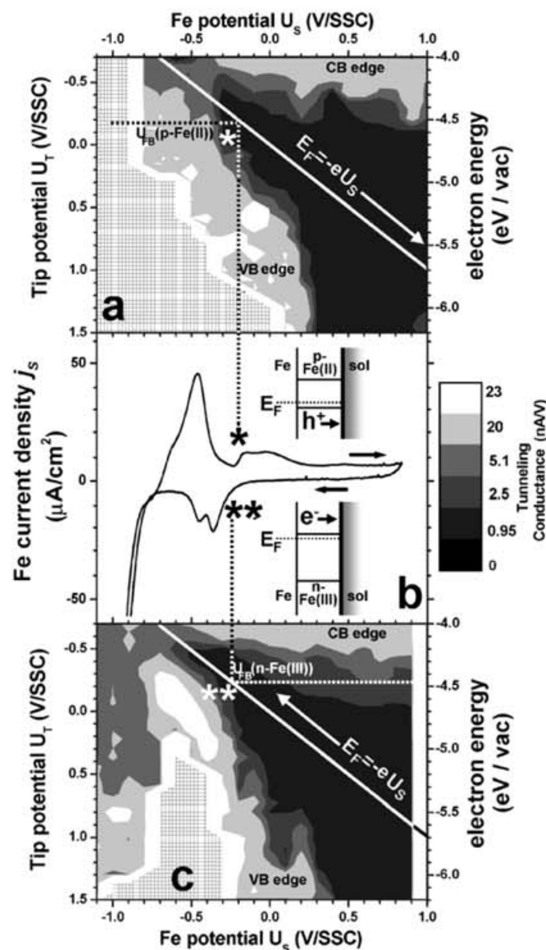

Fig. 2. Conductograms of the Fe oxidation–reduction process in pH 7.5 borate buffer. Plots were obtained from series of ECTS spectra at different sample and tip potentials (U_S and U_T, respectively). Starting from an electrochemically reduced Fe(0) surface, ECTS spectra were collected while oxidizing the sample to increasingly higher U_S (a), and then reducing back to the metal (c). All spectra were obtained at constant tunneling gap of ~1.6 nm. The U_{FB} of p-Fe(II) and n-Fe(III) obtained from Fig. 1 are shown by dashed lines in the energy y-axis. The diagonal line indicates the position of the Fermi energy of the Fe electrode. The asterisks mark the onset of the transitions Fe(II) → Fe(III) (*) and Fe(III) → Fe(II) (**). (b) Cyclic voltammogram of the Fe electrode showing the macroscopic oxidation–reduction processes over the entire surface, for comparison with the conductogram. U_S scan rate of 5 mV/s. The inset schemes show the band diagrams of p-Fe(II) at $U_S = U_{FB}$(p-Fe(II)) (above) and n-Fe(III) at $U_S = U_{FB}$(n-Fe(III)) (below).

(1) at $U_S \leqslant -700$ mV the iron sample is fully reduced to metallic state (Fe(0)) and displays a linear ECTS behavior with high conductance values that correspond to a high density of states, as expected for the metallic behavior of the Fe electrode within this electrochemical range (Fig. 2a). Note that the limited U_T range for $U_S < -700$ mV is due to saturation of the STM pre-amplifier, but this is not an intrinsic limitation of the technique. The Fe(0) state is concurrent with the HER as previously reported [10].
(2) Within the range $-600 < U_S < -300$ mV, the Fe(0) → Fe(II) transition takes place, with the corresponding release of Fe^{2+}(aq) species into the solution and for-

mation of a hydrated Fe(II) oxide layer according to the chemical equilibrium $Fe(OH)_2(s) \leftrightarrow Fe^{2+}(aq) + OH^-(aq)$ [10,15,18,19]. We find that ECTS spectra in this range display a non-linear characteristic: a narrow gap of low conductance flanked by two higher conductance regions in the conductogram. The cathodic and anodic high conductance regions display an exponential behavior (see p-Fe(II) curve in Fig. 3a), and correspond respectively to electron exchange with the CB and VB of the oxide. The U_{FB}(p-Fe(II)) measured by EIS lies within the narrow ECTS conductance gap, indicating that p-Fe(II) changes from depletion to accumulation as U_S is increased toward positive values. The FB situation is depicted in the upper inset of Fig. 2b and agrees with the observed M–S behavior.

(3) Within the range $-300 < U_S < 1000$ mV (passive plateau in the voltammogram, Fig. 2b), an Fe(III) oxide layer is formed whose n-type properties have been extensively characterized [15,16,18] (the FB situation is indicated in the lower inset of Fig. 2b). At $U_S = 500$ mV, the ECTS curve is non-linear (see n-Fe(III) curve in Fig. 3a) with a separation between exponential branches in agreement with the reported bandgap for the Fe passive film ($E_g = 1.6$–1.9 eV) [26] and with the bandedge energy from previous ECSTM data ($U_{CB} = -350$ mV) [18]. At higher potentials within this range ($U_S = +700$ mV, end of passive plateau in Fig. 2b), the positive branch in ECTS spectrum decreases and almost disappears (Fig. 3a). This feature appears in the conductogram as a diagonal stripe in the low energy range that corresponds to the VB edge (Fig. 2a and c, lower region). The CB region in the conductogram remains approximately constant with U_S (see horizontal bright stripe in Fig. 2a and c, upper region) and results from tip electron injection into the CB [18,23]. However, the VB region in the conductogram results from h^+ injection into the VB, because the n-Fe(III) oxide depletion at high U_S values prevents electron transfer to the solution. Indeed, this VB current can be maintained by recombination with electrons at slight depletion (upper inset of Fig. 3a), but not under strong depletion conditions (lower inset of Fig. 3a) which makes the VB region in the conductograms disappear (note that the barrier is non-tunnelable: 5 nm of SCL at

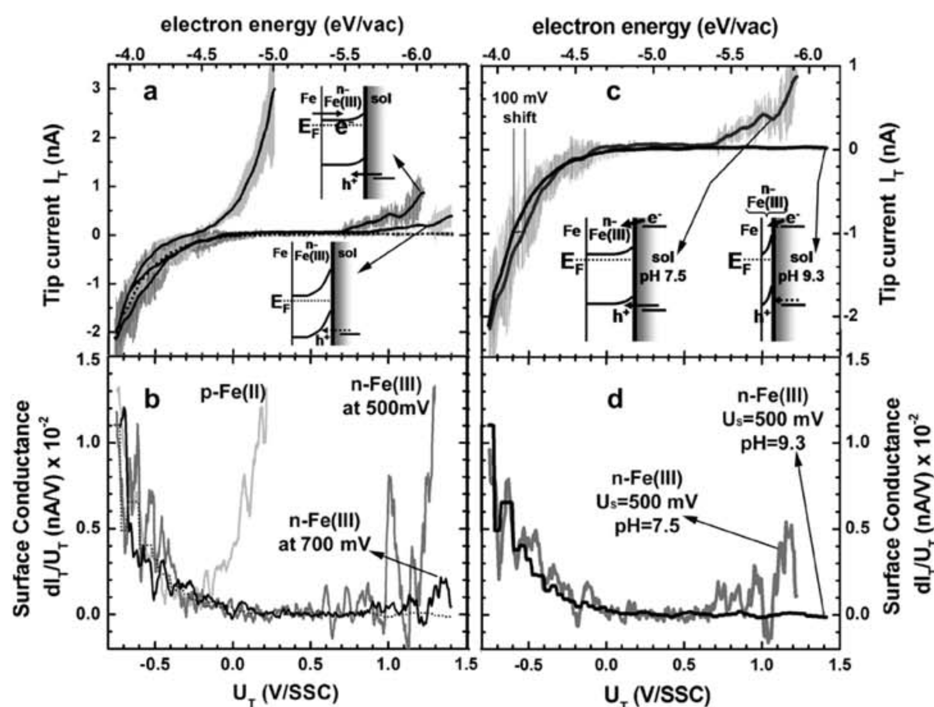

Fig. 3. ECTS spectra of the Fe|oxide|electrolyte interface (top) and their corresponding conductance curves (down): (a, b) Dependence with the potential of passive film formation: solid line corresponds to the spectra recorded at different Fe oxidation states (U_S) in pH 7.5 borate buffer within the p-Fe(II) and n-Fe(III) electrochemical ranges. The ECTS spectrum of c (pH 9.3) is added as a guidance (dotted line). The insets in (a) show band diagrams of the n-Fe(III) oxide at two different band bendings ($U_S = 500$ mV above, and 700 mV below). (c, d) Dependence with the pH of passive film formation: spectra at $U_S = 500$ mV of the n-Fe(III) oxide grown in borate buffer of pHs 7.4 and 9.3. Inset plots represent the band diagram of both situations. Initial setpoint conditions were the same for all curves: $I_T = 2$ nA and $U_T = -800$ mV. All spectra are averages of $N \geqslant 10$ curves and grey bands indicate the standard deviation at each potential.

$U_S = 500$ mV [17,18]). In the potential range $0 < U_S < 1000$ mV, the energy barrier in the SCL together with the absence of surface states in the bandgap of the oxide, limit the availability of charge carriers at the oxide surface. Hence, the reactivity of the electrode is very low despite the large applied potential, which is mostly used in bending the bands. Our measurements thus demonstrate that the passivity of iron is largely based on the energy barrier created at the oxide/electrolyte interface, as previously predicted by Sato and Gerischer [21,22]. Since many metal oxides other than iron are n-type semiconductors with large bandgap values [27], it is likely that this mechanism has a broad validity.

Conductograms also provide an explanation for how the electrochemical processes occurring on the Fe electrode surface are coupled to the observed electronic transitions. The diagonal lines $E_F = -eU_S$ in Fig. 2a and c indicate the position of the Fermi energy of the Fe electrode in the conductogram. The experimental U_{FB} of p-Fe(II) and n-Fe(III) have been outlined as dashed lines in Fig. 2a and c, respectively, to help the interpretation. The onset of the main current peaks in the voltammogram corresponding to the transitions Fe(II) → Fe(III) (one asterisk in Fig. 2a) and Fe(III) → Fe(II) (two asterisks in Fig. 2c), occur at the intersection point between E_F and U_{FB} of p-Fe(II) and n-Fe(III), respectively. At these points, charge carriers become available for reaction at the electrode surface: in the positive-going scan of the voltammogram, the current peak corresponding to the oxidation Fe(II) → Fe(III) occurs when E_F approaches a high conductance region of the VB in the conductogram (one asterisk in Fig. 2a). As U_S is increased within the Fe(II) range, the band bending increases, bringing the p-Fe(II) oxide to accumulation for $U_S > U_{FB}$(p-Fe(II)). Majority carriers (h^+ in p-Fe(II)) are thus driven to the surface, giving rise to the anodic current flow and the Fe(II) → Fe(III) transition (Fig. 4A–C). Once the Fe(III) is completely developed at higher U_S (in the n-Fe(III) region), E_F does not approach high conductance regions and hence no reactions are observed along the passive plateau in the voltammogram, because no charge carriers are available for reaction. The electrode is thus passivated. In the negative-going scan of the voltammogram, the conductogram shows reversibility in the electronic properties as expected in this medium (Fig. 2c). In order for the cathodic current flow and the Fe(III) → Fe(II) transition to occur (two asterisks in Fig. 2b), U_S must come close to the FB potential of n-Fe(III) and allow electrons to accumulate near the surface (Fig. 4D–F). Note that a low conductance bandgap is again present after the reduction peak, which means that the full reduction Fe(II) → Fe(0) is only achieved at more negative potentials.

The conductograms of Fig. 2 show at a glance that electron injection into the CB is always possible at the suitable tip potentials [18]. The CB edge is thus independent of the

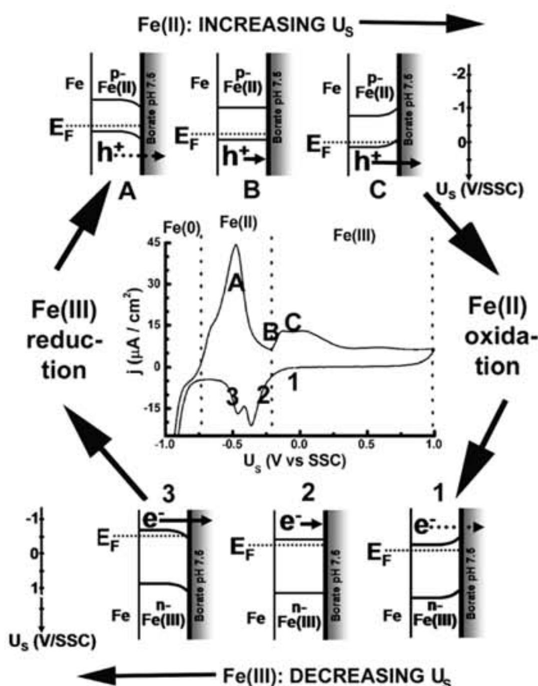

Fig. 4. Current flows and resulting electrochemical processes in the reversible Fe(II) ↔ Fe(III) transition, during positive (top) and negative (down) going scans. (A–C) In p-Fe(II), increasing U_S results in hole accumulation at the electrode surface, which allows film oxidation to Fe(III). (D–F) The n-Fe(III) film is depleted of electrons at high U_S. Decreasing U_S allows electrons to accumulate at the surface and promote film reduction to Fe(II). The cyclic voltammogram is added to indicate the Fe sample oxidation state (U_S) of each situation through corresponding markers.

electrode potential (it is *pinned*) and most of the applied potential is dropped in the SCL of the semiconductor, which corresponds to a fairly ideal semiconductor|liquid interface.

In order to quantify ECTS data, the averaged spectra (Fig. 3a and c) can be fitted to a 2-exponential function considering electron transfer between the STM tip and both the CB and the VB of the Fe oxide [29]:

$$I = I_{VB} \exp[e\alpha_{VB}(U_T - U_{VB})/k_BT] - I_{CB} \exp[-e\alpha_{CB}(U_T - U_{CB})/k_BT] \quad (1)$$

This relation is similar to the Butler–Volmer, where I_{VB} and I_{CB} correspond to tunneling exchange currents between tip and the VB and CB, respectively, containing the kinetic constants of electron exchange [29]. The exponential factors α_{VB}, α_{CB} correspond to apparent tunneling transfer coefficients with the VB and the CB, respectively (assuming one-electron reactions), and are related to the reversibility of the processes. The values U_{VB}, U_{CB} are the VB, CB edge potentials (obtained from EIS measurements and previous electrochemical STM data [18]) and thus U_T–U_{VB} and U_T–U_{CB} are true reaction overpotentials

Table 1
Electrochemical kinetic parameters of the electronic exchange for Fe(II) and Fe(III) oxides obtained by fitting ECTS plots to Eq. (1) at different sample electrochemical potentials (U_S)

Constant	Borate pH 7.5			Borate pH 9.3
	p-Fe(II)	n-Fe(III)		
	$U_S = -400$ mV	$U_S = +500$ mV	$U_S = +700$ mV	$U_S = +500$ mV
I_{VB}	1.05	10	0.01	0.02
I_{CB}	–	−0.66	−0.75	−0.41
α_{VB}	0.14	0.13	0.01	0.10
α_{CB}	–	0.14	0.07	0.12
r^2	0.9999	0.9999	0.9999	0.9999

See Section 3 for details on U_{FB}, E_g, U_{CB} and U_{VB} values used in fits at each pH value.

considering isoenergetic electron exchange with the bands [27]. To fit the spectra in the Fe(III) range ($U_S = 500$ and 700 mV) we have used the following parameters: At pH 7.5 ($U_S = +500$ mV and $U_S = +700$ mV, Fig. 3a) bandedges are $U_{CB} = -350$ mV and $U_{VB} = +1450$ mV [18], taking a bandgap of 1.6 eV [26]. At pH 9.3 ($U_S = +500$ mV, Fig. 3c) $U_{FB} = -340$ mV corresponding to bandedges of $U_{CB} = -450$ mV and $U_{VB} = +1350$ mV (see previous section). Since the bandgap of p-Fe(II) oxide has not been reported, we have approached $U_{VB} \approx U_{FB} = -200$ mV to fit only the anodic (VB) branch of the ECTS curve in Fig. 3a and b. The results are summarized in Table 1. For Fe(III) in slight depletion ($U_S = +500$ mV), the apparent transfer coefficients are very similar in both bands while the exchange current is lower for the CB. Under strong depletion ($U_S = +700$ mV), the decrease in VB current arises from a 1000-fold reduction in exchange current and a 10-fold reduction in apparent transfer coefficient, with comparably minor changes in the CB parameters. The decrease in VB exchange current is in good agreement with the decrease in the macroscopic kinetic constant of metal dissolution that characterizes the passivation phenomenon [1].

In order to demonstrate that the decrease of the kinetic constant of the VB electron transfer is related to the passivation process, we recorded ECTS spectra of the Fe(III) passive film grown in borate buffer solution at pH 9.3. As pH is increased, the current plateau in the passive electrochemical range of the cyclic voltammogram decreases compared to pH 7.5 [10], indicating a more efficient blockage against further oxidation and hence, better passivation. The ECTS spectrum at $U_S = 500$ mV in borate buffer pH 9.3 (Fig. 3c and d) shows a 500-fold reduction in current exchange (I_{VB}) as compared to pH 7.5 (Table 1), with very little change in the transfer coefficient (α_{VB}). This indicates that an efficient energy barrier at the oxide|electrolyte interface is created at earlier U_S in pH 9.3 than in pH 7.5. Two reasons can account for this result: the n-Fe(III) U_{FB} value shifts at around −50 mV/pH while the doping density remains almost constant (see EIS data in the previous section). This results in a −100 mV band edge shift from pH 7.5 to 9.3 (right inset of Fig. 3c), which manifests in ECTS spectrum as: (1) a ~100 mV shift in the CB edge in the ECTS spectrum (Fig. 3c), and (2) a 500-fold reduction of I_{VB} that makes the VB branch disappear (Fig. 3c). In addition, the constant capacitance–U_S region in the M–S plots of Fig. 1 indicates that the thin n-Fe(III) film grown at pH 9.3 is fully depleted of e^- at $U_S = 500$ mV (see discussion above). In this case, charge exchange between solution and the iron electrode may proceed by direct tunneling through the ~2.5 nm depleted oxide film (right inset, Fig. 3c), which further accounts for the observed I_{VB} decrease.

4. Conclusions

We have measured *in situ* the electron energy spectrum of an Fe electrode during its reversible electrochemical oxidation and reduction in borate buffer medium at different pHs by using EIS and ECTS techniques. While Fe(III) displays an n-type behavior in agreement with previous reports, Fe(II) is a highly doped, narrow bandgap, p-type semiconductor. We find that the main Fe redox transitions on the iron electrode surface (p-Fe(II) → n-Fe(III) and n-Fe(III) → p-Fe(II)) result from the availability of free charge carriers at every U_S value, which control the electron energy barriers at the oxide|solution interface. Similarly, the passivity of iron results from the build-up of an energy barrier in the n-Fe(III) oxide and the absence of states available for charge exchange within almost 1.5 eV below the CB edge. Increasing the sample potential in the n-Fe(III) passive plateau results mostly in increasing the band bending inside the oxide and decreasing the electron concentration, without changing the band edge energy at the surface. Tunneling spectra in solution further provide the kinetic parameters of electron transfer between the ECSTM probe and the VB and CB of the Fe oxide films. Between $U_S = 0.5$ V and 0.7 V/SSC in the Fe(III) region, passivity is explained as a 1000-fold decrease in the tunneling exchange current with the VB (I_{VB}) and 10-fold reduction in the apparent tunneling transfer coefficient α_{VB}. At pH 9.3, passivity of n-Fe(III) oxide is more efficient than at pH 7.5, as a result of a 100 mV bandedge shift toward higher energies which gives rises to a 500-fold decrease of I_{VB} at the same $U_S = 500$ mV/SSC.

Combining ECTS and EIS techniques allows to quantify the surface electronic structure of electrode|electrolyte interfaces, in order to understand their redox behavior. This method can be further used to investigate passivity

1602 I. Díez-Pérez et al. / Electrochemistry Communications 8 (2006) 1595–1602

breakdown in aggressive media [30], to probe the energy levels of organic monolayers [31] and to study electron exchange mechanisms in redox proteins.

Acknowledgements

This work was supported by a grant of MEC (Ministry of Education and Culture) under Project CTQ2004-08046-C02-01. P.G. acknowledges financial support of the MEC through the program Ramón y Cajal. We thank P. Allongue for useful discussions and the Scientific–Technical Services of the University of Barcelona for use of their facilities.

Appendix A. Supplementary data

Supplementary data associated with this article can be found, in the online version, at doi:10.1016/j.elecom.2006.07.015.

References

[1] C. Schönbein, Annalen der Phys. Chem. 37 (1836) 390.
[2] J. Kolchakov, T. Tzvetkoff, M. Bojinov, Appl. Surf. Sci. 249 (2005) 162.
[3] V. Maurice, G. Desert, S. Zanna, M-P. Bacos, P. Marcus, Nat. Mat. 3 (2004) 687.
[4] M.F. Toney, A.J. Davenport, L.J. Oblonsky, M.P. Ryan, C.M. Vitus, Phys. Rev. Lett. 79 (1997) 4282.
[5] L.J. Oblonsky, A.J. Davenport, M.P. Ryan, H.S. Isaacs, R.C. Newman, J. Electrochem. Soc. 144 (1997) 2398.
[6] A.J. Davenport, L.J. Oblonsky, M.P. Ryan, M.F. Toney, J. Electrochem. Soc. 147 (2000) 2162.
[7] C. Puncktt, M. Bölscher, H.H. Rotermund, A.S. Mikhailov, L. Organ, N. Budiansky, J.R. Scully, J.L. Hudson, Science 305 (2004) 1133.
[8] R. Sonnenfeld, P.K. Hansma, Science 232 (1986) 211.
[9] H-H. Strehblow, V. Maurice, P. Marcus, Electrochim. Acta 46 (2001) 3755.
[10] I. Díez-Pérez, P. Gorostiza, F. Sanz, C. Müller, J. Electrochem. Soc. 148 (2001) B307.
[11] S.M. Lindsay, Y. Li, J. Pan, T. Thundat, L.A. Nagahara, P. Oden, J.A. DeRose, U. Knipping, J. Vac. Technol. B9 (1991) 1096.
[12] A. Schreyer, L. Eng, H. Böhni, J. Vac. Technol. B14 (1996) 1162.
[13] G. Abadal, F. Pérez-Murano, N. Barniol, X. Borrisé, X. Aymerich, Ultramicroscopy 66 (1996) 133.
[14] K. Azumi, K. Araki, M. Seo, J. Electroanal. Chem. 427 (1997) 15.
[15] M. Büchler, P. Schmuki, H. Böhni, J. Electrochem. Soc. 145 (1998) 609.
[16] M. Buchler, P. Schmuki, H. Bohni, T. Stenberg, T. Mäntylä, J. Electrochem. Soc. 145 (1998) 378.
[17] E. Sikora, D.D. Macdonald, J. Electrochem. Soc. 147 (2000) 4087.
[18] I. Díez-Pérez, P. Gorostiza, F. Sanz, J. Electrochem. Soc. 150 (2003) B348.
[19] C.J. Rubim, J. Electrochem. Soc. 140 (1993) 1601.
[20] S. Virtanen, P. Schmuki, M. Büchler, H. Isaacs, J. Electrochem. Soc. 146 (1999) 4087.
[21] N. Sato, Corr. Sci. 31 (1990) 1.
[22] H. Gerischer, Corr. Sci. 29 (1989) 191.
[23] I. Díez-Pérez, A.G. Güell, F. Sanz, P. Gorostiza, Anal. Chem., in press.
[24] A.G. Güell, I. Díez-Pérez, P. Gorostiza, F. Sanz, Anal. Chem. 76 (2004) 5218.
[25] H. Gerischer, W. Ekardt, Appl. Phys. Lett. 43 (1983) 393.
[26] S.M. Wilhelm, K.S. Yun, L.W. Ballenger, N. Hackerman, J. Electrochem. Soc. 126 (1979) 419.
[27] S.R. Morrison, Electrochemistry at Semiconductor and Oxidized Metal Electrodes, Plenum Press, New York, 1980.
[28] M.J. Madou, B.H. Loo, K.W. Frese, S.R. Morrison, Surf. Sci. 108 (1991) 261.
[29] E.V. Kasatkin, M.F. Reznik, E.B. Neburchilova, Russ. J. Electrochem. 39 (2003) 265.
[30] I. Díez-Pérez, C. Vericat, P. Gorostiza, F. Sanz, Electrochem. Commun. 8 (2006) 627.
[31] C. Vericat, I. Díez-Pérez, P. Gorostiza, F. Sanz, Meet. Abstr. Electrochem. Soc. 601 (2006) 1213.

Supporting data

Electronic Barriers in the Iron Oxide Film Govern its Passivity and Redox Behavior: Effect of Electrode Potential and Solution pH.

I. Díez-Pérez[a], F. Sanz[a,b,*] and P. Gorostiza[b,*]

[a] *Laboratory of Electrochemistry and Materials (LCTEM), Department of Physical Chemistry, University of Barcelona, Martí i Franquès 1, 08028 Barcelona, Spain*

[b] *Centre de Referència en Bioenginyeria de Catalunya, Parc Científic de Barcelona, Josep Samitier 1-5, Barcelona 08028, Spain*

* Corresponding authors. Address: Laboratory of Electrochemistry and Materials (LCTEM), Department of Physical Chemistry, University of Barcelona, Martı´ i Franquès 1, 08028 Barcelona, Spain. Fax: +34 934021231.

E-mail addresses: fsanz@ub.edu (F. Sanz), pau.gorostiza@ub.edu (P. Gorostiza).

Supporting data

Details of some experimental procedures are given:

Passive film growth.— The passive film was grown following a two-steps procedure as in previous works [10,18]. It consists on a first electrochemical potential step (thickening stage) within the Fe(II) active range (peak I in fig. 1a), followed by a second potential step into the desired potential region (passivation stage). This treatment allowed to maximize the thickness of the passive layer at the different pH values [10].

ECTS measurements.— Previous experiments allowed us to determine the tunneling barrier height of 0.26±0.04 eV for electron transfer from the ECSTM tip to the CB of the Fe passive film, which appears to be independent of the Fe electrode potential [23]. These results allowed us to fix the same initial tunneling conditions for the different ECTS spectra as a function of the electrode potential (U_S).

The smoothed fit on the ECTS curves has been superimposed in figure 3 and used for exponential fitting. The corresponding conductance curves were numerically differentiated from the smoothed spectra.

We wanted to point out some observations on the conductograms: a slight decrease on the CB edge value at lower electrode potentials U_S is observed (see Fig. 3(a)). This fact is due to the low set points used at the lowest U_S values in the Fe(II) electrochemical range to maintain a constant tunneling junction along the entire conductogram (at U_S=-700 mV the setpoint current is 0.14 nA). At such low tunneling

currents the CB branch is poorly observed because the initial tunneling current is close to the noise level of the ECSTM tip.

It is also straightforward to obtain the experimental energy diagram of the passive film on Fe at every electrode potential U_S (oxidation state) by simply taking a vertical profile on the same conductogram [23].

Chapter 5

Fe passivity breakdown in chloride media

5.1 GENERAL

In this chapter, the passivity breakdown process on iron polycrystalline substrates in the presence of chloride is studied by means of EIS and ECTS techniques. The knowledge acquired in the previous chapter concerning the *in situ* electronic structure of the Fe passive film as well as the process of *electronic passivation* occurring within the electrochemical passive range, gave us a privileged position to tackle into the mechanisms through which the surface electronic barrier on the Fe passivated surface is destroyed in the presence of Cl^- anions and that finally produces electrode corrosion. The conductogram of Fe oxidation process in the presence of chloride evidences the absence of surface electronic passivation.

The focus of this chapter is then on the elaboration of an electrochemical model that matches with the observed electronic changes under these experimental conditions. *Ex situ* complementary data is also required to complete the proposed model. The showed experimental data demonstrate the capability of the ECTS technique to directly probe SS at the electrode│electrolyte interface without the help of an equivalent electronic circuit. These characteristics surpass the capabilities of other classical electrochemical methods like the EIS, where, in addition, the dependence of the response frequency of the different SS makes it difficult any further quantification.

The detailed results of this chapter are presented in the following publication:

- *The iron passive film breakdown in chloride media may be mediated by transient chloride-induced surface states located within the band gap*, Electrochem. Commun., **8** (2006) 627.

5.2 THE IRON PASSIVE FILM BREAKDOWN IN CHLORIDE MEDIA MAY BE MEDIATED BY TRANSIENT CHLORIDE-INDUCED SURFACE STATES LOCATED WITHIN THE BAND GAP

Reference: I. Díez-Pérez, C. Vericat, P. Gorostiza and F. Sanz, *The iron passive film breakdown in chloride media may be mediated by transient chloride-induced surface states located within the band gap*, Electrochem. Commun., **8** (2006) 627.

Reprinted from the above publication, © Elsevier 2006, with permission from Elsevier.

Available online at www.sciencedirect.com

Electrochemistry Communications 8 (2006) 627–632

electrochemistry communications

www.elsevier.com/locate/elecom

The iron passive film breakdown in chloride media may be mediated by transient chloride-induced surface states located within the band gap

I. Díez-Pérez [a], C. Vericat [a], P. Gorostiza [b,*], F. Sanz [a,*]

[a] *Laboratory of Electrochemistry and Materials (LCTEM), Department of Physical Chemistry, University of Barcelona, Martí i Franquès 1, Barcelona 08028, Spain*

[b] *Centre de Referència en Bioenginyeria de Catalunya, Parc Científic de Barcelona, Josep Samitier 1, Barcelona 08028, Spain*

Received 30 December 2005; received in revised form 25 January 2006; accepted 1 February 2006

Abstract

Despite its tremendous scientific and economic impact, the mechanism that triggers metal passive film breakdown in the presence of aggressive ions remains under discussion. We have studied the iron passive film in chloride media using X-ray photoelectron spectroscopy (XPS), electrochemical impedance spectroscopy and electrochemical tunneling spectroscopy (ECTS). Ex situ XPS reveal that the film consists exclusively of an Fe(III) oxide without chloride content. In situ ECTS has been used to build up conductance maps of the Fe electrode during its electrochemical oxidation in a borate buffer solution and its breakdown when the film is grown in the presence of chloride. This conductograms provide direct and in situ experimental evidence of chloride-induced surface states within the band gap of the oxide film (~3.3 eV). These states enable new charge exchange pathways that allow hole capture at the surface of the n-type Fe(III) oxide. The blocking of VB processes that occurs in the iron passive film is no longer present in chloride media, and electrode corrosion can proceed through these new states. We propose a simple 3-step mechanism for the process, in which chloride anions form an oxidizing Fe(II) surface intermediate but do not participate directly in the reaction.

© 2006 Elsevier B.V. All rights reserved.

Keywords: Electrochemical tunneling spectroscopy; Electronic band structure; Fe passive film; Aqueous chloride corrosion; Semiconductor decomposition; Interface states

1. Introduction

After decades of study, the exact mechanism of the Fe passive film breakdown in chloride solution is still a subject of debate. A number of explanations have been proposed for this process, involving an initial adsorption of chloride anions on the oxide layer [1,2] that finally leads to chemical dissolution of the oxide film. The electrochemical process is known to have a local character taking place on very specific sites on the oxide layer which might contain structural defects, impurities or inhomogeneities on the film thickness [3]. However, the early step of the mechanism that triggers the initialization of pitting corrosion is still controversial. There is some evidence that the electronic properties of passive layers are directly coupled with the susceptibility to pitting corrosion in aggressive media like chloride containing solutions [4–7]. Most of the metal passive films present a variety of semiconducting properties [8], the Fe passive film being one of the most extensively studied. The Fe passive film behaves as a heavily doped n-type semiconductor with Fe(II) species acting as electron donors [9–11]. The electronic structure of the Fe passive film/electrolyte interface has been quantitatively elucidated in the previous works [9–11,13]. Among the different established models on passive film breakdown [3], the Fe passive film case in chloride media has been suggested to be triggered by the adsorption of chloride anions on the oxide surface which could modify its electronic properties and thus, the band structure of the oxide film/electrolyte contact [5,6,14]. A purely electronic breakdown mechanism [1–3]

* Corresponding authors. Tel.: +34 934 021 240; fax: +34 934 021 231.
E-mail addresses: pau.gorostiza@ub.edu (P. Gorostiza), fsanz@ub.edu (F. Sanz).

1388-2481/$ - see front matter © 2006 Elsevier B.V. All rights reserved.
doi:10.1016/j.elecom.2006.02.003

can be ruled out since the Fe passive film is only tens of nanometers thick and the electronic avalanche due to acceleration of electrons by the electric field is not enough to produce the required ionization by electronic impact [8]. The migration or inclusion of chloride anions is also unlikely since the Fe passive film behaves as an electronic conductor [15] and no chloride species are detected within the film during oxide growth as extensively analyzed by ex situ and in situ spectroscopic techniques [16,17].

In the present contribution, we characterize the morphological, chemical and electronic properties of the Fe passive film in chloride-containing borate buffer solutions, in the passive breakdown regime (at potentials above the breakdown potential value, U_B). ECTS technique [18–20] has been employed to in situ monitor the tunneling spectra of the Fe electrode/liquid interface as it is anodically oxidized from the metallic state to the passive region. These results suggested that iron passivity is due to the formation of an energy barrier in the n-Fe(III) film under strong depletion conditions, and thus to the absence of charge carriers available for reaction [12]. Here we measure how this scenario is changed in the presence of chloride anions, and we find that their adsorption from the electrolyte enables new charge exchange pathways that allow electrode corrosion. Chloride thus forms surface intermediates with unique chemical and electronic properties that are key elements to understand passivity breakdown and the initiation of pitting corrosion on iron and other metallic electrodes in aggressive chloride media.

2. Experimental details

2.1. Sample and electrolytes

Mechanically polished iron polycrystalline disks were used as working electrodes and prepared as previously described [12] (see supplementary data). The electrolyte used in the measurements was pH 7.5 borate buffer solutions (prepared from 0.3 M H_3BO_3 and 0.0375 M $Na_2B_4O_7 \cdot 10H_2O$ solutions) either containing 5 mM NaCl or without chlorides. In all cases pro-analysis purity grade chemicals from Merck (Darmstadt, Germany) and Milli-Q water of 18 MΩ cm were used.

2.2. Electrochemical measurements

Thick and well-controlled Fe oxide films were obtained as previously described [11,12]. Briefly, prior to the passivation potential step, the native oxide film was electrochemically reduced, and a thick Fe(II) film was precipitated at −0.55 V for times longer than 10 min (see supplementary data). Cyclic voltammetry and capacitance measurements were performed using an EcoChemie Autolab PSTAT 12 equipped with an impedance module, and controlled by the Autolab GPES 4.9 software package. A Tait-type electrochemical cell with a large area Pt counter electrode and a Ag/AgCl reference electrode, the latter connected to the working solution through a Luggin capillary, was used. The Fe working electrodes were fixed at the bottom of the cell with a Viton ring, and their exposed area was 0.28 cm^2. All measurements were made with deaerated borate solutions and under nitrogen atmosphere. Experimental details for impedance measurements are given in the supplementary data. All potential values presented in this work are quoted versus the SSC reference electrode.

2.3. ECTS measurements

ECTS measurements were performed in a STM system (Pico-SPM, Molecular Imaging, USA) using an Teflon electrochemical cell modified to incorporate a miniaturized double-membrane SSC reference electrode and a large area Pt wire as a counter electrode. The STM was controlled by a Nanoscope IIIa electronics (Veeco Instruments, USA) connected to the STM through a BNC-connectors break out box that allows external application of voltage ramps to the tip and high rate data capturing. Tip and iron potentials (U_T and U_S, respectively) were independently controlled versus the same SSC electrode through a bipotentiostat (Picostat, Molecular Imaging, USA). In the paper, U_T and U_S are directly quoted in the electrochemical scale (SSC), instead of using the sample bias ($U_S - U_T$), so that they can both be placed in different energy diagrams.

Tunneling spectra were recorded by scanning U_T while keeping U_S constant. Typically, our U_T ramps spanned up to 2.2 V at rates up to 20 V/s in order to minimize tip drift. These ramps require extremely well insulated STM tips which are home-made following a new procedure [21]. The ECTS set up and performance of ECTS spectra and conductance maps (or conductograms) have been described in detail elsewhere [13]. Briefly, conductograms were obtained by horizontally stacking series of conductance–potential curves and representing them in a 3-D plot. The X-axis represents the Fe electrode oxidation state or sample potential (U_S), and the Y-axis represents tip potential (U_T versus SSC) and electron energy converted to the absolute physical scale (vacuum level, right axis). The Z grey scale indicates higher (brighter) and lower (darker) conductance regions of the electrode/electrolyte interface. Conductograms were recorded at a constant tunneling gap [13].

3. Results and discussion

3.1. Electrochemical study

Fig. 1(a) shows the anodic branch of the voltammogram of a polycrystalline Fe electrode in borate buffer solutions at pH 7.5 in the absence of Cl^-(aq) and with 5 mM Cl^- concentration. Different features can be observed. First, the position and charge of the anodic peaks in the potential range previous to passivity breakdown ($U_S < U_B$) do not change in the presence of Cl^- anions. Small differences in

I. Díez-Pérez et al. / Electrochemistry Communications 8 (2006) 627–632 629

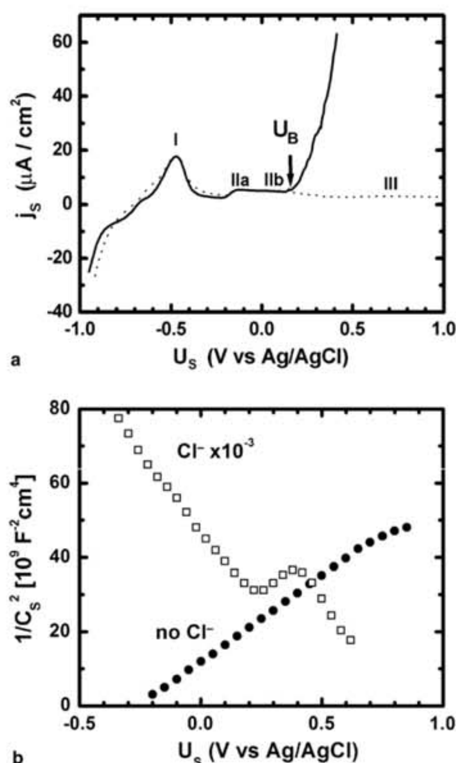

Fig. 1. (a) Anodic voltammetric scans of the Fe electrode in borate buffer solution at pH 7.5 in the absence (⋯⋯) and in the presence of 5 mM of Cl^-(aq) (—). Scan rate was 5 mV/s. (b) MS representations of the capacitance data in the absence (solid circle) and the presence of 5 mM of Cl^-(aq) (open square).

the anodic charge of peak I may be due to variations in the surface roughness of the polycrystalline Fe electrode [12], but no Fe(II) chelating effects are observed. No changes are observed in either peak IIa (corresponding to $Fe(OH)_3$ precipitation from electro-oxidation of Fe^{2+}(aq) [9,10,12]) and peak IIb which initiates oxidation of the previous Fe(II) film to an Fe(II)/Fe(III) oxide film whose crystalline structure has been largely studied [22]. Therefore, oxide film growth seems to be poorly affected by the presence of Cl^- anions (see [14] and EIS data below) and proceed through previously characterized electrochemical processes in this media [12]. This fact is also in good agreement with the previous studies of Fe passivation in similar media at low passivation potentials [16]. Since the onset of passivity breakdown (U_B) is shifted toward positive potentials at decreasing chloride concentrations [2,3], it is possible to adjust the Cl^- content in solution so that the entire transition between passive state and film breakdown can be seen. At 5 mM Cl^- in borate buffer of pH 7.5, the U_B value appears at around 200 mV (Fig. 1(a)) which lies within the Fe passive region. Once U_B is reached, a strong hysteresis in the cathodic scan is observed, indicative of electrode corrosion [2].

Electrochemical Impedance Spectroscopy (EIS) was used to characterize the semiconducting properties of the oxide film [11]. Fig. 1(b) shows the Mott–Schottky plot (MS) of the Fe(III) oxide in the absence of Cl^- and in 5 mM Cl^-. In the absence of Cl^-, the Fe(III) passive film presents an n-type behavior within the entire passive region as indicated by the linear positive slope, with a donor density (N_D) of 10^{21} cm^{-3} and a Flat Band potential (U_{FB}) of −280 mV, in agreement with the previous works [9–11]. In the presence of 5 mM Cl^-, the MS plot is essentially unchanged if $U_S < U_B$ during passive oxide growth (not shown), but is strongly modified once U_B is crossed: Fig. 1(b) shows a MS plot with a negative slope, which is usually associated to an inversion behavior. Due to the dynamic conditions at which this capacitance data is recorded, no quantitative data can be obtained; however, the strong observed inversion behavior will be compared with the ECTS results (see Section 3.3).

3.2. Surface morphology and chemical analysis

The morphology of the epitaxial iron oxide film in borate buffer (Fig. 2(a)) is strongly changed by the presence of 5 mM chloride (Fig. 2(b)). After application of $U_S > U_B$ in 5 mM Cl^-, the film displays needle-like features that suggest a surface precipitation process. This oxide layer can be readily detached with regular adhesive tape.

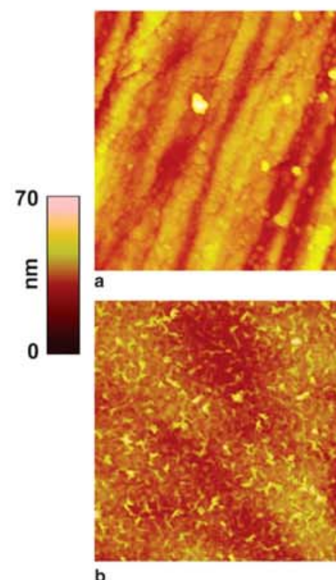

Fig. 2. 1.5 × 1.5 µm^2 topographic AFM images of the Fe oxide film formed at U_S = 0.9 V for 15 min in the absence (a) and in the presence of 5 mM of Cl^-(aq) (b). Thick oxide films were grown following an electrochemical 2-steps procedure (see supplementary data). Samples were withdrawn from the solution under potentiostatic conditions, rinsed with MilliQ water and blown dry with nitrogen.

630 I. Díez-Pérez et al. / Electrochemistry Communications 8 (2006) 627–632

In order to investigate the chemical nature of the layer that develops on the Fe electrode surface during early stages of corrosion in chloride media, we have performed ex situ XPS measurements. The depth profile analysis reveals that only an Fe(III) form is present in the surface oxide (Fig. 3), in contrast to the Fe(II)/Fe(III) structure observed on the stable passive film grown in the absence of Cl^-(aq) [12,22]. In addition, no Cl incorporation into the film is detected along the depth profile (Fig. 3, inset), in agreement with the previous studies [2,16].

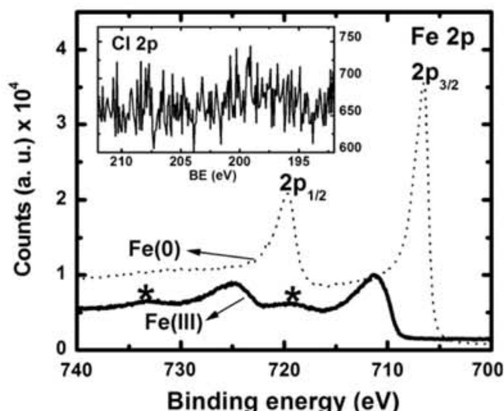

Fig. 3. XPS spectra (Fe 2p region) of the Fe oxide film formed at $U_S = 0.6$ V for 15 min in the presence of 5 mM of Cl^-(aq), before (solid line) and after (dotted line) 30 min Ar^+ sputtering to remove the film. The sample was transferred ex situ as in the AFM experiments. The 2p peak energy before sputtering corresponds to Fe(III) oxide exclusively. The peaks marked with asterisks correspond to shake-up satellites. The bare metal Fe(0) is reached after 30 min of Ar^+ sputtering. Cl 2p signal was simultaneously collected during the sputtering cycles (inset spectrum) showing no-Cl incorporation within the oxide layer.

3.3. ECTS measurements

The effect of chloride on the conductogram of Fe electrode in borate buffer pH 7.5 is shown in Fig. 4 for the entire Fe passivation process: from the metallic state ($U_S = -1$ V) to the transpassive region ($U_S = 1$ V). Anodic voltammetric scans of Fig. 1(a) have been aligned below each conductogram in order to correlate the conductance of the surface film to the faradaic processes occurring on the electrode at every potential U_S. Note that voltammogram and conductogram are recorded in separate experiments.

The conductogram of the Fe electrode oxidation in the absence of chloride is shown in Fig. 4(a) and has been discussed in detail elsewhere [23]. Essentially, there are three main electrochemical ranges: (1) At very negative potentials ($-1\ \text{V} < U_S < -700$ mV), a high conductance region is observed as corresponds to the expected metallic behavior of the Fe electrode within this range [10–12]. (2) In the Fe(II) range ($-600\ \text{mV} < U_S < -300$ mV), a low

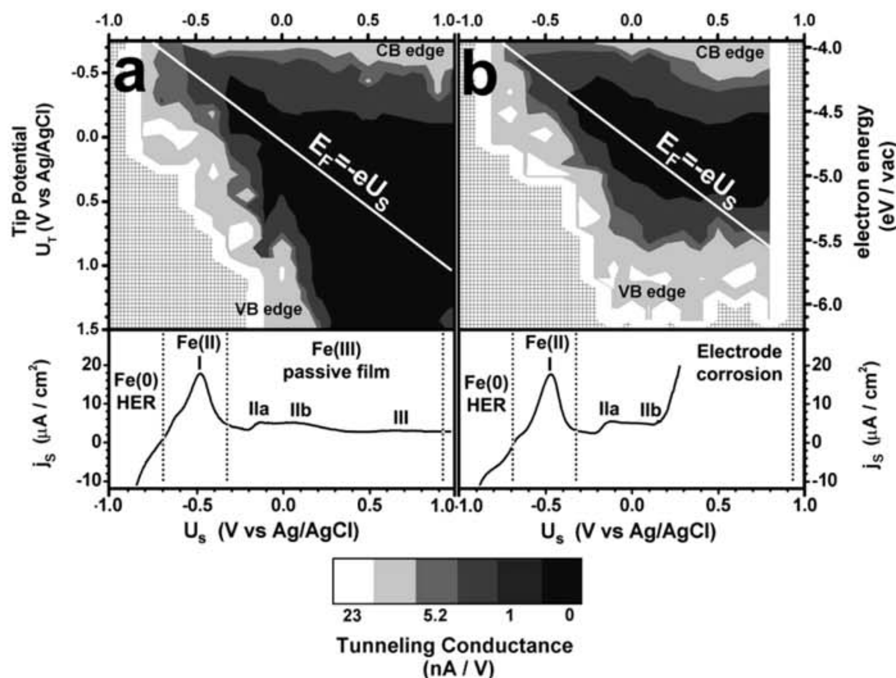

Fig. 4. Conductograms of the Fe electrode in borate buffer at pH 7.5 in the absence (a) and in the presence of 5 mM of Cl^-(aq) (b). Anodic scans of Fig. 1 have been aligned below to aim the interpretation. HER denotes hydrogen evolution reaction.

conductance region (dark) appears between two high conductance branches. They correspond to the conduction band (CB, bright horizontal band above) and valence band (VB, bright diagonal band below). (3) In the Fe(III) passive region (-200 mV $< U_S < 1$ V), the low conductance band gap is widened with increasing U_S values. The observed position of the CB in the conductogram is in good agreement with the n-type behavior of the Fe(III) oxide formed within this range [8–11]. At high U_S values, the n-Fe(III) passive layer is under depletion and its surface energy barrier (Φ) is correspondingly increased. As a result, the VB conductance in the passive region is dramatically reduced until it is no longer measurable (200 mV $< U_S < 1$ V). Surface passivation of the Fe electrode can then be interpreted in terms of the effective blocking of VB conduction [23].

For U_S ranges corresponding to metallic and Fe(II) oxidation states, the conductogram in 5 mM chloride (Fig. 4(b)) is essentially the same, in agreement with the absence of Cl^- species within the Fe passive film during anodic oxidation in chloride solution (Fig. 3). However, a high conductance in the VB region prevails beyond peak IIb and throughout the entire passive region (lower bright horizontal band in Fig. 4(b)), which is concurrent with the onset of passivity breakdown observed in the voltammogram (Fig. 4(b), below). This high conductance region must correspond to chloride-induced electronic states that give rise to a new charge exchange pathway. As mentioned above, Fe passivation is partially due to the blocking of VB conduction in the n-Fe(III) oxide [11,13,15,23]. At U_S values in the passive region, the n-Fe(III) oxide passive layer is depleted of electrons [8] thus creating a non-tunnelable space charge region (SCL) of around 5 nm thick and a surface energy barrier Φ [11]. The high concentration of oxygen vacancies at the oxide/solution interface [22] correspond to Fe(II) species in the oxide that can be ionized to Fe(III) and act as donor impurities [9,10]. As proposed by Sato [14], chloride species might approach the surface of the Fe oxide layer and act as a reducing agent by partially releasing an electron. At this point, the adsorbed Cl^- species would induce electron acceptor surface states in the band gap [6,14]. This view is strongly supported by the high VB conductance region that we directly observe by ECTS below $\sim$3.3 eV. Another possibility would be that Cl^- species partially reduce the Fe(III) layer, thus increasing the effective doping concentration and thinning of the SCL down to tunnelable distances [8]. This is unlikely because it would require: (1) a large depth profile fraction of iron to be in the Fe(II) form and (2) the presence of a relatively high concentration of chloride in the thick passive film, neither of which are detected by XPS (Fig. 3) and by AES and SIMS [2,16].

The appearance of surface states near the VB in chloride media enables new charge exchange pathways between the oxide and the solution, thus unblocking charge exchange with the VB and allowing electrode corrosion. The overall process can be summarized as follows:

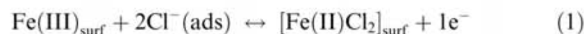

$$\mathrm{Fe(III)_{surf}} + 2\mathrm{Cl^-(ads)} \leftrightarrow [\mathrm{Fe(II)Cl_2}]_{\mathrm{surf}} + 1\mathrm{e^-} \quad (1)$$

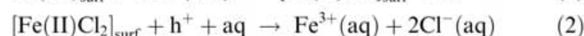

$$[\mathrm{Fe(II)Cl_2}]_{\mathrm{surf}} + \mathrm{h^+} + \mathrm{aq} \rightarrow \mathrm{Fe^{3+}(aq)} + 2\mathrm{Cl^-(aq)} \quad (2)$$

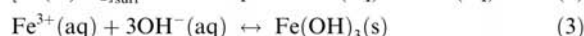

$$\mathrm{Fe^{3+}(aq)} + 3\mathrm{OH^-(aq)} \leftrightarrow \mathrm{Fe(OH)_3(s)} \quad (3)$$

being $[\mathrm{Fe(II)Cl_2}]_{\mathrm{surf}}$ the intermediate formed at the Fe passive film surface. Reaction (1) corresponds to surface intermediate formation by partial electron donation of the chloride anions, and gives rise to acceptor electronic levels near the VB at the oxide surface [14]. The surface intermediate formula has been adjusted simply to balance the reaction, but has no implications on its stoichiometry. Reaction (2) is the electrochemical oxidation of the surface intermediate at high anodic potentials, and can be thermodynamically characterized by the intrinsic decomposition energy ${}_pE_{dec}$ of $[\mathrm{Fe(II)Cl_2}]_{\mathrm{surf}}$ [8,24]. This value is useful to predict whether a semiconductor is susceptible to decompose in contact to a certain electrolyte. For iron in chloride media, and taking into account all chemical equilibriums (see reaction (3)), calculations yield ${}_pE_{dec} = 2.4$ eV. This value lies below the VB edge of the n-Fe(III) oxide film (Fig. 5) and predicts that iron will not decompose unless electronic degeneracy is reached [24]. Indeed, in the absence of chloride, decomposition of the n-Fe(III) oxide film does not occur and the electrode remains passivated. However, the presence of chloride gives rise to new electronic states at the surface that are partially filled with holes when E_F approaches the surface state energy (Fig. 4(b)). Thus, this state probably facilitates inversion and electronic degeneracy at the surface [24]. The potentials needed to produce high hole concentration at the surface (and electrode corrosion) are thus shifted from 1.1 V (transpassive region in the absence of chloride) to 0.2 V in 5 mM chloride. The h^+ trapped at the oxide surface are oxidizing agents that allow

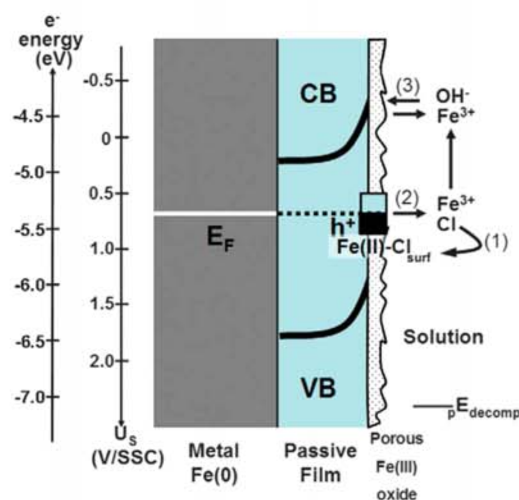

Fig. 5. Schematic representations of the band diagram of the Fe/passive film/borate buffer interface in the presence of 5 mM of Cl^-(aq) and the chemical equilibriums involved in the electrode corrosion when E_F reaches the energy level of the Cl-induced states.

Fe(II) to Fe(III) transition (reaction (2)) and the release of chloride to the solution. The Fe^{3+}(aq) species rapidly precipitate on the surface as a hydrated Fe(III) oxide, according to chemical equilibrium (3) which is completely shifted toward the right hand side (K_{PS}(Fe(III)) = 10^{34} [12]). This porous oxide layer is unable to passivate the surface against further corrosion (see Section 3.2). Note that the chloride released in (2) is not consumed in the reaction and can be subsequently adsorbed on the surface (Fig.5), which may explain why relatively small amounts of this anion are enough to trigger the breakdown of iron passivity.

4. Conclusions

We have analyzed the morphologic, chemical and electronic properties of the passive film on iron grown in the presence of chloride, in order to understand the mechanism of passivity breakdown. We have found that chloride is not incorporated within the oxide film, which is exclusively in the Fe(III) form. Recent progress in ECTS has made it possible to build the conductogram of an electrode in situ, and we have compared it between chloride solution and stable passivation conditions. In the presence of chloride, we have obtained direct and in situ experimental evidence of chloride-induced surface states within the band gap of the oxide film (~3.3 eV). These states enable new charge exchange pathways that allow hole capture at the surface of the n-type Fe(III) oxide. The blocking of VB processes that occurs in the stable iron passive film is no longer present in chloride media, and electrode corrosion can proceed through these surface states. We propose a simple 3-step mechanism for the process, in which chloride anions form an oxidizing Fe(II) surface intermediate but do not participate directly in the reaction.

Acknowledgements

This work was supported by a grant of Ministry of Education and Science (MEC) under Project CTQ2004-08046-C02-01. P.G. acknowledges financial support of the MEC through the program Ramón y Cajal. We thank the Scientific-Technical Services of the University of Barcelona for the use of facilities. C.V. acknowledges financial support from the Secretaría de Estado de Universidades e Investigación, MEC, Spain.

Appendix A. Supplementary data

Supplementary data associated with this article can be found, in the online version, at doi:10.1016/j.elecom.2006.02.003.

References

[1] H.-H. Strehblow, in: P. Marcus, J. Oudar (Eds.), Corrosion Mechanisms in Theory and Practice, second ed., Marcel Dekker Inc., New York, 2002, p. 201.
[2] B. MacDougall, M.J. Graham, in: P. Marcus, J. Oudar (Eds.), Corrosion Mechanisms in Theory and Practice, second ed., Marcel Dekker, Inc., New York, 2002, p. 143.
[3] N. Sato, Corr. Sci. 31 (1990) 1.
[4] W. Li, J.L. Luo, Electrochem. Commun. 1 (1999) 349.
[5] Y.F. Cheng, J.L. Luo, Electrochim. Acta 44 (1999) 2947.
[6] Z. Szklarska-Smialowska, Corr. Sci. 44 (2002) 1143.
[7] F. Di Quarto, M. Santamaria, Corrosion engineering, Sci. Technol. 39 (2004) 71.
[8] S.R. Morrison (Ed.), Electrochemistry at Semiconductor and Oxidized Metal Electrodes, Plenum Press, New York, 1980.
[9] M. Büchler, P. Schmuki, H. Böhni, J. Electrochem. Soc. 145 (1998) 609.
[10] M. Buchler, P. Schmuki, H. Böhni, T. Stenberg, T. Mäntylä, J. Electrochem. Soc. 145 (1998) 378.
[11] I. Díez-Pérez, P. Gorostiza, F. Sanz, J. Electrochem. Soc. 150 (2003) B348.
[12] I. Díez-Pérez, P. Gorostiza, F. Sanz, C. Müller, J. Electrochem. Soc. 148 (2001) B307.
[13] I. Díez-Pérez, A.G. Güell, F. Sanz, P. Gorostiza, submitted for publication.
[14] N. Sato, J. Electrochem. Soc. 129 (1982) 255.
[15] M. Bojinov, T. Laitinen, K. Mäkelä, T. Saario, J. Electrochem. Soc. 148 (2001) B243.
[16] R. Gotees, B. MacDougall, M.J. Graham, Electrochim. Acta 31 (1986) 1299.
[17] Y.-T. Chin, B.D. Cahan, J. Electrochem. Soc. 139 (1992) 2432.
[18] G. Abadal, F. Pérez-Murano, N. Barniol, X. Borrisé, X. Aymerich, Ultramicroscopy 66 (1996) 133.
[19] K. Azumi, K. Araki, M. Seo, J. Electroanal. Chem. 427 (1997) 15.
[20] P. Hugelmann, W. Schindler, J. Phys. Chem. B 109 (2005) 6262.
[21] A.G. Güell, I. Díez-Pérez, P. Gorostiza, F. Sanz, Anal. Chem. 76 (2004) 5218.
[22] M.F. Toney, A.J. Davenport, L.J. Oblonsky, M.P. Ryan, C.M. Vitus, Phys. Rev. Lett. 79 (1997) 4282.
[23] I. Díez-Pérez, P. Gorostiza, F. Sanz, J. Electrochem. Soc., submitted for publication.
[24] H. Gerischer, J. Vac. Sci. Technol. 15 (1978) 1422.

Supplementary data

The Iron Passive Film Breakdown in Chloride Media May Be Mediated by Transient Chloride-Induced Surface States Located within the Band Gap.

I. Díez-Pérez[a], C. Vericat[a], P. Gorostiza[b,*] and F. Sanz[a,b,*]

[a] *Laboratory of Electrochemistry and Materials (LCTEM), Department of Physical Chemistry, University of Barcelona, Martí i Franquès 1, 08028 Barcelona, Spain*

[b] *Centre de Referència en Bioenginyeria de Catalunya, Parc Científic de Barcelona, Josep Samitier 1-5, Barcelona 08028, Spain*

* Corresponding authors. Address: Laboratory of Electrochemistry and Materials (LCTEM), Department of Physical Chemistry, University of Barcelona, Martı´ i Franquès 1, 08028 Barcelona, Spain. Fax: +34 934021231.

E-mail addresses: fsanz@ub.edu (F. Sanz), pau.gorostiza@ub.edu (P. Gorostiza).

Supplementary data

2. Experimental details

2.1. Sample and electrolytes

The samples used in this study were mechanically polished polycrystalline iron disks 99.99%, 0.3 mm thick and 10 mm in diameter. The chemical purity of this surface was previously checked *ex situ* by X-ray photoelectron spectroscopy XPS. The polishing procedure involved a first step of grinding by silicon carbide polishing papers 30, 9, 5, 3, and 1 μm particle size, successively and then finishing with 0.3 μm aluminum oxide powder. Between each polishing step, the iron surfaces were sonicated in Milli-Q water and ethanol. Before each experiment the samples were thoroughly rinsed in different solvents in order to remove organic contamination from the surface, followed by a final rinse in Milli-Q water. With this treatment we obtained a mirror-like surface with a mean roughness of typically less than 2 nm.

2.2. Electrochemical measurements.

In order to have a thick 20 nm oxide layer where a deep space-charge region SCL could be completely developed, the oxide film was formed following a two-step procedure [11]. Before oxidation, the native oxide was removed by applying a potential of -1.05 V for 15 min. The first oxide-forming step was made by scanning the potential from -1.05 to -0.55 V at 5 mV/s rate, where the Fe(0) to Fe(II) process takes place. Then, the potential was held for 10 min in order to let the Fe(II) oxide film grow completely, as previously reported [12]. Finally, the potential was scanned

again from -0.55 V to a selected potential in the passive region Fe(III) oxide range and held there for 30 min, until a residual current of 0.5 μA was reached.

EIS measurements were collected using an excitation signal of 25 mV amplitude and 1 KHz frequency. The potential was scanned from 0.9V to -0.2V in the absence of chloride and from 0.6V to -0.2V in 5mM chloride after breakdown. Control experiments in chloride before breakdown were carried out between 0.2V and -0.2V. The scan rate was 5mV/s.

2.4. Ex situ AFM and XPS measurements.

Atomic force microscopy *(*AFM) measurements were conducted in air at room temperature using an extended multimode AFM head with a Nanoscope IIIa controller (Veeco Instruments, CA). All AFM images were performed in tapping mode with silicon cantilevers of 35 N/m spring constant (Nanosensors, Germany).

X-ray photoelectron spectroscopy (XPS) measurements were carried out using a Perkin-Elmer PHI 5500 model. The samples were excited with an Al k$\propto$ source which provides an energy resolution of 0.42 eV. An Ar^+ ion gun was used to acquire depth profiles of the iron samples.

3. Results and discussion

3.1. Electrochemical study

Note that quantification of the MS data (U_{FB} and doping) in figure 1b is complicated due to the dynamic conditions at which capacitance data must be recorded: When the electrode breaks down, a simple parallel capacitor-resistor equivalent circuit [9-11] is not enough to fit the data. Thus, we kept the maximum

electrode current below 100μA/cm^2 to prevent strong modification of the interface (this corresponds to U_S below 0.6V/SSC, see Fig. 2b), and we simply compared the capacitance behavior with and without chloride using the same measuring parameters (ac amplitude and frequency). The linear, negative slope MS plot can be interpreted as inversion of the n-Fe(III) electrode.

3.4. Additional comments on the discussion.

Of course, other considerations should be also taken into account once the corrosion process begins. Mechanical damage of the protective passive layer can occur during chemical dissolution of the film and thus, local film thinning can take place creating a weaker point that finally develops in a pit formation. Other local specific events that may also occur on these polycrystalline surfaces concerns on the different corrosion rate that can be associated to specific points where a high density of defects or the presence of inclusions are present [2,16]. However, the low time scale and local character of the ECTS measurement make it possible to address these problems. In short, future work is being performing on the study of the local metastable pitting that takes place few mV previous U_P (see voltammogram of Fig. 1). ECTS will be then used to analyze the different electronic properties of the Fe passive film with spatial resolution at the nanometric scale.

Chapter 6

Conclusions

The iron passivity in nearly neutral *pH*s has been the main focus of this Ph.D. thesis. The process has been studied from an electrochemical approach and the work covers the entire electrochemical potential range from the Fe metallic state to the pre-passive and passive states and ending with the transpassive breakdown of the oxide layer. The study has been focused on the dynamics of the passive film growth, as well as on the fundamental mechanisms of electron transfer across the Fe│passive film│electrolyte interface, with the aim of understanding the redox behavior of the passivated Fe electrode in front of a particular electrolytic environment. In order to reach the most reliable picture of these mechanisms, the work has been performed *in situ* and at the *nanometer scale*. For that purpose, an important block of this thesis has been devoted to the technical development of new methodologies to provide with this information.

Since the results are presented as a compendium of scientific papers, the introduction presented in chapter 1 has the purpose to extensively review the basic concepts on *Semiconductor Electrochemistry* that have been employed during the results discussion. In the first section, special emphasis on the energy level distribution at the semiconductor│electrolyte interface, and on the basic expressions to describe electron transfer across this interface, has been placed. Following up with previous subject, the second section reviews the impact of the electrochemical semiconductor model on metal passive films. The particular highly defective structure of the semiconductor oxides on passive layers confers, in most cases, particular electronic properties like for example high doping densities and/or the appearance of new localized energy states within the bandgap. The thickness of the oxide film appears to be also a key parameter in electron transfer through passive layers, being 20 Å thickness the limit below which the film can be directly tunneled. In general, semiconducting properties can be more easily evidenced on thicker oxide layers where the current carried by electrons and holes is larger than the direct tunneling component through the film. Therefore, they can be treated within the framework of the semiconductor model. The last part of the introduction corresponds to a complete summary of the last experimental advances on *in situ* measurements of the most outstanding metal passive films. As for the iron case, the passive layer consists on a duplex structure with an inner crystalline layer (so-called *natural* passive layer) whose structure has been quantitatively determined as a spinel lattice with a different level of sites occupancy with results in a high density of cation vacancies. This particular crystalline structure confers a fairly ideal *n*-type semiconducting behavior to the Fe passive layer with particularly high density of donor levels, as compare to its bulk phase. In most of the experimental conditions used in the Fe passive film preparation, an outer hydrated ferric layer grows on top of the *natural* passive layer.

In chapter 2, the new experimental procedures developed during this Ph.D. work has been described in detail. Throughout this thesis, special efforts have been put on the design of new procedures to prepare Pt/Ir STM probes for their use in highly conductive electrolytic

environments. The methodology combines the use of a special potential-programmed electrochemical method to sharp the tip with an insulating procedure involving the use of highly hydrophobic electrophoretic paints. The success of the final preparation method of such STM probes has allowed the elaboration of a detailed methodology for capturing reliable tunneling spectra form the electrode | electrolyte interface. The tunneling data is presented in the form of 2-dimensional representation so-called *Conductograms*, which monitors the *in situ* electronic structure of the electrode surface while it is electrochemically oxidized and/or reduced in a particular electrolytic environment. Conductograms then constitute the redox fingerprint of an electrode in the working electrolyte and serves to predict its redox behavior in front of a particular electro-active species. Besides, other technical details like a special design of the STM electrochemical cell incorporating a miniaturized Ag/AgCl reference electrode (SCE), have been also detailed.

The electrochemical passivity on a polycrystalline iron electrode has been studied in chapters 3 and 4. The cyclic voltammetry characterization as a function of the *pH* evidences the existence of a duplex structure whose thickness increases as the medium *pH* is decreased. At the lowest *pH*s, the anodic process $Fe(0) \rightarrow Fe^{2+}(aq)$ is enhanced thus producing a two-fold effect: on the one hand, the growth mechanism of the pre-passive layer proceeds via oxidation and precipitation process, which allows to reach a higher film thickness. Successive nucleations followed by 2-dimensional growth are observed *in situ* by ECSTM as the mechanism for the film formation within the electrochemical active region, where most of the oxide passive film growth takes place. On the other hand, the higher generated concentration of $Fe^{2+}(aq)$ during this process gives rise to the formation of a ferric outer layer by electro-oxidation at higher potentials. Moreover, within the entire electrochemical passive region, *in situ* ECSTM imaging evidences the absence of topographic changes on the passivated Fe surface, as well as the nanocrystalline nature of the Fe passive film. The acquired knowledge on the dynamics of iron passive film growth allows to fix a 2-step potential procedure to grow thick oxide layers of thicknesses up to 20 nm. Capacitance data shows that such thick passive layers present an extended ideal *n*-type behavior over the entire electrochemical passive range. These electronic properties were initially probed by ECSTM imaging at different tunneling conditions. While tunneling is possible within a wide range of energy levels in the active electrochemical range, within the passive range electrons can be injected at high energy levels only, thus evidenced the existence of a space charge region in the semiconducting passive film. The position of the conduction band edge and, as consequence, the STM tunneling conditions for the *in situ* passive film imaging can be quantitatively determined.

In chapter 3, the cathodic electrochemical reduction of the iron passive film has been also revisited by using well-oriented Fe thin film electrodes. The final step in the reduction process of the oxide film is univocally assigned to the voltammetric peak located at a potential of -1 V/SCE, thanks to the higher resolution of the cyclic voltammogram obtained on such Fe substrates. The cathodic process is fully characterized at different *pH*s and hydrodynamic conditions, thus concluding that the chemical nature of the final product for the Fe oxide cathodic reduction corresponds to an Fe(II) oxide structure.

Finally, the whole iron passivation process has been followed by ECTS and capacitance measurements as presented in chapter 4. The electronic transitions occurring on the iron electrode surface as a function of its oxidation state are directly observed in the corresponding conductogram. In short, the Fe electrode undergoes two successive electronic transitions: a

high, constant conductance indicates the Fe(0) metallic state at very negative potentials close to the hydrogen electrode reaction. Stepping into the pre-passive layer, a *p*-Fe(II) semiconducting behavior is observed whose electronic spectrum displays a high conductance behavior, possibly associated to high doping levels and/or low bandgap. Increasing the potential into the passive region, an *n*-Fe(III) oxide film is observed whose apparent bandgap in the spectrum is in good agreement with those furnished by photo-electrochemical determinations. Within the passive region, the valence band branch in the tunneling spectra diminishes as the applied potential is increased resulting in a perfect rectification behavior at high anodic potentials close to the transpassive range. These results suggest that passivity on iron may be explained as an *electronic passivation* process consisting on the formation of an effective electric barrier at the oxide│electrolyte interface that prevents electrons to be extracted from the semiconducting oxide. The electronic exchange at the different electrochemical ranges can be quantified by fitting the corresponding individual tunneling spectra to a double exponential kinetic model, which provides with values of exchange currents and transfer coefficients for the electron exchange with the main electronic bands. This electronic passivation has been also studied at higher *pH* values whose corresponding *in situ* tunneling spectra show an effective electronic barrier at earlier applied potential, thus suggesting a better electronic passivation process for the iron passive films formed in higher *pH* media.

The last chapter 5 of this Ph.D. deals with one of the most challenging issues in fundamental electrochemistry: passivity breakdown in chloride media. We have analyzed the conductogram of the passivation process in the presence of chloride. The appearance of a new valence band branch at early electron energies suggests the formation of a surface state at the oxide│electrolyte interface that may be associated to the transient formation of a surface Fe-Cl complex. This new energy level within the oxide bandgap is able to mediate electrons between the valence band and the electrolyte, thus destroying the previous electronic barrier. In view of these results, a complete picture of the corrosion process is proposed as a 3-step chemical stages, where chloride ions uniquely forms an oxidizing Fe(II) surface intermediate but do not participate directly in the overall reaction. The role of chloride as the catalyst of the process is suggested.

To end with this conclusion chapter, we found useful to shortly list the specific goals achieved during this Ph.D. work:

1. A comprehensive compendium of the last advances on *in situ* studies on metal passive layers has been elaborated.
2. An ECSTM set up has been successfully designed to perform *in situ* STM measurements under a rigorous electrochemical control.
3. A simple methodology to elaborate Pt/Ir probes for their application in advanced electrochemical STM measurements, like ECTS, has been developed.
4. The two previous goals have allowed to build up a complete protocol to record and represent reliable tunneling spectroscopic data from the electrode│electrolyte interface. The accurate measurement of electronic barrier heights becomes the critical stage on this issue.

5. The duplex structure of the Fe passive layer is further supported by the wide voltammetric analysis performed at different *pH*s.

6. The growth kinetics of the pre-passive oxide layer has been followed at the nanometer scale. Within this electrochemical range, most of the passive film growth takes place.

7. The rate of the oxide growth and the resulting thickness of the passive film have been characterized.

8. The cathodic dissolution process of the Fe passive film has been revisited by using new *ultra-flat* Fe substrates. The final reduction step of an Fe(II) oxide layer has been firstly reported and characterized as a function of different experimental parameters.

9. The topography of the Fe passive layer at high positive potentials has been characterized, and the absence of surface kinetics has been evidenced.

10. The electron transfer across the pre-passive and passive layers has been quantified by ECSTM, thus concluding that the observed redox behavior in the passive state corresponds to an electronic passivation at the oxide│electrolyte interface.

11. *In situ* tunneling spectra from the Fe│borate buffer interface have been recorded within the entire Fe electrochemical range; from the Fe metallic region to the passive state at high positive potentials. Three different regimes, in term of the electronic properties, have been characterized during the oxidation process: metallic, *p*-type and *n*-type behaviors.

12. The electronic passivation (point 10) has been further demonstrated by fitting the tunneling spectra recorded as a function of the electrochemical potential and electrolyte *pH*. Electronic passivation is observed as the blockage of the VB current in the ECTS spectrum.

13. The passivity breakdown process has been firstly characterized by *ex situ* techniques, giving rise to a general view of the chemical nature and topography of the corrosion products.

14. *In situ* tunneling spectra have been collected during passivity breakdown in the presence of chloride. The observed abrupt change in the electronic properties is based on the appearance of a local energy level in the middle of the oxide band gap.

15. A proposed mechanism for the passivity breakdown process is based on the formation of a transient Fe(II)-Cl complex at the oxide surface that is further oxidized by the presence of holes, thus facilitating the dissolution of the film.

Appendix A

ECTS studies of thiol-modified Au(111)

A.1 INTRODUCTION

The potential applications of self-assembled mono-layers (SAMs) for the construction of molecular electronic devices at nanoscale dimensions [147,148] have motivated many studies of electron transport across alkanethiol molecules, at progressively lower scale electrical contacts with metallic or semiconducting solids. A key quality of many SAMs is their intrinsically low electrical conductance, a passive but essential feature for the realization of nanoscale electronics. Organic SAMs are intriguing alternatives to SiO2 as electrically insulating materials. Well-ordered SAMs are uniform in thickness and can be designed with tunable interfacial properties, providing unique processing advantages for device fabrication. The structural diversity of thiol molecules allows to cover a wide range of device engineering applications, for example, SAMs composed of bifunctional molecules have enabled the layered deposition of conductive or semiconductive nano-particulate films [149].

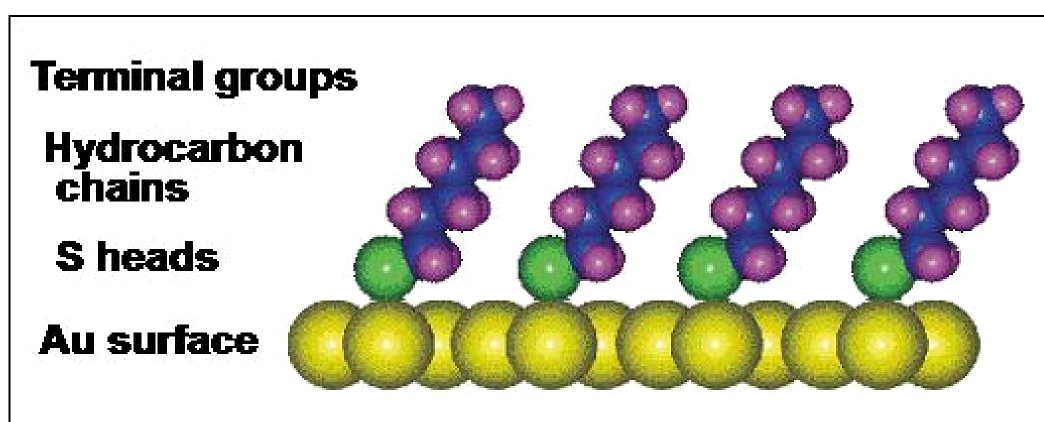

Figure A.1: Molecular model of a alkanethiol-modified Au(111) electrode. Note that the thickness of the organic layer depends on both molecular length and tilt packing.

As for fundamental studies of ET across SAMs, self-assembled monolayers of alkanethiol on Au(111) single crystal electrodes have been chosen as model systems (see Fig. A.1). Important amount of the work on that sense has been performed by conventional electrochemical techniques like CV and EIS [150,151]. However, they do not take into account monolayer defects (like *pinholes*, variation in local composition, *etc.*) which could indeed provide an alternative path for ET across the organic layer. The local character of the electrical measurements made on these systems is then a major issue in the way to build up a complete picture of the ET process through a metal|thiol interface. In general, the structure of SAMs has been extensively studied by using different local techniques such as STM and/or

AFM, and other bulk spectroscopies like helium diffraction, x-ray photoelectron spectroscopy (XPS) or thermal desorption [152].

Studies of electron transport at a local level, or even at a single molecule level, can be reached by using SPM techniques. They have provided valuable information in UHV, in air and in liquid environments [153,154]. Ideally, one would like to place the STM probe tip directly over a molecule within a SAM and measure its conductance as a function of the applied V_{Bias}. However, direct measurements of this type are often frustrated by difficulties in the precise determination of the tip-molecule separation.

These structures can be employed in wet applications such as molecular recognition, protein adsorption, and templates for crystallization of inorganic salts. In these cases, insight into the ET through a metal│thiol│electrolyte interface is required. As we have had the opportunity to learn during this PhD. work, ECSTM technique offers the opportunity to obtain quantitative structural and electronic (through ECTS application) information of an solid│electrolyte interface under electrochemical control. In this Appendix, an ECTS study of the metal│thiol│electrolyte interface is presented for the first time. These preliminary results aim to demonstrate that the capability of this technique can be extended beyond the study of passivity which opens up a wide range of possibilies.

A.2 EXPERIMENTAL DETAILS

Sample preparation

Au(111) single crystals (MaTeck [155]) were electropolished (at +10 V in 0.1 M H_2SO_4, then 10 min in 1 M HCl to remove the oxide), thoroughly rinsed with Milli-Q water, annealed in a butane flame and gently cooled under Ar flow. The freshly prepared Au(111) samples were incubated in 50 μM decanethiol ethanolic solutions for at 24 h at room temperature to obtain SAMs with high density of ordered domains (see Fig. A2A). In the following, we will use the notation thiol-Au(111) substrate to refer to the modified-Au(111) substrate. With the use of single crystals (instead of evaporated *Au films*) flat terraces of at least 0.5 μm can be routinely achieved, and this ensures that the tip will always be placed on flat, defect-free regions of the surface, covered by ordered thiol domains (see Fig. A2B), when the feedback is disconnected to record the ECTS spectra (see section 2.4).

Voltammetry

CV were performed in deaerated 0.1 M KOH solutions using a conventional electrochemical glass cell with Ag/AgCl as reference electrode (SSE) and a Pt wire as counter electrode. Scan rate was 5 mV/sec. CV was also performed in the ECSTM cell (described below) after each series of measurements to ensure that no desorption of the SAM had occurred during the experiment.

ECSTM & ECTS measurements

ECSTM and ECTS measurements were performed in a STM system (Pico-SPM, Molecular Imaging, USA [156]) using a Teflon electrochemical cell modified to incorporate a miniaturized real SSE and a Pt wire as counter electrode. The electrolyte was deaerated 0.1 M

KOH. An accurate and independent control of both tip (U_{tip}) and sample ($U_{electrode}$) potentials versus the same SSE was achieved through a bi-potentiostat (Picostat, Molecular Imaging, USA [156]). During the measurements the whole cell was in an inert (Ar) atmosphere. The STM was controlled by a Nanoscope IIIa electronics (Veeco Instruments, USA [157]), connected to the STM through a break out box that allows external application of fast voltage ramps to the tip and high rate data capturing of the ECTS curves with a digital oscilloscope (Tektronix TDS210, USA [158]).

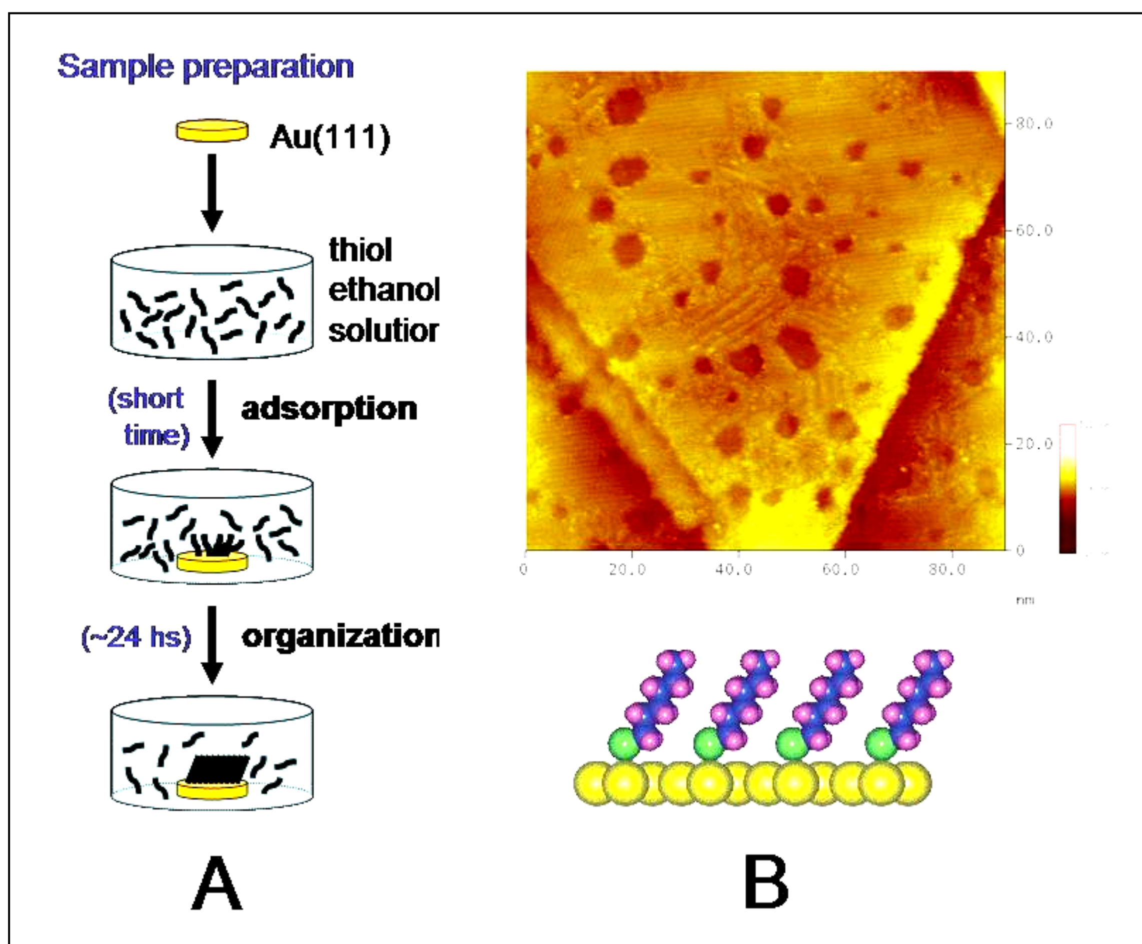

Figure A.2: (A) Schematic representation of the deposition process of the thiol monolayer onto the Au(111) substrate. (B) ECSTM image of a freshly prepared decanethiol-Au(111) sample. Ordered thiol domains are observed in the image center as small stripe patters. Imaging conditions: $U_{electrode}$=-200 mV, U_{tip}=-500 mV and i_{Tipt}=0.5 nA.

Conventional ECSTM images of the surface were previously recorded in order to choose a flat region of the sample with only monoatomic or diatomic gold vacancies (commonly called *pits*, see Fig. A2B), which always appear on such interfaces as a result of the strong interaction between the gold and the thiol S heads [165]. Also, only when the forward and reverse tip scans (*trace and retrace*) were identical and the images showed minimum drift distortion, the ECTS measurements were carried out. Moreover, to ensure that the tip was always placed on a flat region of the sample and that the surface had not been damaged after performing an ECTS spectrum, ECSTM imaging was done after capturing each ECTS curve. Two types of measurements are performed:

1. **Tip tunneling current (I_{Tip}) versus tip-sample distance (s) measurements**: the tip was initially placed at an s values within the SAM, at It values that did not damage the organic monolayer. The feedback was disabled and the tip-sample distance was separated 3 nm away from the surface while I_{Tip} was recorded. $U_{electrode}$ and U_{tip} potentials were kept constant. The feedback was then re-enabled. The whole process had a time scale of a few milliseconds using tip retracting rates of around 1 μm/sec thus ensuring that the drift in s remains negligible. Values of $U_{electrode}$ and U_{tip} ranged as -0.8 V ≤ $U_{electrode}$ ≤ -0.1 V and -0.9 V ≤ U_{tip} ≤ -0.5 V, respectively. The initial fixed tunneling current under feedback conditions ($i_{setpoint}$) was 2 nA. More than 20 curves were averaged for each U_{tip}-$U_{electrode}$ pair.

2. **I_{Tip} versus U_{tip} measurements**: The $U_{electrode}$ and the initial U_{tip} values ($U_{tip,0}$) were varied as -1.2 V ≤ $U_{electrode}$ ≤ -0.1 V and -0.9 V ≤ $U_{tip,0}$ ≤ -0.7 V respectively, and $i_{setpoint}$ values were compensated as function of the initial Bias voltage (see section 2.4 for further experimental details). As it was rationalized in section 2.4, $U_{tip,0}$ was adjusted in a way that good ECSTM imaging conditions were obtained prior to the capture of the tunneling spectra. The feedback was then disconnected and U_{tip} was ramped at a rate in the order of 20 V/sec while recording I_{Tip}. Finally, $U_{tip,0}$ is applied again and the feedback is restored. Only those curves whose final I_{Tip} was less than 10% different from $I_{tip,0}$ were acquired. More than 20 curves were averaged for each Us. Leak electrochemical I_{Tip} were subtracted by recording blank spectra at 3 nm away from the surface for each $U_{electrode}$ value.

For further details on the experimental procedure concerning ECTS methodology, check the experimental section and supporting material in section 2.4.

A.3 RESULTS AND DISCUSSION

A.3.1 Electrochemical and ECSTM characterization

Figure A.3 shows a characteristic CV signal of a decanethiol-Au(111) electrode immersed in the working electrolyte. The main electrochemical processes, voltammetric peaks labeled as I and I' (following the same notation as in chapter 3) in the figure, correspond to the anodic thiol (RS) re-adsorption:

$$Au + RS^- \rightarrow Au - RS + e^- \qquad \text{(a1)}$$

and to the reversed process, the cathodic thiol desorption:

$$Au - RS + e^- \rightarrow Au + RS^- \qquad \text{(a2)}$$

where -R corresponds in this case to a decane chain. The overall process is indeed very simple; at potentials below peak I', the thiol bond (Au-S) is broken through the interfering of an e^- charge carrier going to the solid surface (see section 1.2.4.4) as it occurs on a semiconducting passive film. The e- is then captured by the –S atom thus promoting the de-attachment of the anionic thiol molecule from the Au(111) surface into the electrolyte. The whole process can be followed *in situ* by recording ECSTM images at different $U_{electrode}$ (see example of a

similar experiment in section 3.2). Figure A.3 inset shows a couple of ECSTM images recorded at far above the peak I' ($U_{electrode}$ =-500 mV/SSE) and right at the onset of peak I' ($U_{electrode}$ =-1 V/SSE). A wide electrochemical range of almost 1 V over peak I represents the *passive thiol region* where the organic layer remains stable at the Au surface. The disruption of the organic monolayer is observed by the formation of small micellar aggregates as a result of the low solubility of the thiol in the aqueous medium (see micelle representation in Fig. A.3 inset). Micellar aggregates then slowly diffuse from the Au surface into the solution bulk and so they are progressively no longer observed in the ECSTM images. After this process takes place, the electrochemical thiol re-adsorption described in equation (a1) corresponds to the reversed process in which an e^- is transferred from the anionic thiol (which is oxidized) to the Au(111) electrode. By integrating the charge in both peaks, it is observed that the efficiency in peak I diminishes because the corresponding electrochemical process is hindered by both diffusion of the micelles toward the electrode surface and the disruption of the micellar architecture. The last stage is required for the thiol molecule to access the electron surface electrode where the electron exchange takes place.

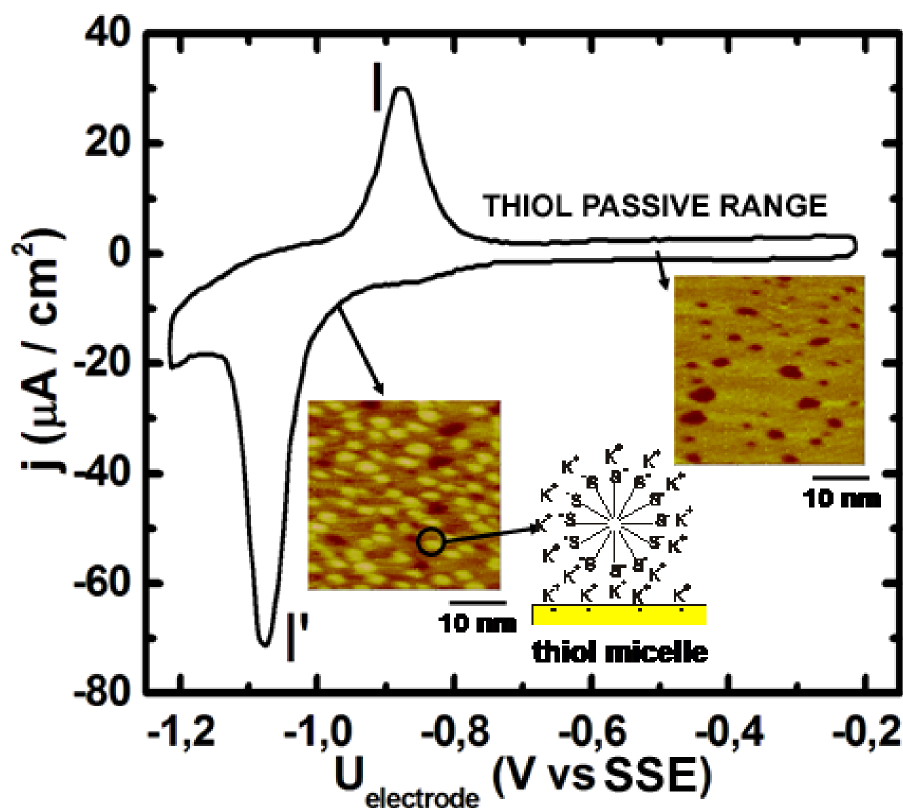

Figure A.3: CV signal of a thiol-modified Au(111) electrode in 0.1 M KOH. The inset figure shows two ECSTM images at the potential ranges corresponding to *passive* thiol region (right) and onset of reductive desorption (Eq. (a2)) (left). A short representation of a thiol micelle is included in the center.

This particular redox behavior is also found for similar alkanethiol-Au(111) systems, being the molecular length the dominant parameter controlling the electron tunneling transfer across the interface. The addition of other chemical groups or insaturations within the molecular structure will strongly modify the electronic properties of the organic layer [166].

A.3.2 Barrier height (ϕ_B) measurements

The aim of these experiments is to determine the quantitative and local picture of the ET across the Au│decanethiol│electrolyte interface using the ECTS technique within a wide electrochemical range and so building up the quantitative band diagram for this particular case. In chapters 2, 4 and 5, the use of the barrier height (ϕ_B) determination on both metal and oxidized surfaces served us to fix the starting tunneling conditions in ECTS. However, an accurate determination of ϕ_B as a function of $U_{electrode}$ can also provide with information about the distribution of energy levels at the studied interface. Since the film thickness of these organic monolayers is in the order of 15Å (depending on the specific thiol molecule), it is reasonable to approach this system to metal│ insulator│metal junction, where a formal tunneling mechanism dominates the ET. *Simmons* simplification constitutes a good approach to this system, since it allows to calculate the i_{tunnel} for an infinite, plane parallel plate, as long as $\phi_B > V_{Bias}$. Under this approximation the effective barrier height can be determined from [164]:

$$\phi_B = \frac{\beta^2 h^2}{32\pi^2 m^*} \times (\ln 10)^2 \qquad \text{(a3)}$$

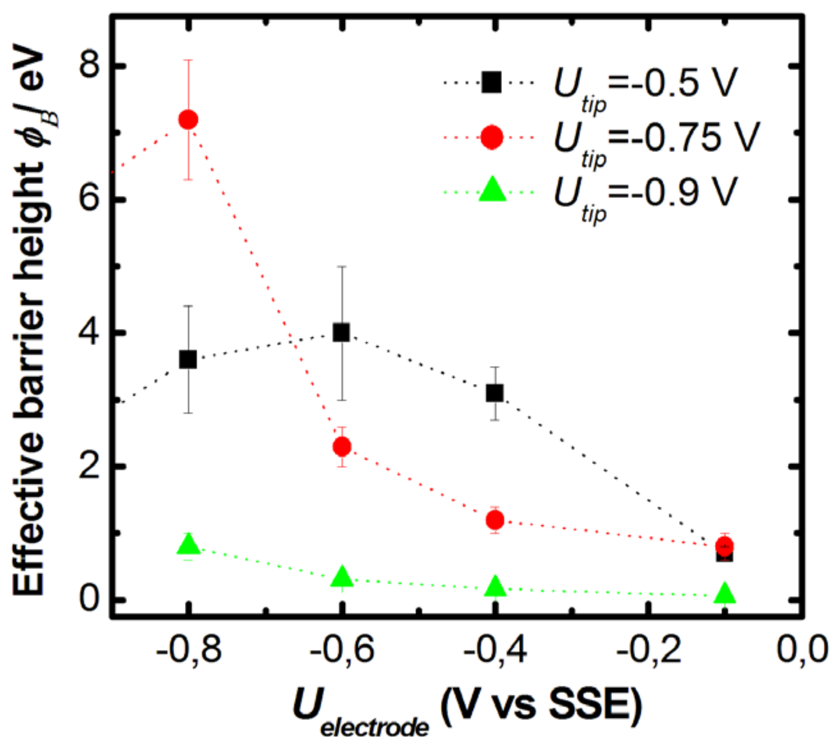

Figure A.4: Three series of barrier heights ϕ_B measurements as a function of $U_{electrode}$ at different U_{tip} within the thiol passive region (see Fig. A.3).

where β =d(log i_{tunnel})/ds and other terms have their usual meaning. Barrier heights can then be determined from the experimental slope of the I_{Tip} versus s curves (see section 2.4) using equation (a3). Figure A.4 shows a *compendium* of the results corresponding to ϕ_B measurements at different $U_{electrode}$ and U_{tip} values. Two important features are deduced: firstly the barrier values abruptly increases as the $U_{electrode}$ approaches the peak I', and

secondly, those values obtained at U_{tip}= -0.9 V/SSE are significantly lower than those at higher U_{tip} and, more interestingly, they present a weak dependence with $U_{electrode}$.

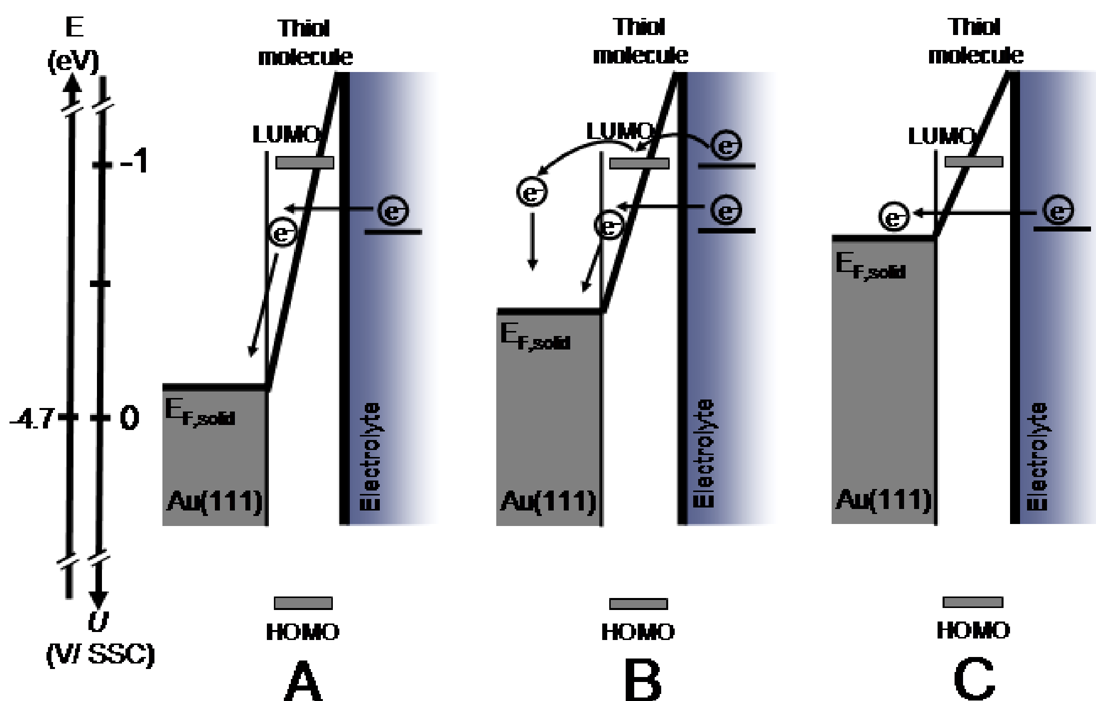

Figure A.5: Tunneling ET through the Au│decanethiol│electrolyte interface. The triangular barrier displays a thinner SCL at more negative $U_{electrode}$. At U_{tip} near the LUMO level, e^- hopping decreases the average barrier.

The results in figure A.4 allow us to build up a first band diagram model for the Au│decanethiol│electrolyte interface which helps to explain its redox behavior. Figure A.5 summarizes the proposed model that accounts for the observed behavior of the measured electronic barriers at the different electrochemical conditions. As far as U_{tip} is far from electronic states within the alkylthiol (*i.e.* well below the *lowest unoccupied molecular orbital* (LUMO) of the thiol) the interface can be modeled as a simple triangular barrier across the dielectric molecular layer whose effective thickness increases as $U_{electrode}$ becomes more negative (see Fig. A.5A-C). This fact is in agreement with the reduction of ϕ_B observed for U_{tip}= -0.75 V as $U_{electrode}$ is changed from –0.8 to –0.1 V (circles in Fig. A4). In addition, higher ϕ_B values and a more pronounced reduction versus $U_{electrode}$, are found for U_{tip}= -0.5 V (squares in Fig. A4) according to an effective wider barrier (see tip energy levels in Fig. A.5A and C). However, the low barrier and weak $U_{electrode}$ dependence of ϕ_B at U_{tip}= -0.9V (triangles in Fig. A4) can be the result of U_{tip} approaching the LUMO level of the alkyl thiol molecule in the film. In this case, the mechanism of ET changes from the previous direct tunneling through a triangular barrier to a probably a resonance tunneling assisted by the LUMO level through which electrons can hop before reaching the Au substrate (Fig. A.4B). If this interpretation is correct, these results allow to locate the LUMO of the molecule around –0.9V (-3.8 eV in the vacuum scale, see Eq. (1.1)). This ET mechanism could be compared to the observed tunneling transfer assisted by SS at the semiconductor oxide │electrolyte interface (see section 1.2.4.3).

A.3.3 ECTS measurements

ECTS spectra from the Au(111)│decanethiol│electrolyte interface were also recorded at different $U_{electrode}$ following the same methodology described in section 2.4. The obtained tunneling spectra display a linear behavior at all $U_{electrode}$ values within the thiol passive region (see Fig. A.6), whereas rectification behaviors like those obtained on semiconductor│electrolyte interfaces (chapter 4) were never observed. This fact is in good agreement with the proposed band model in figure A.5; firstly, the observed linear behavior in the ECTS spectra over a more than 1.5 V energy window below the LUMO level (Fig. A.6), is consistent with the thin dielectric barrier created at the thiol layer within this electron energy range. Moreover, we can also follow the conductance of the surface electrode with the applied potential $U_{electrode}$ by monitoring the slope of the ECTS spectrum. As preliminary results, a sudden increase of the conductance at $U_{electrode}$= -0.6 V is observed. We have tentatively associated this abrupt conductance increase to the *ionic permeation* occurring when $U_{electrode}$ approaches the onset of peak I', as has been proposed to occur through the thiol layer at potentials right before its electrochemical thiol desorption [165]. The mechanism of this process is still under debate. In short, it is not clear whether this conductance increase is produced by a local decrease in the molecular density of the organic layer, thus allowing easy ionic permeation, or alternatively, it may be due to a net change in the 2-dimensional lattice arrangement that gives rise to a less compact and more conductive configuration. As far as $U_{electrode}$ does not cross peak I', this conductance behavior appears to be reversible, in agreement with reversible structural changes observed by ECSTM for this system [160], and so it can not be related to a thiol desorption process.

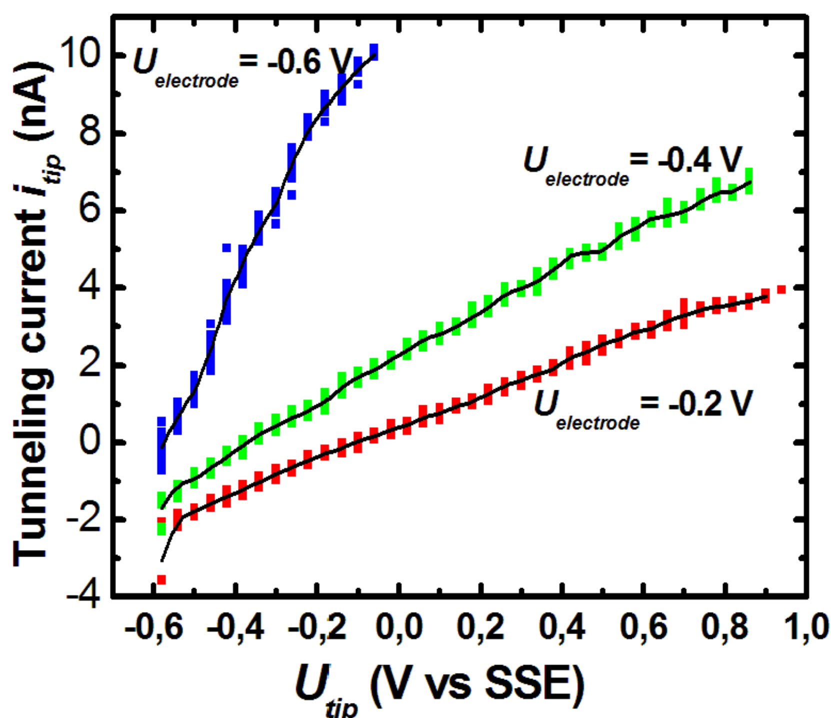

Figure A.6: ECTS spectra of the Au│decanethiol│electrolyte interface at different $U_{electrode}$. Initial tunneling conditions: $U_{tip,0}$= -0.6 V and $i_{setpoint}$ compensated as a function of Bias (see experimental section).

It must be stressed here that all these assumptions concerning the tunneling mechanism account for the dielectric energy range only and, therefore, additional conductance increases may be also observed when probing higher energy levels (more negative U_{tip} values) near the LUMO which would then correspond to a different ET through the thiol film more than a structural modification of the layer itself.

A.4 CONCLUSIONS

Summing up, it is demonstrated that ECTS is a promising tool to study *in situ* quantitative electron transport through molecular architectures immersed in a particular electrolytic environment. The preliminary results on the Au(111)│decanethiol│electrolyte interface allow us to propose a simple mechanism for the electron transport across this layer, based on a direct non-resonant tunneling transfer in a fairly ideal triangular barrier. Moreover, rearrangement processes within the thiol monolayer that may give rise to different redox behavior of the modified electrode, can be locally detected through variations in the interface electronic conductance.

Appendix B

Symbols and acronyms

As far as possible, the recommendations of the International Union of Pure and Applied Chemistry (IUPAC) have been used for the units, symbols and acronyms employed throughout this Ph.D. thesis. Most of them are described in *Terminology in semiconductor electrochemistry and photoelectrochemical energy conversion*, Pure and Applied Chemistry **63** (1991) 569. Hereby, a selection of the most used symbols and acronyms employed in the present work is provided for reference:

#	Activated/transition state
α	Transfer coefficient
χ	Electron affinity
$\Delta\phi_{SC}^{o}$	Potential drop in the semiconductor at the equilibrium
$\Delta\phi_{d}$	Potential drop in the Diffuse layer
$\Delta\phi_{el}$	Potential drop in the electrochemical double layer
$\Delta\phi_{H}$	Potential drop in the Helmholtz layer
$\Delta\phi_{M/O}$	Potential drop at the metal | oxide interface
$\Delta\phi_{O/E}$	Potential drop at the oxide | electrolyte interface
$\Delta\phi_{ox}$	Potential drop across the passive film
$\Delta\phi_{ref}$	Potential drop at the Ref. electrode | electrolyte interface
$\Delta\phi_{SC}$	Potential drop in the semiconductor (SCL potential)
$\Delta\phi_{Total}$	Total potential drop across the interface
ΔG^{0}	Gibbs free energy under equilibrium conditions
ΔG_{ox}	Gibbs free energy of the oxidized species
ΔG_{red}	Gibbs free energy of the reduced species
ε_0	Permittivity of vacuum ($8.85 \cdot 10^{-14}$ $CV^{-1}cm^{-1}$)
ε_{ox}	Dielectric constant of the oxide layer
Φ	Work function
ϕ	Galvani potential
ϕ_B	Local barrier height
η	Overpotential
η_{SC}	Semiconductor overpotential
φ	Mean free path of charge carriers in the semiconductor
κ	Dielectric constant
λ	Reorganization energy of the solvation shell
μ_C	Doping level in an *n*-type semiconductor
μ_V	Doping level in a *p*-type semiconductor

ν	Kinematic viscosity of the electrolytic medium
v_R	Richardson velocity
Θ	Electron tunneling probability
ρ	Charge density
$\rho(E)$	Distribution of energy states at the solid
σ	Transmission coefficient of the activated state
υ	Vibration frequency
ω	Electrode rotation speed
Ω	Molecular volume per cation M^{n+}
$[Ox]$	Oxidized species in the electrolyte
$[Red]$	Reduced species in the electrolyte
A	Area
c_{el}	Ionic concentration in either in ions/cm^3 or in M (mol/l)
c_{ox}	Concentration of oxidized species in the electrolyte bulk
c_{red}	Concentration of reduced species in the electrolyte bulk
$c_{S,ox}$	Concentration of oxidized species at electrode surface
$c_{S,red}$	Concentration of the reduced species at electrode surface
C	Capacitance
C_d	Diffuse (Gouy) layer capacitance
C_{el}	Electrochemical (electrolyte) double layer capacitance
C_H	Helmholtz (compact) layer capacitance
C_{SC}	Semiconductor capacitance
C_{Total}	Total interface capacitance
$c_{V_O^{2+}}$	Oxygen vacancies concetration
d	Oxide film thickness
D_{ox}	Diffusion coefficient of the oxidized species in solution
D_{red}	Diffusion coefficient of the reduced species in solution
e	Electron charge ($1.60 \cdot 10^{-19}$ C)
e^-	Electron (charge carrier)
E_A	Acceptor energy level
E_a	Activation energy
E_{CB}	Conduction band energy
E_{Cf}	Mobility conduction band
E_D	Donor energy level
E_F	Fermi energy
$E_{F,redox}$	Fermi energy in the electrolyte
$E_{F,solid}$	Fermi energy in the solid
E_g	Bandgap energy
E_I	Ionization energy
E_{IS}	Energy level of the interface state
E_L	Localized energy level
E_{mg}	Mobility gap
E_{Ox}	Energy of the unoccupied state of the redox system
E_{Red}	Energy of the occupied state of the redox system
$E_{S,CB}$ or $U_{S,CB}$	Conduction band edge energy or potencial

$E_{S,Cf}$	Mobility conduction band edge energy
$E_{S,VB}$ or $U_{S,VB}$	Valence band edge energy or potential
E_{SS}	Energy level of the surface state
$E_{S,Vf}$	Mobility valence band edge energy
E_{TS}	Energy level of the trap state
E_{vac}	Vacuum level
E_{VB}	Valence band energy
E_{Vf}	Mobility valence band
E_a^0	Initial activation energy
E_{redox}^0	Fermi energy in the electrolyte at the equilibrium
${}_nE_{decomp}$	Decomposition energy level created by electrons
${}_nE_F$	Fermi level in an *n*-type semiconductor
${}_pE_{decomp}$	Decomposition energy level created by holes
${}_pE_F$	Fermi level in an *p*-type semiconductor
$f(E)$	Fermi distribution function of electrons
F	Faraday constant
F_S	Field strength
h	Planck constant
$\hbar$	Reduced Planck constant $h/(2\pi)$
h^+	Hole (charge carrier)
i_{tunnel}	Tunneling current
I	Ionic strength (given in M)
I_{tip}	Total STM tip current
j	Current density
j_0	Exchange current density
j_{cap}	Capacitive current density
j_{ETR}	Current density of the electron transfer reactions
j_{ITR}	Current density of the ion transfer reactions
j_{Total}	Total current density
$J_{V_O^{2+}}$	Flux of anion vacancies
j_0^{CB}	Exchange current density at CB
j_0^{VB}	Exchange current density at VB
j_{CB}^{ox}	Current density of the oxidation process at CB
j_{CB}^{red}	Current density of the reduction process at CB
j_{diff}^{ox}	Current density of diffusion-controlled oxidation process
j_{diff}^{red}	Current density of diffusion-controlled reduction process
$j_{\lim}^{ox}$	Limiting current density of an oxidation process
$j_{\lim}^{red}$	Limiting current density of an reduction process
j_{VB}^{ox}	Current density of the oxidation process at VB
j_{VB}^{red}	Current density of the reduction process at VB
k'	Pre-exponential factor
k_0	Rate constant under equilibrium conditions

k_B	Boltzmann constant ($8.6 \cdot 10^{-5}$ eV/K)
k_{ox}	Rate constant of the oxidation reaction
k_{red}	Rate constant of the reduction reaction
k_{SP}	Equilibrium constant of the solubility product
L_{diff}	Diffusion layer thickness of the electrolyte species
m^*	Effective electron mass
M	Number of mobile ions per surface area unit
M_i^{n+}	Interstitial metal cation
n	Electron density
n_0	Electron density in the solid bulk
N	Density of electronic states
N_a	Avogadros' number
N_A	Density of acceptor states
N_{CB}	Effective density of states at the CB bottom
N_D	Density of donor states
N_M^{ox}	Total number of M^{n+} per unit area of oxide
n_S	Electron density at the solid surface
N_S	Local density of states
$n_{S,0}$	Electron density at the solid surface at the equilibrium
N_{Site}	Total number of adsorption sites
N_{SS}	Density of surface states
N_{VB}	Effective density of states at the VB top
O_i^{2-}	Interstitial oxygen anion
p	Hole density
p_0	Hole density in the solid bulk
p_S	Hole density at the solid surface
$p_{S,0}$	Hole density at the solid surface at the equilibrium
Q	Charge
Q_{el}	Charge stored at the interfacial electrolyte
Q_{ox}	Accumulated charge in the oxide film
Q_{Solid}	Charge stored at the solid surface
R	Universal gas constant (8.3145 J/mol K
Ref.	Reference
s	STM tip-surface distance
T	Temperature (given in K)
U_B	Breakdown potential
$U_{electrode}$	Applied electrode potential
U_{tip}	Applied tip potential
U_{FB}	Flat band potential
U_{FP}	Flade potential
U_{OCP}	Open circuit potential
U_P	Passive film formation potential
U_{redox}	Redox potential in the electrolyte
U_{redox}^0	Redox potential in the electrolyte at the equilibrium
U_{FB}^n	Flat band potential for an *n*-type semiconductor

U_{FB}^{p}	Flat band potential for a *p*-type semiconductor
${}_{n}U_{decomp}$	Redox decomposition potential mediated by electrons
${}_{p}U_{decomp}$	Redox decomposition potential mediated by holes
V_{Bias}	Bias voltage (STM formalism)
V_{M}^{n-}	Metal cation vacancy
V_{O}^{2+}	Oxygen anion vacancy
x_{OHP}	OHP separation
AFM	Atomic Force Microscopy
CB	Conduction band
CV	Cyclic voltammetry
ECSTM	Electrochemical Scanning Tunneling Microscopy
ECTS	Electrochemical Tunneling Spectroscopy
EIS	Impedance Electrochemical Spectroscopy
ET	Electron transfer
ETR	Electron transfer reactions
GDP	Gross domestic product
HER	Hydrogen electrode reaction
HOMO	Highest occupied molecular orbital
IHP	Inner Helmholtz plane
IS	Interface state
ITR	Ion transfer reactions
LCTEM	Laboratory of Electrochemistry and Materials
LDOS	Local density of states
LUMO	Lowest unoccupied molecular orbital
MSE	Mercurious sulphate electrode
OCP	Open circuit potential
OER	Oxygen electrode reaction
OHP	Outer Helmholtz plane
PDM	Point defect model
SAM	Self-assembled monolayer
SCE	Saturated Calomel reference electrodes
SCL/SCR	Space charge layer/region
SEM	Scanning electron microscopy
SERS	Surface Enhanced Raman Spectroscopy
SHE	Saturated hydrogen electrode
SPM	Scanning probe microscopy
SS	Surface state
SSE	Silver/Silver chloride reference electrode
STM	Scanning Tunneling Microscopy
UHV	Ultra high vacuum
VB	Valence band
XANES	X-ray absorption near edge
XPS	X-ray photoelectron spectroscopy
XRD	X-ray diffraction

Appendix C

Selected publications

A list of selected publications by the author related to this Ph.D. thesis:

Publications in Peer-review journals

I. Díez-Pérez, P. Gorostiza, M.-C. Bernard, P. Allongue, F. Sanz, submitted to *Journal of Physical Chemistry B* (2006).

I. Díez-Pérez, P. Gorostiza and F. Sanz, *Electrochemistry Communications*, in press (2006).

I. Díez-Pérez, A. G. Güell, P. Gorostiza and F. Sanz, *Analytical Chemistry*, in press (2006).

I. Díez-Pérez, C. Vericat, P. Gorostiza and F. Sanz, *Electrochemistry Communications*, **8**, 627 (2006).

A.G. Güell, I. Díez-Pérez, P. Gorostiza and F. Sanz, *Analytical Chemistry*, **76** (2004) 5218.

R. Díaz, S. Joiret, A. Cuesta, I. Díez-Pérez, P. Allongue, C. Gutiérrez, P. Gorostiza and F. Sanz, *Journal of Physical Chemistry B*, **108** (2004) 8173.

D. Bevilaqua, I. Díez-Pérez, C. S. Fugivara, F. Sanz, A. V. Benedetti and O. Garcia Jr., *Bioelectrochemistry*, **64** (2004) 79.

D. Bevilaqua, I. Díez-Pérez, C. S. Fugivara, F. Sanz, O. Garcia Jr. and A. V. Benedetti, *Journal of Brazilian Chemical Society*, **14** (2003) 637.

R. Díaz, I. Díez-Pérez, P. Gorostiza, F. Sanz and J. R. Morante, *Journal of Brazilian Chemical Society*, Phantoms Report, **14** (2003) 523.

I. Díez-Pérez and F. Sanz in *Scanning Probe Microscopy: Basic Concepts and Applications*, **1** (2003) 75.

I. Díez-Pérez, P. Gorostiza and F. Sanz, *Journal of the Electrochemical Society*, **150** (2003) B348.

I. Díez-Pérez, P. Gorostiza, F. Sanz and C. Müller, *Journal of the Electrochemical Societyy*, **148** (2001) B307.

I. Díez-Pérez, P. Gorostiza, F. Sanz and C. Müller in *Scanning probe techniques for materials characterization at nanometer scale*, D. C. Hansen, H. S. Issacs and K. Sieradzki (eds.), Electrochemical Society Proceedings Volume **2000-35** (2000) 122.

Oral presentations in international scientific meetings

I. Díez-Pérez, P. Gorostiza, F. Sanz and C. Müller, "*Estudio de la dinámica superficial y de las propiedades eléctricas de las capas pasivantes de óxido de Fe mediante STM"*, II Congreso de Fuerzas i Túnel, Santiago de Compostela (Spain), September 2000.

I. Díez-Pérez, P. Gorostiza, F. Sanz and C. Müller, *"Surface Dynamics and Electric Properties of the Passive Film on Iron by in situ STM"*, 198th Meeting of The Electrochemical Society, Phoenix (USA), October 2000.

I. Díez-Pérez, P. Gorostiza, F. Sanz, C. Müller and P. Allongue, *"Electronic properties and surface dynamics of iron passive films by EC-STM"*, STM, Vancouver (Canada), July 2001.

R. Díaz, I. Díez-Pérez, P. Gorostiza, F. Sanz, and J. R. Morante, *"Tin oxide thin films: electronic properties and growth mechanism under electrochemical control"*, 201th Meeting of The Electrochemical Society, Philadelphia (USA), May 2002.

I. Díez-Pérez, P. Gorostiza and F. Sanz, *"Direct evidence of the electronic conduction of the passive film on iron by ECSTM"*, GRC Gordon conference, New Hampshire (USA), July 2002.

I. Díez-Pérez, P. Gorostiza and F. Sanz, "*Electronic Properties and Surface Dynamics of Fe and Sn Passive Films by EC-STM"*, ISE International Society of Electrochemistry, Düsseldorf (Germany), September 2002.

R. Díaz, I. Díez-Pérez, P. Gorostiza and F. Sanz, *" Electrochemistry of tin in borate buffer solutions: an in situ Raman study"*, MRS Materials Research Society, San Francisco (USA), April 2003.

I. Díez-Pérez, A. G. Güell, P. Gorostiza and F. Sanz, *"Probing the electronic structure of dynamics of the passive film on Fe by ECSTM and ECTS"*, Electrochem'03, Southampton (UK), September 2003.

I. Díez-Pérez, A. G. Güell, P. Gorostiza and F. Sanz, *"Estudio de la dinámica de crecimiento y de las propiedades electrónicas de óxidos de hierro mediante EC-STM/EC-STS"*, IV Congreso de Fuerzas i Túnel, Vic (Spain), September 2004.

I. Díez-Pérez, A. G. Güell, P. Gorostiza and F. Sanz, *"In situ formation of a passive layer by EC-STM/EC-STS"*, Seeing at the nanoscale, Grenoble (France), October 2004.

I. Díez-Pérez, A. G. Güell, P. Gorostiza and F. Sanz, *"Probing the electronic properties of Fe/Oxide/liquid interfaces by ECSTM and ECTS"*, Electrochem'05, Newcastle (UK), September 2005.

I. Díez-Pérez, C. Vericat, P. Gorostiza and F. Sanz, *"Electrochemical tunneling spectroscopy provides a fingerprint of electrode reactivity: Conductance maps"*, *Invited speaker*.

C. Vericat, I. Díez-Pérez, P. Gorostiza and F. Sanz, *"In situ study of the electronic properties of akanethiol SAMs on Au(111)by ECTS"*, 209th Meeting of The Electrochemical Society, Denver (USA), May 2006.

I. Díez-Pérez, A. G. Güell, P. Gorostiza and F. Sanz, *"Electrochemical formation of a semiconducting metal oxide observed by in situ tunneling spectroscopy"*, GRC Gordon conference, New Hampshire (USA), July 2006. *Invited speaker*.

I. Díez-Pérez, P. Gorostiza and F. Sanz, *"Electrochemical Tunneling Spectroscopy provides a fingerprint of electrode reactivity: Conductance maps"*, Forum on Electrochemistry and Innovation, Porto (Portugal), October 2006. *Invited speaker*.

Appendix D

Resum en català

Pròleg

UNA MICA D'HISTÒRIA

L'any 1836 Schönbein [1] va donar per primera vegada la definició *formal* de "passivació": és el fenomen pel qual la reacció de dissolució d'un metall es troba cinèticament dificultada tot i que, en les mateixes condicions, està termodinàmicament afavorida. Des de llavors han passat gairebé dos segles i i trobo sorprenent que encara sigui un tema de debat intens i que generi tantes publicacions (comunicacions, articles, llibres especialitzats...). Així mateix, com que passivació i corrosió són dos conceptes estretament relacionats, no és d'estranyar que aquests temes despertin un gran interès entre la comunitat científicotècnica. Donaré un parell d'exemples per tal d'il·lustrar aquest fet: als Estats Units, l'any 2002, els danys ocasionats per la corrosió van suposar el 3,1% del producte interior brut (PIB) i l'any 2004 les pèrdues econòmiques van ascendir a 364 bilions de dòlars, despesa similar a la causada per l'huracà Katrina. A Europa les dades són igualment espectaculars ja que la corrosió provoca la pèrdua d'un 4% en l'economia global. Increïble, no? Recordo un comentari molt encertat sobre tot això de Bob Rapp, de la Ohio State University, en el seu article *"Corrosion, a study of degradation"* publicat a *Materials Today* (març de 2006): "mentre es tolerin aquestes pèrdues anuals, la corrosió suposarà la catàstrofe tècnica de més magnitud de la nostra era". Per a molts investigadors del camp de la corrosió, aquest és el veritable leitmotiv per estudiar la corrosió dels metalls i aliatges amb més aplicacions industrials: Fe, Cu, Ni, acers, aliatges magnètics... i l'última conseqüència de tots aquest fests és el ressorgiment d'un nou camp d'investigació anomenat Ciència i Enginyeria de la Corrosió, que gaudeix actualment de nombrosos adeptes i que ja ha protagonitzat els simposis més rellevants en les principals reunions d'electroquímica i tecnologia de l'estat sòlid. Aquest interès creixent es basa en què es podran dissenyar mètodes més nous i robustos de protecció contra la corrosió quant més es coneguin els mecanismes pels quals aquesta actua. La seguretat i el correcte funcionament de molts dispositius, màquines i equipaments depèn de la protecció contra la corrosió com ara vaixells i plataformes marítimes, circuits electrònics, canonades subterrànies, pròtesis, vehicles de transport, empaquetaments alimentaris, tancs per a productes químics o plantes purificadores d'aigua.

D'altra banda, cal veure com s'ha mantingut durant tant temps l'activitat investigadora en el tema de la corrosió i, especialment, com han evolucionat els estudis sobre corrosió dels sistemes metàl·lics en medi aquós. Inicialment, els estudis fonamentals es van abordar amb l'Electroquímica ja que el fenomen de la corrosió involucra processos redox. El típic sistema

experimental de tres elèctrodes ha ofert la possibilitat de controlar de manera acurada la cinètica dels processos redox que tenen lloc sobre una superfície metàl·lica durant la seva passivació i/o corrosió en certs electròlits aquosos. Durant dècades, les tècniques electroquímiques convencionals (mesura del potencial de corrosió, cronoamperometria, coulombimetria, voltametria cíclica...) es van aplicar exclusivament a l'estudi de la corrosió aquosa. Es van obtenir les primeres descripcions fonamentals del comportament de la corrosió d'una gran varietat d'elèctrodes metàl·lics en diferents medis aquosos i es van establir els seus mecanismes (electro)químics de passivació i corrosió. Després, l'aparició de les tècniques d'Espectroscòpia d'Impedància Electroquímica (EIS) va permetre d'elaborar els primers models elèctrics complexos de la interfície òxid passivant | electròlit. Però no va ser fins a mitjans del segle XX quan Mott y Schottky [2,3] van fixar, separadament, les bases del model de capa d'òxid passivant semiconductora sobre metalls demostrant, per primera vegada, les propietats rectificadores del contacte metall | semiconductor. Això significà l'inici de la "quimera de l'or" per a la passivació metàl·lica, que va assolir el seu màxim esplendor amb el model del semiconductor de Gerischer [4] cap als anys 60. En els vint anys següents, molts investigadors van aplicar sistemàticament aquest model per interpretar quantitativament la cinètica de les reaccions de transferència d'electrons (ETR) i d'ions (ITR) a la interfície metall | electròlit. Cal mencionar especialment els treballs de Sato durant els anys 80 [5], que estenien el model de Gerischer per tal d'explicar l'inici de la transpassivació i la corrosió per picadura com a processos electroquímics responsables de la corrosió de l'elèctrode. A la introducció d'aquesta tesi es fa una breu revisió d'aquests dos mecanismes.

A més de l'electroquímica, una altra qüestió rellevant sobre les capes passivants és l'elucidació de la seva estructura. L'estructura atòmica de la capa és important ja que sovint determina les propietats elèctriques que, finalment, en controlen les propietats protectores. Així mateix, els defectes estructurals també juguen un paper important en el creixement i corrosió de la capa passivant. Des de mitjans del segle passat fins ara s'ha recopilat una quantitat considerable de dades espectroscòpiques *ex situ* [6,7]. No obstant això, la capa passivant pot patir canvis estructurals durant el seu trasllat físic des del medi electroquímic fins a la cambra *ex situ* d'experiments d'espectroscòpia i, per tant, s'ha fet especial èmfasi en l'ús de mètodes *in situ*. En aquest aspecte apareixen dues restriccions importants a l'hora d'aplicar aquestes tècniques: el poc gruix de les capes (de l'ordre de pocs nanometres) i la necessitat d'un control electroquímic acurat en el medi aquós on aquestes es formen. Però en les últimes dues dècades hi ha hagut els progressos tècnics més importants en aquesta direcció. Rubim i Devine [8,9] van dur a terme els primers intents aplicant l'Espectroscòpia Raman Intensificada sobre Superfície (SERS) i van desenvolupar els primers models estructurals de la interfície capa passivant | electròlit sobre un elèctrode de ferro sota diferents potencials electroquímics aplicats. Com que l'aplicació de la SERS està limitada a aquells sistemes metàl·lics que provoquin una intensificació raonable del senyal Raman, s'han aplicat amb èxit alguns trucs experimentals amb la intenció d'incrementar la relació resposta – soroll, com ara la deposició de nanopartícules sobre la superfície de l'òxid o l'ús d'un film metàl·lic com a elèctrode en lloc d'utilitzar-ne tot el volum. Tot i això cal sacrificar, en molts casos, l'electroquímica real del sistema [10,11]. Posteriorment, la recerca s'ha dirigit cap a altres projectes que apliquen tècniques basades en la radiació sincrotró per a l'elucidació *in situ* de l'estructura de la capa. Els primers resultats importants es publiquen durant la dècada dels 90, en els treballs de Davenport [12,13] sobre capes passivants de ferro, i que han esdevingut els

models estructurals més citats fins al moment. D'entre les tècniques espectroscòpiques de radiació sincrotró més emprades, les més adequades per resoldre l'estructura i la química de les capes d'òxid sota control electroquímic són la XANES d'alta resolució *in situ* (X-ray absorption near edge structures) i la difracció *in situ* de raigs X sincrotró (XRD). Els projectes que es duen a terme actualment en el nostre laboratori apunten en aquesta direcció, on s'intenta superar el repte experimental que suposa implementar un dispositiu electroquímic dins una línia sincrotró.

Finalment, també cal tenir en compte les contribucions de les tècniques de microscòpia de sonda (SPM) al camp de la corrosió. A partir de la primera demostració de Bard i els seus col·laboradors [14] l'any 1986 sobre la capacitat de les tècniques SPM per treballar en medi líquid i sota control electroquímic, es van començar a publicar altres exemples d'aplicació d'aquesta metodologia sobre capes passivants [15,16]. Vull destacar el treball presentat per O'Bockris a principis dels 90 [17], on mostra les primeres imatges obtingudes a escala nanomètrica, mitjançant microscòpia túnel d'escombrat electroquímic (ECSTM), de la superfície d'un elèctrode de ferro mentre s'oxida reversiblement en una solució tampó d'àcid bòric. Tot i les limitacions experimentals, he de reconèixer que sento una gran devoció per aquest treball ja que representa el punt de partida de la nostra recerca i obre un ampli ventall de possibilitats. Actualment, les tècniques SPM han contribuït notablement al camp de l'electroquímica en un sentit molt ampli. Si es fa una breu recerca acotada als últims 5 anys dels conceptes "electroquímica" i "STM" o "AFM" en qualsevol base de dades científica, es troben més de 100 referències, algunes d'elles en relació amb revistes prestigioses com *Science* o *Nature*. Això és una prova evident del continu desenvolupament que experimenten les tècniques SPM i que s'estén a altres disciplines científiques en el mateix ordre de magnitud. Podem trobar exemples actuals en aquest àmbit en els treballs de Ryan i Marcus [18-20], sobre capes passivants de ferro i coure respectivament, que demostren la capacitat de la tècnica ECSTM per obtenir resolució atòmica *in situ* de les capes d'òxid passivants. Però el principal problema consisteix a interpretar les dades de STM *in situ* dels òxids semiconductors ja que hi ha poc coneixement sobre les condicions túnel inicials i, per tant, dels nivells de distribució electrònica de la interfície òxid | líquid. Aquest punt requereix especial atenció per tal d'elaborar un estudi en profunditat. Totes aquestes qüestions son tractades en aquesta tesi i en constitueixen el bloc principal.

Després d'aquest breu viatge a través de la història de la passivació des dels seus inicis fins a l'actualitat, podem afirmar que ens trobem davant una matèria multidisciplinar i que el seu major progrés en l'àmbit electroquímic ha tingut lloc gràcies a l'estreta interacció amb altres camps com ara la física de l'estat sòlid, la ciència de superfícies, l'equilibri químic, l'espectroscòpia avançada, les tècniques de microscòpia, etc. Vull apuntar que, com a matèria, també la corrosió aquosa ha evolucionat de manera gradual aprofitant els nous avanços científics i/o tecnològics en altres camps. I, a la vista, no sembla haver-hi fi.

MOTIVACIÓ

Aquesta tesi va néixer en el millor dels ambients: des que em vaig embarcar en el projecte de tesi al departament de Química Física, vaig tenir tots els elements necessaris per endinsar-

me en el camp interdisciplinar de les capes passivants. El nostre grup de recerca formava part del Laboratori de Ciència i Tecnologia Electroquímica de Materials (LCTEM), amb més de vint anys d'experiència en processos d'electroquímica aplicada com l'electrodeposició de Ni i Zn sobre substrats de base ferro [21, 22]. Llavors hi havia un gran interès a obtenir més informació sobre els mecanismes de passivació – corrosió que tenen lloc sobre la superfície dels substrats metàl·lics més utilitzats a la indústria. Amb aquesta idea, vam triar el ferro com a objecte d'estudi i en vam dur a terme una caracterització electroquímica preliminar. Com en treballs anteriors [12, 17], es va triar un medi tampó de borat com a electròlit de treball ja que oferia les condicions més estables i reproduïbles i permetia que els resultats obtinguts fossin compatibles amb dades ja establertes. En uns primers experiments, vam observar que el creixement electroquímic d'una capa d'òxid passivant sobre la superfície de l'elèctrode de ferro pot determinar les propietats del recobriment que s'hi electrodepositi després a sobre. Per il·lustrar aquest fenomen, la figura 1 mostra els primers estadis de l'electrodeposició de Zn sobre dos substrats diferents de ferro policristal·lí, un procés rutinari en moltes aplicacions industrials. D'entrada, és evident que la morfologia del recobriment obtingut sobre la superfície prèviament passivada (fig. 1A) és completament diferent de l'obtinguda sobre la superfície no passivada (fig. 1B) i això afectarà les seves propietats finals com la duresa, la resistència a la corrosió i la rugositat superficial. Aviat ens vam adonar que la capa passivant no actua només com a mera barrera física sinó que, a més, les seves propietats elèctriques determinen fortament el comportament redox de la superfície que cobreix. Això va fer que invertíssim els nostres esforços a elaborar un diagrama **quantitatiu** de bandes electròniques del sistema Fe | capa passivant | electròlit de contacte el qual, d'altra banda, ens ha servit de base per explicar els primers estadis de qualsevol procés redox que es desenvolupi a la interfície òxid | solució tampó.

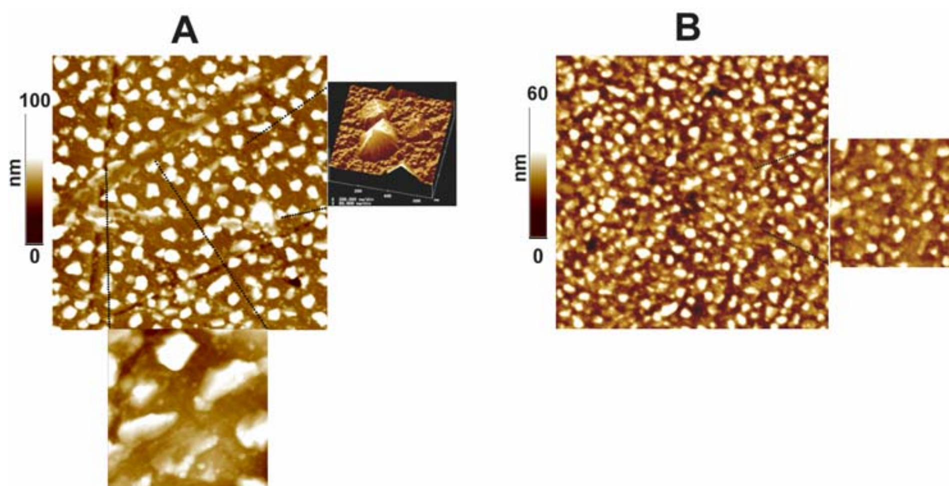

Figura 1: Imatges de microscòpia de forces atòmiques (AFM) que mostren els primers estadis de l'electrodeposició de Zn sobre un elèctrode de Fe: (A) passivat (B) no passivat.

Les perspectives inicials d'aquesta aventura eren prometedores. Per una banda, Pau Gorostiza acabava de presentar la tesis titulada "*Metal deposition on silicon from fluoride solutions*" i establia al nostre laboratori les bases de l'electroquímica de semiconductors. Per l'altra, el nostre grup estava embarcat en un projecte paral·lel que involucrava l'ús de les tècniques SPM com a principal mètode de caracterització. L'estructura de la present tesi va sorgir de la combinació d'ambdós fets. Després d'una intensiva caracterització electroquímica

del sistema escollit, vam aconseguir acoblar la configuració experimental de tres elèctrodes a un microscopi STM. Va caldre un disseny acurat de la cel·la però el resultat va ser un sistema ECSTM robust que va permetre les primeres mesures topogràfiques i elèctriques *in situ* de la interfície òxid de Fe | tampó de borat sota un estricte control electroquímic. A més, es van emprar tècniques *ex situ* de microscòpia i espectroscòpia per tal d'elaborar els primers mecanismes de creixement d'òxid i els primers diagrames quantitatius de bandes electròniques de la capa passivant de ferro. Convençuts que les diferents transicions electròniques de la superfície d'òxid de ferro governen la seva passivitat i el seu comportament redox, vam voler anar més enllà en la caracterització elèctrica i ens vam embarcar en el disseny d'una nova metodologia d'espectroscòpia túnel electroquímica (ECTS). Tot i que aquesta ja havia estat provada sobre silici [23, 24], la seva aplicació es veia dificultada per qüestions tècniques. Al llarg dels dos anys següents del desenvolupament d'aquest doctorat, vam treballar per solucionar els principals problemes tècnics i presentar, per primera vegada, un procediment per enregistrar *in situ* espectres electrònics reproduïbles de la interfície elèctrode | electròlit en funció de l'estat d'oxidació del substrat, els beneficis del qual van més enllà d'aquesta tesi tal i com es veu en l'últim capítol d'aquesta memòria. A més, el procés reversible d'oxidació del ferro constituïa un sistema idoni per a validar la nova metodologia. La combinació de l'ECTS amb les dades de capacitància de la pròpia interfície va resultar ser una eina especialment útil per determinar el seu diagrama de bandes en una escala quantitativa d'energies. Finalment, els últims anys del doctorat s'han dedicat a l'anàlisi i interpretació de les dades d'espectroscòpia túnel *in situ* que es van emprar, primerament, per a l'elaboració d'un mecanisme complet de la formació i dissolució de la capa passivant de ferro; en segon lloc, per revisar el concepte de passivació des d'un punt de vista electrònic i, per últim, per entrar en la caracterització electrònica quantitativa del procés de corrosió de l'elèctrode de ferro en presència de clorurs. La conclusió d'aquest últim estudi és potser la idea més important d'aquest projecte de tesi, ja que és on es veu l'aplicació real de la tècnica a un procés amb un impacte tècnic rellevant.

A nivell personal, em calia una etapa prèvia d'aprenentatge en els camps de l'electroquímica de semiconductors i de l'SPM per tal d'afrontar la tesi. Una part important del coneixement de les tècniques SPM l'he adquirida durant una estada al laboratori del Dr. Miquel Salmeron al Lawrence Berkeley National Lab (Berkeley, CA), l'any 2000, on em vaig familiaritzar amb els modes de treball avançats d'SPM. Més tard, el 2003, una segona estada al laboratori del Dr. Philippe Allongue (París) em va servir per reforçar conceptes bàsics sobre l'electroquímica de semiconductors amb referència a la resposta capacitativa i també per treballar amb capes d'Au/Fe, fet que ens va aportar nous elements per a l'estudi del mecanisme de creixement de l'òxid de ferro.

OBJECTIUS

Com a objectiu principal, la finalitat d'aquesta tesi es aconseguir un diagrama quantitatiu *in situ* del comportament redox d'un elèctrode de ferro en tot el seu rang de potencial electroquímic i en el seu electròlit de treball. Més concretament, primer es vol caracteritzar electroquímicament el sistema i després desenvolupar una nova metodologia electroquímica *in situ* per tal d'obtenir:

- La caracterització cinètica *in situ* del creixement de l'òxid en tot el rang electroquímic de l'oxidació del ferro.

- La caracterització *in situ* de les propietats electròniques de l'*electro*superfície del ferro dins el mateix rang electroquímic.

ESTRUCTURA DE LA MEMÒRIA

Aquesta memòria de tesi té format de compilació d'articles. Això significa que els principals resultats es presenten tal i com es van publicar en cadascuna de les respectives revistes. L'estructura general es pot dividir en tres blocs.

Bloc 1: fixa els fonaments científics i tècnics necessaris per a la discussió i interpretació dels resultats. Es compòn dels següents capítols:

- El **capítol 1** comença amb una breu visió general dels conceptes bàsics de l'electroquímica de semiconductors, amb especial èmfasi en la descripció termodinàmica de la interfície semiconductor | solució. Tot seguit, es descriuen els models generals pel cas de la capa d'òxid i es revisa el concepte de passivació. També es repassa, breument, la cinètica de transferència electrònica i els models clàssics de corrosió i de creixement de l'òxid. Aquest capítol acaba amb un resum detallat dels avanços més recents en els estudis fonamentals del procés passivació-corrosió sobre elèctrodes metàl·lics emprant tècniques *in situ*. Al llarg d'aquesta introducció, la capa de ferro passivada és el principal sistema d'interès i es fa especial esment en els mètodes de caracterització estructural dels elèctrodes.

- El **capítol 2** descriu detalladament el sistema ECSTM experimental i la metodologia emprada per dur a terme l'espectroscòpia túnel sobre la interfície elèctrode | solució. S'expliquen els fonaments de la tècnica, així com les nostres principals contribucions incloent-hi els tres treballs que n'han resultat.

Bloc 2: és el bloc principal de la tesi i correspon als estudis electroquímics dels processos de passivació i corrosió sobre un elèctrode de ferro policristal·lí. Consta de tres capítols:

- El **capítol 3** descriu els procediments de preparació de les mostres i la caracterització prèvia *ex situ*, tant topogràfica com morfològica, dels elèctrodes de ferro policristal·lí. En un primer article es discuteixen les dades obtingudes en un estudi complet de la cinètica de creixement de l'òxid de ferro mitjançant ECSTM i s'aprofundeix en alguns dels punts més crítics del seu mecanisme. A part, es fa un estudi de la passivació d'elèctrodes de ferro en capa prima que complementa la caracterització estructural i que permet completar els mecanismes químics de formació i reducció de la capa d'òxid de ferro. Globalment, aquests resultats representen la base experimental principal pels

estudis subsegüents. Un segon article recull els primers resultats sobre propietats electròniques de la capa de ferro passivant obtinguts per ECSTM i els primers càlculs de paràmetres semiconductors de la mateixa.

- Els detalls del **capítol 4** es recullen en una publicació dedicada a l'estudi *in situ* de les propietats electròniques durant l'oxidació de l'elèctrode de ferro, des del seu estat metàl·lic fins a la passivació de la seva superfície. Això involucra les mesures de l'espectre electrònic i de la barrera d'energia superficial mitjançant ECTS a dos pH diferents. La quantificació d'aquestes mesures servirà de model per tal de preveure la reactivitat de l'elèctrode en un cert medi electrolític.

- El **capítol 5** presenta en format d'article, de nou, els resultats que descriuen el procés de corrosió del ferro en un medi electrolític que conté clorurs. La metodologia descrita en el capítol anterior s'aplica aquí per estudiar la influència dels clorurs sobre les propietats electròniques de la capa de ferro passivant i per explicar com aquests canvis poden tenir lloc en els inicis de la corrosió de l'elèctrode. És necessària alguna caracterització *ex situ* addicional per tal de donar un diagrama complet de les primeres etapes del procés.

Bloc 3: després dels blocs introductori i principal es recull la conclusió general d'aquesta tesi doctoral en el **capítol 6**. Dins aquest bloc també es tenen en compte tres apèndixs. L'**apèndix A** presenta un estudi preliminar sobre les propietats electròniques *in situ* d'elèctrodes d'or funcionalitzats amb molècules simples de decanotiol, com a exemple de l'aplicabilitat de la metodologia ECTS. El sistema estudiat és completament diferent (Au | tiol | electròlit) però té un enorme impacte en el camp de l'enginyeria microelectrònica. En l'**apèndix B** es dóna una llista de referències bibliogràfiques relacionades amb aquesta tesi. En l'**apèndix C** es recullen les abreviatures i símbols emprats al llarg d'aquesta memòria.

Introducció

LA INTERFÍCIE SEMICONDUCTOR | SOLUCIÓ

L'electroquímica de semiconductors apareix com a disciplina a mitjans dels 50, quan es van comercialitzar els primers monocristalls de germani i silici [25]. Des de llavors, l'estudi dels elèctrodes semiconductors ha estat motivat per les seves immediates aplicacions industrials com ara dispositius fotoelectroquímics de conversió d'energia (cèl·lules solars) [26], plantes de tractament de residus orgànics [27], fabricació de dispositius microelectrònics [28] o fotografia [29]. Tradicionalment, es considerava que un elèctrode era un simple conductor electrònic de baixa resistivitat/resistència que actuava com a font d'electrons. Però actualment està clar que la reactivitat química de la superfície de l'elèctrode juga un paper important i està directament relacionada amb les propietats electròniques del substrat. Per això l'ús d'elèctrodes semiconductors en processos, per exemple, d'electrocatàlisi, corrosió i creixement cristal·lí, ha experimentat un creixement substancial.

En aquest capítol introduirem els principals conceptes necessaris per a la interpretació dels resultats experimentals. Pretenem subratllar els trets més importants de la interfície semiconductor | electròlit, no fer-ne pas un repàs exhaustiu, amb especial èmfasi en la fase semiconductora ja que és la menys familiar des del punt de vista electroquímic. Per a més detall, consultar [30-32].

Formació de la doble capa elèctrica. Zona de càrrega espacial (SCR) d'un semiconductor

Quan s'introdueix un semiconductor en un electròlit, l'energia del nivell de Fermi del semiconductor s'iguala a l'energia del parell redox de l'electròlit. Això provoca una redistribució de la densitat de càrrega tant en el semiconductor com a la interfície, creant una *doble capa elèctrica*. Aquest és un concepte electroquímic molt important ja que la doble capa controla els processos (electro)químics a la superfície de l'elèctrode. En una interfase metall | electròlit, la densitat de càrrega es distribueix al llarg de la superfície del metall ja que la densitat de portadors de càrrega és molt elevada (de l'ordre de 10^{22} cm^{-3}). En canvi, en el cas d'un semiconductor, la distribució es dóna en tota una zona, anomenada zona de càrrega espacial (SCR), que es pot estendre fins a una distància considerable de la interfície, ja que la densitat de portadors de càrrega és més petita (de l'ordre de 10^{17} cm^{-3}). Aquest fet fa que, en relació amb l'estudi de la transferència electrònica, la interfície semiconductor | electròlit sigui particularment més complexa que la interfície metall | electròlit. La igualació dels nivells de Fermi de cadascuna de les dues fases es dóna a potencial de circuit obert (OCP), ja que no s'aplica cap potencial extern. El resultat de l'acumulació de càrregues a la SCR és l'aparició d'un camp elèctric que produeix un doblegament de les bandes d'energia del semiconductor, com es mostra a la figura 1.1 i que presenta un esquema complet de la distribució de càrrega al llarg de la interfície semiconductor | electròlit.

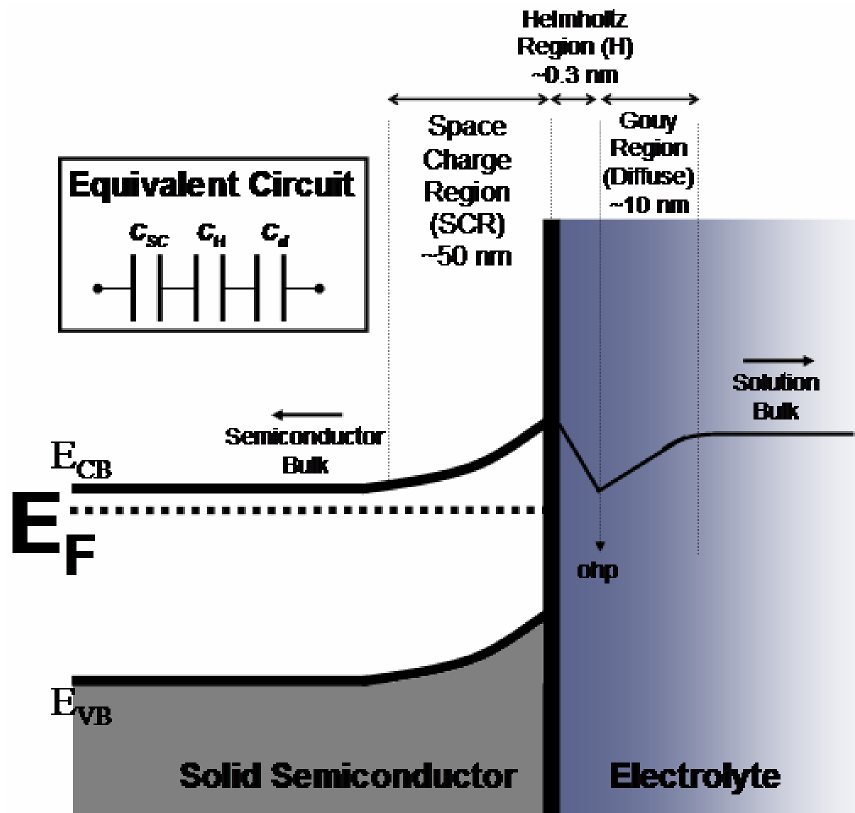

Figura 1.1: Esquema de la doble capa creada a la interfície semiconductor | electròlit. La SCR és molt més ample que la capa de Helmholtz. El gruix de la capa de Gouy-Chapman (capa difusa) correspon a la caiguda de potencial a l'electròlit i es pot negligir sempre que es treballi amb concentracions iòniques prou elevades.

En absència de flux de corrent, la interfície es pot representar com una composició de varis condensadors en sèrie (veure el circuit equivalent representat a la figura 1.1), on cadascun representa una regió o doble capa per separat. Cada condensador tindrà una càrrega emmagatzemada que es pot expressar com una capacitat C_x, i una diferència de potencial, $\Delta\phi_x$. Per tant, la interfície tindrà associada una capacitat, C_{Total} així com també una diferència de potencial, $\Delta\phi_{Total}$.

$$\frac{1}{C_{Total}} = \frac{1}{C_{SC}} + \frac{1}{C_{el}} \tag{1.1}$$

$$\Delta\phi_{Total} = \Delta\phi_{SC} + \Delta\phi_{el} \tag{1.2}$$

on *SC* és el semiconductor, *el* l'electròlit (concretament la capa de Helmholtz ja que considerem negligible la contribució de la capa de Gouy) i ϕ el potencial de Galvani.

Per tal de conèixer aquesta $\Delta\phi_{Total}$ així com per aplicar qualsevol potencial extern, cal emprar un elèctrode de referència. El potencial d'elèctrode ($U_{elèctrode}$) es pot escriure en funció de la diferència de potencial a la interfície segons la relació 1.3, on la constant estarà determinada per l'elèctrode de referència utilitzat:

$$U_{electrode} = \Delta\phi_{Total} + constant \tag{1.3}$$

La figura 1.2 representa la variació del potencial i la distribució de càrrega a la interfície. Si es considera una densitat de càrrega (ρ) uniforme, i que no hi ha dependència del potencial en les coordenades en les coordenades y i z, la distribució de càrrega a través de la doble capa elèctrica en la direcció perpendicular a la interfície, x, es pot obtenir integrant l'equació de Poisson (relació 1.4).

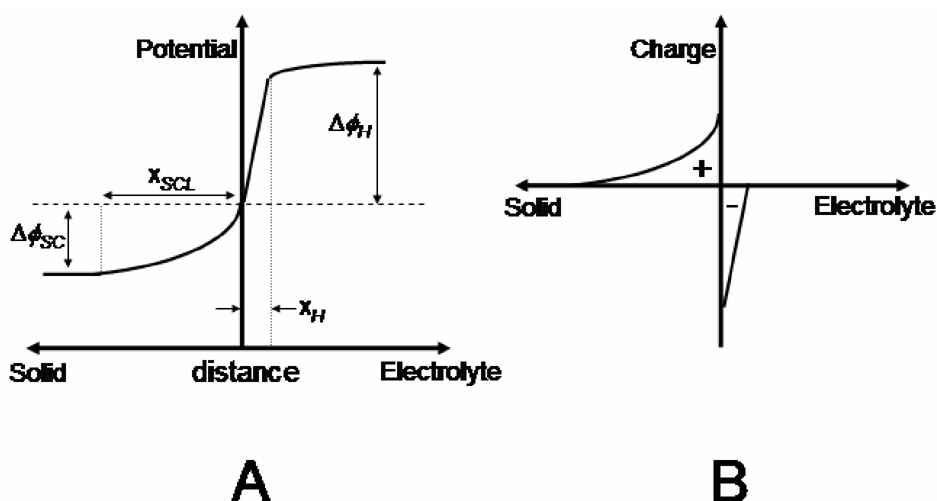

Figura 1.2: Potencial (A) i distribució de càrrega (B) a la interfície semiconductor | electròlit. Notar que, en les condicions experimentals habituals, $x_{SCR}>x_H$. [31].

$$\frac{d^2U(x)}{d^2x} = \frac{\rho(x)}{\kappa\varepsilon_0} \tag{1.4}$$

Aplicació d'un potencial extern: variacions a la SCR

En electroquímica de semiconductors ens interessa estudiar l'efecte de l'aplicació d'un potencial extern sobre la distribució de càrregues a la interfície ja que, en moltes condicions experimentals (elevada força iònica, absència d'adsorció específica i d'estats superficials...) això afecta essencialment a la zona de càrrega espacial (SCR) i es pot negligir la contribució de la capa de Helmholtz a la capacitat de la interfície (equació 1.1) i el problema es redueix a un anàlisi exhaustiu de la SCR.

Com a regla general, quan s'aplica un potencial d'elèctrode o extern ($U_{electrode}$), l'estructura de bandes es desplaça per contrarestar-lo i mantenir les propietats electròniques del material però l'energia de les bandes a la superfície del semiconductor es manté pràcticament constant, creant la SCR. Es diu que gran part del $U_{electrode}$ aplicat s'inverteix en el doblegament de les bandes (*bandedge pinning*). En comparació, en una interfície metall | electròlit no hi ha formació de SCR i es diu que tot el $U_{electrode}$ es deixa caure cap a la doble capa electrolítica

($\Delta\phi_{el}$). Es poden donar diferents situacions en funció de la diferència entre el potencial aplicat i el potencial de banda plana, que es defineix a continuació.

A) Potencial de banda plana, U_{FB}

A la superfície d'un elèctrode semiconductor hi ha càrregues lliures mentre que, a la zona de càrrega espacial contigua hi ha càrregues fixes o immòbils. Com hem vist, això provoca la diferència de potencial $\Delta\phi_{SC}$. Si s'aplica un potencial extern que compensi aquest $\Delta\phi_{SC}$, l'energia electrònica a la superfície del semiconductor serà la mateixa que en tot el seu volum, la diferència de potencial s'anul·la, no hi haurà doblegament de les bandes i, per tant, no hi haurà intercanvi net de càrrega a la interfície ($Q_{solid} = Q_{el} = 0$). El potencial aplicat és anàleg al potencial de càrrega zero dels metalls i s'anomena, per als semiconductors, potencial de banda plana, U_{FB}.

La figura 1.3 resumeix, per a un semiconductor de tipus n i un de tipus p, les principals situacions que es poden donar en funció del potencial aplicat.

A continuació detallarem cadascuna de les situacions però, per simplificar, considerarem només el cas del semiconductor tipus n. A més, cal tenir present que, tot i que poden existir comportaments capacitatius molt complexos, es farà un anàlisi tenint en compte que no hi ha altres formes on emmagatzemar la càrrega que no sigui la SCR. És a dir, en les condicions experimentals abans esmentades: elevada força iònica, absència d'adsorció específica i d'estats superficials, altres fonts de portadors de càrrega...

B) Depleció. $U_{electrode} > U_{FB}$ sobre un semiconductor tipus n

Si s'aplica un petit $U_{electrode}$ (anòdic) sobre U_{FB}, s'extrauran quantitats moderades de portadors majoritaris de càrrega del semiconductor. La superfície queda en un estat de **depleció** o exhausta de portadors mòbils de càrrega i es produeix un doblegament de la banda cap amunt (figura 1.3B). Integrant l'equació 1.4 s'obté una distribució parabòlica per a la variació de potencial:

$$U(x) = \frac{eN_D}{2\kappa\varepsilon_0}(x - x_0)^2 \qquad (1.5)$$

on N_D és la densitat de donadors, x_0 és el gruix de la SCR i $x=0$ representa la superfície del semiconductor. Cal tenir en compte la condició de contorn de camp zero per la qual $dU/dx=0$ quan $U(x_0)=0$. D'acord amb l'equació 1.5, la barrera d'energia superficial que veu l'electró (figura 1.3B) és:

$$U_S = \frac{eN_D x_0^2}{2\kappa\varepsilon_0} \qquad (1.6)$$

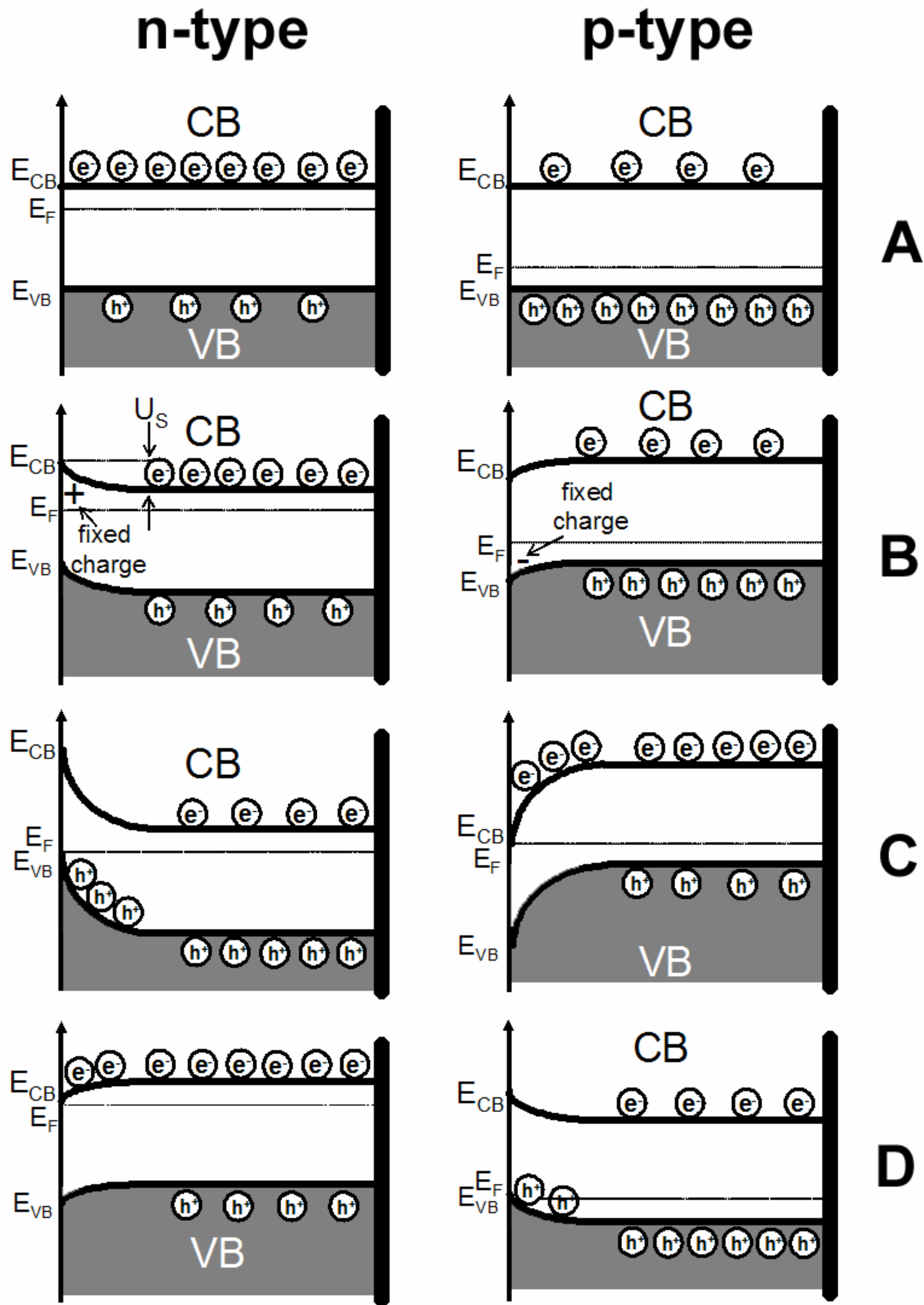

Figura 1.3: Diagrames de bandes d'un elèctrode semiconductor sota l'efecte de l'aplicació d'un potencial $U_{electrode}$. Segons com sigui aquest en relació amb al valor d'U_{FB}, es poden donar els següents casos:

		Tipus n	Tipus p
A	Banda plana	$U_{electrode} = U_{FB}$	
B	Depleció	$U_{electrode} > U_{FB}$	$U_{electrode} < U_{FB}$
C	Inversió	$U_{electrode} >> U_{FB}$	$U_{electrode} << U_{FB}$
D	Acumulació	$U_{electrode} < U_{FB}$	$U_{electrode} > U_{FB}$

i que es coneix com a equació de Schottky. Aquesta situació es pot comparar amb la unió de Schottky estudiada per la interfície metall | semiconductor [31, 47]: l'electròlit del sistema electoquímic, amb una densitat equivalent de portadors (de l'ordre de 10^{22} cm^{-3}), s'assimila al metall de la unió Schottky tradicional. Posarem un exemple de capa passivant d'òxid semiconductor tipus n: si prenem U_S=1V, assumim $\kappa=10$ i $N_D=10^{20}\ cm^{-3}$ per l'*n*-òxid, s'obté un gruix de la SCR de ~40 Å, molt més gran que el gruix de la capa de Helmholtz. Aquest gruix de la SCR correspon a un òxid semiconductor altament dopat, com els que es troben habitualment en les capes passivants metàl·liques. Pel silici, on la N_D=10^{18} cm^{-3}, s'obté un gruix de la SCR de centenars d'Å.

Així doncs, sota condicions de depleció, la fase que domina la transferència electrònica serà la SCR del semiconductor i a l'equació 1.1 es pot negligir el terme corresponent a l'electròlit ($\boldsymbol{C_{Total} \approx C_{SC}}$). La capacitat total de la interfície s'avalua segons:

$$C_{SC} = \frac{dQ_{SC}}{d\phi_{SC}} \tag{1.7}$$

i la càrrega total a la SCR es calcula directament segons:

$$Q_{SC}\left(\frac{C}{cm^2}\right) = eN_D x_0 \tag{1.8}$$

Normalment s'inclou un factor de correcció per la contribució dels electrons de la banda de conducció a U_S, de valor k_BT/e (0.025 V). Tenint en compte això i introduint la relació 1.6 a la 1.8, s'obté:

$$Q_{SC} = \sqrt{2\kappa\varepsilon_0 eN_D}\sqrt{U_S - \frac{k_BT}{e}} \tag{1.9}$$

que es pot derivar per tal d'obtenir la capacitat:

$$C_{SC} = \sqrt{\frac{\kappa\varepsilon_0 eN_D}{2}} \cdot \frac{1}{\sqrt{U_S - \frac{k_BT}{e}}} \tag{1.10}$$

Aquesta expressió s'anomena *relació de Mott-Schottky* i és la més aplicada per obtenir el comportament electrònic bàsic d'un elèctrode semiconductor submergit en un electròlit. Es pot reescriure de forma més útil si substituïm a l'equació 1.10 el valor de U_S en funció del potencial d'elèctrode (equació 1.11):

$$\Delta\phi_{SC} = U_S = U_{electrode} - U_{FB} \tag{1.11}$$

$$\frac{1}{C_{SC}^2} = \frac{2}{\kappa\varepsilon_0 e N_D} \cdot (U_{electrode} - U_{FB} - \frac{k_B T}{e}) \tag{1.12}$$

Experimentalment, la capacitat total (C_{Total}) d'una interfície sòlid | electròlit es pot deduir a partir de les dades d'impedància obtingudes mitjançant EIS que s'ajusten a un model elèctric simple (figura 1.4). Una representació molt útil és la de Mott-Schottky (MS), que representa el valor de $1/C^2$ en funció del $U_{electrode}$. El pendent de la recta (positiu per al tipus p) és una mesura de la densitat de portadors, N_D, i l'ordenada en l'origen determina la U_{FB}.

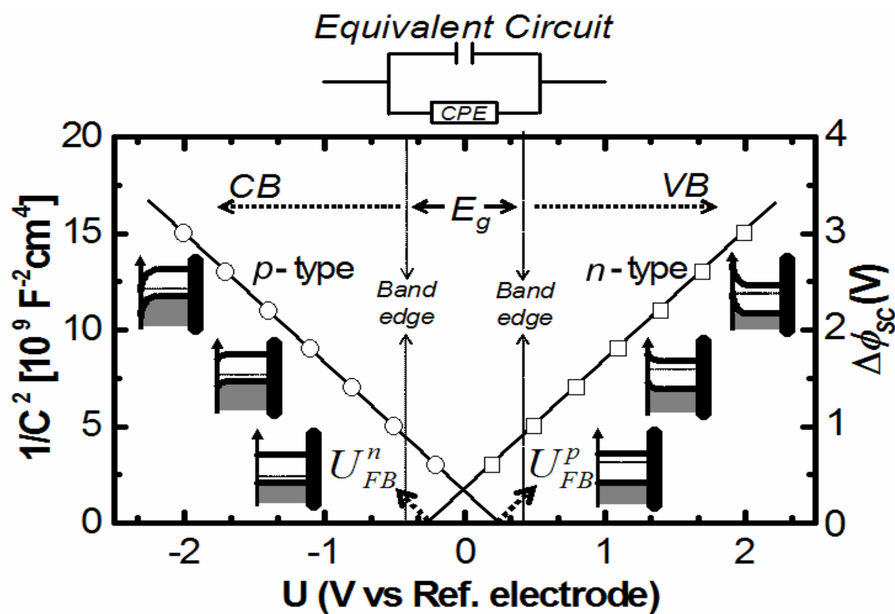

Figura 1.4: Representacions Mott-Schottky (MS) per semiconductors de tipus n i dde tipus p, sota condicions de depleció. Es mostra la seqüència de doblegament de bandes des de la situació de banda plana i el circuit equivalent més emprat per ajustar les dades d'impedància.

C) Inversió. $U_{electrode} >> U_{FB}$ sobre un semiconductor tipus n

Si s'aplica un potencial molt anòdic, la superfície del semiconductor queda ionitzada ja que s'extreuen tots els portadors majoritaris de càrrega. Els agents acceptors i donadors a prop de la superfície estan ionitzats i es produeix un doblegament excessiu de la banda (figura 1.3C). Per tal de mantenir-lo, hi ha depleció d'electrons tant de la CB com de la VB. Així, quan s'extreuen els electrons de la VB (injecció de buits), el semiconductor de tipus n condueix a través dels portadors minoritaris, h^+ en aquest cas, i la superfície experimenta un comportament d'**inversió** cap a tipus p.

La distribució de càrrega dins la capa d'inversió es pot avaluar si considerem que hi ha una nova zona de càrrega de portadors minoritaris a prop de la superfície, representada per una distribució de Boltzmann en el segon terme de l'equació de Poisson (1.4) que s'integra aplicant la condició de contorn de camp zero:

$$\left(\frac{dU}{dx}\right)^2 = \left(\frac{2}{\kappa\varepsilon_0}\right)\cdot\left(eU(x)N_D + p_b kT \cdot e^{\left(\frac{eU(x)}{kT}-1\right)}\right) \tag{1.13}$$

on p_b representa la densitat global de buits.

El primer terme de l'equació 1.13 correspon a les espècies ionitzades fixes i, per tant, la *fase* que domina el perfil de càrrega a la interfície és el segon terme, la capa inversa representada per la distribució de Boltzmann. Pel semiconductor tipus n, el valor de p_b és molt petit i es requereix d'aplicar elevats potencials per tal que el segon terme de l'expressió 1.13 sigui comparable al primer. Una SCR inversa té un gruix habitual de 10 nm [48], significativament menor que el gruix de la SCR sota condicions de deplećió. Tanmateix, si la densitat de càrrega dels portadors minoritaris a la capa d'inversió és prou baixa com perquè el gruix de la capa sigui més gran (varis ordres de magnitud) que el gruix de la doble capa de l'electròlit, l'aproximació $\boldsymbol{C_{Total} \approx C_{SC}}$ és vàlida, i s'obtindrà una inversió en el pendent de la representació MS.

D) Acumulació. $U_{electrode} < U_{FB}$ sobre un semiconductor tipus n

Si s'aplica un potencial catòdic a l'elèctrode, els portadors majoritaris de càrrega (electrons) són llavors injectats a la superfície del semiconductor i s'hi acumulen. El resultat és que la banda es doblega cap avall (figura 1.3D) i es crea una SCR d'**acumulació**. En aquest cas la distribució de potencial tindrà, evidentment, un signe oposat comparat amb la capa de deplećió ja que ara contribueixen els ions dopants fixos més l'excés de càrrega lliure acumulada. La distribució de càrrega a la capa d'acumulació s'obté de manera anàloga a l'equació 1.13:

$$\left(\frac{dU}{dx}\right)^2 = \left(\frac{2en_b}{\kappa\varepsilon_0}\right)\cdot\left(\frac{kT}{e}e^{\left(\frac{-eU(x)}{kT}-1\right)} + U(x)\right) \tag{1.14}$$

on $U(x)$ és ara un potencial negatiu. El primer terme de l'equació 1.14 està relacionat amb l'excés de portadors majoritaris de càrrega a la superfície del semiconductor, a partir del qual es calcula el gruix de la SCR, que dóna valors comparables de l'ordre de ~10 nm [48]. Es important ressaltar que, quan s'acumulen portadors de càrrega a la superfície, la seva densitat es pot aproximar a la densitat a l'electròlit (determinada per la concentració iònica) i que C_{SC} és de l'ordre de C_{el} i aquest terme no es pot negligir de l'equació 1.1. En aquest cas, la diferència de potencial total a la interfície semiconductor | electròlit té dues contribucions: la de la SCR i la de la doble capa de l'electròlit [49, 50]. Quant més negatiu sigui $U_{electrode}$ menys contribució hi haurà de la SCR. La situació extrema es dóna a potencials molt catòdics, on la contribució de la SCR és negligible i la fase que domina la transferència electrònica és l'electròlit ($\boldsymbol{C_{Total} \approx C_{el}}$). L'elèctrode semiconductor es comporta com un metall i en aquestes condicions no es pot utilitzar la representació MS ja que C_{el} no depèn del potencial aplicat. L'acumulació de càrrega a la superfície del semiconductor promou normalment processos

redox que generen un flux de corrent a través de la interfície i que provoca transformacions químiques a la capa d'òxid.

Semiconductors tipus p

Si ara considerem els buits com a portadors majoritaris de càrrega i se segueix el mateix raonament que per al semiconductor de tipus n, podem obtenir els diferents comportaments a la SCR equivalents (figura 1.3A-D). Veiem que és un tipus de semiconductor té un comportament invers a l'altre tipus. És a dir, per exemple, un semiconductor de tipus p en condicions de depleció experimenta un doblegament de la banda cap avall ja que s'extreuen buits (h^+) de la seva superfície.

En qualsevol cas, la idea més important a tenir en compte quan s'estudia la zona de càrrega espacial d'un elèctrode semiconductor és que, si modifiquem el potencial extern aplicat a l'elèctrode, podrem produir qualsevol forma de distribució de càrrega a la superfície del semiconductor.

La presència de portadors de càrrega disponibles a la superfície de l'elèctrode (determinats pel tipus de SCR) afecten les reaccions electroquímiques. Per exemple, la creació d'una capa d'acumulació en un elèctrode semiconductor tipus n pot permetre la transferència de càrrega cap a l'electròlit, si els nivells d'energia d'aquest estan disponibles (per exemple, si hi ha espècies redox actives). Al contrari, sota condicions de depleció, es crearà una barrera d'energia que bloquejarà la reactivitat superficial.

Resultats i discussió

DESENVOLUPAMENT DE LA METODOLOGIA EXPERIMENTAL

En aquest projecte de tesi s'han utilitzat moltes tècniques de caracterització des de les més estàndard fins a les més específiques, en les quals se centra l'atenció. El desenvolupament d'una metodologia de treball específica constitueix una gran part d'aquesta tesi, tant per l'extensió com per la importància, ja que les tècniques emprades van més enllà de l'estudi de la passivitat, com es pot veure en l'apèndix A.

Es poden definir tres parts diferents:

1. La descripció de la tècnica ECSTM amb especial èmfasi en el disseny de la configuració de 4 elèctrodes i l'establiment de les bases dels actuals mètodes de preparació de sondes ECSTM.

2. Els mètodes de preparació de sondes i la descripció d'un nou procediment que permet l'ús d'aquestes en aplicacions d'espectroscòpia túnel electroquímica *in situ*: permet l'elaboració de puntes de Pt/Ir amb corrents electroquímics residuals inferiors a 1 nA quan el potencial de la punta s'escombra a velocitats elevades de fins a 20 V/s.

3. El protocol per enregistrar espectres túnel *in situ* de la interfície elèctrode | electròlit. Cal tenir especial cura a escollir les condicions túnel inicials apropiades per tal d'obtenir reproduïbilitat durant tota l'oxidació de l'elèctrode. Es demostra que aquestes condicions particulars es poden determinar amb mesures de l'alçada de la barrera a diferents potencials d'elèctrode i de punta.

Les següents publicacions presenten els resultats detallats i es poden trobar al capítol 2 d'aquesta memòria.

- *Electrochemistry in Scanning Probe Microscopy: Basic Concepts and Applications*. Phantoms Report (2003) 75-81.

- *Preparation of Reliable Probes for Electrochemical Tunneling Spectroscopy* Anal. Chem. **76** (2004) 5218-5222.

- *Electrochemical Tunneling Spectroscopy to fingerprint electrode electronic structure*, Anal. Chem. **78** (2006) 7325.

PASSIVITAT DEL Fe: ELECTROQUÍMICA I ECSTM

El procés de passivació en substrats de ferro policristal·lí s'estudia mitjançant tècniques electroquímiques i ECSTM. L'objectiu és aprofundir en aqueslls aspectes cinètics del procés que encara resten desconeguts.

Es poden definir dues parts:

1. L'anàlisi de la formació de l'estructura dúplex de la capa passivant de ferro a diferents pH. El procés s'estudia en els rangs electroquímics activant i passivant on es formen, respectivament, les capes prepassivant i passivant. Es proposen els mecanismes electroquímics per cada interval amb especial èmfasi en com influeixen els equilibris químics en l'estructura final i en el gruix de la capa superficial d'òxid. L'ECSTM s'aplica per tal de seguir *in situ* les primeres etapes del creixement de la capa prepassivant a escala nanomètrica. A més, amb l'anàlisi de les imatges de ECSTM i altres mesures *ex situ* addicionals, s'obtenen altres paràmetres com ara la velocitat de creixement de l'òxid i el gruix de capa assolit.

2. La reducció electroquímica catòdica de la capa passivant de Fe. Es preparen substratsde Fe orientats especialment per a aquest estudi,. La seva estructura superficial ultrafina produeix un retard en la reacció de l'hidrogen a l'elèctrode que permet la caracterització de tot el procés catòdic, que queda emmascarat en els elèctrodes policristal·lins.

Les següents publicacions presenten els resultats detallats i es poden trobar al capítol 3 d'aquesta memòria.

- *First Stages of Electrochemical Growth of the Passive Film on Iron*, J. Electrochem. Soc., **148** (2001) B307.

- *The cathodic reduction of the iron passive film grown on ultra-flat iron thin films*, (2006) submitted to J. Phys. Chem. B.

PASSIVITAT DEL Fe: ESTRUCTURA ELECTRÒNICA *IN SITU*

El procés de passivació del ferro en substrats poli cristal·lins s'estudia mitjançant les tècniques EIS, ECSTM i ECTS. L'objectiu és elaborar un diagrama d'energies el més complet possible per la interfície elèctrode | electròlit en tot el seu rang de potencial electroquímic. Primerament, es va emprar l'ECSTM per tal de comprovar els principals camins de conducció electrònica a través de la interfície elèctrode | electròlit en els diferents rangs de potencial electroquímic. Això s'aconseguí estudiant l'estabilitat de la imatge túnel en funció del potencial de punta. Seguidament, s'enregistren individualment espectres túnel *in situ* de la interfície en cada interval de potencial i s'ajusten a un model cinètic simple doble exponencial. L'estructura electrònica de l'òxid de Fe en funció dels seus estats d'oxidació en pot analitzar quantitativament *in situ*. Es repassa el concepte de *passivitat electrònica* en vista de l'estructura electrònica obtinguda en la regió passivant, així com també s'analitza el procés en funció del pH del medi i del potencial d'elèctrode i s'obté una descripció completa i consistent.

A partir dels conductogrames, es poden observar les principals transicions a la superfície de l'elèctrode de Fe i la reversibilitat en les propietats electròniques quan s'oxida i es redueix l'elèctrode. Les àrees més clares en els conductogrames representen nivells d'energia redox activants que poden actuar com a camins electrònics per properes reacions redoc amb les espècies electroactives de la solució. Les reaccions anòdica i catòdica de la capa passivant de Fe es produeixen quan el nivell de Fermi de l'elèctrode sòlid s'aproxima a una zona de conductància elevada. Al final s'obté un diagrama de bandes dinàmic per a tot el procés.

Els resultats i tots els detalls s'han publicat en el següent article, que s'adjunta en el capítol 4 d'aquesta memòria.

- *Direct Evidence of the Electronic Conduction of the Passive Film on Iron by EC-STM*, J. Electrochem. Soc., **150** (2003) B348.

- *Electronic barriers in the iron oxide film govern its passivity and redox behavior: Effect of electrode potential and solution pH*, Electrochem. Commun., **8** (2006) 1595.

INTERRUPCIÓ DE LA PASSIVACIÓ DEL Fe EN UN MEDI DE CLORURS

Mitjançant les tècniques EIS i ECTS s'estudia la interrupció del procés de passivació en substrats de Fe policristal·lí. S'apliquen els coneixements adquirits en relació amb l'estructura electrònica *in situ* de la capa així com el procés de *passivació electrònica* que es produeix a la superfície en el rang electroquímic passivant. Els resultats que se n'obtenen permeten afrontar els mecanismes pels quals es destrueix la barrera electrònica de la superfície passivada en presència d'anions clorur i que acaba produint la corrosió de l'elèctrode. El conductograma del procés d'oxidació del Fe en presència de clorurs evidencia l'absència de passivació electrònica de la superfície quan la concentració de clorurs és baixa. Es pretén elaborar un model electroquímic que encaixi amb els canvis electrònics observats en aquestes condicions experimentals. Per tal de complementar les dades electròniques, caldran mesures *ex situ* addicionals *ex situ*.

Els resultats i tots els detalls s'han publicat en el següent article, que s'adjunta en el capítol 5 d'aquesta memòria.

- *The iron passive film breakdown in chloride media may be mediated by transient chloride-induced surface states located within the band gap*, Electrochem. Commun., **8** (2006) 627-632.

Conclusions

El principal objectiu d'aquesta tesi doctoral ha estat l'estudi de la passivació del ferro en un interval de pH neutre. Aquest procés s'ha seguit des d'un punt de vista electroquímic i comprèn tot el rang de potencial des de l'estat metàl·lic, la formació dels òxids prepassivant i passivant fins al trencament transpassivant de la capa. L'estudi s'ha centrat en la dinàmica del creixement de la capa passivant així com en els mecanismes de transferència d'electrons a la interfície Fe | capa passivant | electròlit amb l'objectiu d'entrendre el comportament redox de l'elèctrode de Fe passivat davant d'un determinat medi electrolític. Per tal d'establir un esquema d'aquests mecanismes, s'ha realitzat un treball *in situ* i a *escala nanomètrica*. Per això una part important d'aquesta tesi versa sobre el desenvolupament tècnic de noves metodologies que proporcionin aquesta informació.

La tesi inclou una àmplia revisió dels conceptes bàsics de l'*Electroquímica de semiconductors* i que s'apliquen durant la discussió dels resultats. S'ha fet especial èmfasi en la distribució de nivells d'energia a la interfície semiconductor | electròlit i les expressions bàsiques per tal de descriure la transferència electrònica que hi tenen lloc. S'ha repassat també el model electroquímic semiconductor aplicat a les capes passivants metàl·liques. L'estructura de defectes dels òxids semiconductors en les capes passivants confereix propietats electròniques particulars com, per exemple, elevades densitats de dopatge i/o l'aparició de nous estats d'energia localitzada al bandgap. En la transferència electrònica el paràmetre clau resulta ser el gruix de la capa: es pot transferir per efecte túnel a través de capes amb gruixos de fins a 20 Å. En general, les capes primes d'òxid presenten propietats semiconductores i, per tant, es pot aplicar el model semiconductor. S'ha fet un resum complet sobre els principals avanços experimentals de mesura *in situ* dels sistemes passivants metàlics més importants. En el cas del ferro, la capa passivant consisteix en una estructura dúplex: una capa cristal·lina interna (capa passivant *natural*) amb estructura d'espinel·la però amb diferent nivell de llocs ocupats que provoca una elevada densitat de vacants de cations i que confereix un comportament ideal de tipus *n* a la capa, i una capa ferrosa hidratada externa que creix sobre la capa passivant natural en la majoria de condicions experimentals emprades en la preparació de la capa.

Quant als nous procediments experimentals desenvolupats durant la tesi, s'han dedicat molts esforços a dissenyar nous mètodes de preparació de sondes STM de Pt/Ir per a ser usades en medis electrolítics altament conductors. Es combina l'ús d'un mètode electroquímic de potencial programat per recobrir la punta amb un procediment aïllant basat en l'ús de pintures electroforètiques hidròfobes. L'èxit del mètode de preparació d'aquestes sondes ha permès d'enregistrar espectres túnel de la interfície elèctrode | electròlit. Les dades obtingudes es representen en *conductogrames* que mostren *in situ* l'estructura electrònica de la superfície de l'elèctrode mentre s'oxida i/o es redueix en un medi electrolític determinat. Els conductogrames constitueixen l'emprenta dactilar redox d'un elèctrode en l'electròlit de treball i serveixen per preveure el seu comportament redox en funció d'espècies electroactives. A més a més, també s'ha descrit el disseny d'una cel·la electroquímica STM especial que incorpora un elèctrode de referència Ag/AgCl miniaturitzat (SSE).

S'ha estudiat la passivitat electroquímica d'un elèctrode de ferro policristal·lí. La caracterització mitjançant voltametria cíclica en funció del pH evidencia l'existència d'una estructura dúplex el gruix de la qual creix a mesura que el pH del medi disminueix. A pH baix, el procés anòdic $Fe(0) \rightarrow Fe^{2+}(aq)$ té un doble efecte: per una banda, el mecanisme de creixement de la capa prepassivant es per oxidació i la precipitació permet arribar a un gruix més gran de capa. Per ECSTM s'observa *in situ* la nucleació i el creixement bidimensional subsegüent així com el mecanisme de la formació de la capa en la regió activa electroquímica, on es dóna la major part de creixement de l'òxid passivant. D'altra banda, l'elevada concentració de $Fe^{2+}(aq)$ generada durant aquest procés fa veure que es crea una prima capa externa ferrosa per electro-oxidació a elevats potencials. A més, en tota la regió electroquímica passivant, les imatges de ECSTM *in situ* evidencien l'absència de canvis topogràfics a la superfície passivada de ferro, així com la naturalesa nanocristal·lina de la capa en aquest rang de potencial. El fet de conèixer la dinàmica de creixement de la capa ha permès d'establir un procediment en dos passos de potencial per a fer créixer el gruix de les capes d'òxid de fins a 20 nm. Les dades de capacitat mostren que aquestes capes presenten una comportament ideal de tipus *n* en tot el rang electroquímic passivant. Aquestes propietats electròniques es proven inicialment a diferents condicions túnel però, mentre que en el rang electroquímic actiu l'efecte túnel és possible en un ampli interval de de nivells d'energia, en el rang passiu els electrons han de ser injectats a valors elevats d'energia i es posa així en evidència l'existència d'una regió de càrrega espaial en la capa semiconductora passivant. La posició de la banda de conducció i, en conseqüència, les condicions túnel STM per enregistrar *in situ* la capa passivant es poden determinar quantitativament.

S'ha revisat la reducció electroquímica catòdica de la capa de ferro passivant emprant elèctrodes de capa prima de Fe orientat. L'etapa final del procés de reducció de la capa d'òxid s'assigna unívocament al pic voltamètric a potencial –1 V/SSE, gràcies a l'elevada ressolució del voltamograma obtingut en aquests substrats. S'ha caracteritzat totalment el procés catòdic a diferents pH i les condicions hidrodinàmiques i es conclou que la naturalesa química de la capa d'òxid de ferro final correspon a una estructura d'òxid de Fe(II).

S'ha seguit el procés sencer de passivació del ferro mitjançant ECTS i mesures de capacitat. En el corresponent conductograma, s'observen les transicions electròniques que es donen a la superfície de l'elèctrode de ferro en funció del seu estat. L'elèctrode experimenta dues transicions electròniques successives: a potencials molt baixos, una conductància elevada i constant indica l'estat metàl·lic Fe(0). Passant a la capa prepassivant, aquesta mostra un comportament semiconductor *p*-Fe(II) i el seu espectre electrònic mostra un bandgap petit. Incrementant el potencial, s'observa una capa d'òxid de *n*-Fe(III) que té un bandgap de l'ordre del que s'obté mitjançant determinacions fotoelectoquímiques. A la regió passivant, la banda de valència disminueix així que s'incrementa el potencial aplicat i presenta un comportament rectificador perfecte a elevats potencials anòdics propers al rang transpassiu. Aquests resultats suggereixen que la passivitat del ferro es pot explicar com un procés de *passivació electrònica* que consisteix en la formació d'una barrera elèctrica efectiva a la interfície òxid | electròlit que prevé l'extracció dels electrons de l'òxid semiconductor. L'intercanvi electrònic a diferents rangs electroquímics es pot quantificar ajustant els espectres túnel individuals a un model cinètic doble exponencial i que proporciona valors de corrent d'intercanvi i coeficients de transferència entre les principals bandes electròniques. El procés de passivació també s'ha

estudiat a elevats pH i les dades túnel *in situ* mostren una barrera electrònica efectiva així que s'aplica potencial, la qual cosa implica que el procés és millor.

El trencament de la passivitat en un medi de clorurs és una de les qüestions més desafiants de l'electroquímica fonamental i també s'ha estudiat en aquesta tesi. S'ha analitzat el conductograma del procés de passivació en presència de clorurs. L'aparició d'una nova banda de valència a les primeres energies electròniques indica la formació d'un estat superficial a la interfície òxd | electròlit que es pot associar a la formació transitòria d'un complex Fe-Cl superficial. Aquest nou nivell d'energia pot servir de canal pels electrons entre la banda de valència i l'electròlit destruint la barrera electrònica prèvia. En vista d'aquests resultats, s'ha proposat un esquema complet del procés de corrosió on els ions clorur tan sols formen un intermedi superficial amb el Fe(II) però no participen directament en la reacció global de catàlisi.

Agraïments

Si es té en compte que aquesta és molt probablement una de les seccions de la tesi que més es consulta, he de confessar que no se'm dóna gens bé aquest tipus de rituals. La gent que m'ha ajudat, sigui directa o indirectament, al llarg d'aquest recorregut sap que tindrà sempre el meu recolzament i l'ajuda que d'alguna manera li pugui oferir. Espero haver transmès aquest sentiment al llarg d'aquest temps i que aquesta secció d'agraïments constitueixi purament una mera formalitat.

En primer lloc, vull agrair als meus directors de tesi, el Dr. Fausto Sanz i el Dr. Pau Gorostiza, el seu recolzament continu. Sempre que penso en ells me n'adono de totes les coses que m'han aportat no solament a nivell científic, sinó també a nivell personal. El meu caràcter més aviat pessimista s'ha vist eclipsat per la seva injecció de positivisme i entusiasme. Ells m'han fet veure que, moltes vegades, els objectius no estan tan lluny com de vegades pot semblar.

Vull agrair molt especialment a totes aquelles persones amb qui he tingut alguna col·laboració científica, dins i fora del marc de la meva tesi, el fet d'haver-me permès aportar el meu granet de sorra als seus projectes. L'amistat sorgida de les llargues hores de feina compartida m'han obert horitzons cap a d'altres camps completament diferents al d'aquest treball. A la Mireia (*Olivator*), la Sandra i a l'Òscar (Farmàcia, UB), al David i al Marc (Campus Bellvitge, UB), al Marcelo, a l'Ariadna, a l'Stephanie, al Carlos (*Willy*) i al Zoubir (Química Orgànica, UB), a la Susanna (*la sussy*) i al Nourdin (Electrònica, UB), al Frederic i a la Sandra (Enginyeria Química, UPC) i a la Muriel (*Mu*) (Química Física, UB). I segur que em deixo molta gent. A tots ells, per les hores compartides, i als seus directors de treball que han permès la col·laboració, un fort agraïment.

Seguint amb la llista anterior, vull donar un especial agraïment als Drs. Miquel Salmeron (Lawrence Berkeley Laboratory) i Philippe Allongue (Université Pierre et Marie Curie) pel temps que em van dedicar durant la meva estada als seus laboratoris. M'agradaria afegir aquí el nom d'algunes persones que vaig conèixer durant aquestes visites i amb les quals vaig compartir grans moments: l'Òscar, el Pepe, el Max, la Carmen, el Guillaume i el Lauren. A tots ells he d'agrair el seu ajut dins i fora del laboratori, la seva amistat i, en alguns casos, la fructífera interacció científica.

Voldria expressar també la meva gratitud a tota la gent dels Serveis Científicotècnics (SCT). A les *Montses* i al Ramon Fontarnau per la confiança que han dipositat en mi per portar endavant la Unitat de Tècniques Nanomètriques. Als companys de feina: al Joan (el *caiman*), al Lorenzo, al Quim (*en Portell*), a l'Anna i al Jordi (*els Ulot*), a la Marisol (la *punky*, enhorabuena por la criatura) a l'Eva (per *mirar-nos* tantes sondes d'AFM al SEM), a

l'Elisenda (quines llargues xerrades a l'hora de dinar) i a tota la resta de l'equip de l'edifici SCT *històric*.

Vull agrair a tota la gent del departament de Química Física el seu recolzament, en especial a tots aquells amb el quals he compartit llargues hores de treball experimental als laboratoris d'electroquímica; a l'Eva García i al Mustafa amb els qui vaig compartir els meus primers *pinitos*, a la Teresa, a l'Eva (la *pelli*) i a l'Albert, i al Salvador i al PPMari (els *tiris*).

A tots els *nanos* (nanomètrics) del laboratori del Fausto, altrament dits *Faustoboys*, per l'excel·lent clima de treball creat (que bé que s'està al laboratori amb tots vosaltres, nois): al Raül (el *Reiul*) i a l'Albert que m'han acompanyat en aquest viatge des del principi, a l'Aleix (el *cheitu*) a qui he d'agrair la seva dedicació en el què ha estat la gran batalla de les puntes, al Sergi (de professió *Master of caimans* i *nanomechanics*), al Gerard (àlias *Geraldus Faldus*; quin bon caràcter, nen, no canviïs i vigila la fricció), al Jordi (el *nanu*) el meu company de fatigues, (gràcies per la teva paciència, nen), a Felipe i Diego (el *pinche* i el *boludo*) que ja s'han adaptat perfectament al grup de treball, i a la Carolina (*Carooola*), amb qui vaig passar llargues hores davant l'STM i la persona que em va ensenyar totes les meravelles sobre el "*Tractat de preparació de superfícies d'Au*", i per últim a la Lorena i a la Sandra, les nostres super-becàries que han posat un toc d'ordre a la caòtica Unitat de Nanomètriques. En aquest grup vull incloure també una persona que va haver de patir de molt a prop el meu mal humor durant les primeres patacades experimentals, l'Eli.

No podria passar per alt l'aportació a la meva formació per part d'alguns professors i investigadors visitants que han passat pel laboratori. Al Fernando (*cabezón*) que em va iniciar en el fabulós món de les tècniques SPM, i als professors Assis i Sadao dels quals vaig aprendre innombrables mètodes i procediments en mesures electroquímiques.

El largo recorrido que representa hacer una tesis no seria posible sin el soporte moral de la família y los amigos. A esos que siempre han estado a mi lado apoyándome y animándome, sobre todo en los momentos más difíciles, a todos ellos les quiero dedicar este trabajo. En especial a mis padres (*Loli* y *Fifo*), que me lo han dado todo y siempre han confiado en mi ciegamente, y a mi hermana (*Patra*) por su enorme generosidad y afecto (*no hace falta que os diga que os quiero un montón a los tres*). Llegados a este punto, debería incluir una lista interminable de amigos, pero creo que será más realista mentar a mis *incondicionales*, a los que siempre estan allí cuando los necesitas, a mis amigos del alma: los Juanjos (el *callao* y el *bicho*), grácias por vuestra larga amistad, espero que no acabe nunca.

També m'agradaria fer extensiu aquest agraïment als nois del *basket*, que han hagut de suportar més d'un dels meus partits dolents quan els experiments no sortien. Per cert, no se si hauria d'agrair aquí al meu tendó d'Aquiles que va fer *figa* durant un d'aquests partits i em va tenir apartat un parell de mesos durant els quals vaig poder escriure la introducció d'aquesta tesi.

Vull reservar aquest espai per dues persones que han estat molt especials per a mi al llarg d'aquest procés. La primera és en Pau, codirector del treball, company de penes al laboratori i

amic, tot. Només se m'acut dir-te que me n'alegro d'haver-te conegut, nen, treballar tots aquests anys al teu costat ha estat realment una passada en tots els sentits. Espero poder-ne compartir molts més. Gràcies per tot. L'altra persona és la meva companya sentimental, la *bitxu*, a la qual he d'agrair tant la seva infinita paciència com les llargues hores perdudes ajudant-me a redactar aquest manuscrit. Encara no sé si seré a l'alçada de correspondre't per tot el que has fet per mi. Un petó enorme.

Per acabar, m'agradaria també incloure aquí a tota la gent de la planta 7 (i annexos) amb els quals he compartit molt bons moments al llarg dels darrers anys de tesi: al Nacho (*super-cabeza*), a a Mònica, a l'Elena, al Patxi, a l'Anna (*kornepunks*), a la Laia (*laiator*), al Micky i al Santi (*ya sé que no sois de metalurgia pero vais en el pack*), al Xavi (*enhorabuena papi*), a l'Anna (*magrasonator*) i em deixaré algú. Una forta abraçada a tots.

I a la noia del Servei de Fotocòpies de química, una de petita (no recordo el nom) i molt simpàtica per atendre'm amb paciència durant l'edició d'aquesta tesi.

Sé que em deixo gent. De fet, n'estic completament segur, però també sé que, si em coneix una mica, no m'ho tindrà en compte.

Finalment, vull alertar a tothom qui vulgui fer una tesi doctoral, de quins són els seus efectes secundaris (veure figura adjunta).

Començament

Final

References

[1]. C. Schönbein, *Annalen der Physik und Chemie.*, **37** (1836) 390.

[2]. N. F. Mott, *Proc. Roy. Soc. (A)*, **171** (1939) 27.

[3]. W. Schottky, *Zeits. Physik*, **113** (1939) 367.

[4]. H. Gerischer in *Advances in electrochemistry and electrochemical enginnering*, Interscience Publishers, New York, USA **139** (1961).

[5]. N. Sato *J. Electrochem. Soc.* **129** (1982) 255.

[6]. (a) C. L. Foley, J. Kruger and C. J. Bechtoldt, *J. Electrochem. Soc.* **114** (1967) 994; (b) D. F. Mitchell, G. I. Sproule and M. J. Graham, *Appl. Surf. Sci.*, **21** (1985) 199.

[7]. M. P. Ryan, D. E. Williams, R. J. Chater, B. M. Hutton and D. S. McPhail, *Nature*, **415** (2002) 770.

[8]. J. C. Rubim and J. Dünnwald, *J. Electroanal. Chem.*, **258** (1989) 327.

[9]. L. J. Oblonsky, S. Virtanen, V. Schroeder and T. M. Devine, *J. Electrochem. Soc.*, **144** (1997) 1604.

[10]. J. Gui and T. M. Devine, *J. Electrochem. Soc.*, **138** (1991) 1376.

[11]. P. Allongue and S. Joiret, *Physical Review B*, **71** (2005) 115407.

[12]. A. J. Davenport, L. J. Oblonsky, M. P Ryan and M. F. Toney, *J. Electrochem. Soc.*, **147** (2000) 2162.

[13]. M. F. Toney, A. J. Davenport, L. J. Oblonsky, M. P. Ryan and C. M. Vitus, *Phys. Rev. Lett.*, **79** (1997) 4282.

[14]. H.-Y. Liu, F.R.F. Fan, C.W. Lin and A.J. Bard, *J. Am. Chem. Soc.*, **108** (1986) 3838.

[15]. J. Li and D. J. Meier, *J. Electroanal. Chem.*, **454** (1977) 53.

[16]. O. Khaselev and J. M. Sykes, *Electrochim. Acta*, **42** (1997) 2333.

[17]. R. C. Bhardwaj, A. González-Martín and O'M. Bockris, *J. Electrochem. Soc.*, **138** (1991) 1901.

[18]. M. P. Ryan, R. C. Newman and G. E. Thompson, *J. Electrochem. Soc.*, **142** (1995) L177.

[19]. J. Kunze, V. Maurice, L. H. Klein, H.-H. Strehblow and P. Marcus, *J. Phys. Chem. B*, **105** (2001) 4263.

[20]. J. Kunze, V. Maurice, L. H. Klein, H.-H. Strehblow and P. Marcus, *Corrosion Science*, **46** (2004) 245.

[21]. C. Muller, M. Sarret and E. García, *Corrosion Science*, **47** (2005) 307.

[22]. M. Sarret, C. Muller and A. Amell, *Surf. Coat. Technol.*, **201** (2006) 389.

[23]. E. Tomita, N. Matsuda, K. Itaya, *J. Vac. Technol. A*, **8** (1990) 534.

[24]. G. Abadal, F. Pérez-Murano, N. Barniol, X. Borrisé and X. Aymerich, *Ultramicroscopy*, **66** (1996) 133.

[25]. C. G. B. Garrett and W. H. Brattain, *Physical Review*, **99** (1955) 376.

[26]. L. A. Harris and R. H. Wilson, *Annu. Rev. Mater. Sci.* 1978, p. 99.

[27]. M. R. Hoffmann, S. T. Martin, W. Choi and D. W. Bahnemann, *Chem. Rev.* **95** (1995) 69.

[28]. P. A. Ostermayer and R. H. Burton, *Appl. Phys. Lett.* **43** (1983) 642.

[29]. J. W. M. Jacobs, *J. Phys. Chem.* **90** (1986) 6507.

[30]. S. R. Morrison, *Electrochemistry at Semiconductor and Oxidized Metal Electrodes*, Plenum Press, New York, USA (1980).

[31]. R. Memming, *Semiconductor Electrochemistry*, Wiley-Vch, Weinheim, Germany (2001).

[32]. P. Gorostiza, *Ph.D. Thesis*, University of Barcelona, Barcelona (1999). Available on-on line at http://www.qf.ub.es/a2/nano/docs/thesis.pdf

[33]. J. O'M. Bockris, A. K. N. Reddy and M. Gamboa-Aldeco, *Modern Electrochemistry*, Kluwer Academic/Plenum Publishers, vol. **2A**, New York (2000).

[34]. H. Gerischer and W. Ekardt, *Appl. Phys. Lett.* **43 (**1983) 393.

[35]. (a) J. Frank, *Trans. Faraday Soc.*, **21** (1925) 536; (b) E. C. Condon, *Phys. Rev.*, **32** (1928) 858.

[36]. R. R. Dogonadze, A. M. Kuznetsov and A. A. Chernenko, *Russ. Chem. Rev.* **34** (1965) 759.

[37]. R. A. Marcus, *J. Chem. Phys.* **43** (1965) 679.

[38]. J. M. Costa, *Cinética Electrodica*, Editorial Alambra, Madrid (1981).

[39]. H. Bluhm, T. Inoue and M. Salmeron, *Surf. Sci.*, **462** (2000) L599.

[40]. T. W. Healy, D. E. Yates, L. R. White and D. Chan, *J. Electroanal. Chem.* **80** (1977) 57.

[41]. M. Hoffmann-Perez and H. Gerischer, *Ztschr. Elektrochem., Ber. Bunsenges. Phys. Chem.* **65** (1961) 77.

[42]. M. J. Madou, B. H. Loo, K. W. Frese and S. R. Morrison, *Surf. Sci.* **108** (1991) 261.

[43]. K. Micka and H. Gerischer, *J. Electroanal. Chem.* **38** (1972) 397.

[44]. P. Lemasson, A. M. Baticle and P. Vennereau, *Surf. Sci.* **59** (1976) 177.

[45]. Electrocatalisis, una ref con TiO2 ??

[46]. S. M. Sze, *Physics of Semiconductor Devices*, 2nd edition, John Wiley & Sons, New York (1981).

[47]. P. F. Schmidt, *J. Electrochem. Soc.* **115** (1968) 168.

[48]. S. R. Morrison, *The Chemical Physics of Surfaces*, Plenum Press, New York, USA (1977).

[49]. H. Gerischer and R. McIntyre, *J. Chem. Phys.* **83** (1985) 1363.

[50]. G. Oskam and P. C. Searson, *J. Phys. D: Appl. Phys.* **31** (1998) 1927.

[51]. R. J. Hamers in *Scanning Tunneling Microscopy I*, H.-J. Güntherodt and R. Wiesendanger (Eds.), Springer-Verlag, Berlin, Germany (1991).

[52]. J.–N. Chazalviel, *Electrochimica Acta*, **33** (1988) 355.

[53]. P. Allongue, in *Modern Aspects of Electrochemistry*, **23**, B. E. Conway, J. O'M. Bockris, R. E. White, editors. Plenum Press, New York, USA (1992).

[54]. A. J. Bard, A. B. Bocarsly, F. R. F. Fan, E. G. Walton, M. S. Wrighton, *J. Am. Chem. Soc.* **102** (1980) 3671.

[55]. R. Memming, in *Topics in Current Chemistry*, Springer Verlag, Heidelberg, Germany **169** (1994).

[56]. R. A. Marcus, *Ann. Rev. Phys. Chem.* **15** (1964) 155.

[57]. H. Gerischer in *Physical Chemistry*, **4**, M. Eyring *et al.*, editors. Academic Press, New York (1970).

[58]. We will use the standard electrochemical convention of current signs: $j>0$ (anodic current) denotes oxidation of species in solution or e^- injection (h^+ withdrawal) into the solid electrode, while $j<0$ (cathodic current) denotes reduction of species in solution or e^- withdrawal (h^+ injection) from the solid electrode.

[59]. P. van Rysselberghe, *Electrochimica Acta*, **8** (1963) 583,709.

[60]. R. Memming in *Comprehensive Treatise of Electrochemistry*, **7**, B. E. Conway *et al.*, editors. Plenum Press, New York (1983).

[61]. W. W. Gärtner, *Phys. Rev.* **116** (1959) 84.

[62]. P. H. Rieger, *Electrochemistry*. Prentice-Hall International Editions, Englewood Cliffs, NJ (1992).

[63]. A. J. Bard and L. R. Faulklner, *Electrochemical Methods: fundamentals and applications.* John Wiley & Sons, New York, USA (1980).

[64]. V. G. Levich, *Physicochemical Hydrodynamics*. Prentice Hall, Englewood, NJ (1962).

[65]. R. M. Cornell and U. Schwertmann, *The Iron Oxides: Structures, Properties, Reactions, Occurrence and Uses.* Verlagsgesellschaft, Weinheim, Germany (1996).

[66]. J. W. Schultze, *Materials Chem. Phys.*, **22** (1989) 417.

[67]. S. Trasatti, *Electrodes of Conductive Metallic Oxides*, Elsevier Sci. Publ., Oxford (1980).

[68]. U. Stimming and J. W. Schultze, in *Modern Aspects of Electrochemstry*, **17** (1986) 357.

[69]. J. W. Schultze and L. Elfenthal, *J. Electroanal. Chem.* **204** (1986) 153.

[70]. M. Pourbaix, *Atlas d'equilibres électrochimiques*. Gautier-Vil·lar & Cie, Paris, France (1963).

[71]. N. Cabrera and N. F. Mott, *Rep. Prog. Phys.*, **12** (1948) 267.

[72]. F. P. Fehlner and N. F. Mott, *Oxid. Met.*, *2* (1970) 59.

[73]. C. Y. Chao, L.-F. Li and D. D. Macdonald, *J. Electrochem. Soc.*, **128** (1981) 1187.

[74]. C. Y. Chao, L.-F. Li and D. D. Macdonald, *J. Electrochem. Soc.*, **129** (1982) 1874.

[75]. A. K. Vijh, *Electrochemistry of Metals and Semiconductors*, Marcel Dekker, NY (1973).

[76]. N. F. Mott and E. A. Davis, *Electronic processes in non-crystalline Solids*, Clarendon, Oxford (1979).

[77]. A. T. Fronhold, Jr., *Theory of metal oxidation*, North-Holland N-H, NY, **1** (1976).

[78]. P. Schmuki, *J. Solid State Electrochem.*, **6** (2002) 145.

[79]. U. König and J. W. Schultze in *Interfacial Electrochemistry*, A. Wieckowski (Ed.), Marcel Dekker, NY (1999).

[80]. N. Sato and M. Cohen, *J. Electrochem. Soc.*, **111** (1964) 512.

[81]. N. Sato and T. Notoya, *J. Electrochem. Soc.*, **114** (1967) 585.

[82]. D. D. Macdonald, *J. Electrochem. Soc.*, **139** (1992) 3434.

[83]. S. Schmickler, *Ber. Bunsenges. Phys. Chem.*, **82** (1978) 477.

[84]. N. J. Tao, *Phys. Rev. Lett.*, **73** (1996) 846.

[85]. S. M. Wilhelm, K. S. Yun, L. W. Ballenger and N. Hackerman, *J. Electrochem. Soc.*, **126** (1979) 419.

[86]. H. Kaesche, Corrosion of Metals, Springer-Verlag, Berlin, (2003).

[87]. N. Pérez, *Electrochemistry and Corrosion Science*, Springer-Verlag, NY, (2004).

[88]. Z. Szklarska-Smialowska, *Pitting corrosion of metals*, National Association of Corrosion Engineers, Houston (1986).

[89]. H.-H. Strehblow in *Corrosion mechanisms in theory and practice*, P. Marcus and J. Oudar (eds.), Marcel Dekker, NY (1995).

[90]. F. Hine, K. Komai and K. Yamakawa (eds.), *Localizad corrosion*, Elsevier, London (1988).

[91]. T. P. Hoar, D. C. Meras and G. P. Rothwell, *Corrosion Science*, **5** (1965) 279.

[92]. K. J. Vetter and H.-H. Strehblow, *Ber. Bunsenges. Phys. Chem.*, **74** (1970) 1024.

[93]. N. Sato, *Electrochimica Acta*, **16** (1971) 1683.

[94]. Ya. J. Kolotyrkin, *Corrosion*, **19** (1964) 261t.

[95]. T. P. Hoar and W. R. Jacob, Nature, **216** (1967) 1299.

[96]. H. Gerischer, *J. Vac. Sci. Technol.*, **15** (1978) 1422.

[97]. P. Monnartz, *Metallurgie*, **8** (1911) 160.

[98]. M. Nagayama and M. Cohen, *J. Electrochem. Soc.*, **110** (1963) 670.

[99]. V.Markovac and M. Cohen, *J. Electrochem. Soc.*, **114** (1967) 678.

[100]. M Cohen and K. Hashimoto, *J. Electrochem. Soc.*, **121** (1974) 42.

[101]. R. W. Revie, B. G. Baker and J. O'M. Bockris, *J. Electrochem. Soc.*, **122** (1975) 1460.

[102]. K. Kuroda, B. D. Cahan, G. Nazri, E. Yeager and T. E. Mitchell, *J. Electrochem. Soc.*, **129** (1982) 2163.

[103]. D. F. Mitchell, G. I. Sproule and M. J. Graham, *Appl. Surf. Sci.*, **21** (1985) 199.

[104]. J. Robinson, in *X-Ray Methods in Corrosion and Interfacial Electrochemistry*, A. J. Davenport and J. G. Gordon, II, PV 92-1, p. 239, The Electrochemical Society Proceedings Series, Pennington, NJ (1991).

[105]. R. Sonnenfeld and P. K. Hansma, *Science*, **232** (1986) 211.

[106]. M. Büchler, P. Schmuki and H. Böhni, *J. Electrochem. Soc.*, **145** (1998) 609.

[107]. N. Sato, T. Noda and K. Kudo, *Electrochim. Acta*, **19** (1974) 471.

[108]. B. MacDougall and J. A. Badwell, *J. Electrochem. Soc.*, **135** (1988) 2437.

[109]. T. Ohtsuka and H. Yamada, *Corrosion Science*, **40** (1998) 1131.

[110]. J. C. Rubim, *J. Electrochem. Soc.*, **140** (1993) 1601.

[111]. E. Sikora and D. D. Macdonald, *J. Electrochem. Soc.*, **147** (2001) 4087.

[112]. J. Liu and D. D. Macdonald, *J. Electrochem. Soc.*, **148** (2001) B425.

[113]. K. Azumi, T. Ohtsuka and N. Sato, *J. Electrochem. Soc.*, **134** (1987) 1352.

[114]. M. Bojinov, G. Fabricius, T. Laitinen, K. Mäkelä, T. Saario and G. Sundholm, *Electrochim. Acta*, **45** (2000) 2029.

[115]. M. Bojinov, T. Laitinen, K. Mäkelä and T. Saario, *J. Electrochem. Soc.*, **148** (2001) B243.

[116]. M. Büchler, P. Schmuki, H. Böhni, T. Stenberg and T. Mäntylä, *J. Electrochem. Soc.*, **145** (1998) 378.

[117]. M. Metikos-Hukovic, S. Omanovic and A. Jukic, *Electrochim. Acta*, **45** (1999) 977.

[118]. R. Díaz, S. Joiret, A. Cuesta, I. Díez-Pérez, P. Allongue, C. Gutiérrez, P. Gorostiza and F. Sanz, *J. Phys. Chem. B*, **108** (2004) 8173.

[119]. S. M. Wilhem and N. Hackerman, *J. Electrochem. Soc.*, **128** (1981) 1668.

[120]. Z. Szklarska-Smialowska and W. Kozlowski, *J. Electrochem. Soc.*, **131** (1984) 499.

[121]. V. Schroeder and T. M. Devine, *J. Electrochem. Soc.*, **146** (1999) 4061.

[122]. B. X. Huang, P. Tornatore and Y.-S. Li, *Electrochim. Acta*, **46** (2000) 671.

[123]. H. Y. H. Chan, C. G. Takoudis and M. J. Weaver, *J. Phys. Chem. B*, **108** (2004) 8173.

[124]. L. J. Oblonsky, A. J. Davenport, M. P Ryan, H. S. Isaacs and R. C. Newman, *J. Electrochem. Soc.*, **144** (1997) 2398.

[125]. L. J. Oblonsky, A. J. Davenport, M. P Ryan, H. S. Isaacs and R. C. Newman, *J. Electrochem. Soc.*, **144** (1997) 2398.

[126]. S. Virtanen, P. Schmuki, M. Büchler and H. S. Isaacs, *J. Electrochem. Soc.*, **146** (1999) 4087.

[127]. C. A. Melendres, G. A. Bowmaker, J. M. Leger and B. Beden, *J. Electroanal. Chem.*, **449** (1998) 215.

[128]. D. Zuili, V. Maurice and P. Marcus, *J. Electrochem. Soc.*, **147** (2000) 1393.

[129]. O. Magnussen, J. Scherer, B. M. Ocko and R. J. Behm, *J. Phys. Chem. B*, **104** (2000) 1222.

[130]. T. Tansel and O. M. Magnussen, *Phys. Rev. Lett.*, **96** (2006) 026101.

[131]. H-H Strehblow, V. Maurice and P. Marcus, *Electrochim. Acta*, **46** (2001) 3755.

[132]. D-S. Kong, S-H. Chen, L-J. Wan and M-J. Han, *Langmuir*, **19** (2003) 1954.

[133]. M. Kang and A. Gewirth, *J. Phys. Chem. B*, **106** (2002) 12211.

[134]. F. M. Delnick, and N. Hackerman, *J. Electrochem. Soc.*, **126** (1979) 732.

[135]. T. P. Moffat, H. Yang, F. Ren F. Fan, Allen J. Bard, *J. Electrochem. Soc.*, **139** (1992) 3158.

[136]. J. Halbritter, G. Repphun, S. Vinzelberg, G. Staikov and W. J. Lorenz, *Electrochim. Acta*, **40** (1995) 1385.

[137]. Y. Nagatani, T. Hayashi, T. Yamada and K. Itaya, *Jpn. J. Appl. Phys.*, **35** (1996) 720.

[138]. A. Schreyer, L. Eng and H. Böhni, *J. Vac. Sci. Technol. B*, **14** (1996) 1162.

[139]. K. Azumi, K. Araki and M. Seo, *J. Electroanal. Chem.*, **427** (1997) 15.

[140]. Ph. Hugelmann and W. Schindler, *J. Phys. Chem. B*, **109** (2005) 6262.

[141]. W. Schindler, M. Hugelmann and Ph. Hugelmann, *Electrochim. Acta*, **50** (2005) 3077.

[142]. J. Kunze, V. Maurice, L. H. Klein, H.-H. Strehblow and P. Marcus, *Electrochim. Acta*, **48** (2003) 1157.

[143]. V. Maurice, L. H. Klein and P. Marcus, *Surf. Interface Anal.*, **34** (2002) 139.

[144]. S. Ahn, H. Kwon and D. D. Macdonald, *J. Electrochem. Soc.*, **152** (2005) B482.

[145]. Y.-T. Chin and B. D. Cahan, *J. Electrochem. Soc.*, **139** (1992) 2432.

[146]. C. Punckt, M. Bölcher, H. H. Rotermund, A. S. Mikhailov, L. Organ, N. Budiansky, J. R. Scully and J. L. Hudson, *Science,* **205** (2004) 1133.

[147]. J. Chen, M. A. Reed, A. M. Rawlett and J. M. Tour, *Science*, **286** (1999) 1550.

[148]. R. P. Andres, S. Datta, D. B. Janes, C. P. Kubiak and R. Reifenberger, in *Handbook of Nanostructured Materials and Nanotechnology*, H. S. Nalwa (ed.), Academic Press, New York, **3** (2000) 179.

[149]. R. P. Andres, T. Bein, M. Dorogi, S. Feng, J. I. Henderson, C. P. Kubiak, W. Mahoney, R. G. Osifchin and R. Reifenberger, *Science*, **272** (1996) 1323.

[150]. T. T.-T. Li and M. J. Weaver, *J. Am. Chem. Soc.*, **106** (1984) 6107.

[151]. S. B. Sachs, S. P. Dudek, R. P. Hsung, L. R. Sita, J. F. Smalley, M. D. Newton, S. W. Feldberg and C. E. D. Chidsey, *J. Am. Chem. Soc.*, **119** (1997) 10563.

[152]. A. Ulman, *Chem. Rev.*, **96** (1996) 1533.

[153]. L. A. Bumm, J. J. Arnold, M. T. Cygan, T. D. Dunbar, T. P. Burgin, L. II. Jones, D. L. Allara, J. M. Tour and P. S. Weiss, *Science*, **271** (1996) 1705.

[154]. L. A. Bumm, J. J. Arnold, T. D. Dunbar, D. L. Allara and P. S. Weiss, *J. Phys. Chem. B*, **103** (1999) 8122.

[155]. MaTeck (*http://www.mateck.de*).

[156]. Molecular Imaging (*http://www.molec.com*).

[157]. Digital Instruments (*http://www.veeco.com*).

[158]. Tektronix (*http://www.tek.com*).

[159]. K. Edinger, A. Gölzhäuser, K. Demota, C. Wöll and M. Grunze, *Langmuir* **9** (1993) 4.

[160]. P. Ramirez, R. Andreu,; J. J. Calvente, C. J. Calzado and G. López-Pérez, *J. Electroanal. Chem.*, **582** (2005) 179.

[161]. J. G. Simmons, *J. Appl. Phys.*, **34** (1963) 1793.

[162]. J. Calvente, G. López-Pérez, P. Ramirez, H. Fernandez, M. A. Zon, W. H. Mulder and R. Andreu, *J. Am. Chem. Soc.*, **127** (2005) 6476.

[163]. C. Vericat, G. Andreasen, M. E. Vela, H. Martin and R. C. Salvarezza, *J. Chem. Phys.*, **115** (2001) 6672.

[164]. G. Binning, H. Röhrer, Ch. Gerber and E. Weibel, *Phys. Rev. Lett.*, **49** (1982) 57.

[165]. J. K. Gimzewsky and J. Sass in *Proceedings of ICP Comference on Condesed Matter, Physics Aspects*, World Scientific, Singapore (1991) 303.

[166]. J. Tersoff and D. R. Hamann, *Phys. Rev. B*, **31** (1985) 805.